

Habilitation thesis

Associate professor Dorin LELEA

Politehnica University of Timisoara

Timisoara, Romania

May, 2012

Table of contents

<i>Abstract</i>	1
<i>The professional and scientific achievements</i>	3
1. The experimental research on microchannel heat transfer and fluid flow	3
1.1 Introduction	3
1.2 Description of the experimental setup	4
1.3 Data reduction	6
1.4 Experimental uncertainties	7
1.5 Numerical details.....	8
1.6. Results and discussion.....	9
1.7. Concluding remarks.....	14
2. The axial conduction influence on partial heating of the microchannels	15
2.1 Frictional losses evaluation of a water flow in microtubes	15
2.1.1. Introduction	15
2.1.2. Problem description.....	16
2.1.3. Numerical details.....	18
2.1.4. Results and discussion.....	19
2.1.5. Conclusions	22
2.2 The heat transfer aspects on a conjugate partial heating of the microtubes	22
2.2.1. Introduction	22
2.2.2. Numerical details.....	24
2.2.3. Results and discussion.....	26
2.2.4. Conclusions	33
2.3 The heat transfer and fluid flow of a partially heated microchannel heat sink	33
2.3.1. Numerical details.....	35
2.3.2. Results and discussion	37
2.3.3. Conclusions	39
2.4 Effects of temperature dependent thermal conductivity on Nu number behavior in micro-tubes	39
2.4.1. Numerical details.....	41
2.4.2. Results and discussion.....	43
2.4.3. Conclusions	45
3. The viscous dissipation effect on heat transfer and fluid flow in micro-tubes and microchannel heat sinks	45
3.1 The viscous dissipation effect on heat transfer and fluid flow in micro-tubes	45
3.1.1. Numerical details.....	47
3.1.2. Results and discussion.....	49

Habilitation thesis

3.1.3. Conclusions	51
3.2 The developing heat transfer and fluid flow in micro-channel heat sink with viscous heating effect.....	51
3.2.1. Numerical details.....	53
3.2.2. Results and discussion.....	56
3.2.3. Conclusions	59
4. The microtube heat sink with tangential impingement jet.....	59
4.1 The microtube heat sink with tangential impingement jet and variable fluid properties ..	59
4.1.1. Problem description and numerical details.....	60
4.1.2. Results and discussion.....	63
4.1.3. Conclusions	68
4.2 Effects of inlet geometry on heat transfer and fluid flow of tangential micro-heat sink	68
4.2.1. Problem description and numerical solution	70
4.2.1.1. Numerical details.....	70
4.2.1.2. The experimental validation of the numerical model.....	73
4.2.2. Results and discussion.....	75
4.2.3. Conclusions	78
4.3 The tangential micro-heat sink with multiple fluid inlets.....	78
4.3.1. Problem description and numerical solution	78
4.3.2. Results and discussion.....	82
4.3.3. Conclusions	84
5. The micro-tube heat transfer and fluid flow of nanofluids	84
5.1 The micro-tube heat transfer and fluid flow of water based Al₂O₃ nanofluid with viscous dissipation	84
5.1.1. Numerical details.....	86
5.1.2. Results and discussion.....	88
5.1.3. Conclusions	93
5.2 The performance evaluation of Al₂O₃/water nanofluid flow and heat transfer in microchannel heat sink	93
5.2.1. Numerical details.....	93
5.2.2. The code validation	96
5.2.3. Results and discussion.....	98
5.2.4. Conclusions	102
6. The thermal and hydrodynamic analysis of the extended surfaces used for compact heat exchangers.....	102
6.1 Problem Description	103
6.2 Numerical Details.....	104
6.3 Thermal and Hydrodynamic Characteristics.....	105
6.4. Hydrodynamic Results.....	106
6.5. Thermal Results.....	106

Habilitation thesis

6.6. Performance Evaluation.....	107
6.7. Conclusions	108
<i>Professional development plan</i>	109
<i>References</i>	112

Abstract

Since the *Phd* thesis elaborated in 1997 the professional activities in the field of research and education had the topics related to thermal engineering. Until 2002 the topics were mostly in the field of compact heat exchangers and numerical modeling of thermal phenomena. In 2002 research activities were performed at the University of Tokyo Institute of Industrial Science through the project made in Prof. Shigefumi Nishio laboratory with the following title: Study of Microchannel Heat Sinks for LSI Chip Cooling. Considering, at that time the available results about experimental research on microchannel heat transfer and fluid flow characteristics, one can conclude that there were a large scattering in the obtained results. This was especially serious in the case of the heat transfer results. For example, there is an optimum size of channels in the so-called microchannel heat sink and the result of optimization depends strongly on the heat transfer characteristics in microchannels. So, this was the reason for making the experimental research on single-phase microtube heat transfer. The research report was published in the International Journal of Heat and Mass Transfer [24] that was cited 93 times since 2005. After that, the research activities in the field of microchannel heat transfer and fluid flow were further developed at the Politehnica University of Timisoara and Laboratory for numerical simulations in thermal engineering. The issues that were considered were related to influence of fluid properties, wall axial conduction, partial heating and viscous heating on heat transfer and fluid flow behavior in microchannels. It has to be state that for these phenomena the proper numerical codes were developed based on finite volume method considering microtubes and microchannel heat sinks.

Moreover, in order to optimize the microscale thermal devices the various flow configurations were considered. The new concept of microchannel heat sink with tangential impingement jet at the inlet cross section was proposed. Following this research, it was concluded that both, lower peak temperature and lower temperature difference are associated to jet impingement heat sink. Therefore, an additional effort regarding the inlet manifold is fully justified considering the thermal benefits.

Besides, research on thermal and fluid dynamics phenomena were realized in order to investigate the fundamental issues regarding the swirling flow and heat transfer augmentation in the microchannel heat sinks. It was concluded that the axial velocities are higher near the tube wall and decreases in the axis of the tube. In addition, the reverse flow is observed in the core of the tube. On the mechanism of the heat transfer, it has to be emphasized that the acceleration of the fluid flow and higher axial velocities near the tube wall are responsible for the heat transfer enhancement. In the same report, the optimization of the inlet cross-section was realized. It was found that wider and shorter rectangular cross-section is more suitable if the analysis is made on a fixed pumping power basis.

Furthermore, the micro-heat sinks with multiple inlets were studied. It was found that in the case of tangential micro-heat sink with three inlet cross-sections the temperature distribution is dependent on the position of the second inlet jet if the first one is fixed at the center of the microtube. If the analysis is made on a fixed pumping power basis, the minimum temperatures are higher for multiple inlets compared with the micro-heat sink with single inlet jet. Moreover, the micro-heat sink with multiple inlet jets has the lower temperature difference on a bottom surface between the inlet and outlet of the microtube.

Another topic that was analyzed in the recent year is related to the nanofluid flow in the microchannels. Both the microtube and microchannel heat sinks configurations were considered. The water based Al_2O_3 nanofluid was used in the analysis with the homogenous model used for numerical prediction of the heat transfer and fluid flow through

microchannels, along with the two relations for viscosity [132,140] and one for thermal conductivity [139] that gives the acceptable deviation compared with experimental results.

As for the future professional plan, it was intended to establish and develop the laboratory for experimental research of microscale devices similar to that used at the University of Tokyo. It was proposed to perform the experimental research on single-phase and two-phase fluid flow and heat transfer in tangential microchannel heat sink.

Besides, the numerical analysis of mixing phenomena in microchannels is proposed. Moreover, the nanofluid passive mixing in microchannels has an immediate application in the area of process industry and Bio-MEMS for nanodrug delivery. In this case the the mixing length is crucial issue so the configurations that insures the rapid mixing will be developed. In addition, the nanofluid flow and heat transfer in tangential microchannel heat sink will be analyzed.

Some of the experiences obtained through the research topics presented above, were included in the courses taught by the author at the undergraduate and graduate level related to Numerical methods in thermal engineering and Design of thermal systems.

It has to be emphasized that the topics related to the microchannel heat transfer and fluid flow were analyzed in the frame of PCE-IDEAS Research grant 670/2009 financed by the Romanian National Research Council CNCS-UEFISCDI.

Teza de abilitare

Rezumat

De la susținerea tezei de doctorat elaborată în 1997, activitățile profesionale în domeniul cercetării și educației au avut subiecte legate de inginerie termică. Până în 2002, subiectele au fost în mare parte în domeniul schimbătoarelor de căldură compacte și a modelării numerice a fenomenelor termice. În 2002, activitățile de cercetare au fost efectuate la Universitatea din Tokyo, Institutul de Științe Industriale în cadrul proiectului realizat în laboratorul Prof. Shigefumi Nishio c următorul titlu: *Study of Microchannel Heat Sinks for LSI Chip Cooling*. Având în vedere rezultatele disponibile din domeniul cercetării experimentale privind transferul de căldură în microcanale și caracteristicile de curgere a fluidului, s-a putut concluziona că a existat o dispersie mare a rezultatelor obținute. Acest lucru a fost deosebit de grav în cazul rezultatelor referitoare la transferul de căldură. De exemplu, există o dimensiune optimă a microcanalelor din microdispozitivul termic iar rezultatul optimizării depinde foarte mult de caracteristicile termice ale microcanalelor. Prin urmare, acesta a fost motivul pentru care s-a realizat cercetarea experimentală a transferului de căldură monofazic prin microtuburi. Raportul de cercetare a fost publicat într-o lucrare în revista *International Journal of Heat and Mass Transfer* [24], care a fost citată de 93 de ori începând cu anul 2005. După aceea, activitățile de cercetare în domeniul transferului de căldură și curgerii prin microcanale au fost dezvoltate la Universitatea Politehnica din Timișoara în cadrul laboratorului de simulări numerice în domeniul ingineriei termice. Aspectele care au fost luate în considerare au fost legate de influența proprietăților fluidelor, conducției termice axiale prin peretele microcanalului, încălzirii parțiale sau încălzirii vâscoase. Trebuie menționat că pentru analiza fenomenelor enumerate mai sus, au fost dezvoltate programe numerice proprii considerând atât microtuburi cât și microdispozitive termice.

Mai mult, în scopul de a optimiza micro-dispozitivele termice, diverse configurații de curgere au fost luate în considerare. Noul concept de micro-dispozitiv termic cu jeturi tangențiale pe direcția de curgere a fost introdus. În urma acestei cercetări, sa ajuns la concluzia că atât, temperaturi maxime cât și diferențe de temperaturi mai mici sunt asociate cu microdispozitive termice având configurația de curgere cu jeturi tangențiale. Prin urmare, un efort suplimentar în ceea ce privește racordul de admisie este pe deplin justificat având în vedere beneficiile termice.

De asemenea, au fost studiate micro-dispozitivele termice cu jeturi tangențiale multiple. S-a constatat că în cazul micro-dispozitivului cu trei jeturi distribuția temperaturii depinde de poziția celei de a doua intrare dacă prima secțiune este fixată în mijlocul microcanalului. În cazul în care analiza se face în baza puterii de pompare fixe, temperaturile minime sunt mai mari pentru dispozitive cu intrări multiple, comparativ cu micro-dispozitivul de căldură cu un singur jet. În schimb, micro-dispozitivul termic cu intrări multiple are o diferență de temperatură intrare/ieșire mai mică pe suprafața de contact cu sursa de căldură.

Totodată, recent s-a realizat un studiu referitor la transferul de căldură și curgerea nanofluidelor prin microtuburi și microdispozitive termice. Nanofluidul cu particule de Al_2O_3 și apă a fost luat în considerare iar modelarea numerică s-a realizat în baza modelului monofazic cu doua relații matematice: una pentru conductivitatea termică [139] și a doua pentru viscozitate [132,140]. Rezultatele obținute au avut abateri acceptabile de rezultatele experimentale.

În privința planurilor profesionale de viitor se are în vedere realizarea unui laborator de cercetări experimentale în domeniul micro-dispozitivelor termice, în faza inițială cu

Teza de abilitare

instalația similară celei folosite la Universitatea din Tokyo [24]. Se propune în prima fază o cercetare experimentală asupra performanțelor termice și fluidodinamice ale microdispozitivelor cu jeturi tangențiale atât în regim monofazic, cât și bifazic.

De asemenea, se propune o analiză numerică a fenomenelor de amestecare a fluidelor prin microcanale. Mai mult, se are în vedere amestecarea nanoparticulelor cu fluidul de bază fenomen cu aplicație imediată în domeniul industriei de proces sau Bio-MEMS pentru administrarea dirijată a medicamentelor. În acest caz, lungimea de amestec este crucială și prin urmare vor fi dezvoltate configurații care asigură amestecare rapidă. Totodată va fi analizată curgerea și transferul de căldură a nanofluidelor prin microdispozitive cu jeturi tangențiale.

Unele dintre experiențele obținute în cadrul programelor de cercetare au fost incluse în programele unor discipline ținute de autor precum modelarea numerică a fenomenelor termice sau proiectarea sistemelor termice.

Trebuie menționat că o parte din cercetarea referitoare la transferul termic prin microcanale a fost realizată în cadrul grantului de cercetare PCE – IDEI CNCS-UEFISDI nr. 670/2009.

The professional and scientific achievements

1. The experimental research on microchannel heat transfer and fluid flow

1.1 Introduction

The term “micro-channel” comes to be used in some engineering fields but its definition is dependent on researchers. As is well known, the conventional heat transfer theory predicts that heat transfer coefficient of fully developed laminar flow in a channel increases if the cross-section of the channel decreases [1]. Tubes or channels of smaller size are therefore chosen to attain a high heat transfer coefficient. For example, such tubes or channels are used to manage the power dissipation in LSI chips. On the other hand, μ - TAS (Micro Total Chemical Analyzing System) [2], MEMS (Micro Electrical-Mechanical Systems) and bio - chips [3] consist of the network of channels of small cross-sectional size manufactured with micro processing techniques. To develop such systems, we have to obtain a good understanding of flow and diffusion characteristics. In the present report, the tubes or channels utilized in such fields are called “microchannels”. In the past decade, a large number of research reports considering microchannel heat transfer, have been presented. Since the topic of the present research was water flow and heat transfer, only reports on liquid as the working fluid will be reviewed.

Celata et al. [4], investigated experimentally single phase heat transfer of R 114 in a stainless steel tube of the diameter $D = 0.130$ mm. They have found that friction factor is in good agreement with the Hagen-Poiseuille theory [5] as far as the Re - number is below 583. For heat transfer characteristics, they have found that Nu is not constant but depends on Re.

Mala et al. [6], experimentally investigated the flow characteristics of water through microtubes of $D_i = 50 - 254$ μm . Two types of microtubes are used, and they are silica fused and stainless steel tubes. It is observed that for low values of Re the experimental data of $f\text{Re}$ agree well with a theory. On the other hand with increasing Re significant deviation from the conventional theory comes to be observed. Also, this deviation increases as the tube diameter decreases. They reported also an early transition from the laminar to turbulent flow.

Judy et al. [7], examined experimentally the flow characteristics of water, hexane and isopropanol, in fused silica micro tubes with $D_i = 20 - 150$ μm for $\text{Re} = 20 - 2000$. Their results indicated that the values of $f\text{Re}$ agree well with the conventional Stokes flow theory [5] for $D_i = 100$ and 150 μm . For $D \leq 75$ μm , the experimental results deviates from the conventional value of $f\text{Re}=64$ towards lower values, although it preserved a constant value over the tested range of Re. Li et al. [8], investigated experimentally the flow characteristics of deionized water in the glass ($D_h = 79.9 - 166.3$ μm), silicon ($D_h = 100.25 - 205.3$ μm) and stainless steel tubes ($D_h = 128.76 - 179.8$ μm). The length of the tubes was long enough to ensure that the flow is fully developed. They have found that there is no difference from the conventional and the value of $f\text{Re}$ is almost 64 for the smooth tubes made of glass or silicon, and 15 - 37 % higher than 64 for the stainless steel tubes. The transition from laminar to turbulent flow is observed in the range $\text{Re} = 1700 - 2000$.

Yang et al. [9], examined experimentally the flow characteristics of water, R-134a and air in small tubes of $D_h = 0.171 - 4.01$ mm for the laminar and turbulent flow regimes. The laminar - turbulent transition was observed in the range of $\text{Re} = 1200 - 3800$ and it is increasing with decreasing the tube diameter. The friction factor, in the case of liquids, agrees well with conventional Blasius and Poiseuille equations in the turbulent and laminar regime, respectively.

Peng et al. [10], investigated the heat transfer and flow characteristics of methanol and water. Microchannels of four different sizes are used, with a channel width ranging from 0.31 mm to 0.75 mm. The transition from the laminar flow occurs at $Re = 300$, and to the fully turbulent flow at $Re = 1000$.

Qu et al. [11], investigated the heat transfer of water flows through trapezoidal silicon microchannels. They have found that Nu number is much lower than conventional theoretical values.

Peng and Peterson [12], investigated experimentally heat transfer through rectangular microchannels with binary mixtures of water and methanol as a working fluid. They have analyzed both the influence of mixture concentration and channel geometry on heat transfer coefficient. They also found early transition from the laminar to turbulent regime, and the critical Re-number decreases as the hydraulic diameter of the channel decreases.

Peng and Peterson [13], investigated experimentally both the laminar and turbulent heat transfer and fluid flow characteristics of water through microchannels with $D_h = 0.133 - 0.367$. They have found a strong dependence of heat transfer and hydrodynamic characteristics on the channel size.

Gao et al. [14], investigated experimentally the heat transfer and flow characteristics of demineralized water flows through microchannels with $D_h = 0.1 - 1$ mm. The friction factor was in good agreement with conventional theoretical results for channels but the experimental data of Nu are much lower than the conventional theoretical results for smaller values of D_h .

Agostini et al. [15], investigated experimentally the heat transfer and flow characteristics of R134a through a multichannel configuration with $D_h = 0.77$ and 1.17 mm. In the case of the friction factor results there is a reasonable agreement with conventional theoretical results, both in the laminar and the turbulent regime. However, the experimental results of Nu are dependent on Re for both laminar and turbulent regimes.

Considering the available results about experimental research on microchannel heat transfer and fluid flow characteristics, one can conclude that there is a large scattering in the obtained results. This is especially serious in the case of the heat transfer results. For example, there is an optimum size of channels in the so-called microchannel heat sink and the result of optimization depends strongly on the heat transfer characteristics in microchannels. So, this was the reason for making the research on single-phase microtube heat transfer.

1.2 Description of the experimental setup

The experimental setup, used in the present study, was designed in the way that it allows the analysis of a developing heat transfer and fluid flow. The schematic view of the experimental apparatus is presented in Fig. 1.1.

Distilled water is the working fluid that is driven in a microtube with a micropump (NS type NP – KX – 110) for volume flow rates 0.01 – 10 ml/min. A microchannel is placed inside a vacuum chamber to eliminate heat loss to ambient. The temperature of water, at the inlet of the microtube was kept at a prescribed value by using a counter-flow heat exchanger, placed before the microchannel. Water was circulated between the heat exchanger and a constant temperature bath to maintain the inlet temperature. Filters of 2 μm were set both before the microchannel and before the pump, for suppressing particles to enter inside the test tube.

The microtube was heated by Joule heating with an electrical power supply (Yokogawa 2558) and the input heat was measured by a digital power meter (Yokogawa WT 200). The electrodes connected to the microtubes have a diameter of $d = 250 \mu\text{m}$. In the present experiments, the exit of the tube was kept at the atmospheric pressure. So, the pressure drop through the microtube was determined by measuring the pressure at the inlet of

the test section with a pressure transducer (Kyowa PGM 2 KC and PGM 5 KC). The mass flow rate was determined by measuring the weight of water flowing out from the tube with a digital balance.

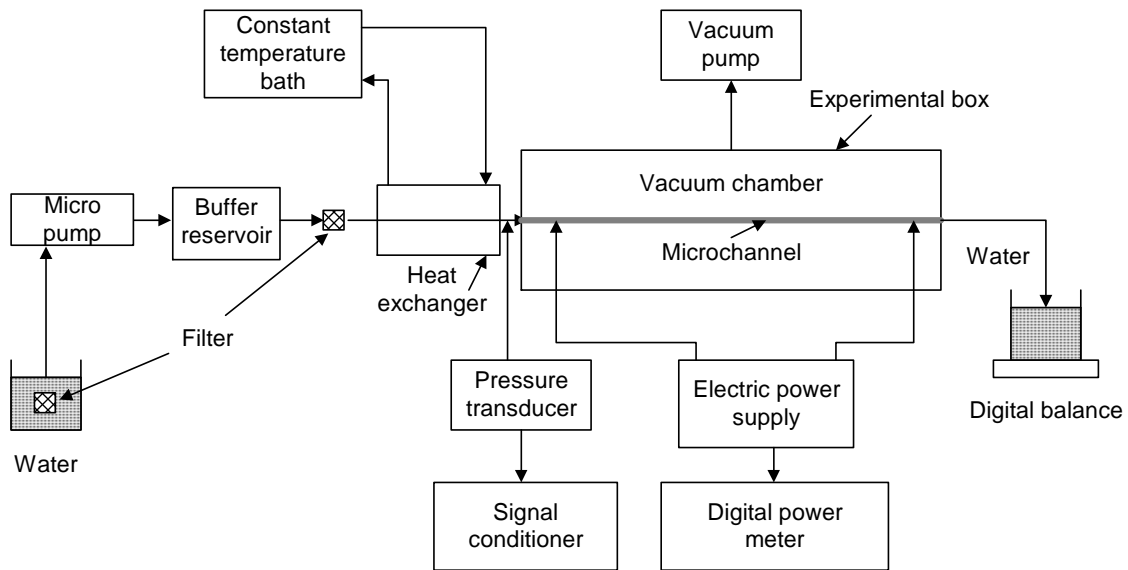


Fig. 1.1. Schematic representation of the experimental setup.

The mean temperature of water was measured at both the entrance and the exit cross section of the experimental setup using K-type thermocouples. The same type thermocouples were used for measuring outer wall temperatures of the microtube. The diameter of all thermocouples was 50 μm and the thermocouple locations are presented in the Fig. 1.2.

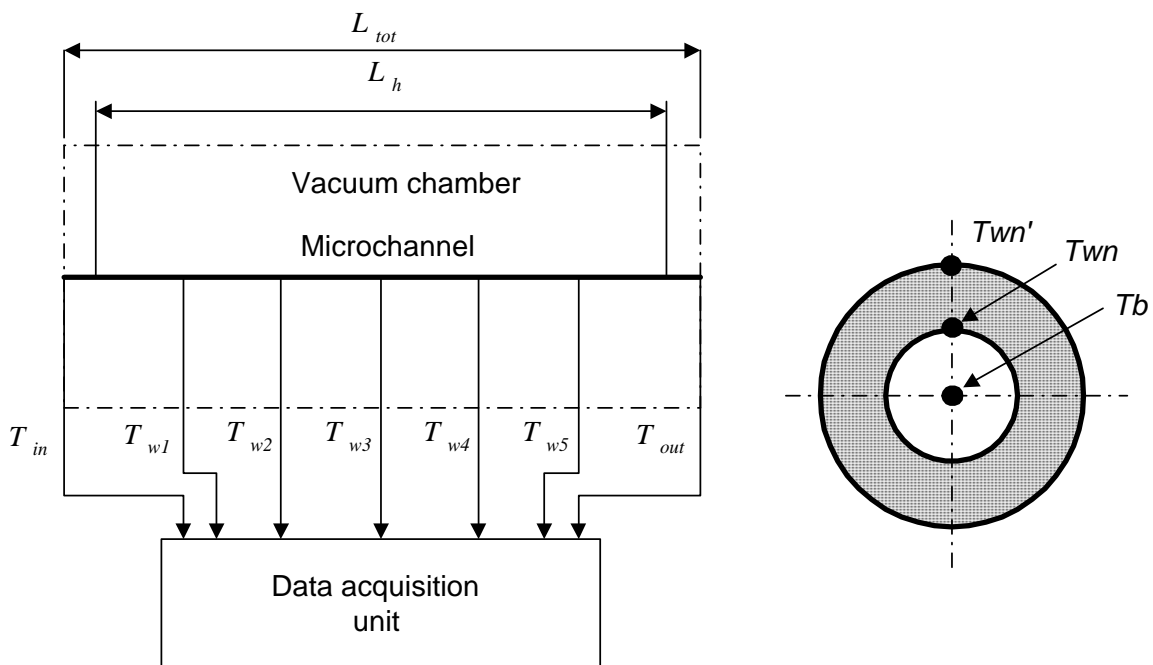


Fig. 1.2. The position of the thermocouples

The tubes were made of stainless steel SUS 304 and the experimental conditions are listed in Table 1. The tubes were heated electrically dissipating the heat in the range $Q = 0.5 - 2$ W.

Table 1 Tube geometry description

Tube nr.	D_i / D_o [μm]	Heating length L_h [mm]	Total length L_{tot} [mm]	Heat input Q [W]	Heat rate q_o [W/m^2]
1	500/700	250	600	0 and 2	3640
2	300/500	95	123	0, 1 and 2	6705 and 13409
3	125.4/300	53	70	0, 0.5 and 0.75	10015 and 15022

1.3 Data reduction

The friction factor is calculated by Eq. (1) based on the experimental data of mass flow rate and the pressure drop due to the friction inside the microtube Δp_f ,

$$f = \frac{L_{tot}}{D_i} \frac{\Delta p_f}{\rho \cdot u_m^2} \quad (1.1)$$

On the other hand, in the present experiment the total pressure drop along the test section is measured. The total pressure drop includes the pressure drop at the inlet and outlet portion of the experimental set-up, pressure drop due to the contraction and expansion of the cross sectional area, pressure drop required for acceleration of the fluid and frictional pressure drop. So, the total pressure drop Δp , can be expressed with the following equation,

$$\Delta p = \Delta p_c + \Delta p_1 + \Delta p_{core} - \Delta p_e + \Delta p_2 \quad (1.2)$$

The pressure drop through the tube, Δp_{core} , is expressed by the following equation:

$$\Delta p_{core} = \Delta p_f + \Delta p_a \quad (1.3)$$

Here, Δp_a , is the pressure drop due to acceleration of the fluid and given by,

$$\Delta p_a = \frac{G^2}{\rho_{in}} \left(\frac{\rho_{in}}{\rho_{out}} - 1 \right) \quad (1.4)$$

Pressure drop due to the contraction is calculated by

$$\Delta p_c = \frac{G^2}{2 \cdot \rho_{in}} (1 - \sigma^2 + K_c) \quad (1.5)$$

Pressure drop due to the expansion is calculated by the following equation

$$\Delta p_e = \frac{G^2}{2 \cdot \rho_{out}} (1 - \sigma^2 - K_e) \quad (1.6)$$

The coefficients K_c and K_e respectively, depends on σ and Re and can be obtained from [5].

Pressure drop at the inlet portion of the experimental setup is defined as

$$\Delta p_1 = \frac{128 \cdot M \cdot L_1 \cdot v_{in}}{\rho_{in} \cdot \pi \cdot D_1^4} \quad (1.7)$$

Pressure drop at the outlet portion of the experimental setup is defined as

$$\Delta p_2 = \frac{128 \cdot M \cdot L_2 \cdot v_{out}}{\rho_{out} \cdot \pi \cdot D_2^4} \quad (1.8)$$

The local value of Nu is calculated by the following equation:

$$\text{Nu} = \frac{h \cdot D_i}{k_f} \quad (1.9)$$

where h is the local heat transfer coefficient defined by the following equation:

$$h = \frac{q}{T_{wn} - T_{bn}} \quad (1.10)$$

where T_{bn} is the local bulk temperature of water at each point of the wall temperature measurement and it is calculated from the heat balance equation:

$$T_{bn} = T_{in} + \frac{\pi \cdot D_i \cdot L_n \cdot q}{M \cdot c_p} \quad (1.11)$$

T_{wn} is the local wall temperature at the inside of the tube and it is obtained from the one-dimensional heat conduction equation using the measured wall temperature at the outside of the microtube:

$$\frac{d^2 T}{dr^2} + \frac{1}{r} \frac{dT}{dr} + \frac{S_c}{k_s} = \frac{1}{r} \frac{d}{dr} \left(r \frac{dT}{dr} \right) + \frac{S_c}{k_s} = 0 \quad (1.12)$$

where S_c is the internal heat source generated inside the microtube wall by the electric power defined as:

$$S_c = \frac{Q}{L_h \cdot \pi \cdot (R_o^2 - R_i^2)} \quad (1.13)$$

After integration the general solution of the Eq. (1.12) is obtained:

$$T = -\frac{r^2}{4} \frac{S_c}{k_s} + C_1 \ln r + C_2 \quad (1.14)$$

Constants C_1 and C_2 can be obtained by the following boundary conditions:

$$\begin{aligned} r = R_o & \quad T = T_{wn}' \\ r = R_i & \quad k_s \frac{dT}{dr} = q_i = \frac{Q}{2R_i \pi L_h} = \frac{S_c}{2} \frac{R_o^2 - R_i^2}{R_i} \end{aligned}$$

Finally, the local temperature at the inside portion of the microtube wall is obtained by the following equation:

$$T_{wn} = T_{wn}' - \frac{S_c}{4k_s} \left[R_o^2 \ln \left(\frac{R_o}{R_i} \right)^2 - (R_o^2 - R_i^2) \right] \quad (1.15)$$

It should be noted that the fluid properties were estimated at the average temperature of water and they were obtained from Computer package PROPATH v. 10.2.

Finally, Re is calculated by the following equation:

$$\text{Re} = \frac{\rho \cdot u_m \cdot D_i}{\mu} \quad (1.16)$$

1.4 Experimental uncertainties

The uncertainty of experimental results have been estimated following the recommendations and method described by Moffat [16,17]. Analyzing the particular uncertainty results that the main problem is the accuracy of the friction constant results as the outcome of difficulties on determining the inner diameter of the microtube. We can measure the inner diameter of the tubes tested, using the following two methods. One of them was to measure the inner diameter at both ends of microtubes by a high – precision microscope. A

disadvantage of this method is the lack of the information on diameter distribution along the tube axes. The other method was to obtain the average inner diameter of the microtube by measuring the mean outer diameter, length and weight of the tube, and the mean inner diameter was determined by using the density of tube material. In this case the accuracy is affected by the accuracy of the three additional parameters stated above. In the present research the later method was used and the uncertainties of some particular parameters, affected by the uncertainty of the inner diameter, are presented in Table 2.

Table 2 The experimental uncertainties

Parameter	Uncertainty [%]		
	$D_i = 125.4 \mu\text{m}$	$D_i = 300 \mu\text{m}$	$D_i = 500 \mu\text{m}$
Inner diameter, D_i	5.6	0.98	0.4
Mass flow rate, M	0.04	0.04	0.04
Re – number	5.3	0.98	0.4
Friction factor f	18.7	3.9	1.5
Local temperature difference, ΔT_{loc}	5.9	2.8	7.9
Local heat transfer coefficient, h	8.9	3.6	8.9

1.5 Numerical details

In order to discuss experimental results obtained in the present experiments, the velocity and temperature distributions were numerically solved taking account of the temperature variation of fluid properties.

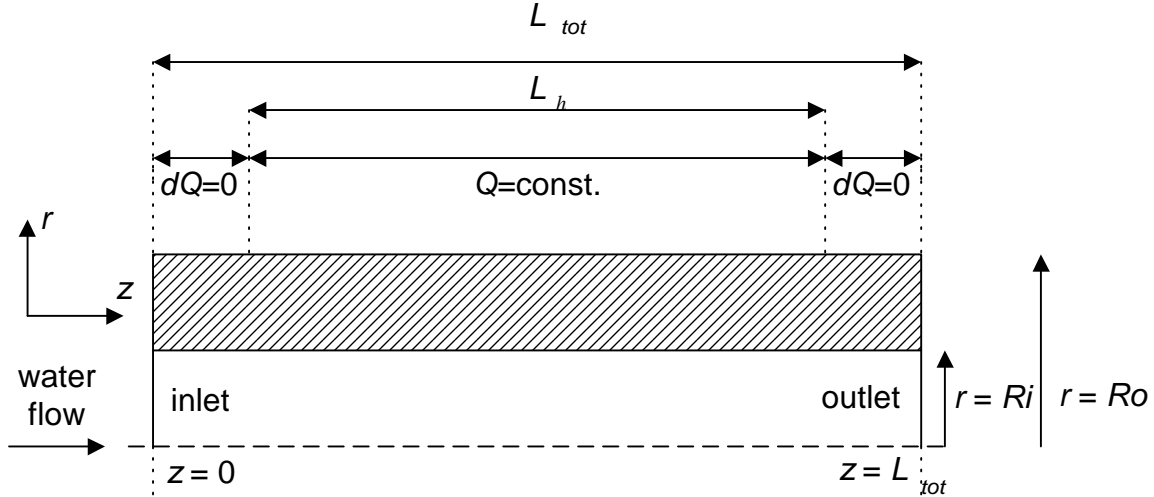


Fig. 1.3. Schematic presentation of the test tube

As mentioned already, in the experimental setup, there were two electrodes at both ends of the test tube. So, as shown in Fig. 1.3, the respective insulated parts were included in the numerical domain. The following set of partial differential equations is used to describe the phenomena:

Continuity equation:

$$\frac{\partial u}{\partial z} + \frac{1}{r} \frac{\partial(r \cdot v)}{\partial r} = 0 \quad (1.17)$$

Momentum equation:

$$\rho \cdot \left(v \frac{\partial u}{\partial r} + u \frac{\partial u}{\partial z} \right) = -\frac{dp}{dz} + \frac{1}{r} \frac{\partial}{\partial r} \left(\mu(T)r \frac{\partial u}{\partial r} \right) \quad (1.18)$$

Energy equation:

$$\rho \cdot c_p \cdot \left(v \frac{\partial T}{\partial r} + u \frac{\partial T}{\partial z} \right) = k \cdot \left[\frac{1}{r} \frac{\partial}{\partial r} \left(r \frac{\partial T}{\partial r} \right) + \frac{\partial^2 T}{\partial z^2} \right] \quad (1.19)$$

At the inlet of the tube, the uniform velocity and temperature field is considered, while at the exit the temperature gradient is equal to zero.

The boundary conditions are:

$$\begin{aligned} z = 0, 0 < r < R_o: & \quad u = u_0, T = T_w = T_0 \\ 0 < z < L_{tot}: & \quad r = 0, \frac{\partial u}{\partial r} = 0, \frac{\partial T}{\partial r} = 0, v = 0 \\ & \quad r = R_i, u = v = 0 \end{aligned}$$

The Joule heating of the tube wall can be expressed either by the uniform heat generation through the tube wall or by the uniform heat flux imposed on the outer surface of the wall. For the latter case, the boundary condition is defined as,

$$\begin{aligned} r = R_o: & \quad q_o = k_s \frac{\partial T}{\partial r} \quad (\text{for the heated portion of the tube}) \\ & \quad k_s \frac{\partial T}{\partial r} = 0 \quad (\text{for the insulated portion of the tube}) \end{aligned}$$

where q_o is the heat flux based on the outer heat transfer area of the tube wall (Table 1).

$$z = L_{tot}, 0 < r < R_o: \quad \frac{\partial T}{\partial z} = 0$$

The partial differential equations (17) – (19) together with boundary conditions, are solved using the finite volume method described in [18].

First, the parabolic flow field condition is considered and the velocity field is solved. The temperature field, as a conjugate heat transfer problem, was then solved using the obtained velocity field. The fluid flow regime is considered to be a steady-state laminar flow with constant fluid properties except for the fluid viscosity that is calculated with following equation:

$$\mu = \mu_0 \cdot e^{\beta(T-T_0)} \quad (1.20)$$

In order to test the grid sensitivity, two grids have been used. The coarser one with 250 cells in radial direction and 400 cells in axial direction and finer grid with 500 and 800 cells in z - and r - direction respectively. Differences in the results of fRe or Nu were smaller than 0.1 %, so the coarser grid has been used for further calculations.

1.6. Results and discussion

1.6.1. Hydrodynamic results

1.6.2. Hydrodynamic results for no-heating fluid flow

The pressure drop from the inlet of the tube up to some axial location can be expressed with the following equation:

$$\frac{\Delta p(z)}{(\rho \cdot u_m^2)/2} = \frac{\Delta p(z)_{f.d.}}{(\rho \cdot u_m^2)/2} + K(z) \quad (1.21)$$

where $\Delta p(z)_{f.d.}$ is the pressure drop in the case of the fully developed flow and $K(z)$ is the incremental pressure drop due to the entrance region effects. Eq. (1.21) can also be written in the following form:

$$\frac{\Delta p(z)}{(\rho \cdot u_m^2)/2} = f \operatorname{Re}_{f.d.} \left(\frac{z}{D_i \cdot \operatorname{Re}} \right) + K(z) \quad (1.22)$$

For a very long tubes (as in the present experiments), the incremental pressured drop for a laminar flow inside the tubes has the following value [19]:

$$K(\infty) = 1.25$$

Finally the fully developed value of the $f \operatorname{Re}_{f.d.}$ can be obtained from the Eq. (1.22).

The numerical and experimental results of $f \operatorname{Re}_{f.d.}$ for $D_i = 300$ and $125.4 \mu\text{m}$ are plotted to Re in Figs. 1.4 and 1.5 respectively. In these figures, the no-heating fluid flows are considered.

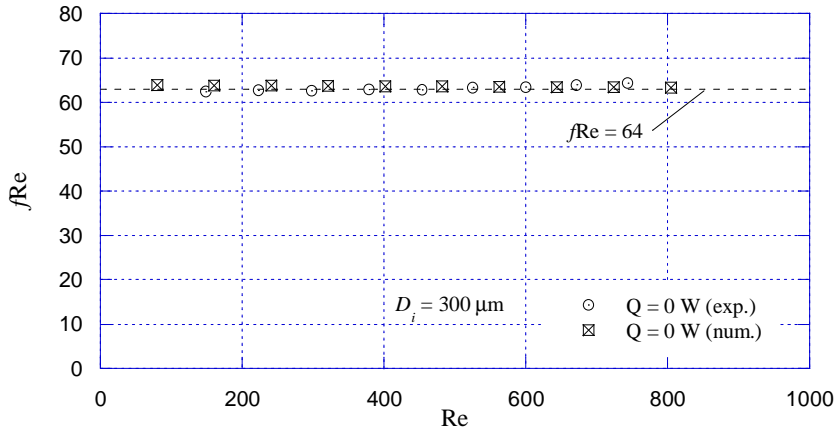


Fig. 1.4. Experimental and numerical results of $f \operatorname{Re}$ for no-heating fluid flow in tube of $D_i = 300 \mu\text{m}$

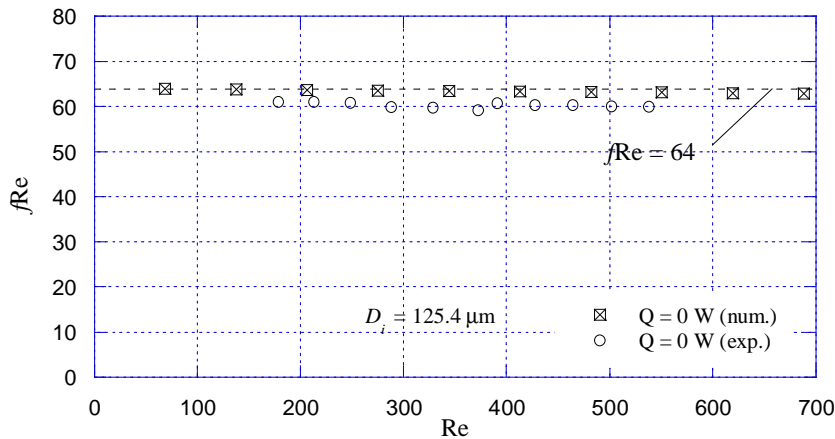


Fig. 1.5. Experimental and numerical results of $f \operatorname{Re}$ for no-heating fluid flow in tube of $D_i = 125.4 \mu\text{m}$

As seen from Figs. 1.4 and 1.5, the obtained results for $fRe_{f.d.}$ are in good agreement with the conventional theoretical value of $fRe = 64$. There is a difference between the experimental and numerical results but this difference is much lower than the experimental uncertainty of the measurements. In short, the present results indicate that the conventional relation of $fRe = 64$ is valid and there is also no evidence on an early transition from laminar to turbulent regime, at least for $D_i > 100 \mu\text{m}$ and the Re range covered in the experiment.

1.6.3. Hydrodynamic results for different input power levels

The numerical and experimental results of fRe under heated conditions for $D_i = 300 \mu\text{m}$ and $500 \mu\text{m}$ are presented in Figs. 1.6 and 1.7 respectively. In the case of the tube with $D_i = 300 \mu\text{m}$, regardless of the input power level, the value of fRe is almost constant both for the numerical and experimental results. It should be noted here that, as shown in Table 1, the heated portion of this tube was almost the same as the total length of the tube.

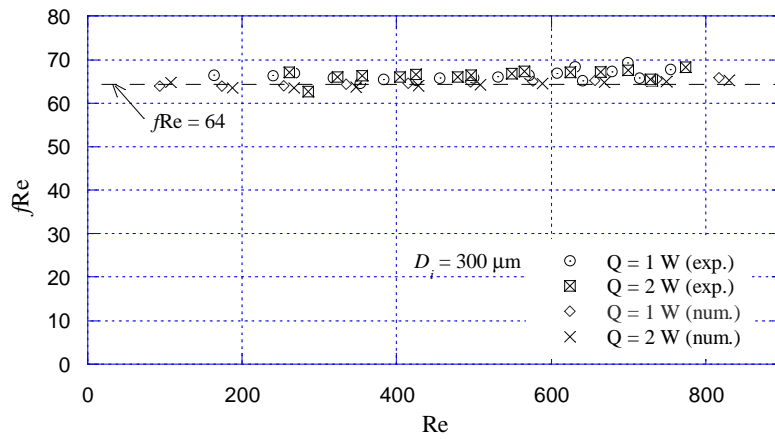


Fig. 1.6. Experimental and numerical results of fRe for different input powers in tube of $D_i = 300 \mu\text{m}$

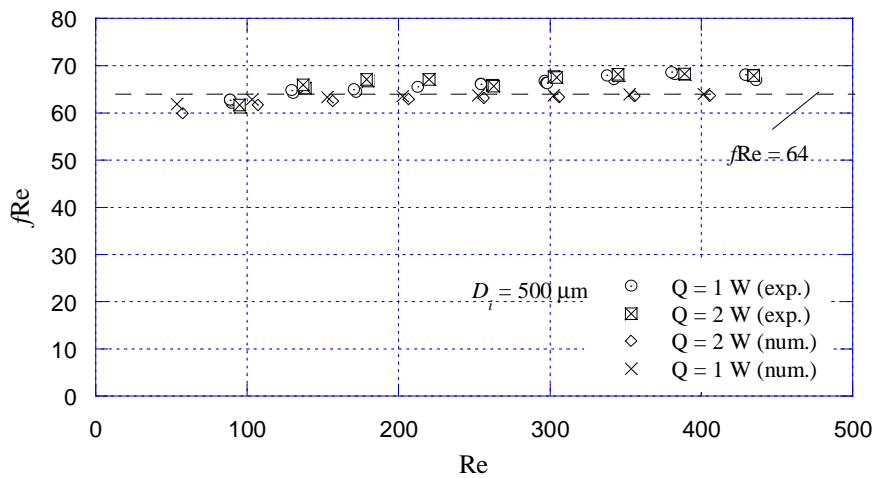


Fig. 1.7. Experimental and numerical results of fRe for different input powers in tube of $D_i = 500 \mu\text{m}$

Contrary, in the case of the tube with $D_i = 500 \mu\text{m}$, the experimental value of $f\text{Re}$ is decreasing with decreasing Re especially in the case of the lower Re where a larger temperature differences between the inlet and outlet of the tube are expected. This behavior of $f\text{Re}$ is also confirmed by the present numerical results plotted in the figures. It should be noted here that, as shown in Table 1, the heated portion of this tube is significantly shorter than the total length and the fluid viscosity is evaluated at the arithmetic mean temperature between the inlet and outlet.

From the equation (1.1) and (1.15), the $f\text{Re}$ can be defined as follows:

$$f \text{ Re} = \frac{2 \cdot \Delta p \cdot D_i^2}{L_{\text{tot}} \cdot u_m \cdot \mu} \quad (1.23)$$

In the case of the no-heating fluid flow, the relationship between the pressure drop and the mean fluid velocity is linear, so the ratio $\Delta p/u_m$ has a constant value. In the case of the fluid flow under heated conditions, due to the lower wall shear stress, the pressure drop and the ratio $\Delta p/u_m$ is not constant but decreases exponentially. When the heated portion of the tube is almost the same as the total length of the tube, the ratio $\Delta p/u_m$ decreases almost at the same rate as the fluid viscosity, with decreasing the mean fluid velocity. Contrary, if the heated portion of the tube is significantly shorter than the total length of the tube, the ratio $\Delta p/u_m$ decreases faster with decreasing the mean fluid velocity, than a fluid viscosity. For the present experimental conditions, the changes in fluid density are negligible.

Taking this into account, the value of $f\text{Re}$ will be constant only for the case when the total length of the tube is heated. In the case of the partial heating, the value of the $f\text{Re}$ will be lower than the conventional relation $f\text{Re} = 64$.

1.6.4. Thermal results

To keep the experimental uncertainty within an allowable level for thermal results in a microtube, special care should be taken of the reduction of heat loss. In the present experiment, the followings were carried out to reduce the heat loss from the microtube. The room temperature was kept at the inlet temperature of water (about $20 \text{ }^\circ\text{C}$) with an air – conditioning unit. As shown in Fig. 1, the microtube was placed in the vacuum chamber. The remaining way of heat transfer to the ambient was heat conduction through the electrodes connected to the tube wall as well as through the power wires connected to the digital power meter. This problem was especially serious in the case of the microtubes, and K – type thermocouples of $50 \mu\text{m}$ in diameter were chosen to minimize the amount of heat loss through five thermocouples placed on the tube wall.

The following value of ε was used as a measure of thermal uncertainty in the present experiment:

$$\varepsilon = \frac{Q_{\text{out}} - Q_{\text{in}}}{Q_{\text{in}}} \cdot 100 \quad (1.24)$$

where Q_{in} is the electrical input power, Q_{out} is the amount of heat transferred to water and this is given by,

$$Q_{\text{out}} = M \cdot c_p \cdot (T_{\text{out}} - T_{\text{in}}) \quad (1.25)$$

In Figs. 1.8 and 1.9, experimental results of ε were presented for microtubes $D_i = 125.4$ and $300 \mu\text{m}$. From both figures it is clear that, as Re decreases, the absolute value of ε increases. The reason may be explained as follows: the outlet temperature of water increases for smaller Re . This results in an increase of the temperature of the electrode placed at the outlet and also results in an increase of heat conduction through it to the ambient.

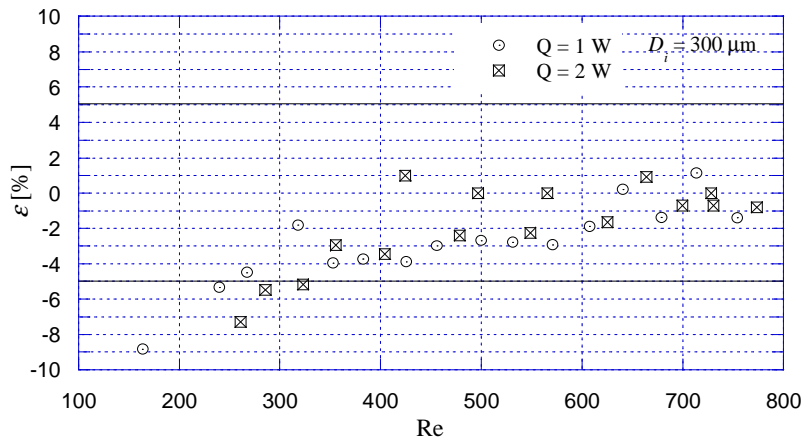


Fig. 1.8. Heat balance for tube of $D_i = 300 \mu\text{m}$

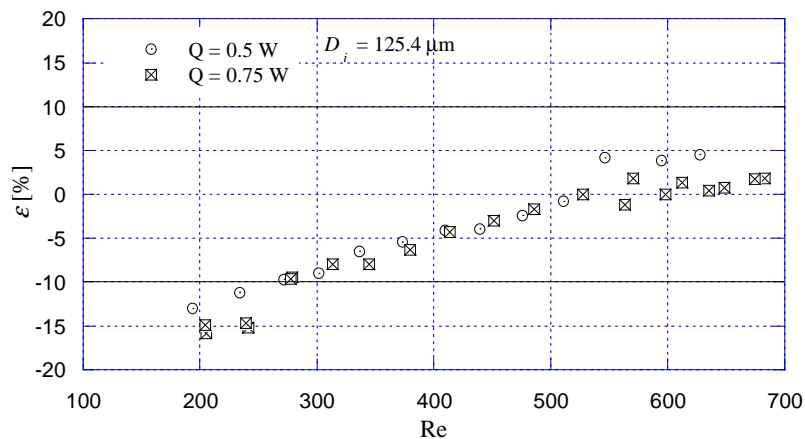


Fig. 1.9. Heat balance for tube of $D_i = 125.4 \mu\text{m}$

If the heat input is very large, the heat losses are larger than an acceptable value. Contrary if the heat input is very low, the temperature difference between the tube wall and water is much lower than an acceptable level. Anyway, the results shown in Figs. 1.8 and 1.9, the value of ε is of $\pm 5\%$ and about $\pm 10\%$ for $D_i = 300 \mu\text{m}$ and $125.4 \mu\text{m}$ respectively.

In Figs. 1.10 – 1.12, the experimental results of the local value of Nu are plotted to the axial location for the respective experimental conditions. The experimental data in Figs. 1.10 – 1.12 indicate that, as predicted by conventional heat transfer theories, the local Nu number defined by equation (1.9) decreases and approaches to the constant value of 4.36 with increasing z . In Fig. 1.13 they are plotted to the non-dimensional axial distance together with the present numerical result and the theoretical values of Shah and London [19]. As seen from Fig. 1.13, the present experimental data are in reasonable agreement with both the numerical and the theoretical results. In short, it can be concluded that, at least for the present experimental conditions, the local value of Nu is in good agreement with conventional theories including the entrance region.

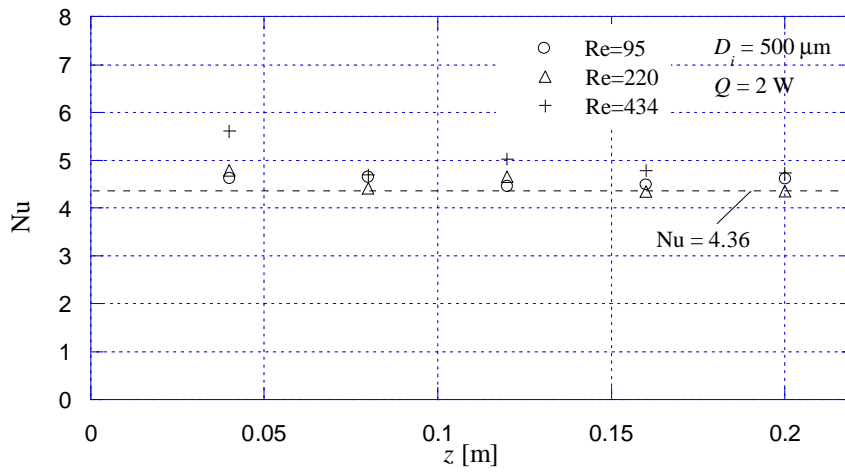


Fig. 1.10. Experimental results of local value of Nu for microtube of $D_i = 500 \mu\text{m}$ and input power of $Q = 2 \text{ W}$

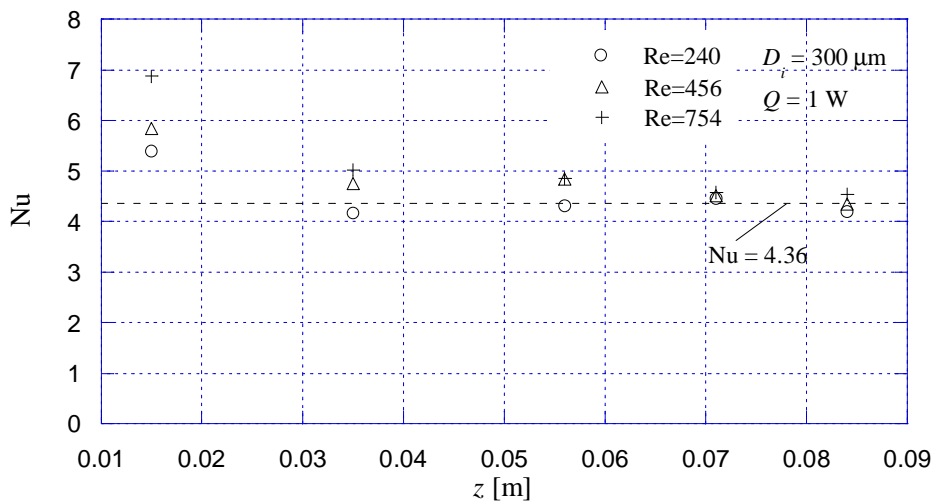


Fig. 1.11. Experimental results of local value of Nu for microtube of $D_i = 300 \mu\text{m}$ and input power of $Q = 1 \text{ W}$

1.7. Concluding remarks

A developing microchannel heat transfer and fluid flow has been analyzed experimentally on tubes of $D_i = 0.1, 0.3$ and 0.5 mm , having water as a working fluid. The experimental results have been compared both with theoretical predictions from literature and results obtained by numerical modeling of the present experiment. The experimental results of microchannel flow and heat transfer characteristics obtained in the present experiments confirms that, including the entrance effects, the conventional or classical theories are applicable for water flow through microchannel of above sizes.

This conclusion does not provide any new aspect, but this is meaningful considering the large scattering in the existing results.

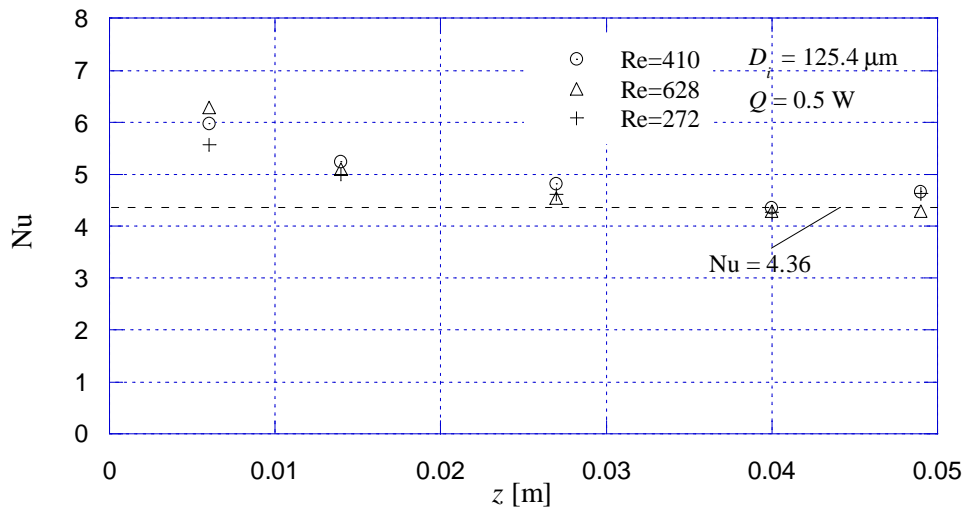


Fig. 1.12. Experimental results of local value of Nu for microtube of $D_i = 125.4 \mu\text{m}$ and input power of $Q = 0.5 \text{ W}$

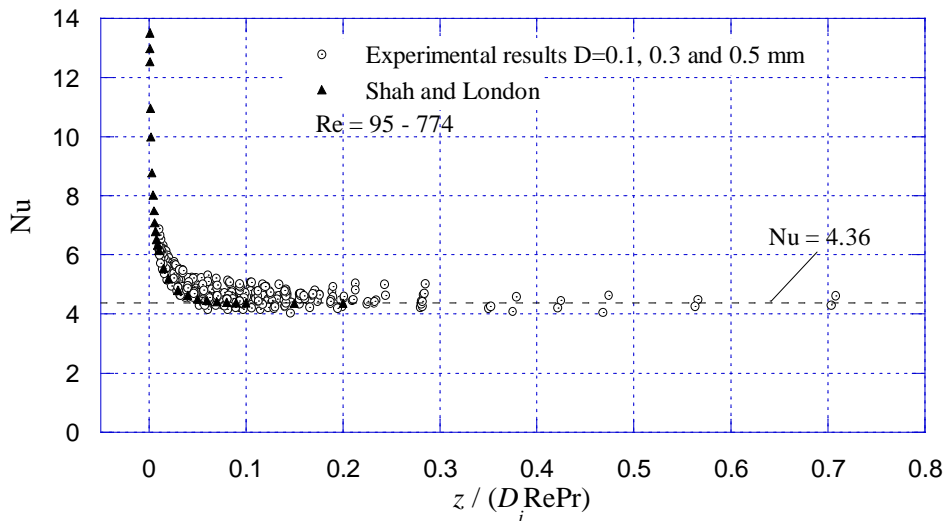


Fig. 1.13. Relation of local value of Nu to non dimensional axial distance for microtubes of $D_i = 125.4, 300 \text{ and } 500 \mu\text{m}$.

2. The axial conduction influence on partial heating of the microchannels

2.1. Frictional losses evaluation of a water flow in microtubes

2.1.1. Introduction

Micro Thermal Systems (MTS) [20], defined as the systems in which the key size has a length scale of a micrometer, could attain the high heat transfer coefficients. For instance,

they are used as the cooling devices for LSI chips. On the other hand μ - TAS (Micro Total Chemical Analyzing System), MEMS (Micro Electric – Mechanical Systems) or bio – chips are some of the examples of MTS. The research reports in this field, concerning the fluid flow characteristics, are mostly oriented to the non-heating fluid flow conditions and a Po is used as comparison criteria. In the real applications, on the other hand, the fluid flow is not always adiabatic but is associated with a large heat fluxes. Moreover the heating length is not always equal to the total length of the tube. In the literature there is a limited number of reports on a non-adiabatic fluid flow characteristics in microchannels.

Urbanek et al. [21] investigated the temperature dependence of Po in microchannel water flow with a channel diameter of 0.1 mm. They have observed that a Po increases with increasing of the water temperature. The viscosity of the water is evaluated at the average temperature between the inlet and the outlet of the tube.

Toh et al. [22] analyzed numerically the heat transfer and fluid flow of microchannel heat sink with the water as a working fluid. They have observed that a Po decreases with decreasing of the Re. In this case the heated length was about the half of the total channel length. The fluid viscosity was also calculated at the average fluid temperature.

Juddy et al [23] investigated the microchannel fluid flow characteristics for different liquid types. Although the fluid flow was adiabatic, they have observed a viscous heating along the fluid flow. Consequently the Po has a constant value, if the fluid viscosity was evaluated at the mean temperature of the water. Contrary if the viscosity was evaluated at the inlet temperature, it decreases as the Re is increasing.

Lelea et al [24] investigated heat transfer and fluid flow through microtubes with water as the working fluid. They have observed that as long as the viscosity is evaluated at the mean temperature of the water and the heated length is equal to the total length of the tube, the Po has a constant value. If the tube was heated partially, the Po decreases slightly with decreasing of the Re. Again the water viscosity was evaluated at the mean temperature between the inlet and outlet of the tube.

The scope of the present paper was to analyze the Po behavior during the heating fluid flow and how the heating position influences the Po. Also, the applicability of the Poiseuille constant to estimate the frictional losses in the case of the heating fluid flow was investigated.

2.1.2. Problem description

Poiseuille [25] has made his experiment with the water as a working fluid on a glass tubes with a diameters ranging from 29 to 140 μm . Based on the results from this experiment, the following relationship has been obtained for a volume flow rate:

$$\dot{V} = \frac{\Delta p \cdot R^4}{\frac{8}{\pi} \cdot l \cdot \mu} \quad (2.1.1)$$

This means that for the same tube under the non-heating fluid flow conditions there is the linear relationship between the pressure drop and a mean fluid velocity,

$$\Delta p = \text{const.} \cdot u_m \quad (2.1.2)$$

Darcy friction factor is defined by the following equation:

$$f = \frac{\Delta p}{\frac{\rho \cdot u_m^2}{2} \cdot \frac{D_i}{L}} \quad (2.1.3)$$

and a Re is defined as:

$$\text{Re} = \frac{\rho \cdot u_m \cdot D_i}{\mu} \quad (2.1.4)$$

So, from (3) and (4) the Po can be obtained in the following form:

$$Po = f Re = \frac{2 \cdot \Delta p \cdot D_i^2}{l \cdot u_m \cdot \mu} \quad (2.1.5)$$

The pressure drop in the equation (2.1.5) is the frictional pressure drop between the inlet and outlet of the tube and the fluid viscosity is evaluated at the average water temperature. At the tube inlet the fluid velocity is considered to be uniform, u_m . As the fluid flow regime is considered to be stationary, the water flow rate through the tube is constant. So the mean fluid velocity will be constant in each of the cross-section and equal to the inlet velocity u_m , defined with the following formulae:

$$u_m = \frac{A \int \rho(T) \cdot u \cdot dA}{\int_A \rho(T) \cdot dA}$$

From equations (2.1.1) and (2.1.5), the well-known value for the Po for the fluid flow through the no-heating tubes, is obtained ($Po = 64$). It has to be stated that in the case of the temperature differences between the inlet and the outlet of the tube, considered in the present report, changes in water densities are small.

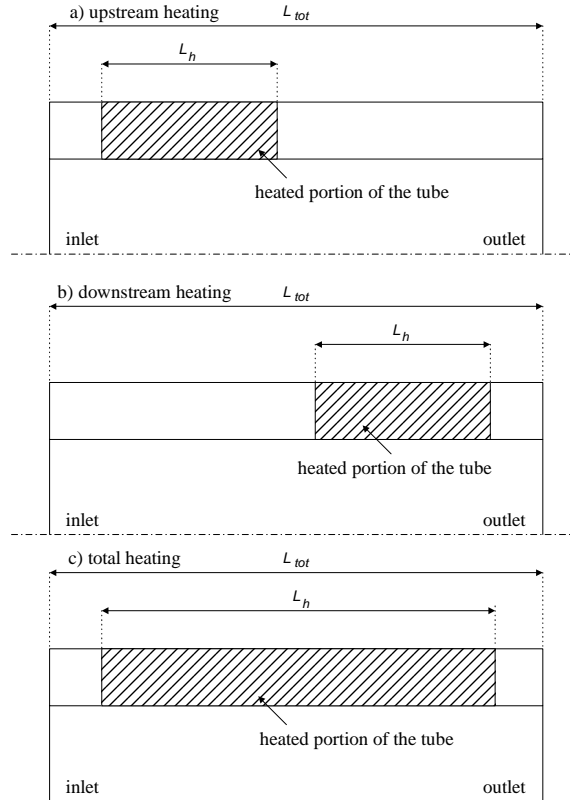


Fig. 2.1.1 Three different heating cases considered for the numerical modeling

To analyze the behavior of the Poiseuille constant for heating fluid flows, three different cases presented in the Fig. 1 are considered:

- upstream heating, when heated length is close to the inlet of the tube followed by the non-heating portion;
- downstream heating when heated length is close to the outlet of the tube preceding by the non-heating portion of the tube;
- total heating when almost the total length of the tube is heated except the side portions which are fixed to the experimental box.

The geometry of the microtube was the same as in the experimental research presented in [24]. The total length of the tube was $L_{tot} = 600$ mm, the heating length $L_h = 250$ mm located upstream and a diameter was $D_i / D_o = 500 / 700$ μm . In the case of the downstream heating the heating length was the same and for the total heating the insulated portions at both ends of the tube were 8 mm. The input power was 2W and the inlet temperature of the water is $t_{in} = 20$ $^{\circ}\text{C}$.

2.1.3. Numerical details

In order to discuss the Po behavior, the velocity and temperature distributions were numerically solved taking into account of the temperature variation of fluid properties.

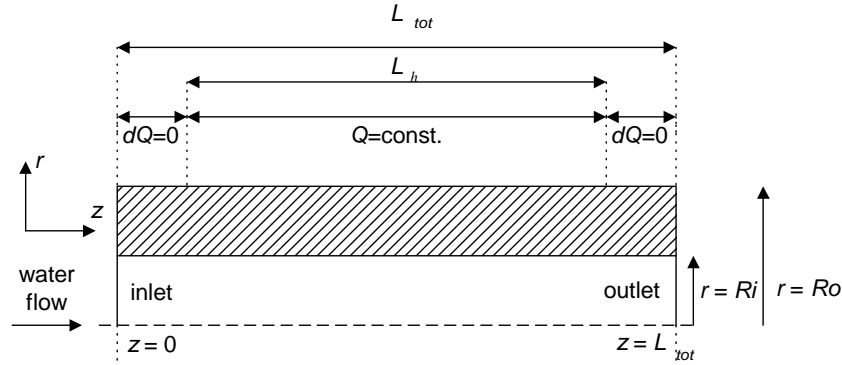


Fig. 2.1.2 The calculation domain

As mentioned already [24], in the experimental setup, there were two electrodes at both ends of the test tube. So, as shown in Fig. 2.1.2, the respective insulated parts were included in the numerical domain. The following set of partial differential equations is used to describe the phenomena:

Continuity equation:

$$\frac{\partial(\rho(T) \cdot u)}{\partial z} + \frac{1}{r} \frac{\partial(r \cdot \rho(T) \cdot v)}{\partial r} = 0 \quad (2.1.6)$$

Momentum equation:

$$\frac{\partial(\rho(T)vu)}{\partial r} + \frac{\partial(\rho(T)uu)}{\partial z} = -\frac{dp}{dz} + \frac{1}{r} \frac{\partial}{\partial r} \left(\mu(T)r \frac{\partial u}{\partial r} \right) \quad (2.1.7)$$

Energy equation:

$$\frac{\partial(\rho(T)c_p(T)vT)}{\partial r} + \frac{\partial(\rho(T) \cdot c_p(T)uT)}{\partial z} = \left[\frac{1}{r} \frac{\partial}{\partial r} \left(k(T) \cdot r \frac{\partial T}{\partial r} \right) + \frac{\partial}{\partial z} \left(k(T) \frac{\partial T}{\partial z} \right) \right] \quad (2.1.8)$$

At the inlet of the tube, the uniform velocity and temperature field is considered, while at the exit the temperature gradient is equal to zero.

The boundary conditions are:

$$\begin{aligned} z = 0, 0 < r < R_o: \quad & u = u_0, T = T_w = T_0 \\ 0 < z < L_{tot}: \quad & r = 0, \frac{\partial u}{\partial r} = 0, \frac{\partial T}{\partial r} = 0, v = 0 \\ & r = R_i, u = v = 0 \end{aligned}$$

The Joule heating of the tube wall can be expressed either by the uniform heat generation through the tube wall or by the uniform heat flux imposed on the outer surface of the wall. For the latter case, the boundary condition is defined as,

$$r = R_o : \quad q_o = k_s \frac{\partial T}{\partial r} \quad (\text{for the heated portion of the tube})$$

$$k_s \frac{\partial T}{\partial r} = 0 \quad (\text{for the insulated portion of the tube})$$

where q_o is the heat flux based on the outer heat transfer area of the tube wall.

$$z = L_{tot}, 0 < r < R_o: \quad \frac{\partial T}{\partial z} = 0$$

The partial differential equations (2.1.6) – (2.1.8) together with boundary conditions, are solved using the finite volume method described in [18].

First, the parabolic flow field condition is considered and the velocity field is solved. The temperature field, as a conjugate heat transfer problem, was then solved as the elliptic problem using the obtained velocity field. The fluid flow regime is considered to be a steady-state laminar flow with variable fluid properties. In order to evaluate fluid properties (density, viscosity and thermal conductivity), the subroutines from Computer package PROPATH v. 10.2 are used in the present code.

A tube wall and water flow inside the tube, are considered as one domain and a harmonic mean values for the transport properties (viscosity, thermal conductivity) are calculated at the solid-liquid interface [18]. The tube material is stainless steel with thermal conductivity $k_s = 15.9 \text{ W/m K}$.

In order to test the grid sensitivity, two grids have been used. The coarser one with 250 cells in radial direction and 400 cells in axial direction and finer grid with 500 and 800 cells in z - and r - direction respectively. Differences in the results of Po were smaller than 0.1 %, so the coarser grid has been used for further calculations.

2.1.4. Results and discussion

In Fig. 2.1.3 numerical and experimental results for the Po versus Re are presented. Both numerical and experimental values of the Po decrease with decreasing of the Re .

In Fig. 2.1.4 numerical results of the Po are plotted to the Re for three different heating cases. One can observe that as long as the heating length of the tube is almost equal to the total length of the tube, the Po has a constant value regardless the Re .

In the case of the upstream heating the Po decreases with Re especially in the case of the lower Re where the higher outlet temperatures are expected. The same results are obtained in [423]. Contrary, in the case of the downstream heating the Po increases as the Re decreases.

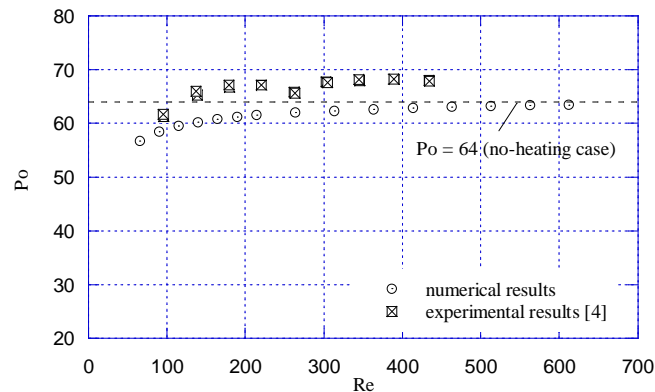


Fig. 2.1.3 Experimental and numerical results of Po for the case of the upstream heating

Accordingly to the equation (2.1.2), in the case of the no-heating water flow, the relationship between the pressure drop and mean fluid velocity is linear. So, this means that a ratio between the pressure drop and mean fluid velocity is constant regardless the flow rate. For the case when the tube wall is heated, the pressure drop decreases due to the lower wall shear stress, so the pressure drop is depending both on mean fluid velocity and temperature of the fluid.

In Fig. 2.1.5 the ratio $\Delta p/u_m$ is plotted to mean fluid velocity for three different heating cases and no-heating fluid flow conditions. Taking into account that Po is constant regardless the Re in the case of the total heating, obviously the ratio $\Delta p/u_m$ and fluid viscosity decrease at the same rate.

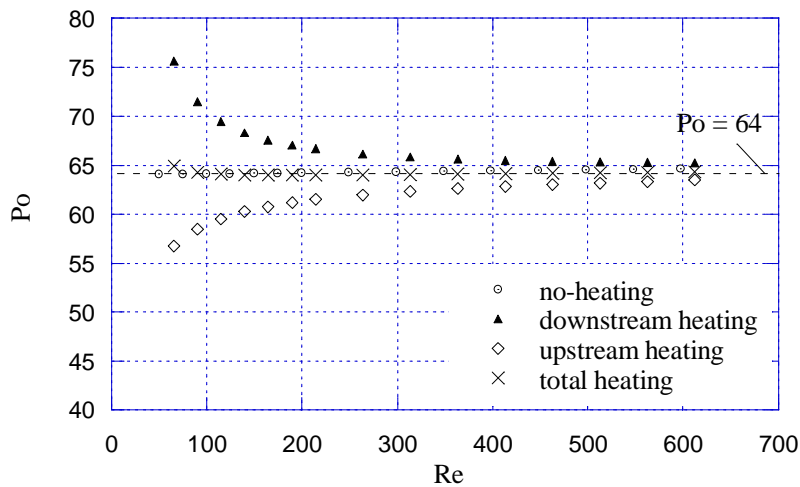


Fig. 2.1.4 Numerical results of Po for different heating cases

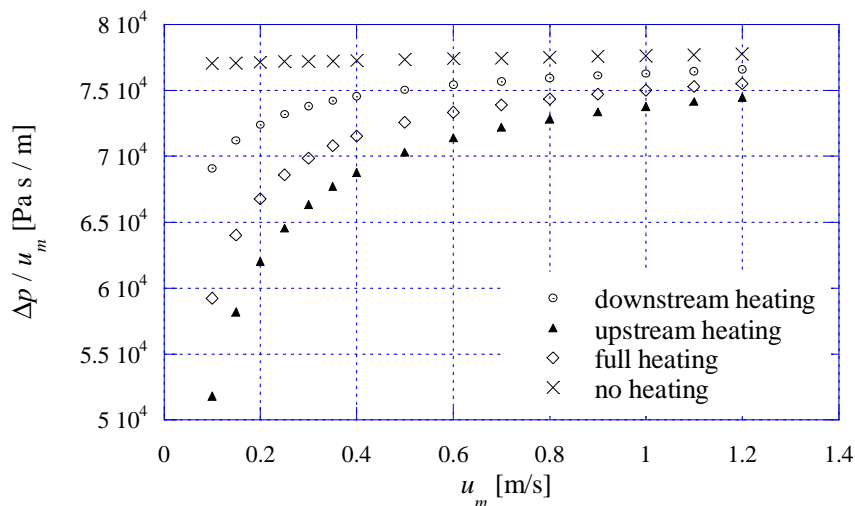


Fig. 2.1.5 The numerical values for the ratio $\Delta p/u_m$ for different heating cases

In the case of the upstream heating the ratio $\Delta p/u_m$ decreases faster than a fluid viscosity especially for lower flow rates. Consequently the Po is decreasing with Re .

In the case of the downstream heating the ratio $\Delta p/u_m$ decreases slightly with flow rate and has almost the same variation as in the case of the no-heating fluid flow. But the fluid viscosity decreases sharply and in this case the Po increases as Re decreases.

A difference in Po depending on the position of the heating can be also explained in the following way. Both the upstream and downstream heating has two portions, heated and isolated, with equal lengths. A difference lies in the fact that in the case of the upstream heating the fluid temperature in the isolated region is higher than the fluid temperature in the isolated region for downstream heating. So, if we define the average water temperature between the heated and isolated fluid flow, this will be higher for the case of the upstream heating. Finally it results in a lower pressure drop and lower value for the Po.

In the Fig. 2.1.6 the local Po_z variation along the tube is presented. The local value of the Po is based on the local pressure difference and the fluid viscosity is based on the local fluid temperature. The mean fluid velocity is same in each cross-section of the tube. In the case of the total heating, the fully developed value of the Po_z is slightly lower than a conventional value, $Po = 64$. In the case of the upstream or downstream heating there is the fully developed value in both heating and non-heating portions of the tube. In both cases, the fully developed value for the heated part of the tube is lower than a fully developed Po_z along the non-heating portion.

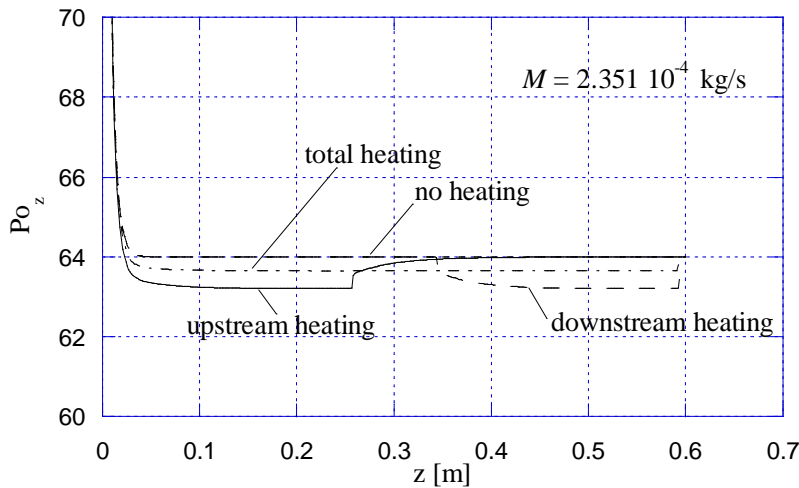


Fig. 2.1.6 The local value of the Po for different heating cases for $M = 2.351 \cdot 10^{-4}$ kg/s

If we assume a definition of the Po as the measure of the frictional losses [22], the question is if the lower value of the Po means the lower frictional losses and consequently the lower pumping power necessary for driving the fluid through the tubes. For this reason the ratio between the pumping power for heating and no-heating cases is presented in Fig. 2.1.7. As the input power is constant, the outlet temperature of the water is presented in the same graph. It is obvious that as the mass flow rate decreases the lower pumping power is requested for each of the heated cases. For example, in the case of the upstream heating, for lower mass flow rates, the pumping power is lower for about 50 %. The pumping power is defined with the following equations:

$$\Pi = M \cdot \frac{\Delta p}{\rho}$$

2.1.5. Conclusions

In the present paper the behavior of the Po is analyzed for the case of the heating fluid flow through microchannels taking into account the heating position. The following conclusions could be summarized:

- The average value of the Po remains constant regardless the Re only in the case of the total heating and when the fluid viscosity is evaluated at the average temperature between the inlet and outlet of the tube;
- In the case of the upstream heating the Po decreases with Re especially for the lower Re . Contrary, in the case of the downstream heating the Po increases as the Re decreases.

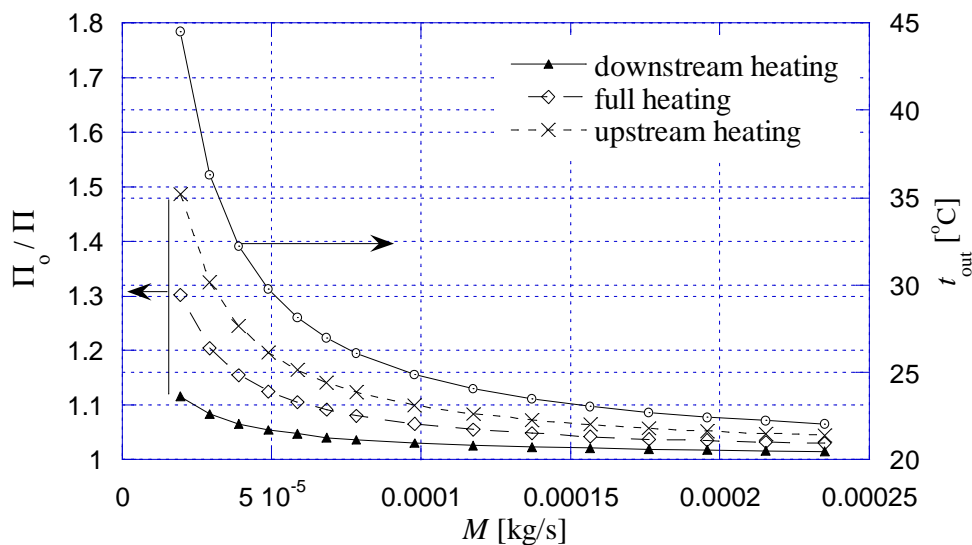


Fig. 2.1.7 The pumping power ratio versus mass flow rate for different heating cases

- Consequently the Po could not be always used as the measure of the frictional losses in the case of the heating fluid flows. Instead the pumping power necessary for driving the fluid through the tubes has to be considered.
- The pumping power for the case when the heating portion is positioned upstream can be up to 50 % lower compared to the no-heating case.

2.2 The heat transfer aspects on a conjugate partial heating of the microtubes

2.2.1. Introduction

The microchannel heat transfer and fluid flow has gained the interest in the last decade due to the downsizing of the thermal devices used in various fields of everyday life. The cooling of the VLSI devices, biomedical applications, micro-heat-exchangers are some of the examples where the fundamentals of the microchannel heat transfer and fluid flow are essential for a proper design of these devices.

It has to be stated that the first microchannel fluid flow experiment was made by Poiseuille [25] in 1870 on a glass tube with internal diameter ranging from 29 to 140 μm with a water as the working fluid and non-heating working conditions. Based on these results, the

well-known relation for the volume flow rate was established and extended lately to the macrochannels.

Tuckerman and Pease [26] have increased the interest on microchannel heat transfer phenomena with the microchannel heat sink used for the cooling of the VLSI devices. Wu and Little [27] [28] have made the microchannel heat transfer and fluid flow experiments used for designing the Joule-Thomson micro-refrigerator. The working fluid in their research was nitrogen and inner diameters of the tubes were from 100 to 300 μm . Their heat transfer and hydrodynamic results shown differences against the conventional results for macro tubes. In the following years, large amount of work have been done in order to explain these discrepancies. Sobhan and Garimella [29] have presented the intuitive review of these papers.

Morini [30] has also presented the review on a single – phase microchannel heat transfer, indicated some of the reasons for a large dispersion of the experimental results. Both gas and liquid flows have been considered.

In the recent years, Lelea et al. [24], have made the experimental research on microtube heat transfer and fluid flow with inner diameters between 100 and 500 μm for laminar regime of the water flow. These results have shown the good agreement with the conventional theories even for the entrance region of the tube. Tiselj et al. [31] have presented the experimental research on microchannel heat transfer and fluid flow of water through the multichannel configuration with triangular cross-section of the channels. The hydraulic diameter was 160 μm and low Re number range (3.2–64) considering the axial conduction in the tube wall. The results are also in good agreement with conventional theories, confirmed also with the numerical modeling using the conventional set of the Navier – Stokes equations. Lee et al. [32] have investigated the laminar fluid flow of the water through the multichannel configuration of the rectangular cross-section with a hydraulic diameter from 318 to 903 μm . Their experimental and numerical results shown that, classical continuum theory can be applied for microchannels, considered in their study. On the other hand, the entrance and boundary effects have to be carefully analyzed in the case of theoretical approach.

Bahrani et al. [33] analyzed the influence of the surface roughness on laminar convective heat transfer and developed the analytical model for estimating this behaviour. The authors found that surface roughness may increase the thermal performance and pressure drop of the microtube. At the same time the convective heat transfer coefficient slightly increases by increasing the wall roughness.

The outcome of the research reports mentioned above, is that special attention has to be paid to macroscale phenomena that are amplified at the microscale. For example, due to a high heat transfer rate, the temperature variable fluid properties have to be considered. Lelea [34] has investigated the influence of the temperature dependent fluid viscosity on Po number. On the other hand the small diameter and large length of the tube can results in viscous heating even in the case of liquid flow, as presented in [35].

On the other hand the axial conduction through the tube wall has to be considered in the case of the microchannel heat transfer due to the high ratio between the inner and outer tube diameter, unusual in the case of the macrochannels. Maranzana et al. [36] have analyzed the influence of the axial conduction in the tube wall on microchannel heat transfer. The fluid flow between the parallel plates as well as the fluid flow in the counter flow heat exchanger was considered. It was found that the axial conduction has the influence on heat transfer parameters as far as the axial conduction number M , defined in this study, is higher than 10^{-2} . In this case the total length of the tube was heated. However, in industrial or laboratory applications, the heating length is not always equal to the total length of the tube.

For this reason, in the present research two cases were considered: the upstream heating where the first half of the tube was heated and downstream heating where the second half of the tube was heated. As the tube material has the great impact on axial conduction

through the tube wall, three different materials are considered, stainless steel, silicon and copper. The axial conduction through the tube wall is decreasing as the Re number is increasing, so the low Re number regime is considered. Moreover, in this paper, the axial conduction influence was analyzed through the input and outlet heat transfer ratio that in fact is the microchannel heat balance or heat losses.

2.2.2. Numerical details

In order to discuss the axial conduction influence, the velocity and temperature distributions were numerically solved taking into account the temperature variation of the fluid properties, procedure described in [18] [24].

The computational domain is presented in Fig. 1, as follows:

The fluid flow domain defined at $r = 0, R_i$ and $z = 0, L$

The temperature field domain defined at $r = 0, R_o$ and $z = 0, L$

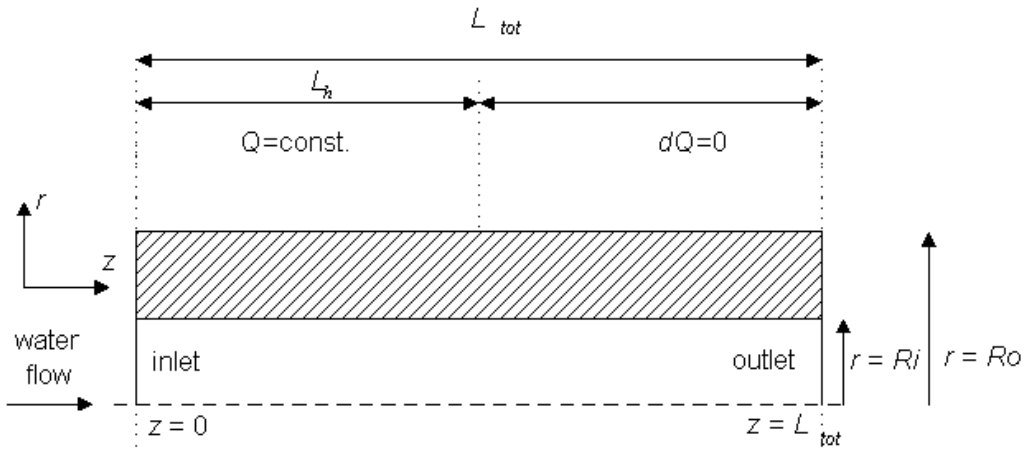


Fig. 2.2.1 The calculation domain

The outer portion of the tube has two parts, the heated and insulated part. So, as shown in Fig. 2.2.2, the respective insulated part was included in the numerical domain. The following set of partial differential equations is used to describe the phenomena, taking into account the variable thermophysical properties of the water:

Continuity equation:

$$\frac{\partial(\rho(T) \cdot u)}{\partial z} + \frac{1}{r} \frac{\partial(r \cdot \rho(T) \cdot v)}{\partial r} = 0 \quad (2.2.1)$$

Momentum equation:

$$\frac{\partial(\rho(T)vu)}{\partial r} + \frac{\partial(\rho(T)uu)}{\partial z} = -\frac{dp}{dz} + \frac{1}{r} \frac{\partial}{\partial r} \left(\mu(T)r \frac{\partial u}{\partial r} \right) \quad (2.2.2)$$

Energy equation:

$$\frac{\partial(\rho(T)c_p(T)vT)}{\partial r} + \frac{\partial(\rho(T) \cdot c_p(T)uT)}{\partial z} = \left[\frac{1}{r} \frac{\partial}{\partial r} \left(k(T) \cdot r \frac{\partial T}{\partial r} \right) + \frac{\partial}{\partial z} \left(k(T) \frac{\partial T}{\partial z} \right) \right] \quad (2.2.3)$$

At the inlet of the tube, the uniform velocity and temperature field is considered, while at the exit the temperature gradient is equal to zero.

The boundary conditions are:

$$\begin{aligned} z = 0, 0 < r < R_o: \quad & u = u_0, T = T_w = T_0 \\ 0 < z < L_{tot}: \quad & r = 0, \frac{\partial u}{\partial r} = 0, \frac{\partial T}{\partial r} = 0, v = 0 \end{aligned}$$

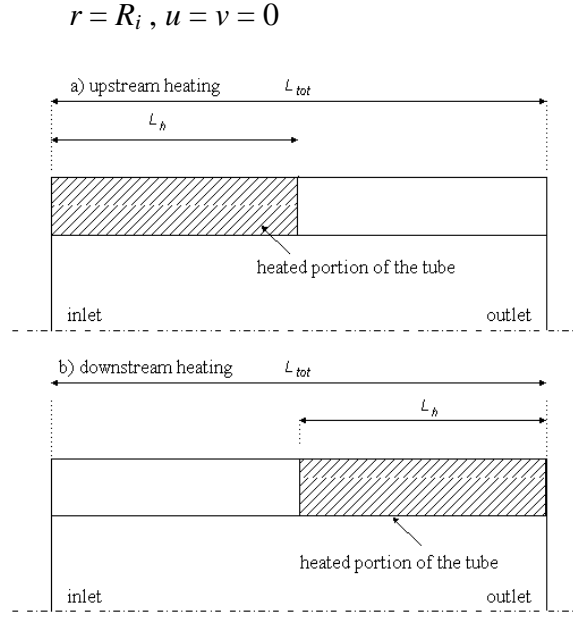


Fig. 2.2.2 The heating positions

The Joule heating of the tube wall can be expressed either by the uniform heat generation through the tube wall or by the uniform heat flux imposed on the outer surface of the wall. For the latter case, the boundary condition is defined as,

$$r = R_o : \quad q_o = k_s \frac{\partial T}{\partial r} \quad (\text{for the heated portion of the tube})$$

$$k_s \frac{\partial T}{\partial r} = 0 \quad (\text{for the insulated portion of the tube})$$

where q_o is the heat flux based on the outer heat transfer area of the tube wall.

$$z = L_{tot}, 0 < r < R_o : \quad \frac{\partial T}{\partial z} = 0$$

The conjugate heat transfer procedure, implies the continuity of the temperature and heat flux at the solid – liquid interface defined as,

$$r = R_i : T_s|_{Ri+} = T_f|_{Ri-}$$

$$k_s \left(\frac{\partial T_s}{\partial r} \right)_{Ri+} = k_f \left(\frac{\partial T_f}{\partial r} \right)_{Ri-}$$

The partial differential equations (2.2.6) – (2.2.8) together with boundary conditions, are solved using the finite volume method described in [18].

First, the parabolic flow field condition is considered and the velocity field is solved. The temperature field, as a conjugate heat transfer problem, was then solved as the elliptic problem using the obtained velocity field. The fluid flow regime is considered to be a steady-state laminar flow with variable fluid properties. In order to evaluate fluid properties (density, viscosity and thermal conductivity), the subroutines from Computer package PROPATH v. 10.2 are used in the present code.

As a consequence of the temperature dependent fluid properties, iterative procedure is needed to obtain the convergence of the fluid properties (viscosity, thermal conductivity, density and specific heat capacity) through the successive solution of the flow and temperature field. A tube wall and water flow inside the tube, are considered as one domain and harmonic mean values for the thermal conductivity are calculated at the solid-liquid interface [18]:

$$k_m = \left(\frac{1-f}{k_s} + \frac{f}{k_f} \right)^{-1}$$

The viscosity in the solid region was set to a very large value, in order to handle discontinuities between these two domains. In order to test the grid sensitivity, two grids have been used. The coarser one with 250 cells in radial direction and 400 cells in axial direction and finer grid with 500 and 800 cells in z - and r - direction respectively. Differences obtained for Pe and Nu were smaller than 0.1 %, so the coarser grid has been used for further calculations.

Although the numerical model was verified with microtube experimental results in [24] and [34], additional validation was made with experimental results of Piva and Pagliarini [37]. In this work, the axial conduction in the copper tube wall was used to simulate the exponential boundary conditions H5. The comparison is presented in Fig. 2.2.3 for copper tubes with $D_i / D_o = 10/12$ mm, total length of $L_{tot} = 750$ mm, water as the working fluid with $Re = 611$ and heat transfer rate $Q = 9.89$ W. The good agreement between the experimental and numerical results is observed.

2.2.3. Results and discussion

The microtube conjugate heat transfer analysis was made for two values of the wall thickness $D_i / D_o = 0.1/0.3$ mm and $0.1/0.5$ mm and three different tube materials, stainless steel ($k = 15.9$ W/m K), silicon ($k = 198$ W/m K) and copper ($k = 398$ W/m K). In order to investigate the axial conduction behaviour in the tube wall, the low Re range was considered $Re < 200$. The input heat transfer rate was constant for all the runs $Q_0 = 0.1$ W.

As it was stated in Faghri and Sparrow [16], in the case of simultaneous wall and fluid axial conduction, the heat transfer coefficient is a function of three unknowns Q , T_w and T_b each of them function of axial distance. So, the main issue is how to estimate the tube wall axial conduction influence on fluid flow and thermal characteristics. In Faghri and Sparrow [38], the non-dimensional parameter was defined as the measure of this influence:

$$I = \frac{k_s \cdot \delta}{k_f \cdot R} \quad (2.2.4)$$

Cotton and Jackson [39] demonstrated that the effect of wall conduction is defined with the following parameter:

$$I = \frac{k_s}{k_f} \cdot \left[\frac{\delta}{D_i} \cdot \left(1 + \frac{\delta}{D_i} \right) \right] \cdot \frac{1}{Pe^2} \quad (2.2.5)$$

More recently, Maranzana et al. [36] defined the axial conduction parameter for two dimensional microchannel fluid flow:

$$I = \frac{r^2 \cdot NTU}{Bi} \quad (2.2.6)$$

Chiou [40] have defined the following conductance number as the parameter for the estimation of the wall axial conduction:

$$I = \frac{A_s}{A_f} \cdot \frac{D_i}{L} \cdot \frac{1}{Pe} \cdot \frac{k_s}{k_f} \quad (2.2.7)$$

From the relations presented above, it is obvious that wall axial conduction depends on thermal conductivity ratio k_s / k_f , Pe and diameters ratio D_e / D_i . The question is what is the practical implication of the axial conduction in the tube wall. For instance, one might be interested in the heat losses and consequently in the overall input and output heat transfer rate

ratio. So, in Figs. 2.2.4 – 2.2.7 the ratio Q / Q_0 versus Re has been presented, where Q is calculated from:

$$Q = \dot{m} \cdot c_p \cdot (T_{out} - T_{in}) \quad (2.2.8)$$

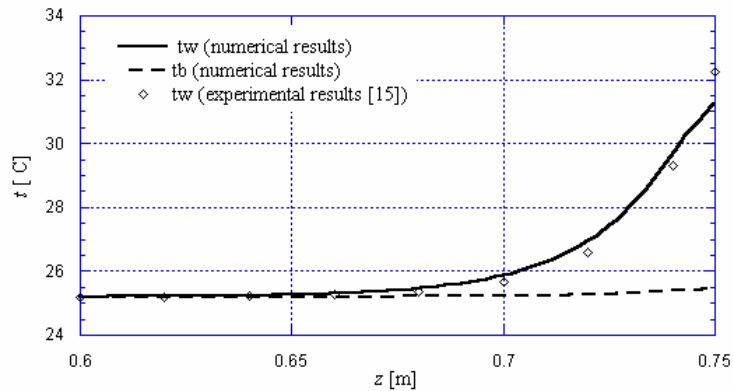


Figure 2.2.3. The code validation with experimental results presented in [15]

From Fig. 2.2.4, one can conclude that in the case of the downstream heating, $D_i/D_o = 0.1/0.3$ mm and for the entire range of Re, there is no axial conduction inside the tube wall, considering that the input heat transfer rate is equal to the output convective heat transfer rate. In the case of the larger diameter ratio $D_i/D_o = 0.1/0.5$ mm (Fig. 2.2.5) and downstream heating, only for the copper tubes and very low Re < 50, the output heat transfer rate is 12 % lower than the input value.

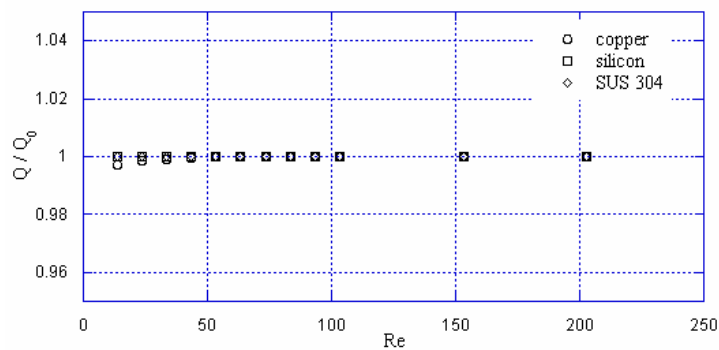


Figure 2.2.4. The heat transfer rate ratio versus Re for downstream heating and diameter ratio $D_i/D_o = 0.1/0.3$ mm

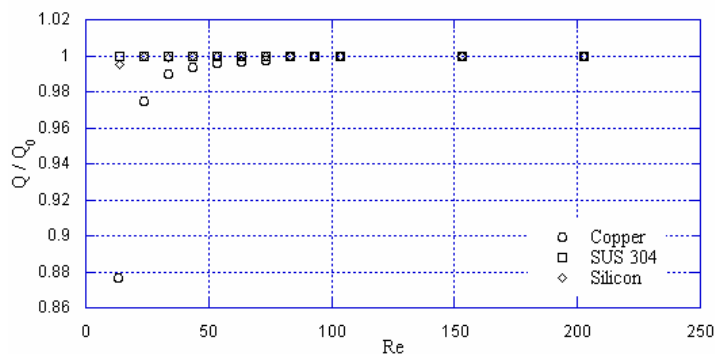


Figure 2.2.5. The heat transfer rate ratio versus Re for downstream heating and diameter ratio $D_i/D_o = 0.1/0.5$ mm

In the case of the upstream heating (Figs. 2.2.6 and 2.2.7), except for the stainless steel tubes, the heat losses are obvious for all other cases. In the case of the silicon tubes, Q/Q_0 is decreasing to 0.9 for $D_i/D_o = 0.1/0.3$ mm, and to 0.75 for $D_i/D_o = 0.1/0.5$ mm.

The highly conducted copper tubes facilitate the axial conduction in the tube wall resulting in heat losses of almost 25 % for $D_i/D_o = 0.1/0.3$ mm and 55 % for $D_i/D_o = 0.1/0.5$ mm.

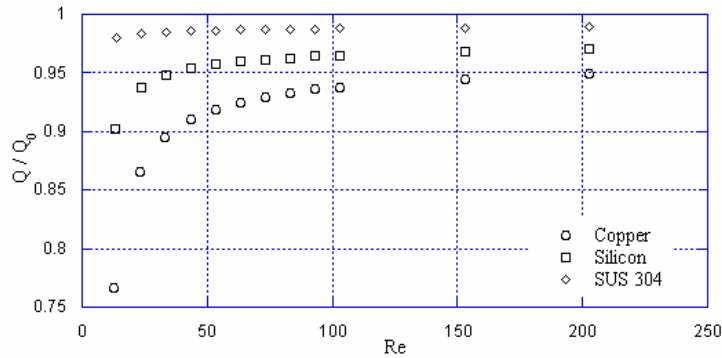


Figure 2.2.6. The heat transfer rate ratio versus Re for upstream heating and diameter ratio $D_i/D_o = 0.1/0.3$ mm

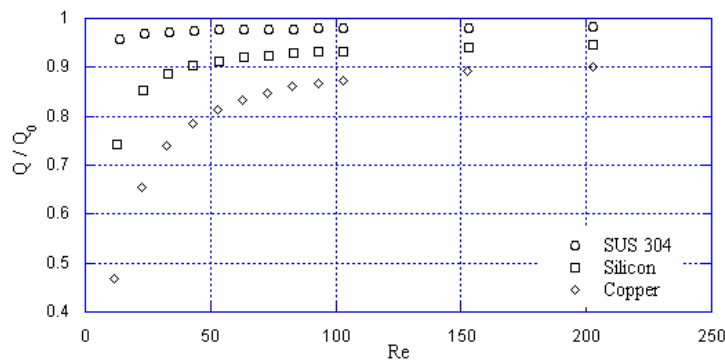


Figure 2.2.7. The heat transfer rate ratio versus Re for upstream heating and diameter ratio $D_i/D_o = 0.1/0.5$ mm

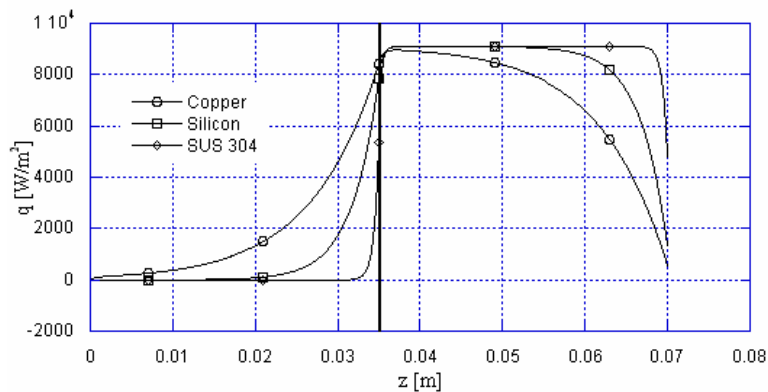


Figure 2.2.8. The heat flux variation versus axial distance for the downstream heating, diameter ratio $D_i/D_o = 0.1/0.3$ mm and $Re = 12.95$

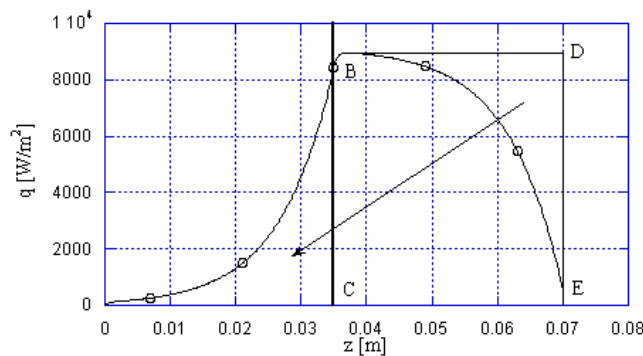


Figure 2.2.9. The heat flux variation versus axial distance for the upstream heating, diameter ratio $D_i/D_o = 0.1/0.3$ mm , $Re=12.95$ and copper tube

It is obvious that Q / Q_0 , depends on the heating position. Apparently, in the case of the downstream heating the wall axial conduction is inactive and the question is if this is the correct prediction. The answer on this uncertainty, one may find from the graph presenting the local heat flux distribution along the fluid flow. The heat flux is calculated at the fluid-solid interface and can be expressed as,

$$q = -k_f \cdot \left(\frac{\partial T}{\partial r} \right)_{r=R_i} \quad (2.2.9)$$

Although the graph in Fig. 2.2.4 indicated the no-axial conduction case for the copper tube with $D_i/D_o = 0.1/0.3$ mm and downstream heating, from Fig. 8 it is clear that axial conduction exists for the silicon and copper tubes. The explanation can be found from Fig. 2.2.9 where the heat flux versus axial distance was presented for the copper tube. It can be seen that heat flux generated in the upstream section, described by surface 0BC is equal to the heat flux loss in the downstream section described by surface BDE.

The same conclusion can be outlined from the local heat flux distribution for the silicon tube. In the case of the stainless steel tube, the heat flux is equal to zero in the upstream section and in the range of the input heat flux in the downstream section.

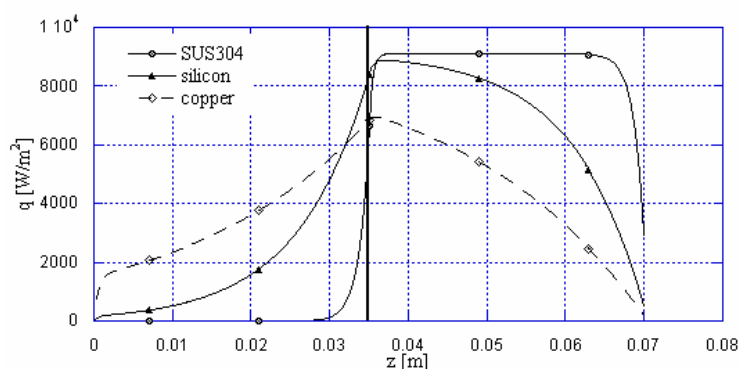


Figure 2.2.10. The heat flux variation versus axial distance for the downstream heating, diameter ratio $D_i/D_o = 0.1/0.5$ mm and $Re = 12.95$

In the case of the tubes with larger wall thickness $D_i/D_o = 0.1/0.5$ mm and lower $Re = 12.95$, the heat flux generated in the upstream section is not equal to the heat flux dispersed in the downstream section (fig. 2.2.10), as a consequence the heat loss is about 12 %. As the Re

is increasing (Fig. 2.2.11), the heat transfer phenomena, is approaching the no-axial conduction case.

In the case of the upstream heating and stainless steel tubes (Figs. 2.2.6 and 2.2.7) the $Q/Q_0 = 1$. The same conclusion can be found from Figs. 2.2.12 and 2.2.13, where heat flux is equal to the input value in the upstream region and equal to zero in the downstream portion of the tube. In the case of the silicon tubes, the input and output heat flux are almost equal as the $Re > 50$. It is also observed that heat flux decreases from input value at the entrance, to zero at the end of the heated portion. This is especially obvious for the case of the greater thickness of the tube wall. As the heat flux is vanishing along the non-heated part of the tube, it is plausible to expect that heat might be dispersed through the inlet part of the tube wall. As the Re is increasing to $Re = 53.53$ and 202.85 , the heat losses are lower and consequently the heat flux is approaching the input value.

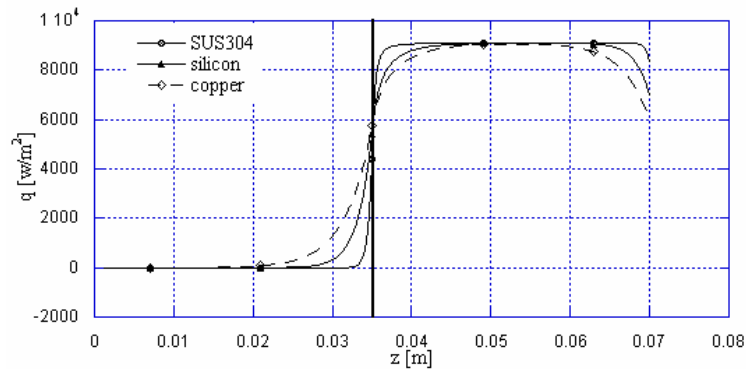


Figure 2.2.11. The heat flux variation versus axial distance for the downstream heating, diameter ratio $D_i/D_o = 0.1/0.5$ mm and $Re = 202.85$

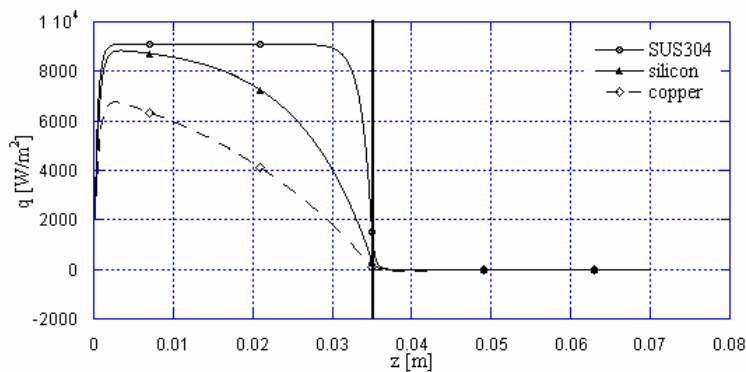


Figure 2.2.12. The heat flux variation versus axial distance for the upstream heating, diameter ratio $D_i/D_o = 0.1/0.5$ mm and $Re = 12.95$

As the thermal conductivity is larger, the latter phenomena is more obvious. From Figs. 2.2.6 and 2.2.7, the output heat transfer rate is decreasing to 75 % of the input heat transfer rate for $D_i/D_o = 0.1/0.3$ mm and to 45 % for $D_i/D_o = 0.1/0.5$ mm. At higher $D_i/D_o = 0.1/0.5$ mm and lower $Re = 12.95$, even the entrance value of the heat flux is considerably lower than the input value.

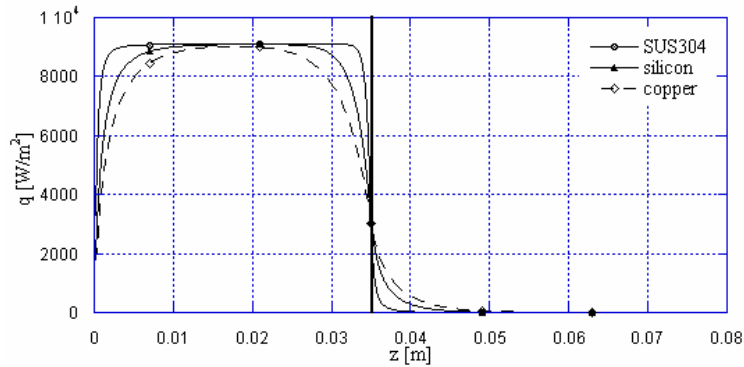


Figure 2.2.13. The heat flux variation versus axial distance for the upstream heating, diameter ratio $D_i/D_o = 0.1/0.5$ mm and $Re = 202.85$

In Fig. 2.2.14 the local variation of the wall and bulk temperature along the tube has been presented for low $Re = 12.95$. In this case a difference between the bulk and wall temperature is very small, so these distributions are overlapping for specific tube material and heating position. The temperature variation in the case of the stainless steel tubes, is the one of no-axial conduction phenomena, with the inlet and maximum allowable temperature in the non-heated and heated sections, respectively. For the silicon tubes and upstream heating, as a consequence of heat losses, the outlet temperature is lower than the maximum temperature like in the case of the no-axial conduction.

As it was shown earlier, in the case of downstream heating, a part of the heat transfer rate was dispersed upstream, so the heat rate was not lost through the outer part of the tube. Consequently, the outlet temperature of the silicon tube is the same as in the case of no-axial conduction phenomena.

Finally, for highly conducted copper tubes and upstream heating, the outlet temperature is considerably lower ($t_b = 34$ °C) compared to the no-axial conduction case temperature ($t_b = 49$ °C). The outlet temperature in the case of the downstream heating is slightly lower ($t_b = 47$ °C) than the no-axial conduction temperature ($t_b = 49$ °C).

For higher $Re = 202.85$, the axial conduction is almost negligible for the silicon and copper tubes, so the outlet temperatures are the same as in the case of stainless steel tubes (Fig. 2.2.15). At the same time, the temperature exhibits the same linear variation as noted in the no-axial conduction case.

In Figs. 2.2.16 and 2.2.17 the local Nu versus non-dimensional axial distance is presented, in order to compare it with the case of the heat transfer and fluid flow through the tubes without the wall axial conduction. Only the heated portion of the tube was considered due to the fact that in the non-heated portion, the H5 exponentially thermal boundary condition is established, that is not relevant to this analysis. Two different values of Re are considered, $Re = 12.95$ (Fig. 2.2.16) and $Re = 202.85$ (Fig. 2.2.17).

First of all, the local Nu distribution has the same behavior, regardless of the tube wall thickness, material and Re , depending only on a heating position. Also, after the entrance region in the so-called fully developed flow the local value of Nu is in the range of the well-known value $Nu = 4.36$. There are sharp changes only near the end of the heating section.

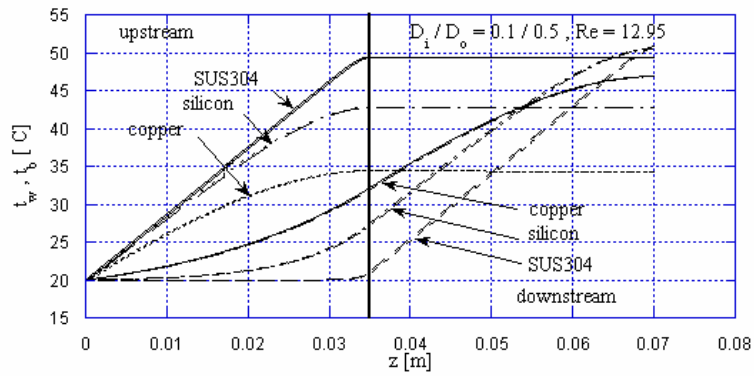


Figure 2.2.14. The wall and bulk temperature variation versus axial distance for various tube materials, $Re = 12.95$ and diameter ratio $D_i/D_o = 0.1/0.5$ mm

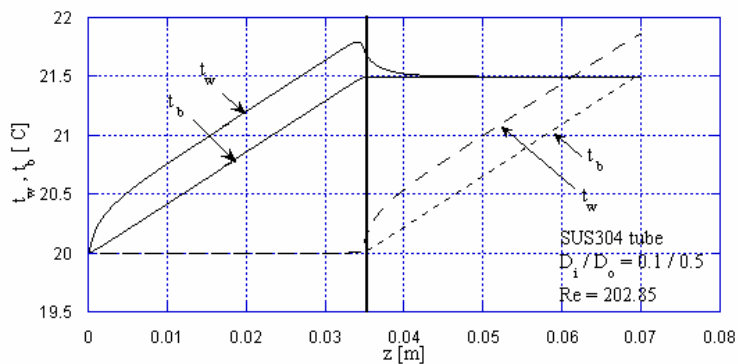


Figure 2.2.15. The wall and bulk temperature variation versus axial distance for copper tube, $Re = 202.85$ and diameter ratio $D_i/D_o = 0.1/0.5$ mm

It is also observed, that in the fully developed region, the local Nu is increasing for the lower $Re = 12.85$. In this case, the higher temperature difference implies the temperature dependent thermal conductivity. In order to verify the latter phenomena, the local Nu value versus non-dimensional axial distance is presented for the case of heating, cooling and constant thermal conductivity (Fig. 2.2.18). As the opposite of the heating case, in the case of cooling, the local Nu is decreasing and for $k = \text{const}$ it remains constant in the fully developed region at $Nu = 4.36$.

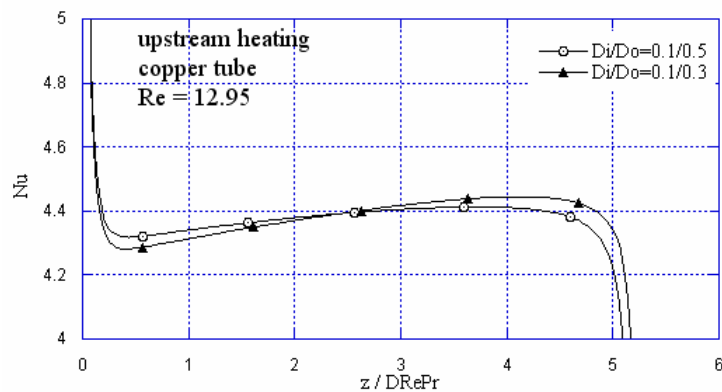


Figure 2.2.16. Relation of local value of Nu to non-dimensional axial distance for copper tube, upstream heating and $Re = 12.95$

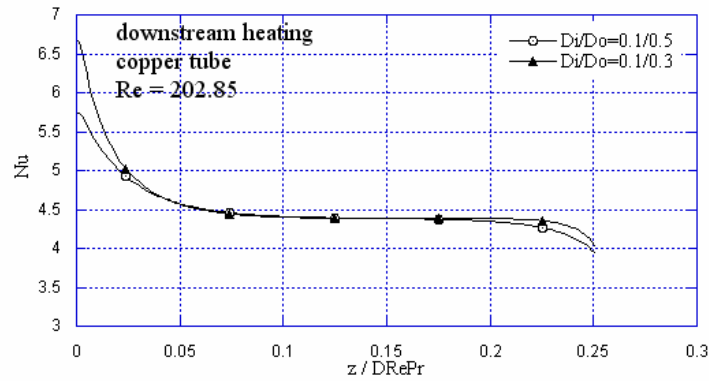


Figure 2.2.17. Relation of local value of Nu to non-dimensional axial distance for copper tube, downstream heating and $Re = 202.85$

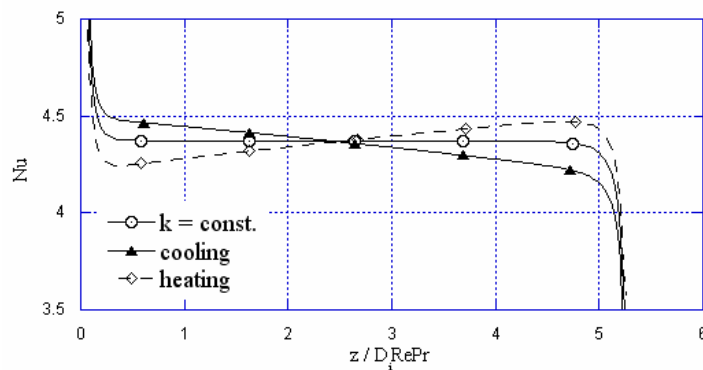


Figure 2.2.18. Relation of local value of Nu to non-dimensional axial distance, for three different modes of the input heat transfer rate, $Re = 12.95$, upstream heating and SUS304.

2.2.4. Conclusions

The conjugate heat transfer of the partially heated microchannels was analyzed numerically, considering the heat losses defined by the heat transfer rate ratio Q / Q_0 . Influence of the heating position, tube material, wall thickness and Re upon the thermal parameters has been considered and the following conclusions were outlined:

- The wall axial conduction has the negligible influence on thermal characteristics of the stainless steel tubes, regardless of the heating position, wall thickness or Re .
- In the case of the upstream heating, the heat is dispersed through the tube wall in the upstream section of the fluid flow so the $Q / Q_0 = 1$ for all the cases except for copper tube of $D_i/D_o = 0.1/0.5$ mm and low $Re = 12.85$.
- The local Nu exhibits the usual distribution as for the non-axial conduction case, except the slightly increasing behaviour (decreasing in the case of cooling) in the fully developed region at low Re , due to the thermal conductivity variations.
- Except the abrupt decreasing of the local Nu at the end of the heating section, the local Nu in the fully developed region has the usual value $Nu = 4.36$.

2.3. The heat transfer and fluid flow of a partially heated microchannel heat sink

It is well known, the conventional heat transfer theory predicts that heat transfer coefficient of fully developed laminar flow in a channel increases if the cross-section of the channel decreases. Tubes or channels of smaller size are therefore chosen to attain a high heat

transfer coefficient. For example, such tubes or channels are used to manage the power dissipation in LSI chips. On the other hand, μ - TAS (Micro Total Chemical Analyzing System), MEMS (Micro Electrical-Mechanical Systems) and bio – chips consist of the network of channels of small cross-sectional size manufactured with micro processing techniques.

The first microchannel heat sink used for VLSI chip cooling was designed and tested by Tuckerman and Pease [26]. It has the water as the working fluid and the heat transfer rate was 780 W/cm^2 with the temperature increase of 71 K. A hydraulic diameter of this device was 100 μm . It was confirmed that a very effective device might be obtained by decreasing the diameter of the channel.

Toh et al. [22] analyzed numerically the heat transfer and fluid flow of microchannel heat sink with the water as a working fluid. They have observed that a Po decreases with decreasing of the Re . In this case the heated length was about the half of the total channel length. It was also found that the properties of water like density, specific heat and thermal conductivity have insignificant effect on Po .

Li et al. [41] analyzed numerically conjugate heat transfer through the silicon microchannel heat sink. The results indicate that thermophysical properties of the liquid can significantly influence both the flow and heat transfer in the microchannel heat sink. The results indicate that variations in the way the Nusselt number is defined may result in different conclusions even using the same experimental data.

Shevade and Rahman [42] investigated convective heat transfer in microchannels with rectangular and square cross sections for volumetric heat generation in the substrate due to an imposed magnetic field. The investigation regarding the velocity and temperature distributions was performed by varying channel aspect ratio, Reynolds number, and heat generation rate in the substrate. It was found that increase in Reynolds number, the outlet temperature decreased and the average Nusselt number increased.

Sung and Mudawar [43] proposed a new hybrid cooling scheme for high-flux thermal management of electronic and power devices. This scheme combines the cooling benefits of micro-channel flow and micro-jet impingement scheme. Despite the relatively poor thermophysical properties of HFE 7100, the proposed cooling scheme facilitated the dissipation of 304.9 W/cm^2 without phase change.

Naphon and Khonseur [44] performed experimental research to investigate the heat transfer characteristics and pressure drop in the micro-channel heat sinks under constant heat flux conditions having the air as the working fluid. The experiments are performed for the Reynolds number and heat flux in the ranges of 200–1000 and 1.80–5.40 kW/m^2 , respectively. It was found that micro-channel geometry configuration has significant effect on the enhancement heat transfer and pressure drop.

Cheng [45] investigated numerically heat transfer and fluid flow of stacked two-layer microchannel heat sink with enhanced mixing passive microstructure with fixed Reynolds number of 14.8. It was found that stacked microchannel with passive structures has better performance than the smooth microchannels. Also, the increase of the ratio of the height of passive microstructure to microchannel height leads to lower thermal resistance.

Lelea et al. [24] analyzed experimentally the microchannel heat transfer of the water flow in tubes with diameters down to 100 μm . The results confirmed that, including the entrance effects, the conventional or classical theories are applicable in this case.

Lelea [34] analyzed numerically the influence of the microtube heating position on the Po behavior. It was found that Po is not a suitable parameter for the hydrodynamic losses evaluation.

Lelea [46] presents numerical modeling of the conjugate heat transfer in microtubes with emphasize on the heating position influence upon the thermal behavior of the microtube.

In most of the studies mentioned above (except [24],[34],[46]), the heating length was the same as the total length of the heat sink. In the electronics cooling applications, the heating length is not always equal to the total length of the channel and consequently, the thermal and hydrodynamic phenomena depend on the heating position. The scope of this chapter is to analyze the influence of the heating position on hydrodynamic and thermal parameters of the micro-heat sink.

2.3.1. Numerical details

The one-layer microchannel heat sink is presented in the Fig. 2.3.1.

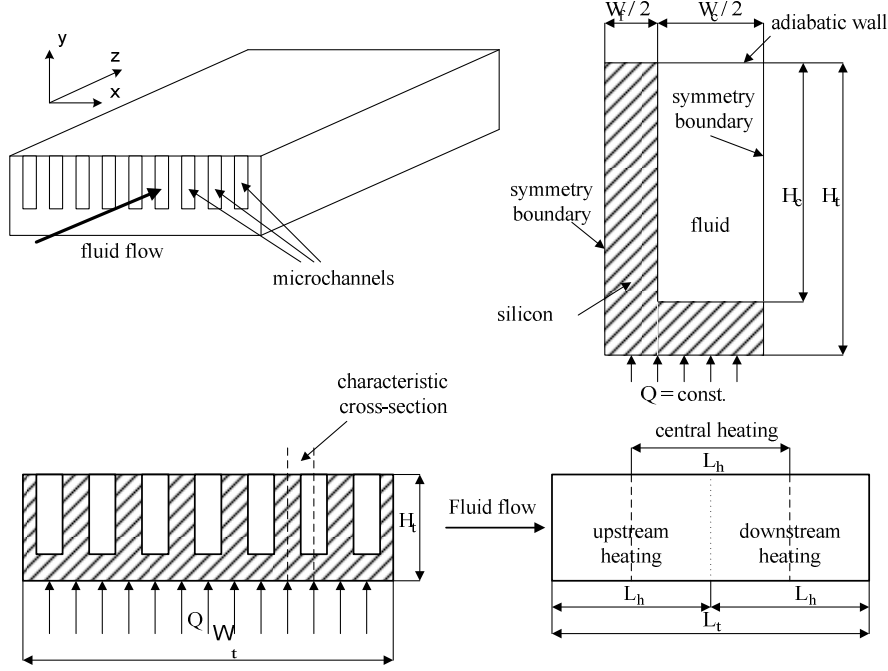


Fig. 2.3.1 The microchannel heat sink, calculation domain and heating positions.

Due to the symmetry plane, the half cross-section of one channel is considered in computations. The conventional set of the Navier-Stokes equations has been used for the conjugate laminar steady state heat transfer and fluid flow, as follows:

The continuity equation:

$$\frac{\partial u}{\partial x} + \frac{\partial v}{\partial y} + \frac{\partial w}{\partial z} = 0 \quad (2.3.1)$$

The momentum equation:

$$\rho \left(u \frac{\partial u}{\partial x} + v \frac{\partial u}{\partial y} + w \frac{\partial u}{\partial z} \right) = -\frac{dp}{dz} + \left(\frac{\partial}{\partial x} \left(\mu \frac{\partial u}{\partial x} \right) + \frac{\partial}{\partial y} \left(\mu \frac{\partial u}{\partial y} \right) \right) \quad (2.3.2)$$

$$\rho \left(u \frac{\partial v}{\partial x} + v \frac{\partial v}{\partial y} + w \frac{\partial v}{\partial z} \right) = -\frac{dp}{dx} + \left(\frac{\partial}{\partial x} \left(\mu \frac{\partial v}{\partial x} \right) + \frac{\partial}{\partial y} \left(\mu \frac{\partial v}{\partial y} \right) \right) \quad (2.3.3)$$

$$\rho \left(u \frac{\partial w}{\partial x} + v \frac{\partial w}{\partial y} + w \frac{\partial w}{\partial z} \right) = -\frac{dp}{dy} + \left(\frac{\partial}{\partial x} \left(\mu \frac{\partial w}{\partial x} \right) + \frac{\partial}{\partial y} \left(\mu \frac{\partial w}{\partial y} \right) \right) \quad (2.3.4)$$

The energy equation (for both fluid and solid):

$$\rho \cdot c_p \cdot \left(u \frac{\partial T}{\partial x} + v \frac{\partial T}{\partial y} + w \frac{\partial T}{\partial z} \right) = k \left(\frac{\partial^2 T}{\partial x^2} + \frac{\partial^2 T}{\partial y^2} + \frac{\partial^2 T}{\partial z^2} \right) \quad (2.3.5)$$

The fluid properties are constant except for fluid viscosity that is evaluated with following equation:

$$\mu(t) = 2.6412018 \cdot 10^{-4} + 0.0014009 \cdot e^{-\frac{t}{31.0578605}}$$

The rest of the fluid properties are evaluated as follows: $\rho = 998.2 \text{ kg/m}^3$, $c_p = 4182 \text{ J/kg K}$, $k_s = 148 \text{ W/m K}$, $k_f = 0.6 \text{ W/m K}$. The following boundary conditions are prescribed for the system of the partial differential equations:

The conjugate heat transfer procedure, implies the continuity of the temperature and heat flux at the solid – liquid interface defined as,

$$x = W_f/2: \quad T_s|_{x+} = T_f|_{x-}$$

$$k_s \left(\frac{\partial T_s}{\partial x} \right)_{x+} = k_f \left(\frac{\partial T_f}{\partial x} \right)_{x-}$$

$$y = H_t - H_c: \quad T_s|_{y+} = T_f|_{y-}$$

$$k_s \left(\frac{\partial T_s}{\partial y} \right)_{y+} = k_f \left(\frac{\partial T_f}{\partial y} \right)_{y-}$$

Also at the inlet cross-section, uniform velocity and temperature field are considered:

$$z = 0$$

$$u = u_{in} \text{ and } T = T_{in}$$

The upper boundary is isolated defined as:

$$k \frac{\partial T}{\partial y} = 0$$

At the outlet of the microchannel the following boundary conditions are prescribed:

$$z = L_t$$

$$\frac{\partial T}{\partial z} = 0$$

At the symmetry boundary:

$$x = w_f/2 + w_c/2$$

$$v = 0; \quad \frac{\partial w}{\partial z} = 0; \quad \frac{\partial u}{\partial z} = 0; \quad \frac{\partial T}{\partial z} = 0$$

The solution procedure is based on the method used in [24], [34] and [46] for microtubes and on the Finite Volume Method described in [18]. First, the parabolic flow field condition is considered and the velocity field is solved. The temperature field, as a conjugate heat transfer problem, was then solved as the elliptic problem using the obtained velocity field. Also k acts as k_s for silicon wall and k_f in the case of the water. At the fluid – solid interface k is calculated as the harmonic mean value. The velocity-pressure coupling is solved using a SIMPLER method. A staggered grid is used for cross-stream velocities with power-law discretization scheme. The results of the grid sensitivity testing for $Re=743$ and central heating, are presented in Fig. 2.3.2. It is observed that a difference between temperature distribution for coarser (15x30x100) and finer grid (25x40x180) is negligible. So, the first one is used for the rest of calculations. Moreover the geometric data and working parameters are presented in the table 1.

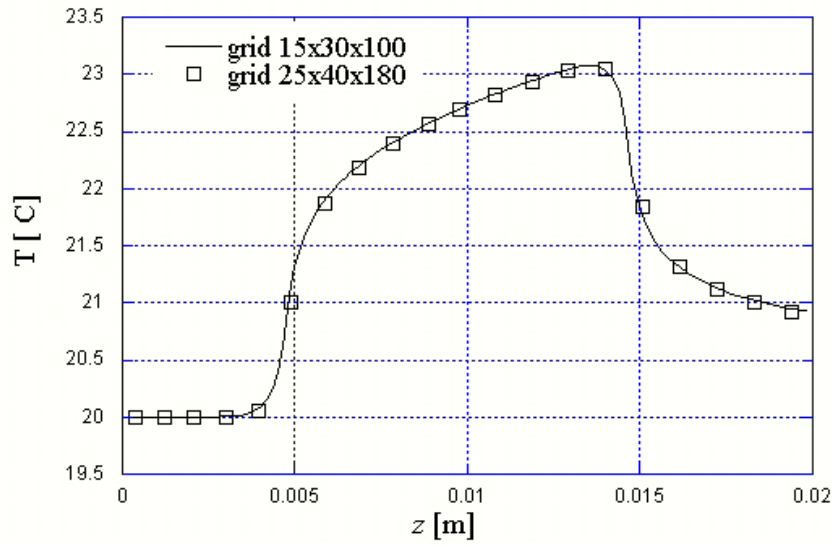


Fig. 2.3.2 The temperature distribution along the micro-heat sink for two grids.

Table 1 The geometric data and working parameters of the microchannel heat sink

w_f μm	w_c μm	H_c μm	H_t μm	L_h cm	L_t cm	w_t cm	q W/cm^2	u m/s	Re
36	64	280	489	1	2	1.5	34.6	0.275-7	34-743

2.3.2. Results and discussion

In the Fig. 2.3.3 the influence of Po variation versus Re is presented for different heating positions, defined as:

$$Po = f Re = \frac{2 \cdot \Delta p \cdot D_h^2}{L_{tot} \cdot u_{in} \cdot \mu} \quad (2.3.6)$$

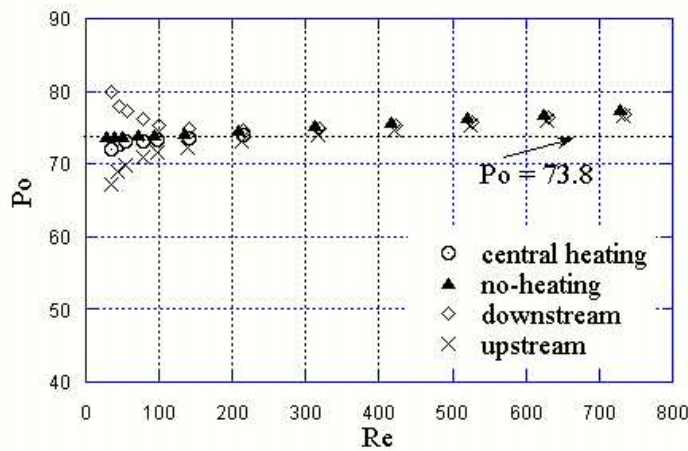


Fig. 2.3.3 Poiseuille number versus Re for different heating positions

It is observed that for low Re and upstream heating, the Po is decreasing as the Re is decreasing. This is the plausible observation considering that an average temperature of the water is increasing and the viscosity decreases. In the case of the downstream heating the Po is increasing while for the central heating the Po has almost the constant value as the Re decreases. In the Fig. 2.3.4 pumping power ratio (between the no-heating and heating case) versus mass flow rate is presented. The pumping power for no-heating case is higher compared to heating cases regardless the heating position. On the other hand as the mass flow rate is increasing, the heating cases are approaching the no-heating condition as the temperature decreases. The pumping power is lower for almost 30 % compared with no-heating flow, for the case of the upstream heating and low Re = 34. For the case of central and downstream heating the benefit is 20 % and respectively 10 %. So the Po is not a suitable parameter for the hydrodynamic losses evaluation for the case of the heating flows. The pumping power is defined with the following equation:

$$\Pi = M \cdot \frac{\Delta p}{\rho} \tag{2.3.7}$$

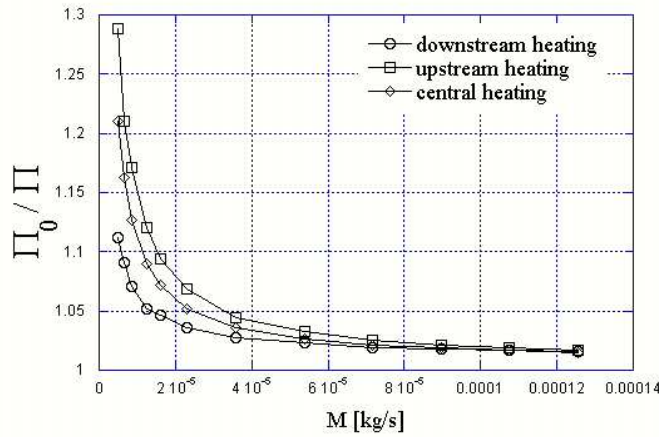


Fig. 2.3.4 The pumping power ratio for no-heating and heating case for various heating positions.

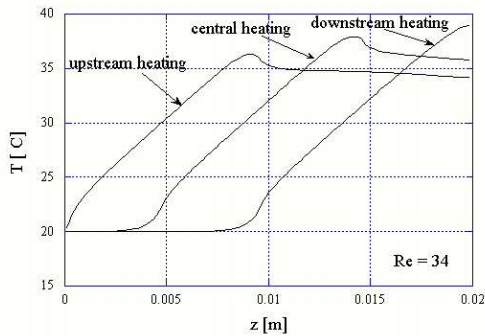


Fig. 2.3.5 The temperature variation at the centerline of the bottom wall versus axial distance for Re = 34

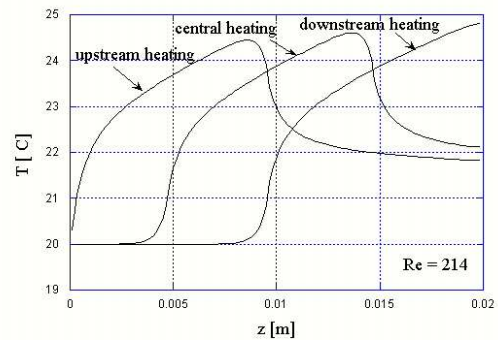


Fig. 2.3.6 The temperature variation at the centerline of the bottom wall versus axial distance for Re = 214

The total length of the tube was $L_{tot} = 2$ cm and the heating length $L_h = 1$ cm. For all the cases, it is observed that temperature at the centerline of the bottom wall of the heat sink is increasing with axial distance. Also the peak value is obtained approximately at $0.85z$, except

for downstream heating. In the case of the lower $Re = 34$, the difference between the temperature of the upstream and downstream heating is almost 20 %. As the fluid velocity is increasing, the outlet temperature is decreasing and the fluid viscosity has a less influence on fluid flow conditions. Consequently, in the case of the higher $Re = 214$, the maximum temperature is almost the same for all cases.

In figure 2.3.7 the thermal resistance versus Re is presented for three different heating positions defined as:

$$R = \frac{T_{\max} - T_{in}}{q} \quad (2.3.8)$$

It might be outlined that thermal resistance is decreasing as the Re is increasing. On the other hand the lowest thermal resistance is observed in the case of upstream heating followed by central and downstream heating. Difference between them is approximately 20 % as Re is lower than 200 and about 10 % for Re greater than 200. The reason for lower thermal resistance in the case of the upstream heating is the axial conduction phenomena downstream the end of the heating length. This results in a lower maximum temperature while the heat is spreading through the sink wall.

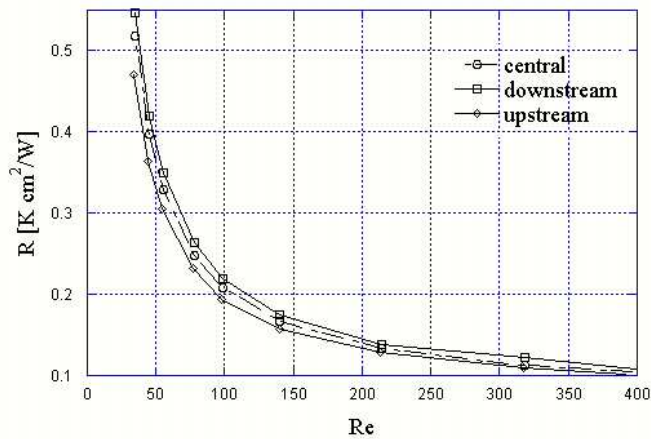


Fig. 2.3.7 The thermal resistance versus Re for various heating positions

2.3.3. Conclusions

The numerical investigation of a partially heated micro-channel heat sink is performed with geometry used in [24]. It is concluded that fluid viscosity has a strong impact on thermal and hydrodynamic behavior of a micro-heat sink. Moreover the heating position influences both the hydrodynamic and thermal characteristics of a micro-heat sink. In the case of hydrodynamic behavior it is observed that pumping power is suitable parameter for estimating the hydrodynamic losses instead of Po number. Considering the thermal performances, the upstream heating has a lower thermal resistance compared with central or downstream heating.

2.4. Effects of temperature dependent thermal conductivity on Nu number behavior in micro-tubes

The microchannel heat transfer and fluid flow has gained the interest in the last decade because of the downsizing of the thermal devices used in various fields of everyday life. The

cooling of the VLSI devices, biomedical applications, micro-heat-exchangers are some of the examples where the fundamentals of the microchannel heat transfer and fluid flow are essential for a proper design of these devices.

Myshan et al. [47] analyzed experimentally a developing heat transfer and fluid flow through rectangular microchannels. The experimental results have been compared with theoretical predictions from the literature and results obtained by numerical modeling of the present experiment. The experimental results of pressure drop and heat transfer confirm that including the entrance effects, the conventional theory is applicable for water flow through micro-channels. Wu and Little [27] have made the microchannel heat transfer and fluid flow experiments used for designing the Joule-Thomson micro-refrigerator. The working fluid in their research was nitrogen and inner diameters of the tubes were from 100 to 300 μm . Their heat transfer and hydrodynamic results shown differences against the conventional results for macrotubes.

Sharath et al. [48] investigated the steady-state heat transfer for laminar flow inside circular microtubes within a rectangular substrate. They have found that the peripheral average Nusselt number increased with increase of Reynolds number, Prandtl number, solid-to-fluid thermal conductivity ratio, and tube diameter-to-wafer thickness ratio. Ambatipudi and Rahman [49] investigated numerically the heat transfer in silicon substrate containing rectangular microchannels. It was found that the Nu number is higher for a system with larger number of channels and Reynolds number. Ng and Poh [50] developed the finite volume code for double layer conjugate heat transfer in microchannels. The computed results revealed the significant deviations in the temperature and velocity profiles under EDL effects.

Hwang and Soong [51] has also presented the investigation on numerical modeling of variable-property microchannel flows with electro-thermo-hydrodynamic interactions. The results also disclose that, compared to those in constant pressure gradient flows based on the same Reynolds number, effects of temperature non-uniformity and variable-property are relatively more pronounced in the constant flow rate flows. Kou et al. [52] investigated numerically the effects of heat transfer characteristics due to various channel heights and widths. It was shown that the optimal channel width is not significantly influenced by the decrease in the channel height when the flow power is fixed at 0.01 W and 0.1 W.

Wang et al. [53] analyzed the general properties of the rarefied diatomic gaseous flow in a microchannels under uniform heat flux boundary conditions. It is concluded that the gas acceleration at higher heat flux is more obvious than that at lower heat flux. Hong and Asako [54] analyzed the gaseous flow through the microchannels and microtubes with constant temperature boundary conditions. They were found a different heat transfer coefficients for each cooled and heated case. The rarefaction and compressibility effects on gaseous flow in microchannels are also investigated by Kavehpour et al. [55] and Sun and Faghri [56].

Celata et al. [57] presented an experimental investigation on single-phase laminar flow in circular microtubes, ranging in diameter from 528 down to 120 μm . Results show a decrease of Nusselt number with decreasing diameter, an axial dependence that is linked to thermal entrance effects and a dependence of the Nusselt number also on Reynolds number. Liu et al. [58] have reported numerical investigation to verify the variable-property effect of thermally developing flow in microchannel cooling passages. It was found a strong non-linear interaction mechanism that prevails in the correlation of Nu_{max} and X_{max} due to high heat flux condition and dramatic rise of liquid temperature. Sung and Mudawar [43] proposed a new hybrid cooling scheme for high-flux thermal management of electronic and power devices. Despite the rather poor thermophysical properties of HFE 7100, the proposed cooling scheme facilitated the dissipation of 304.9 W/cm² without phase change.

Naphon and Khonseur [44] performed experimental research to investigate the heat transfer characteristics and pressure drop in the micro-channel heat sinks under constant heat

flux conditions having the air as the working fluid. It was found that micro-channel geometry configuration has significant effect on the enhancement heat transfer and pressure drop.

Yap et al. [59] investigated the particle transport in microchannels where the size of the particles are comparable with the channel size while Broderick et al. [60] analyzed the thermally developing electro-osmotic flow inside the microtubes.

Herwig and Mahulikar [61] investigated the influence of the variable fluid properties on single-phase incompressible flows through microchannels. Both the cooled and heated flow was considered. With higher heat transfer rates, covering the whole temperature range between freezing and boiling of water, Nu number deviations as high as 28% may occur. It is also shown that Nu number decreases for cooled flows and increases for heated flows. Hong and Cheng [62] investigated numerically laminar forced convection of water in offset strip-fin microchannels network heat sinks for microelectronic cooling. It is found that there is an optimal fin interval and flow direction to minimize the pressure drop or pumping power, and this optimal point depends on the heat flux and maximum wall temperature.

The outcome of the research reports mentioned above is that special attention has to be paid to macroscale phenomena that are amplified at the microscale. For example, due to a high heat transfer rate, the temperature variable fluid properties have to be considered. Lelea [34] and Lelea et al. [24] investigated the influence of the temperature dependent fluid viscosity on Po number.

Therefore, the micro-tube heat transfer and fluid flow was investigated considering the variable fluid properties. The special attention in this case is paid to a temperature dependent thermal conductivity and its influence on a local Nu number. At the same time, two different heat flux directions were considered, heating and cooling with three fluid types: water and two dielectric fluids HFE 7600 and FC-70.

2.4.1. Numerical details

To analyze the temperature dependent thermal conductivity influence on Nu number behavior, the conjugate heat transfer and fluid flow phenomena were numerically solved based on a procedure described in [24].

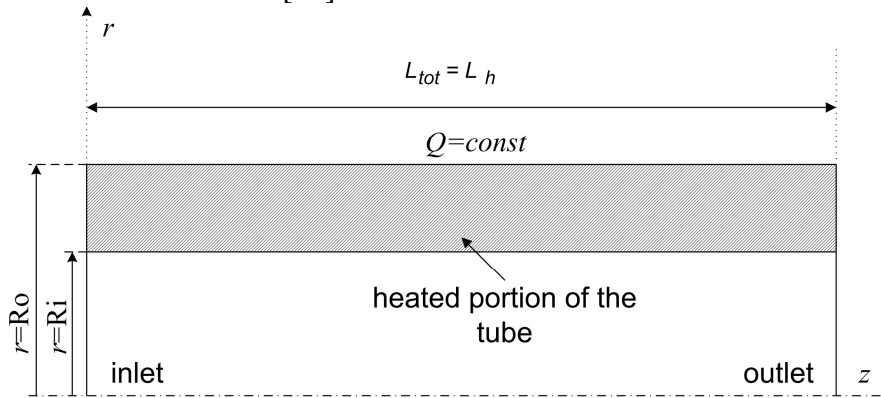


Fig. 2.4.1 The calculation domain

The computational domain is presented in Fig. 2.4.1, as follows:

The fluid flow domain defined at $r = 0, R_i$ and $z = 0, L$

The temperature field domain defined at $r = 0, R_o$ and $z = 0, L$

The following set of partial differential equations is used to describe the phenomena, considering the variable thermophysical properties of the water:

Continuity equation:

$$\frac{\partial(\rho(T) \cdot u)}{\partial z} + \frac{1}{r} \frac{\partial(r \cdot \rho(T) \cdot v)}{\partial r} = 0 \quad (2.4.1)$$

Momentum equation:

$$\frac{\partial(\rho(T)vu)}{\partial r} + \frac{\partial(\rho(T)uu)}{\partial z} = -\frac{dp}{dz} + \frac{1}{r} \frac{\partial}{\partial r} \left(\mu(T)r \frac{\partial u}{\partial r} \right) \quad (2.4.2)$$

Energy equation:

$$\frac{\partial(\rho(T)c_p(T)vT)}{\partial r} + \frac{\partial(\rho(T) \cdot c_p(T)uT)}{\partial z} = \left[\frac{1}{r} \frac{\partial}{\partial r} \left(k(T) \cdot r \frac{\partial T}{\partial r} \right) + \frac{\partial}{\partial z} \left(k(T) \frac{\partial T}{\partial z} \right) \right] \quad (2.4.3)$$

At the inlet of the tube, the uniform velocity and temperature field is considered, while at the exit the temperature gradient is equal to zero.

The boundary conditions are:

$$\begin{aligned} z = 0, 0 < r < R_o: \quad & u = u_0, T = T_w = T_0 \\ 0 < z < L_{tot}: \quad & r = 0, \frac{\partial u}{\partial r} = 0, \frac{\partial T}{\partial r} = 0, v = 0 \\ & r = R_i, u = v = 0 \end{aligned}$$

The Joule heating of the tube wall can be expressed either by the uniform heat generation through the tube wall or by the uniform heat flux imposed on the outer surface of the wall. For the latter case, the boundary condition is defined as,

$$r = R_o: \quad q_o = k_s \frac{\partial T}{\partial r} \quad (\text{for the heated portion of the tube})$$

$$k_s \frac{\partial T}{\partial r} = 0 \quad (\text{for the insulated portion of the tube})$$

where q_o is the heat flux based on the outer heat transfer area of the tube wall.

$$z = L_{tot}, 0 < r < R_o: \quad \frac{\partial T}{\partial z} = 0$$

The conjugate heat transfer procedure, implies the continuity of the temperature and heat flux at the solid – liquid interface defined as,

$$\begin{aligned} r = R_i: \quad & T_s|_{Ri+} = T_f|_{Ri-} \\ & k_s \left(\frac{\partial T_s}{\partial r} \right)_{Ri+} = k_f \left(\frac{\partial T_f}{\partial r} \right)_{Ri-} \end{aligned}$$

The partial differential equations (2.4.1) – (2.4.3) together with boundary conditions are solved using the finite volume method described in [18].

First, the parabolic flow field condition is considered and the velocity field is solved. The temperature field, as a conjugate heat transfer problem, was then calculated as the elliptic problem using the obtained velocity field. The fluid flow regime is considered to be a steady-state laminar flow with variable fluid properties. In order to evaluate fluid properties (density, viscosity, specific heat and thermal conductivity), the relations presented in the table 1 [63] are used in the present code.

In order to test the grid sensitivity, two grids have been used. The coarser one with 250 cells in radial direction and 400 cells in axial direction and finer grid with 500 and 800 cells in z - and r - direction respectively. Differences obtained for Nu were smaller than 0.1 %, so the coarser grid has been used for further calculations. Further details on code validation with experimental results are presented in [24].

Table 1 The fluid properties for water, HFE-7600 and FC-70

	Water	HFE-7600	FC-70
$\rho(t) =$	$1000.0 \cdot (1 - \frac{t + 288.9414}{508929.2 \cdot (t + 68.12963)} \cdot (t - 3.9863)^2)$	$1587.5 - 1.755 \cdot t$	$1984 - 1.93 \cdot t$
$c_p(t) =$	$8958.9 - 40.535 \cdot T + 0.11243 \cdot T^2 - 1.014 \cdot 10^{-4} \cdot T^3$	$3.1631 \cdot t + 1240.2$	$1014 + 1.554 \cdot t$
$k(t) =$	$-0.58166 + 6.355 \cdot 10^{-3} \cdot T - 7.964 \cdot 10^{-6} \cdot T^2$	$0.078 - 0.0003 \cdot t$	$0.07 - 0.00001 \cdot t$
$\mu(t) =$	$2.6412018 \cdot 10^{-4} + 0.0014009 \cdot e^{-\frac{t}{31.0578605}}$	$(1587.5 - 1.755 \cdot t) \cdot 10^{-6} \cdot e^{\frac{464.403382}{t+133} - 2.881482}$	$(83.861 - 6.7963 \cdot t + 0.26049 \cdot t^2 - 0.00559 \cdot t^3 + 6.8501 \cdot 10^{-5} t^4 - 4.4701 \cdot 10^{-7} \cdot t^5 + 1.2037 \cdot 10^{-9} \cdot t^6) \cdot 10^{-6} \cdot \rho(t)$

2.4.2. Results and discussion

The microtube conjugate heat transfer analysis was made for $D_i / D_o = 0.1/0.3$ mm and stainless steel as a tube material with $k = 15.9$ W/m K. To investigate the influence of the temperature dependent thermal conductivity on Nu number behavior, the low Re range was considered $Re < 400$. The input heat transfer rate was constant for all the runs $Q_0 = 0.5$ W considering two heat flux directions: cooling and heating. For the heating case the inlet temperature was $t_{in} = 20$ °C, while for the cooling case t_{in} was equal to the outlet temperature of the heating case.

The local Nu number is defined with the following equation:

$$Nu = \frac{h \cdot D_i}{k(T_{ave})}$$

where h is defined as:

$$h = \frac{q}{T_w - T_b}$$

and the local heat flux is defined as:

$$q = -k_f(T) \frac{\partial T}{\partial r}$$

In the Fig. 2.4.2, the Nu number relation versus axial distance is presented for lower $Re=69.5$ and three different cases. It is observed for cooling case that, after the initial decreasing, the Nu number is increasing in the region where the constant behavior is expecting. In the case of the heating, the Nu number exhibits the opposite relation to cooling case, it is increasing. If the thermal conductivity is constant the Nu number approaches the constant value $Nu = 4.36$ for the constant heat flux case. It has to be emphasized that for the water $Pr = 4.8-6.6$.

If the Re is increasing to $Re = 416.9$ the Nu number exhibits the conventional relation (Fig. 2.4.3). After the initial decreasing it approaches the constant value very close to the conventional one $Nu = 4.36$.

For a dielectric fluid HFE-7600 and lower $Re=70.6$ (Fig. 2.4.4), the local Nu number relation is different compared with the water case. In this case, the Nu number decreases for

heating and increases for cooling, the opposite to previous example with a water as the working fluid. The explanation might be found from the thermal conductivity variation (table 1). For water, the thermal conductivity increases as the temperature increases while in the case of a dielectric fluid HFE-7600 the thermal conductivity decreases as the temperature increases.

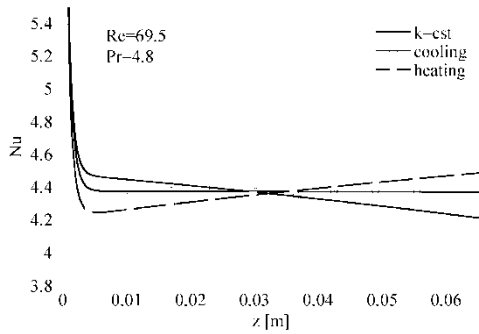


Fig. 2.4.2 The local Nu versus axial distance for water and $Re = 69.5$

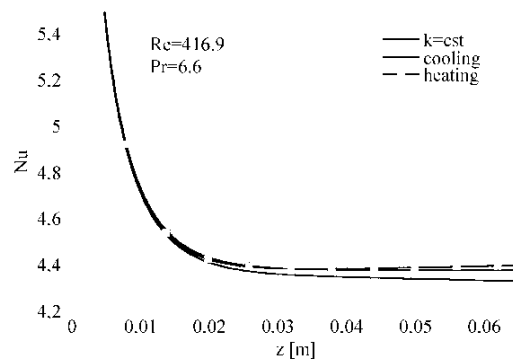


Fig. 2.4.3 The local Nu versus axial distance for water and $Re = 416.9$

If the Reynolds number increases to $Re=284.1$ the Nu number evolution for heating and cooling cases are the same (Fig 2.4.5). Compared to the constant thermal conductivity relation it is observed the longer thermal entrance length as the thermal conductivity is temperature dependent. In this case the Prandtl number is $Pr = 23.6 - 30.5$.

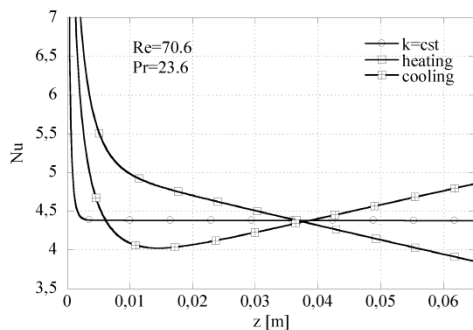


Fig. 2.4.4 The local Nu versus axial distance for HFE-7600 and $Re = 70.6$

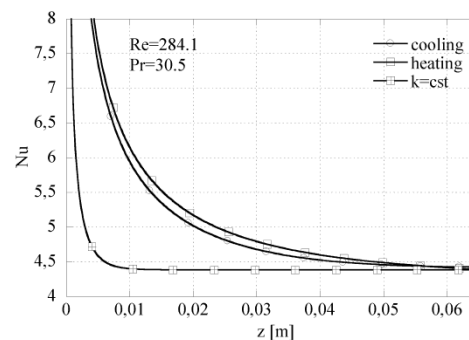


Fig. 2.4.5 The local Nu versus axial distance for HFE-7600 and $Re = 284.1$

For dielectric fluids with higher Pr numbers such as FC-70 (Fig. 2.4.6), where $Re = 14.5$ and $Pr= 200.2$ the Nu number decreases for both cases. Also, the constant thermal conductivity variation of the Nu number is close to the heating and cooling cases. It is observed that the local Nu numbers for cooling are lower than the Nu numbers for heating case. This is explained through the velocity profiles near the wall. In the case of the heated flows, the velocities are higher near the wall, because of the lower viscosity, that implies the higher heat transfer coefficients. Contrary, for the cooled flows the velocities are lower near the wall due to the higher fluid viscosity, and consequently the heat transfer coefficients are lower.

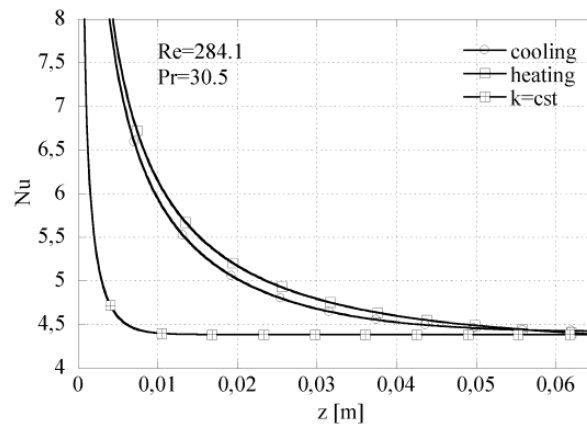


Fig. 2.4.6 The local Nu versus axial distance for FC-70 and $Re = 14.7$

2.4.3. Conclusions

The Nu number behavior on micro-tube heat transfer was investigated for three different fluids: water and two dielectric fluids HFE-7600 and FC-70. At the same time, two heat flux directions are considered, heating and cooling compared with $k=\text{const}$. It is observed that thermal conductivity has the strong influence on local Nu number behavior, as long as the Re is low. For water the Nu number increases as the fluid is heating and decreases as it is cooling. As the Re is increasing the thermal entrance length is longer so the thermal conductivity has a less influence on local Nu number.

For a dielectric fluid HFE-7600, the local Nu number has the opposite behavior compared to the water case. It is increasing while the fluid is cooling and decreases as it is heating. It is explained by the thermal conductivity temperature variation. For dielectric fluids such as FC-70 with very large Pr numbers, the thermal entrance length is very long so the local Nu number has similar variation for both heating and cooling case. In this case the heated flow implies higher Nu numbers compared with the cooled ones.

3. The viscous dissipation effect on heat transfer and fluid flow in micro-tubes and microchannel heat sinks

3.1. The viscous dissipation effect on heat transfer and fluid flow in micro-tubes

The recent technological developments and advances in devices that ensure the comfort of everyday life increases the importance of microchannel heat transfer and fluid flow. The cooling of the VLSI devices, biomedical applications, micro-heat-exchangers are some of the examples where the fundamentals of the microchannel heat transfer and fluid flow are essential for a proper design of these devices. As the scale of the systems is decreasing, the effects like thermal properties variation or viscous dissipation influence the thermal and hydrodynamic behavior and could not be neglected.

Arici et al. [64] made a numerical study related with thermally developing laminar forced convection in a pipe including the wall conductance and viscous dissipation. The viscous dissipation is found to affect both the wall and bulk fluid temperature profiles. Significant viscous dissipation effects have been observed for large Br. Its effect becomes more pronounced downstream.

Koo et al. [35] studied the effects of viscous dissipation on the temperature field and also on the friction factor using dimensional analysis and experimentally validated computer simulations for three different working fluids (water, methanol and iso-propanol) in micro-tubes and micro-channels. The variation of temperature with the Reynolds number was studied for rectangular channels and there was made a comparison between the experimental data and the computational results.

Celata et al. [65] analyzed the issue of scaling effects that cause influential effects when channel geometry is reduced below a certain limit. The results were connected with the role of viscous heating in micro-channel flows, its occurrence in the Navier Stokes equations and also there was made an experimental validation for verifying its presence in practice. The experimental results were compared with the values existing in the literature.

Rands et al. [66] investigated experimentally the laminar-turbulent transition for water flow in circular microtubes with diameters in the range 16.6–32.2 μm and $\text{Re} = 300\text{--}3400$. The fluid temperature rise, due to viscous dissipation, increases with increasing microtube length and decreasing microtube diameter. The viscous heating-induced temperature rise is significant, reaching 35 $^{\circ}\text{C}$ in some cases.

Nonino et al. [67,68] analyzed numerically the effects of viscous dissipation and temperature dependent viscosity in both thermally and simultaneously developing laminar flows of liquids in straight microchannels of arbitrary, but constant, cross-sections. It was shown that, both temperature dependence of viscosity and viscous dissipation effects cannot be neglected in a wide range of operating conditions. In all the computations, the same values of the Reynolds and Prandtl numbers, $\text{Re}=5000$ and $\text{Pr}=5$ at the reference temperature of the fluid have been assumed.

Hung [69] performed the second law analysis to investigate the influence of viscous dissipation in fully developed forced convection for single-phase liquid flow in a circular microchannel under imposed uniform wall heat flux. It is found that, under certain conditions, the effect of viscous dissipation on entropy generation in microchannel is significant and should not be neglected.

Hooman et al. [70,72], analyzed theoretically the role of viscous dissipation on forced convection, with temperature-dependent viscosity and thermal conductivity, through microchannels and micropipes, under isoflux wall boundary condition. The analytical results can be used for macrochannels where continuum assumption, and hence, no-slip condition is still valid.

J van Rij et al. [71] studied numerically the effect of viscous dissipation and rarefaction on rectangular microchannel convective heat transfer rates, subject to H_2 and T thermal boundary conditions. Both analytical and numerical data indicate that effects of viscous dissipation, flow work, and axial conduction are all significant within the slip flow regime for thermally/hydrodynamically developing and locally fully developed Nusselt numbers.

Morini [30] analyzed theoretically the limit of significance for viscous dissipation effects in microchannel flows. The role of the cross-sectional geometry on viscous dissipation as well as the minimum Reynolds number for which viscous dissipation effects can no longer be neglected for fluid flow in micro-channels were determined. It was found that viscous heating decreases the fluid viscosity, so the friction factor decreases as the Reynolds number increases.

Tunc and Bayazitoglu [73] investigated the convective heat transfer for steady laminar hydrodynamically developed flow in microtubes with temperature jump at the wall and viscous heating conditions. It was concluded that Nusselt number takes higher values for cooling and lower for heating.

Turgay and Yazicioglu [74] analyzed numerically the effect of surface roughness on convective heat transfer in two-dimensional parallel plate microchannels. Slip velocity and temperature jump at wall boundaries as well as the viscous dissipation effect were considered. It was found that the presence of axial conduction and viscous dissipation have increasing effects on heat transfer in smooth and rough channels, compared to cases where they are neglected.

Jeong [75] investigated the extended Graetz problem in a flat channel including effects of rarefaction, streamwise conduction and viscous dissipation. The flow is assumed to be fully developed with temperature developing profile. It was shown the Nusselt number decreases as Knudsen number or Brinkman number increases and as Peclet number decreases.

El-Genk and Yang [76] examined the experimental measurements in an attempt to quantify the effect of a potential slip on the reported values of Poiseuille number, determined from the pressure drop measurements in the experiments. It was concluded that the results of recent investigations suggest that a nonslip boundary may not be valid in highly confined and stressed flows.

Yeoun and Yogesh [77] presented the numerical report on conjugate heat transfer during the optical fiber coating process in an axisymmetric applicator considering the viscous dissipation. It was found that the temperature level increased with the fiber speed due primarily to the tremendous viscous dissipation within the fluid at higher speeds, especially in the die.

Judy et al. [23] investigated pressure driven liquid flow through round and square microchannels fabricated from fused silica and stainless steel. Regarding the viscous heating effect, the maximum rise in liquid temperature was 6.2 °C, found at the maximum Reynolds number tested $Re=300$.

The latest research reports revealed the fact that, below the certain tube diameter viscous dissipation can not be neglected at the microscale. At some circumstances the effect of viscous heating could affect the classic behaviors of the convective parameters like Nu or Po numbers. In this chapter the numerical modeling of the simultaneously developing heat flow in the microtubes was reported, considering the variable fluid properties and viscous dissipation term in the energy equation. Three different fluids have been considered water, HFE-7600 and FC-70 during cooling and heating to emphasize the behavior of the local Nu and Po numbers in the presence of viscous heating.

3.1.1. Numerical details

To analyze the temperature dependent thermal conductivity influence on Nu number behavior, the conjugate heat transfer and fluid flow phenomena were numerically solved based on a procedure described in [24].

The computational domain is presented in Fig. 2.4.1, as follows:

The fluid flow domain defined at $r = 0, R_i$ and $z = 0, L$

The temperature field domain defined at $r = 0, R_o$ and $z = 0, L$

The following set of partial differential equations is used to describe the phenomena, considering the variable thermophysical properties of the fluids and viscous dissipation:

Continuity equation:

$$\frac{\partial(\rho(T) \cdot u)}{\partial z} + \frac{1}{r} \frac{\partial(r \cdot \rho(T) \cdot v)}{\partial r} = 0 \quad (3.1.1)$$

Momentum equation:

$$\frac{\partial(\rho(T)vu)}{\partial r} + \frac{\partial(\rho(T)uu)}{\partial z} = -\frac{dp}{dz} + \frac{1}{r} \frac{\partial}{\partial r} \left(\mu(T)r \frac{\partial u}{\partial r} \right) \quad (3.1.2)$$

Energy equation:

$$\frac{\partial(\rho(T)c_p(T)vT)}{\partial r} + \frac{\partial(\rho(T) \cdot c_p(T)uT)}{\partial z} = \left[\frac{1}{r} \frac{\partial}{\partial r} \left(k(T) \cdot r \frac{\partial T}{\partial r} \right) + \frac{\partial}{\partial z} \left(k(T) \frac{\partial T}{\partial z} \right) \right] + \mu \cdot S_v \quad (3.1.3)$$

where the viscous dissipation term is defined as:

$$S_v = 2 \cdot \left[\left(\frac{\partial v}{\partial r} \right)^2 + \left(\frac{v}{r} \right)^2 + \left(\frac{\partial u}{\partial z} \right)^2 \right] + \left[\frac{\partial v}{\partial z} + \frac{\partial u}{\partial r} \right]^2 \quad (3.1.4)$$

At the inlet of the tube, the uniform velocity and temperature field is considered, while at the exit the temperature and velocity gradients are equal to zero.

The boundary conditions are:

$$\begin{aligned} z = 0, 0 < r < R_o: \quad & u = u_0, T = T_w = T_0 \\ 0 < z < L_{tot}: \quad & r = 0, \frac{\partial u}{\partial r} = 0, \frac{\partial T}{\partial r} = 0, v = 0 \\ & r = R_i, u = v = 0 \end{aligned}$$

The Joule heating of the tube wall can be expressed either by the uniform heat generation through the tube wall or by the uniform heat flux imposed on the outer surface of the wall. For the latter case, the boundary condition is defined as,

$$r = R_o: \quad q_o = k_s \frac{\partial T}{\partial r}$$

where q_o is the heat flux based on the outer heat transfer area of the tube wall.

$$z = L_{tot}, 0 < r < R_o: \quad \frac{\partial T}{\partial z} = 0$$

The conjugate heat transfer procedure, implies the continuity of the temperature and heat flux at the solid – liquid interface defined as,

$$\begin{aligned} r = R_i: T_s|_{Ri+} &= T_f|_{Ri-} \\ k_s \left(\frac{\partial T_s}{\partial r} \right)_{Ri+} &= k_f \left(\frac{\partial T_f}{\partial r} \right)_{Ri-} \end{aligned}$$

The partial differential equations (3.1.1) – (3.1.3) together with boundary conditions are solved using the finite volume method described in [18].

First, the parabolic flow field condition is considered and the velocity field is solved. The temperature field, as a conjugate heat transfer problem, was then calculated as the elliptic problem using the obtained velocity field. The fluid flow regime is considered to be a steady-state laminar flow with variable fluid properties. In order to evaluate fluid properties (density, viscosity, specific heat and thermal conductivity), the relations for water, HFE-7600 and FC-70 presented in [63,78] are used in the present code.

In order to test the grid sensitivity, two grids have been used. The coarser one with 250 cells in radial direction and 400 cells in axial direction and finer grid with 500 and 800 cells in z - and r - direction respectively. Differences obtained for Nu were smaller than 0.1 %, so the coarser grid has been used for further calculations. Additionally, the numerical results have been compared with experimental results obtained by Celata et al. [65] and Rands et al. [66] with satisfactory deviation (Fig. 3.1.2).

The following non-dimensional parameters are obtained in the numerical computations, for water (Re=258-1684, Pr=6.4-6.9), HFE-7600 (Re=186-1130, Pr=29.3-32.2) and FC-70 (Re=7.2-43.2, Pr=189.8-317.4). The heat transfer rate imposed on the outer wall of the tube was $Q=0.5$ W.

Darcy friction factor is defined by the following equation:

$$f = \frac{-(dp/dz) \cdot D_i}{\rho \cdot u_m^2 / 2} \quad (3.1.5)$$

and a Re is defined as:

$$\text{Re} = \frac{\rho \cdot u_m \cdot D_i}{\mu} \quad (3.1.6)$$

So, from (3.1.5) and (3.1.6) the local Po can be obtained in the following form:

$$\text{Po} = f \text{Re} = \frac{-2 \cdot (dp/dz) \cdot D_i^2}{u_m \cdot \mu} \quad (3.1.7)$$

While the local Nu number is defined with the following equation:

$$\text{Nu} = \frac{h \cdot D_i}{k(T_m)} \quad (3.1.8)$$

The Brinkman number for constant wall heat flux is defined as:

$$\text{Br} = \frac{u_m^2 \cdot \mu}{q \cdot D_i} \quad (3.1.9)$$

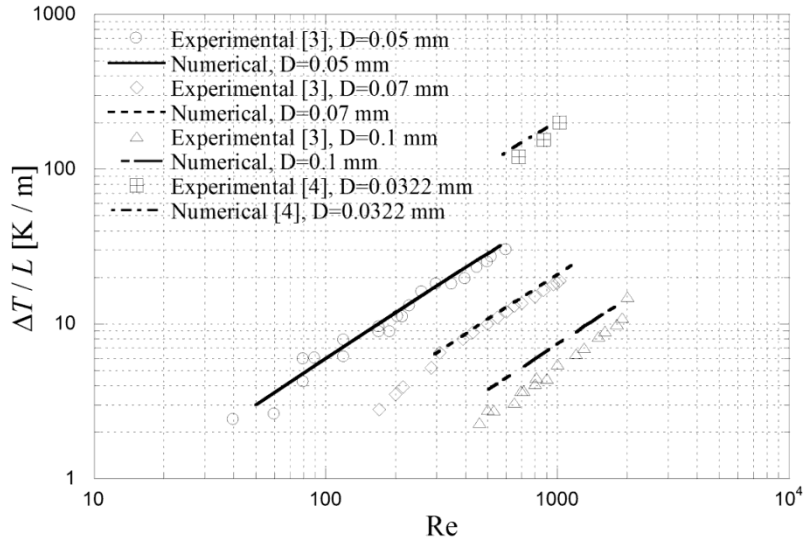


Fig. 3.1.2 The validation of the numerical code with experimental results [65,66] for various diameters of the tube.

3.1.2. Results and discussion

Numerical computations were made for three different $\text{Br} = 0.01, 0.1$ and 0.5 and two heat flux directions: heating and cooling. In the Fig. 3.1.3, the relation of Po versus non-dimensional axial distance is presented for water. It might be observed that Po decreases asymptotically to the fully developed value for circular channels. On the other hand as the Br increases and viscous dissipation influences the fluid flow, the thermal entrance length is longer. On the other hand difference between the cooling and heating case, for specific Br number is observed for $\text{Br} = 0.5$.

In the Fig. 3.1.4 the variation of Po number for HFE-7600 is presented. For the heating case the local distribution of the Po has a conventional behavior with the fully developed value slightly lower than a usual value for a pipe flow ($\text{Po}=64$). As the tube wall is cooled, after initial decreasing, the local Po is increasing and asymptotically is approaching the fully developed value. The opposite behavior of these two cases is explained through the

temperature dependent viscosity. As the fluid is heating the viscosity is decreasing and the pressure gradient is decreasing along the axial distance. On the other hand while the fluid is cooling the viscosity is increasing and the pressure gradient is increasing. Similar to the water flow, the viscous heating is observed for the $Br = 0.1$ and 0.5 . For the later, difference between the cases with and without viscous dissipation is 5 %. It is observed that for cooling with $Br = 0.5$, the Po has the non-heating behavior with fully developed value close to $Po = 64$. The plausible explanation is that viscous heating has the same order of magnitude as the external heating source.

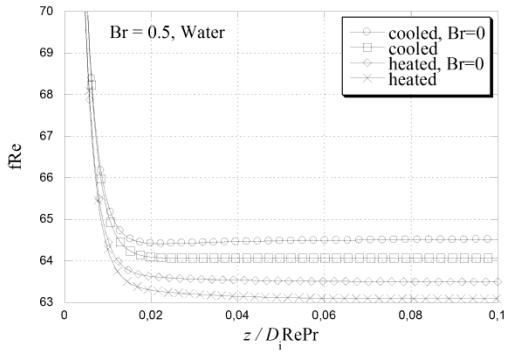


Fig. 3.1.3 The local fRe versus non-dimensional axial distance for water and $Br = 0.5$

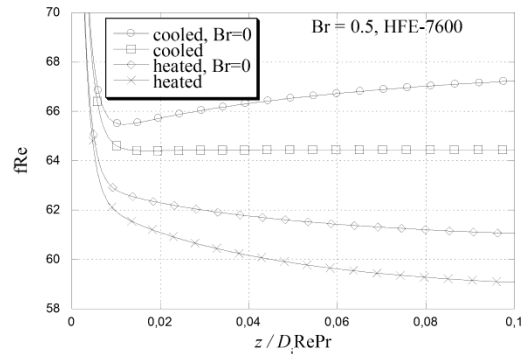


Fig. 3.1.4 The local fRe versus non-dimensional axial distance for HFE-7600 and $Br = 0.5$

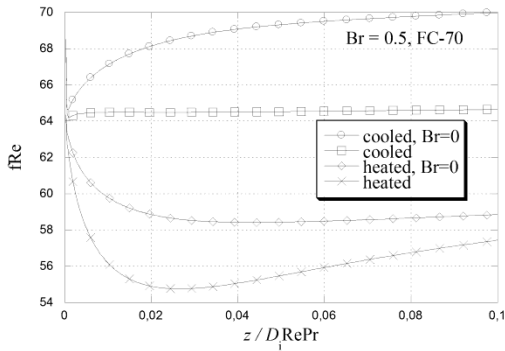


Fig. 3.1.5 The local fRe versus non-dimensional axial distance for FC-70 and $Br = 0.5$

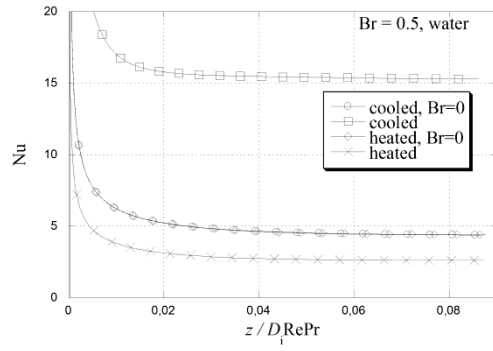


Fig. 3.1.6 The local Nu versus non-dimensional axial distance for water and $Br = 0.5$

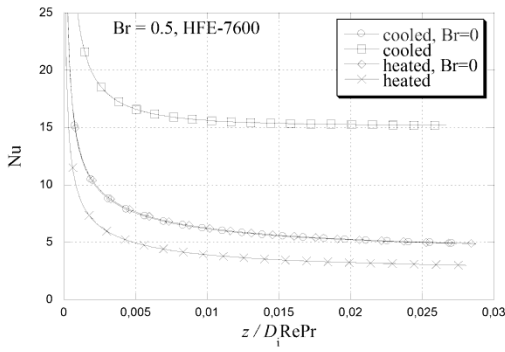


Fig. 3.1.7 The local Nu versus non-dimensional axial distance for HFE-7600 and $Br = 0.5$

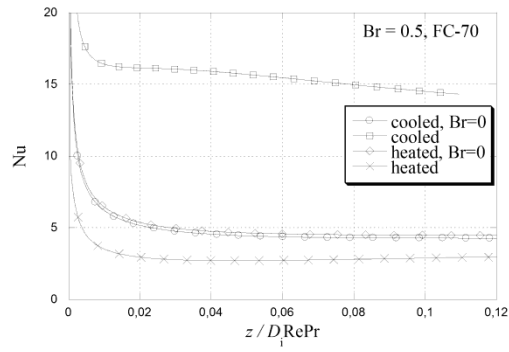


Fig. 3.1.8 The local Nu versus non-dimensional axial distance for FC-70 and $Br = 0.5$

The similar behavior is observed for the FC-70 (Fig. 3.1.5) with longer hydrodynamic entrance length due to a very high fluid viscosity. For $Br = 0.5$ a deviation from the case

where the viscosity heating is neglected is almost 10 %. Once again for the later case and cooling of the fluid, the Po exhibits the non-heating behavior with fully developed $Po = 64$.

In Fig. 3.1.6 the Nu variation versus non-dimensional axial distance is presented for water. For $Br = 0$ the Nu number behavior is in accordance with the conclusions presented in [78] regarding the effect of the fluid thermal conductivity. If the $Br = 0.01$ a deviation from the case that includes the viscosity dissipation is very small. As the Br is increasing a difference is larger and for $Br = 0.5$ the Nu number is almost three times larger for cooling case. Moreover deviation is much larger for cooling case than for heating because of the smaller temperature difference between the tube wall and fluid, in the case of cooling. Also as the Re number increases the Nu number relation for cooling and heating overlaps if the viscous dissipation is excluded.

The similar conclusions are outlined for dielectric fluids HFE-7600 and FC-70 (Fig. 3.1.7 and Fig. 3.1.8). Moreover for $Br = 0.5$ the ratio between the cases with and without viscous dissipation is preserved for all fluids.

3.1.3. Conclusions

The effect of viscous dissipation on micro-tube fluid flow and heat transfer was investigated for three different fluids and two different flux directions, heating and cooling. The following conclusions might be outlined from the presented results:

- The friction factor and Po are affected at $Br=0.5$ for water and starting with $Br=0.1$ for highly viscous fluids HFE-7600 and FC-70. The same conclusion is valid for Nu number relation.
- The Nu number is higher for cooling than for a heating case due to a lower temperature difference as the fluid is cooling. For $Br=0.5$ the Nu number for a cooling case is about three times higher compared with a heating case, regardless the fluid type.
- For $Br=0.5$, cooling case and for all fluid types considered, the Po number approaches conventional fully developed value for pipe flow, $Po=64$. The plausible explanation is that the external cooling and viscous heating are of the same order of magnitude.

3.2. The developing heat transfer and fluid flow in micro-channel heat sink with viscous heating effect

The miniaturization of devices in electronics industry, biomedical applications or process industry raised the interest in microchannel heat transfer and fluid flow. The fundamentals of the microchannel heat transfer and fluid flow are essential for a proper design of these devices. On the other hand, as the scale of the system is decreasing below a certain value, some effects like temperature dependent properties or viscous dissipation have a considerable influence on thermal and hydrodynamic behavior.

Arici et al. [64] made a numerical study related with thermally developing the laminar forced convection in a pipe including the wall conductance and viscous dissipation. The viscous dissipation is found to affect both the wall and bulk fluid temperature profiles. Significant viscous dissipation effects have been observed for large Br . Its effect becomes more pronounced downstream.

Koo et al. [35] studied the effects of viscous dissipation on the temperature field and also on the friction factor using dimensional analysis and experimentally validated computer simulations for three different working fluids (water, methanol and iso-propanol) in micro-tubes and micro-channels. The variation of temperature with the Reynolds number was studied for rectangular channels and there was made a comparison between the experimental data and the computational results.

Celata et al. [65] analyzed the issue of scaling effects that cause influential effects when channel geometry is reduced below a certain limit. The results were connected with the role of viscous heating in micro-channel flows, its occurrence in the Navier Stokes equations and also there was made an experimental validation for verifying its presence in practice. The experimental results were compared with the values existing in literature for compliance.

Rands et al. [66] investigated experimentally the laminar-turbulent transition for water flow in circular microtubes with diameters in the range 16.6–32.2 μm and $\text{Re} = 300\text{--}3400$. The fluid temperature rise, due to viscous dissipation, increases with increasing microtube length and decreasing microtube diameter. The viscous heating-induced temperature rise is significant, reaching 35 $^{\circ}\text{C}$ in some cases.

Nonino et al. [67] analyzed numerically the effects of viscous dissipation and temperature dependent viscosity in both thermally and simultaneously developing laminar flows of liquids in straight microchannels of arbitrary, but constant, cross-sections. It was shown that, both temperature dependence of viscosity and viscous dissipation effects cannot be neglected in a wide range of operative conditions. In all the computations, the same values of the Reynolds and Prandtl numbers, $\text{Re}=500$ and $\text{Pr}=5$ at the reference temperature of the fluid have been assumed.

Chen [79] performed forced convection flow in microchannels with viscous dissipation effect and slip flow regime. It was found that when the viscous dissipation effect is considered the Nu is increasing and then reaches its final value. It also produces a noticeable increase in the fully developed Nusselt number,

Judy et al. [23] investigated pressure driven liquid flow through round and square microchannels fabricated from fused silica and stainless steel. Regarding the viscous heating effect, the maximum rise in liquid temperature was 6.2 $^{\circ}\text{C}$, found at the maximum Reynolds number tested $\text{Re}=300$.

Hooman et al. [70,72], analyzed theoretically the role of viscous dissipation on forced convection, with temperature-dependent viscosity and thermal conductivity, through microchannels and micropipes, under isoflux wall boundary condition. The analytical results can be used for macrochannels where continuum assumption, and hence, no-slip condition is still valid.

J van Rij et al. [71] studied numerically the effect of viscous dissipation and rarefaction on rectangular microchannel convective heat transfer rates, subject to H_2 and T thermal boundary conditions. Both analytical and numerical data indicate that effects of viscous dissipation, flow work, and axial conduction are all significant within the slip flow regime for thermally/hydrodynamically developing and locally fully developed Nusselt numbers.

Morini [30] analyzed theoretically the limit of significance for viscous dissipation effects in microchannel flows. The role of the cross-sectional geometry on viscous dissipation as well as the minimum Reynolds number for which viscous dissipation effects can no longer be neglected for fluid flow in micro-channels were determined. It was found that viscous heating decreases the fluid viscosity, so the friction factor decreases as the Reynolds number increases.

Tunc and Bayazitoglu [73] investigated the convective heat transfer for steady laminar hydrodynamically developed flow in microtubes with temperature jump at the wall and viscous heating conditions. It was concluded that Nusselt number takes higher values for cooling and lower for heating.

Magyari and Barletta [80] analyzed analytically laminar forced convection flow of a liquid in the fully developed region of a pipe with viscous dissipation effect and temperature dependent viscosity.

Jeong [75] investigated the extended Graetz problem in a flat channel including effects of rarefaction, streamwise conduction and viscous dissipation. The flow is assumed to be fully developed with temperature developing profile. It was shown the Nusselt number decreases as Knudsen number or Brinkman number increases and as Peclet number decreases.

El-Genk and Yang [76] examined the experimental measurements in an attempt to quantify the effect of a potential slip on the reported values of Poiseuille number, determined from the pressure drop measurements in the experiments. It was concluded that the results of recent investigations suggest that a nonslip boundary may not be valid in highly confined and stressed flows.

Yeoun and Yogesh [77] presented the numerical report on conjugate heat transfer during the optical fiber coating process in an axisymmetric applicator considering the viscous dissipation. It was found that the temperature level increased with the fiber speed due primarily to the tremendous viscous dissipation within the fluid at higher speeds, especially in the die.

Hung [81] performed the second law analysis to investigate the influence of viscous dissipation in fully developed forced convection for single-phase liquid flow in a circular microchannel under imposed uniform wall heat flux. It is found that, under certain conditions, the effect of viscous dissipation on entropy generation in microchannel is significant and should not be neglected.

The latest research reports revealed the fact that viscous dissipation cannot be neglected at the microscale. At some circumstances the effect of viscous heating could affect the classic behaviors of the convective parameters like Nu or Po numbers. Most of the research reports presented above consider the fully developed flow and only a few of them take into account the variable fluid viscosity and simultaneously developing heat transfer and fluid flow.

Considering these arguments, this chapter deals with numerical modeling of the thermal and hydrodynamic developing laminar fluid flow and heat transfer in the square microchannel-heat sink for $Re < 2100$ and $Pr = 5-30$. The variable fluid viscosity and viscous dissipation term in the energy equation, were considered. Three different fluids have been considered water, HFE-7600 and isopropanol during cooling and heating to emphasize the behavior of the local Nu and Po numbers.

3.2.1. Numerical details

The one-layer microchannel heat sink is presented in the Fig. 2.3.1. Due to the symmetry plane, the half cross-section of one channel is considered in computations. The conventional set of the Navier-Stokes equations has been used for the conjugate laminar steady state heat transfer and fluid flow, as follows:

The continuity equation:

$$\frac{\partial u}{\partial x} + \frac{\partial v}{\partial y} + \frac{\partial w}{\partial z} = 0 \quad (3.2.1)$$

The momentum equation:

$$\rho \left(u \frac{\partial u}{\partial x} + v \frac{\partial u}{\partial y} + w \frac{\partial u}{\partial z} \right) = -\frac{dp}{dz} + \left(\frac{\partial}{\partial x} \left(\mu \frac{\partial u}{\partial x} \right) + \frac{\partial}{\partial y} \left(\mu \frac{\partial u}{\partial y} \right) \right) \quad (3.2.2)$$

$$\rho \left(u \frac{\partial v}{\partial x} + v \frac{\partial v}{\partial y} + w \frac{\partial v}{\partial z} \right) = -\frac{\partial p}{\partial x} + \left(\frac{\partial}{\partial x} \left(\mu \frac{\partial v}{\partial x} \right) + \frac{\partial}{\partial y} \left(\mu \frac{\partial v}{\partial y} \right) \right) \quad (3.2.3)$$

$$\rho \left(u \frac{\partial w}{\partial x} + v \frac{\partial w}{\partial y} + w \frac{\partial w}{\partial z} \right) = -\frac{\partial p}{\partial y} + \left(\frac{\partial}{\partial x} \left(\mu \frac{\partial w}{\partial x} \right) + \frac{\partial}{\partial y} \left(\mu \frac{\partial w}{\partial y} \right) \right) \quad (3.2.4)$$

The energy equation (for both fluid and solid):

$$\rho \cdot c_p \cdot \left(u \frac{\partial T}{\partial x} + v \frac{\partial T}{\partial y} + w \frac{\partial T}{\partial z} \right) = k \left(\frac{\partial^2 T}{\partial x^2} + \frac{\partial^2 T}{\partial y^2} + \frac{\partial^2 T}{\partial z^2} \right) + \Phi \quad (3.2.5)$$

Where viscous dissipation term is defined as:

$$\Phi = \mu \cdot \left\{ 2 \cdot \left[\left(\frac{\partial u}{\partial x} \right)^2 + \left(\frac{\partial v}{\partial y} \right)^2 + \left(\frac{\partial w}{\partial z} \right)^2 \right] + \left(\frac{\partial v}{\partial x} + \frac{\partial u}{\partial y} \right)^2 + \left(\frac{\partial w}{\partial y} + \frac{\partial v}{\partial z} \right)^2 + \left(\frac{\partial u}{\partial z} + \frac{\partial w}{\partial x} \right)^2 \right\} \quad (3.2.6)$$

The fluid properties are constant except for fluid viscosity that is evaluated with the following equations:

- for water:

$$\mu(t) = 2.6412018 \cdot 10^{-4} + 0.0014009 \cdot e^{-\frac{t}{31.0578605}} \quad (3.2.7)$$

- for dielectric fluid HFE-7600 [18]:

$$\mu(t) = (1587.5 - 1.755 \cdot t) \cdot 10^{-6} \cdot e^{\frac{464.403382}{t+133} - 2.881482} \quad (3.2.8)$$

- for isopropanol:

$$\mu(T) = 4.266 \cdot 10^{-7} T^2 - 3.016 \cdot 10^{-4} \cdot T + 5.398 \cdot 10^{-2} \quad (3.2.9)$$

The thermal conductivity of the silicon substrate is $k_s = 148$ W/m K. The following boundary conditions are prescribed for the system of the partial differential equations:

The conjugate heat transfer procedure, implies the continuity of the temperature and heat flux at the solid – liquid interface defined as,

$$x = W_f/2: \quad T_s|_{x+} = T_f|_{x-}$$

$$k_s \left(\frac{\partial T_s}{\partial x} \right)_{x+} = k_f \left(\frac{\partial T_f}{\partial x} \right)_{x-}$$

$$y = H_t - H_c: \quad T_s|_{y+} = T_f|_{y-}$$

$$k_s \left(\frac{\partial T_s}{\partial y} \right)_{y+} = k_f \left(\frac{\partial T_f}{\partial y} \right)_{y-}$$

For the heated portion of the microchannel the following boundary condition is defined:

$y = 0$:

$$q_o = k_s \frac{\partial T}{\partial y}$$

Also at the inlet cross-section, uniform velocity and temperature field are considered:

$z = 0$:

$$u = u_{in} \text{ and } T = T_{in}$$

The upper boundary is isolated defined as:

$$k_s \frac{\partial T}{\partial y} = 0$$

At the outlet of the microchannel the following boundary conditions are prescribed:

$z = L_t$

$$\frac{\partial T}{\partial z} = 0; \frac{\partial u}{\partial z} = 0; v = w = 0$$

At the symmetry boundary:

$$x = W_f/2 + W_c/2$$

$$v = 0; \frac{\partial w}{\partial x} = 0; \frac{\partial u}{\partial x} = 0; \frac{\partial T}{\partial x} = 0$$

$$x = 0$$

$$\frac{\partial T}{\partial z} = 0$$

The microchannel heat sink dimensions are presented in the table 1.

Table 1 The geometric data and working parameters of the microchannel heat sink

w_f	w_c	H_c	H_t	L_h	L_t	w_t	q	Re
μm	μm	μm	μm	cm	cm	cm	W/cm^2	
36	50	50	100	5	5	1.5	35	200-2100

The solution procedure is based on the method used in [24] for microtubes and on the Finite Volume Method described in [18]. First, the parabolic flow field condition is considered and the velocity field is solved. The temperature field, as a conjugate heat transfer problem, was then solved as the elliptic problem using the obtained velocity field. Also k acts as k_s for silicon wall and k_f in the case of the fluid. At the fluid – solid interface k is calculated as the harmonic mean value. The velocity-pressure coupling is solved using a SIMPLER method. A staggered grid is used for cross-stream velocities with power-law discretization scheme. The results of the grid sensitivity testing for water and $\text{Re}=2100$ are presented in Fig. 2. It is observed that a difference between a coarser (15x30x100) and finer grid (25x40x180) is below 0.1 % for bulk temperature and less than 1 % for average wall temperature. So, the first one is used for the rest of calculations.

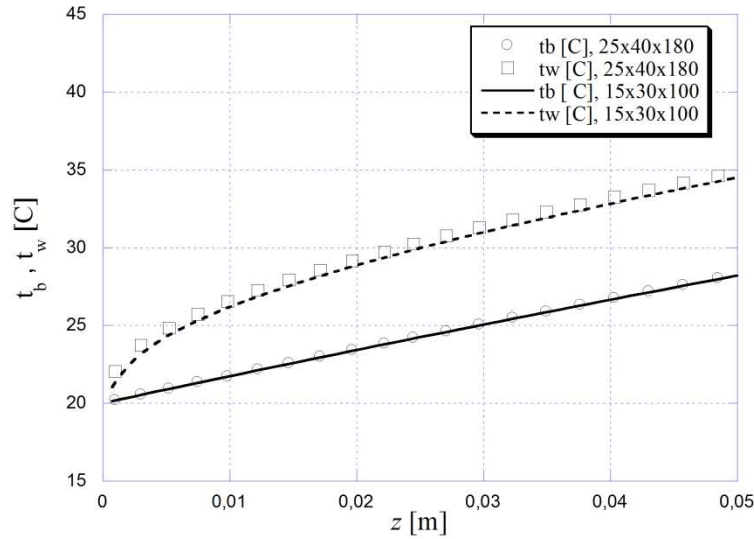


Fig. 3.2.2 The temperature distribution along the micro-heat sink for two grids.

Darcy friction factor is defined by the following equation:

$$f = \frac{-(dp/dz) \cdot D_h}{\rho \cdot u_m^2 / 2} \quad (3.2.10)$$

and a Re is defined as:

$$\text{Re} = \frac{\rho \cdot u_m \cdot D_h}{\mu} \quad (3.2.11)$$

So, from (3.2.5) and (3.2.6) the local Po can be obtained in the following form:

$$Po = f Re = \frac{-2 \cdot (dp/dz) \cdot D_h^2}{u_m \cdot \mu} \quad (3.2.12)$$

While the local Nu number is defined with the following equation:

$$Nu = \frac{h_{ave} \cdot D_h}{k} \quad (3.2.13)$$

Where the average heat transfer coefficient, based on the peripherally averaged heat flux and wall temperature, is defined as:

$$h_{ave} = \frac{q|_{\Gamma}}{t_w|_{\Gamma} - t_b}$$

The conjugate heat transfer and fluid flow of the microchannel heat sink was analyzed also by Li et al. [82] and Lee and Garimella [83] with averaged Nu.

The Brinkman number for constant wall heat flux is defined as:

$$Br = \frac{u_m^2 \cdot \mu}{q \cdot D_h} \quad (3.2.14)$$

The Br has the positive value for heating and negative for cooling. The viscosity in this case is evaluated at the inlet temperature.

3.2.2. Results and discussion

In the Fig. 3.2.3 the temperature variation along the microchannel has been presented for isopropanol and conditions presented in [23] (square microchannel with $D_h = 74.1 \mu m$ $L = 11.4$ cm and $Re = 300$). A difference between the outlet temperature obtained by the numerical code and the experimental outlet temperature is about 3 %. The code validation was also made with experimental results for average Po with viscosity based on the inlet temperature (Fig. 3.2.4). The excellent agreement between the present numerical results and experimental results [23] is observed with a maximum difference of 3 %. In the same figure the average Po variation with Re is presented for water and HFE-7600. For dielectric fluid HFE-7600 the Po is decreasing with Re but at the lower rate compared with isopropanol, because of the lower viscosity. Contrary to isopropanol and HFE-7600, the Po is slightly increasing with Re for water.

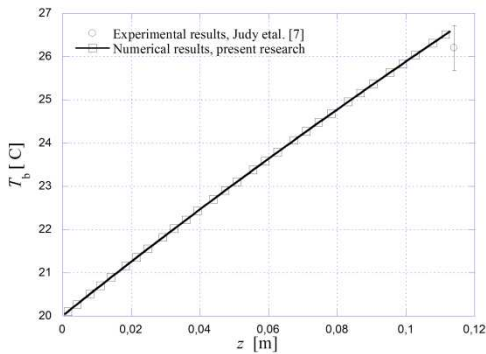


Fig. 3.2.3 The bulk temperature distribution along the micro-heat sink for isopropanol

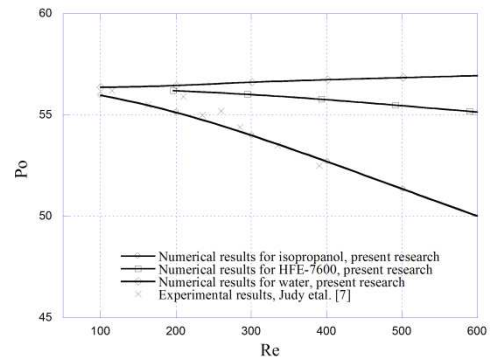


Fig. 3.2.4 The Po variation versus Re for water, HFE-7600 and isopropanol, compared with experimental results [7]

The local Po distribution is presenting in the Figs. 3.2.5-3.2.7 for three working fluids. It is observed that Po is decreasing along the microchannel due to the temperature dependent viscosity. Moreover as the Br is increasing the local Po is increasing in case of heating.

On the other hand for the cooling case, the local Po is increasing for low $Br = -0.002$. As the Br is increasing the local Po is approaching the constant value in the fully developed region. It has to be stated that a fully developed Po is lower than the conventional value for the square channel ($Po = 56.908$).

The plausible explanation for the fully developed Po at a fixed Br is related to the ratio between the heat transfer rate due to viscous dissipation and sensible heat dispersed through the bottom wall of the micro-heat sink. At a certain value of Br (or Re) the ratio between the viscous heating and external cooling is equal to 1. In the Fig. 3.2.8 the ratio between the heat transfer rate from viscous heating and external heating (or cooling) versus Re is presented. The heat transfer rate ratio is equal to unity at $Re = 430$ for isopropanol, at $Re = 1140$ for HFE and at $Re = 1800$ for water.

On the other hand, the fully developed values are observed for water at $Re = 1800$, for HFE-7600 at $Re = 1330$ and for isopropanol at $Re = 480$. Obviously these values are in the range of the heat transfer rate ratio equal to unity.

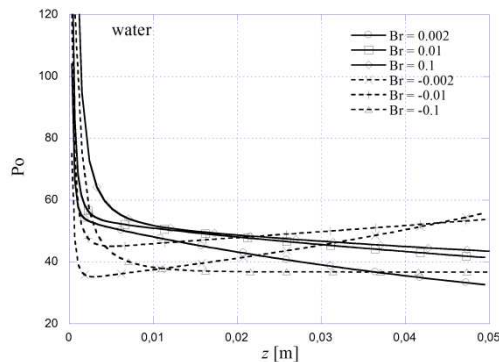


Fig. 3.2.5 The local Po variation along the micro-heat sink for water, various Br and two heat flux directions (heating and cooling)

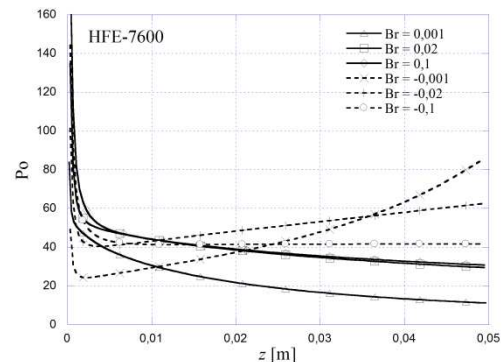


Fig. 3.2.6 The local Po variation along the micro-heat sink for HFE-7600, various Br and two heat flux directions (heating and cooling)

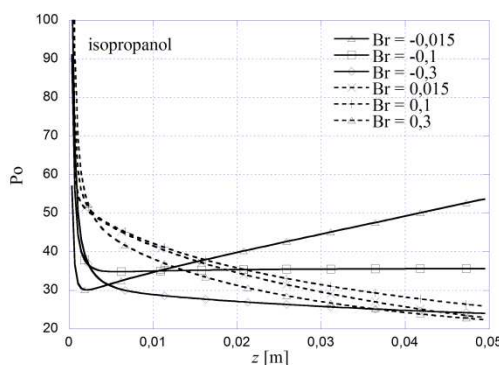


Fig. 3.2.7 The local Po variation along the micro-heat sink for isopropanol, various Br and two heat flux directions (heating and cooling)

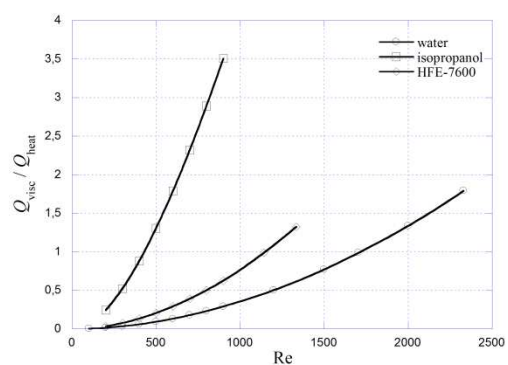


Fig. 3.2.8 The merit of the viscous heating for water, isopropanol and HFE-7600

In the Figs. 3.2.9, 3.2.10 and 3.2.11 the peripherally averaged local Nu versus axial distance is presented. It is difficult to compare the fully developed values for local Nu in the case of the conjugate heat transfer due to the different heating of the side walls. This issue is more complicated in the presence of viscous heating due to the additional internal heat source.

The peripherally average local Nu exhibits the boundary layer flow approaching the fully developed value. For water (Fig. 3.2.9) and low Br = 0.002 (-0.002) the local Nu is approaching the conventional fully developed $Nu_{fd} \cong 3.608$. As the Br is increasing to 0.01 (-0.01) the fully developed value is still preserved with the longer thermal entrance effect. If the Br is increasing to 0.1 the thermal entrance length is increasing and the fully developed value is decreasing to $Nu_{fd} \cong 2.67$. In the case of cooling Br = -0.1, both the thermal entrance length and fully developed $Nu_{fd} \cong 5.42$ are increasing. Deviation from the conventional fully developed value is induced by the temperature difference between the wall and fluid, that increases for heating and decreases in the case of cooling. As the fluid is heating, the wall temperature increases more rapidly than a bulk fluid temperature due to the combined effect of temperature dependent viscosity and viscous heating. Consequently the temperature difference is increasing as the Re or Br is increasing and Nu number is decreasing. The reverse case is true for the cooling case.

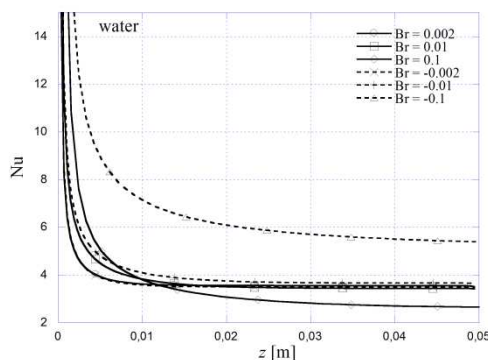


Fig. 3.2.9 The local Nu versus axial distance for water

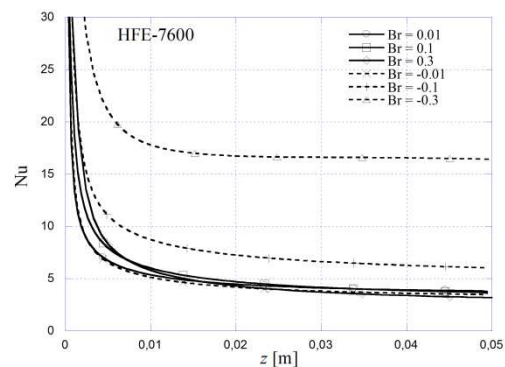


Fig. 3.2.10 The local Nu versus axial distance for HFE-7600

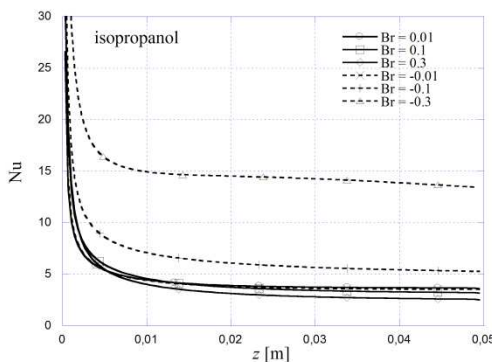


Fig. 3.2.11 The local Nu versus axial distance for isopropanol

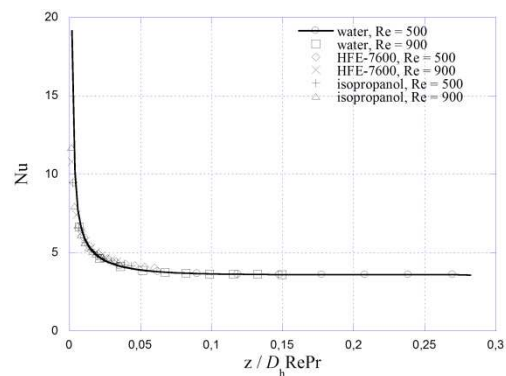


Fig. 3.2.12 The local Nu versus non-dimensional axial distance for water, HFE-7600 and isopropanol

In the Fig. 3.2.10 the local Nu distribution along the microchannel is presented for HFE-7600 and various Br. The similar behavior of the local Nu is observed for higher Br, except for cooling cases. For Br = -0.1 the fully developed local $Nu_{fd} \cong 6.15$ is obtained while for Br = -0.3 the fully developed $Nu_{fd} \cong 16.53$. Once again the thermal entrance length is increasing.

The local Nu versus axial distance is presented for isopropanol in the Fig. 3.2.11. The conventional fully developed value $Nu_{fd} \cong 3.608$ is observed for Br = 0.01 (-0.01). If the Br is increasing to 0.1 the fully developed $Nu_{fd} \cong 3.17$ is decreasing, while for Br = 0.3 further decreasing of the $Nu_{fd} \cong 2.5$ is observed. In the case of cooling and Br = -0.1, the fully

developed $Nu_{fd} \cong 5.38$ is obtained while for $Br = -0.3$ the fully developed $Nu_{fd} \cong 13.46$ is increasing. In the latter case the local Nu is slightly decreasing with axial distance in the fully developed region.

In the Fig. 3.2.12 the local Nu versus non-dimensional axial distance for water, HFE-7600 and isopropanol versus Re is presented for non-viscous heating case. The conventional behavior of the local Nu is observed with the fully developed $Nu_{fd} \cong 3.608$.

3.2.3. Conclusions

The numerical modeling of the simultaneously developing heat and fluid flow in the microchannels with effects of viscous dissipation was discussed. The special attention is focused on a local Nu and Po for three working fluids: water, HFE-7600 and isopropanol with temperature dependent viscosity covering the range $Pr = 5 - 30$. The following conclusions are outlined:

- The local Po decreases with Re for isopropanol and HFE-7600 and increases for water as the viscosity is evaluated at the inlet temperature of the fluid.
- The local Po relation is affected by the viscous dissipation for all Br . As the Br is increasing the local Po is increasing along the microchannel as the fluid is cooled and decreasing as the fluid is heating.
- For a certain value of Br the local Po is achieving the fully developed value as for the non-heating case. The plausible explanation is that the heat transfer rate of the internal source due to viscous heating is equal to the heat transfer rate due to external heat source.
- In the case of thermal results there is a different behavior of local Nu depending on the heat flux direction (heating or cooling). If the fluid is heating the local Nu is decreasing while for cooling the local Nu is increasing. A deviation from the conventional value $Nu_{fd} \cong 3.608$ is higher as the fluid is cooled.

4. The microtube heat sink with tangential impingement jet

4.1 The microtube heat sink with tangential impingement jet and variable fluid properties

The thermal management of the electronic devices and power sources became the challenging issue in the last decade because of both, miniaturization and heat transfer rate increasing. The various cooling solutions have been proposed using both the single and two-phase heat transfer. Since this paper deals with the single phase heat transfer of water, only these cooling solutions will be considered.

The advantage of the single-phase microchannel heat sink, is based on an increase the heat transfer coefficient as the hydraulic diameter is decreasing. Also the channel walls are acting as the fins that increase the heat transfer area. For the case of the microchannel heat sinks, the investigations are made for single layer arrangement [84-87] and double layer arrangement [88-89]. The research has been made experimentally and numerically although the analytical solution based on a porous model has been announced [90-91]. The fractal branching microchannel heat sink was investigated in [92]. Also, the viscous dissipation effect and the slip flow regime were considered for rectangular microchannel heat sinks [93-94]. In addition, the review chapters on micro-heat sinks might be found in [95].

Contrary to the microchannel heat sink, Soliman et al [96] presented the results for the numerical modeling made on microtube heat sink. The constant property laminar heat transfer of the water through the microtubes is considered. It was found that proposed heat sink have higher thermal resistance and requires lower pumping power compared to the microchannel

heat sink for the same Re and hydraulic diameter. On the other hand, based on the unit pumping power, the microtube heat sink can dissipate slightly larger heat rate than the microchannel heat sink.

Besides, Ryu et al [97] have presented the numerical analysis of the manifold microchannel heat sink. It is concluded that this heat sink has better performances than the classical microchannel heat sink, lower thermal resistance and more uniform temperature distribution for the same pumping power. The optimization of the heat sink geometric parameters is done to obtain the best heat transfer characteristics.

For the microchannel heat sinks with large length to diameter ratio and uniform inlet velocity feeding of the channels, the fluid flow and thermal regime are fully developed for almost the total channel length. As the heat transfer coefficient is lower in this case, another option is to induce flow instabilities and consequently to establish developing fluid flow and heat transfer along the channel.

Sung and Mudawar [98] analyzed the hybrid jet impingement microchannel heat sink in turbulent heat transfer and fluid flow. It was shown that the vorticity has the large influence on a zone outside the impingement jet. The stronger attachment of the fluid flow to the heated surface for higher Re is observed. It was also proposed the improved design of the heat sink based on the optimized analysis that lowers the temperature distribution of the heated surface.

Following this review of the cooling solutions used for electronic and high power devices, the microtube heat sink with impingement jet is analyzed. To extend the benefits from the fluid flow attachment to the tube wall, the inlet impingement jet is tangentially positioned to the microtube.

4.1.1. Problem description and numerical details

The microtube heat sink assembly proposed for numerical analysis is presented in the Fig. 4.1.1 and dimensions are given in table 1. It might be observed that feeding of the microtube heat sink is realized through the gaps on the top surface of the heat sink. The cross section of the microtube with the inlet channel is presented in the Fig. 4.1.2. It can be noticed that the microtube is thermally and hydrodynamically symmetrical with respect to the boundary positioned at the half-length of the microtube. So, only the left part of the microtube is analyzed. Lelea et al [24] and Lelea [34,46] have analyzed numerically and experimentally the laminar heat transfer and fluid flow of the water through the single microtube and concluded that conventional theories are applicable to the microtubes with diameters down to 100 μm . Also the Reynolds analogy might be applied for different fluid flow configurations as mentioned in [99,101]. For the phenomena occurring in this case, the set of the Navier-Stokes equations can be used, as follows:

The conservation of mass

$$\frac{\partial(\rho \cdot u_i)}{\partial x_i} = 0 \quad (4.1.1)$$

The conservation of momentum

$$\frac{\partial(u_i \cdot \rho \cdot u_j)}{\partial x_i} = -\frac{\partial p}{\partial x_i} + \frac{\partial}{\partial x_i} \left(\mu \frac{\partial u_j}{\partial x_i} \right) \quad (4.1.2)$$

The conservation of energy

$$\frac{\partial(\rho \cdot c_p \cdot u_i \cdot T)}{\partial x_i} = \frac{\partial}{\partial x_i} \left(k \frac{\partial T}{\partial x_i} \right) \quad (4.1.3)$$

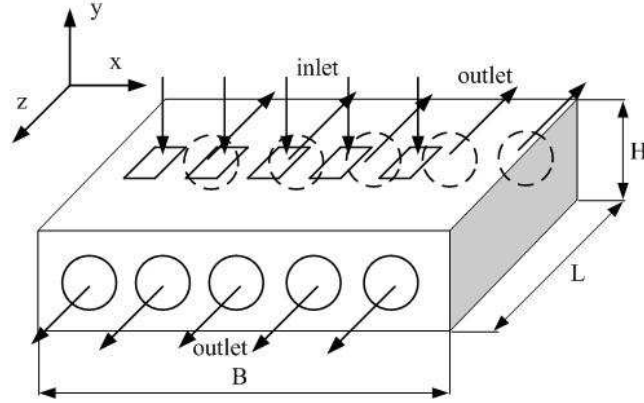


Fig. 4.1.1. The microtube heat sink assembly with tangential impingement jet

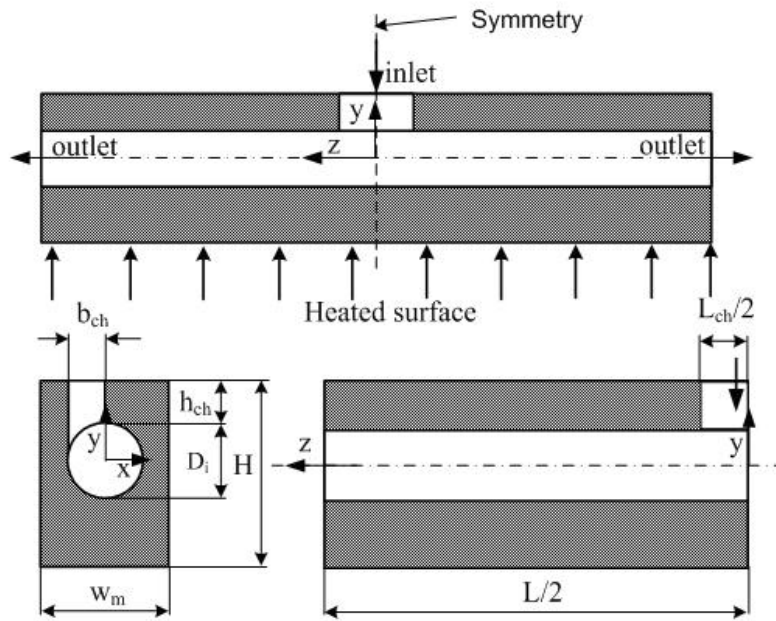


Fig. 4.1.2 The single microtube geometry

For the micro-tube heat sink presented in this paper, the following boundary conditions are settled:

- The fluid flow is stationary, incompressible and laminar;
- The fluid properties were considered as temperature dependent with following equations:

Dynamic viscosity:

$$\mu(t) = 2.6412018 \cdot 10^{-4} + 0.0014009 \cdot e^{-\frac{t}{31.0578605}}$$

Density:

$$\rho(t) = 1000.0 \cdot \left(1 - \frac{t + 288.9414}{508929.2 \cdot (t + 68.12963)} \cdot (t - 3.9863)^2 \right)$$

Thermal conductivity:

$$k(t) = -0.58166 + 6.355 \cdot 10^{-3} \cdot T - 7.964 \cdot 10^{-6} \cdot T^2$$

Specific heat:

$$c_p(t) = 8958.9 - 40.535 \cdot T + 0.11243 \cdot T^2 - 1.014 \cdot 10^{-4} \cdot T^3$$

Table 1 The geometry, thermal and flow conditions of the micro-tube heat sink

B, cm	$H, \mu m$	L, cm	$b_{ch}, \mu m$	L_{ch}, mm	$h_{ch}, \mu m$
1	500	1	150	1	50
$w_m, \mu m$	$D_i, \mu m$	N	$M, kg/s$	Re	T_{in} K
350	300	27	$10 \cdot 10^{-5}$ $110 \cdot 10^{-5}$	-	212 - 2335 293

- The viscous dissipation is neglected because of the low flow rates;
- The uniform velocity field and the constant temperature are imposed at the channel inlet, while at the outlet the partial derivatives of the velocity and temperature in the stream-wise direction are vanishing;
- The conjugate heat transfer between the solid and fluid flow is considered and the no-slip velocity conditions at the solid-fluid interface;

The conjugate heat transfer procedure, implies the continuity of the temperature and heat flux at the solid – liquid interface defined as,

$$x = R_i : T_s|_{R+} = T_f|_{R-}$$

$$k_s \left(\frac{\partial T_s}{\partial x} \right)_{R+} = k_f \left(\frac{\partial T_f}{\partial x} \right)_{R-}$$

$$y = R_i : T_s|_{R+} = T_f|_{R-}$$

$$k_s \left(\frac{\partial T_s}{\partial y} \right)_{R+} = k_f \left(\frac{\partial T_f}{\partial y} \right)_{R-}$$

Also at the inlet cross-section:

$$y = R_i + h_{ch}; R_i - b_{ch} < x < R; 0 < z < L_{ch} / 2$$

$$M = M_{in} \text{ and } T = T_{in}$$

All the outer surfaces of the heat sink are insulated except the bottom one in contact with the chip:

$$y = -[H - (D_i + h_{ch}) + R_i]; -w_m / 2 < x < w_m / 2; 0 < z < L / 2$$

$$q = k_s \frac{\partial T}{\partial y}$$

At the outlet of the microtube the following boundary conditions are prescribed:

$$z = L / 2$$

$$\frac{\partial v}{\partial z} = 0; \frac{\partial w}{\partial z} = 0; \frac{\partial u}{\partial z} = 0; \frac{\partial T}{\partial z} = 0$$

At the symmetry boundaries:

$$z = 0$$

$$\frac{\partial v}{\partial z} = 0; \frac{\partial w}{\partial z} = 0; \frac{\partial u}{\partial z} = 0; \frac{\partial T}{\partial z} = 0$$

$$x = \pm W_m / 2$$

$$\frac{\partial v}{\partial x} = 0; \frac{\partial w}{\partial x} = 0; \frac{\partial u}{\partial x} = 0; \frac{\partial T}{\partial x} = 0$$

The set of the partial differential equations along with the boundary conditions are solved using the Fluent commercial solver [102] with methods described in [18]. The Simple

algorithm is used for the velocity-pressure coupling solution and second order upwind scheme for equations discretization. The under-relaxation factors are used for pressure field ($\alpha = 0.3$) and momentum conservation ($\alpha = 0.7$). The convergence criterion is defined as:

$$R\phi = \frac{\sum_{cells,P} \left| \sum_{nb} a_{nb} \cdot \phi_{nb} + b - a_p \phi_p \right|}{\sum_{cells,P} \left| a_p \phi_p \right|} \quad (4.1.4)$$

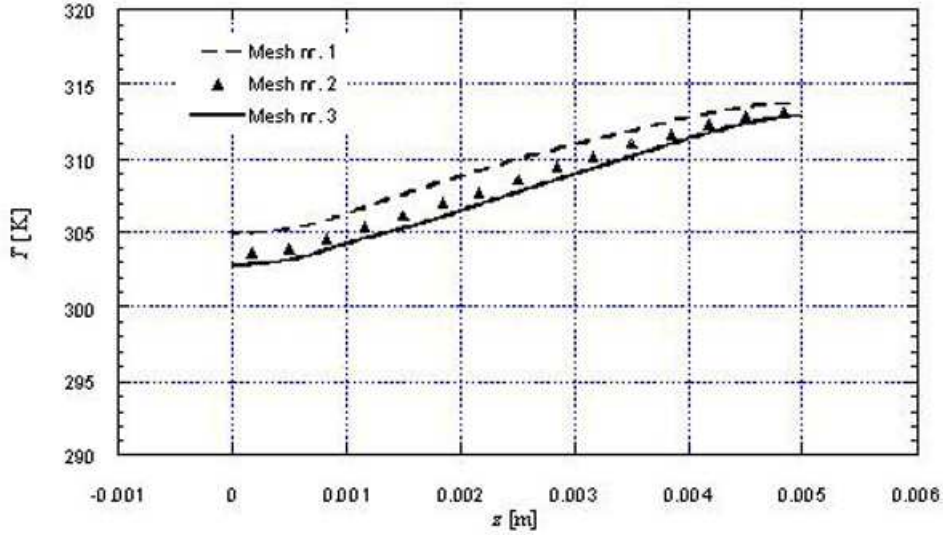


Fig. 4.1.3 Grid independence test

The residuals for velocity components and continuity equation were 10^{-5} and for temperature field 10^{-8} . Three different grids have been used to test the grid sensitivity, 1(414 cells at each cross-section, 200 subdivisions in axial direction with total of 82800 cells), 2 (646,250,161500) and 3 (1020,313,319260). In Fig. 4.1.3 is presented the temperature distribution at the centerline of the heat sink bottom surface for these three grids. A difference between the grids 2 and 3 is about 1.5 % along the axial direction, so the grid nr. 2 is used for further calculations.

4.1.2. Results and discussion

The results obtained for velocity, pressure and temperature filed are used to calculate the main heat sink parameters like thermal resistance and pumping power. The thermal resistance is calculated as:

$$R = \frac{T_{\max} - T_{in}}{q} \quad (4.1.5)$$

while the pumping power is defined as:

$$\Pi = M \cdot \frac{\Delta p}{\rho} \quad (4.1.6)$$

The pressure difference is calculated as a difference between the average values at the inlet and outlet cross-sections:

$$\Delta p = p_{in} - p_{out} \quad (4.1.7)$$

Also the Re is defined as:

$$\text{Re} = \frac{4 \cdot (M / 2)}{\pi \cdot D \cdot \mu} \quad (4.1.8)$$

In the Fig. 4.1.4 the temperature distribution is presented along the heated surface for circular impingement jet heat sink and classic heat sink with front inlet cross-section, and low pumping power $\dot{I}T = 0.003 \text{ W}$. It can be observed that maximum temperature is lower for the jet impingement microtube heat sink ($T=313.21 \text{ K}$ for constant fluid properties and $T = 311.13$ for variable fluid properties) against the classic heat sink ($T=324.14 \text{ K}$). On the hand, the temperature difference along the heated surface is higher for the classic microtube heat sink ($\Delta T=19.2 \text{ K}$) than the jet impingement microtube heat sink ($\Delta T=9.6\text{K}$ for constant fluid properties and $\Delta T=7.8 \text{ K}$ for variable fluid properties). In the jet impingement region the temperature is almost constant, while in the outside region the temperature variation exhibits almost the boundary layer behavior. It means that for very low pumping powers or mass flow rates, the jet zone impingement has negligible influence on outside region toward the microtube outlet cross-section.

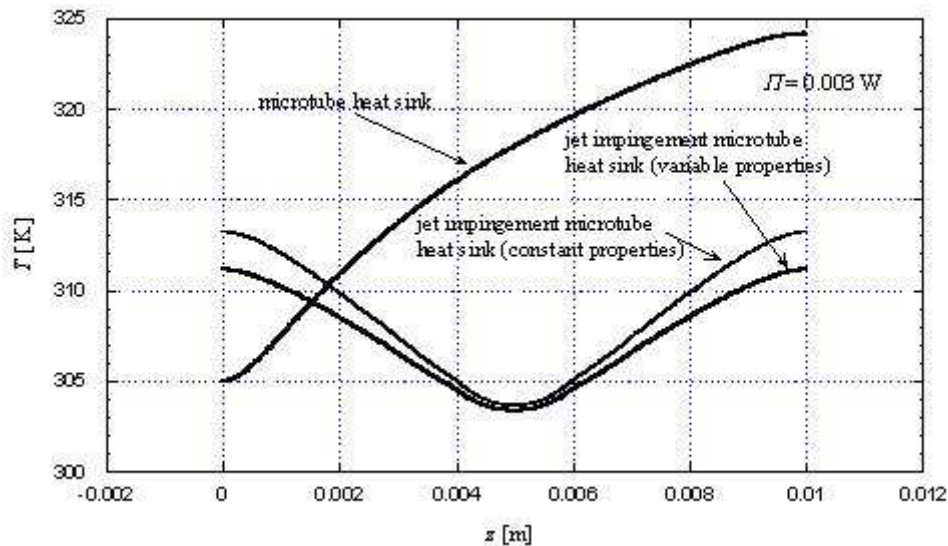


Fig. 4.1.4 The temperature distribution at the bottom heat sink surface along the fluid flow for $\dot{I}T = 0.003 \text{ W}$ and two different configurations

In the Fig. 4.1.5, the temperature distribution along the centerline of the heated surface is presented for two arrangements and higher pumping power. Once again the jet impingement configuration has both lower maximum temperature ($T=304.84 \text{ K}$ for constant fluid properties and $T=304.39$ for variable fluid properties) and lower temperature difference ($\Delta T=2.5 \text{ K}$ for constant fluid properties and $\Delta T=2.23 \text{ K}$ for variable fluid properties) against the classic microtube heat sink ($T=312.82 \text{ K}$) and ($\Delta T=9.8 \text{ K}$). In this case temperature behavior of the jet impingement heat sink has two separate zones outside the jet impingement region, each one with variation similar to boundary layer behavior. This means that the swirl flow created in the jet impingement zone has the impact on a downstream portion of the microtube.

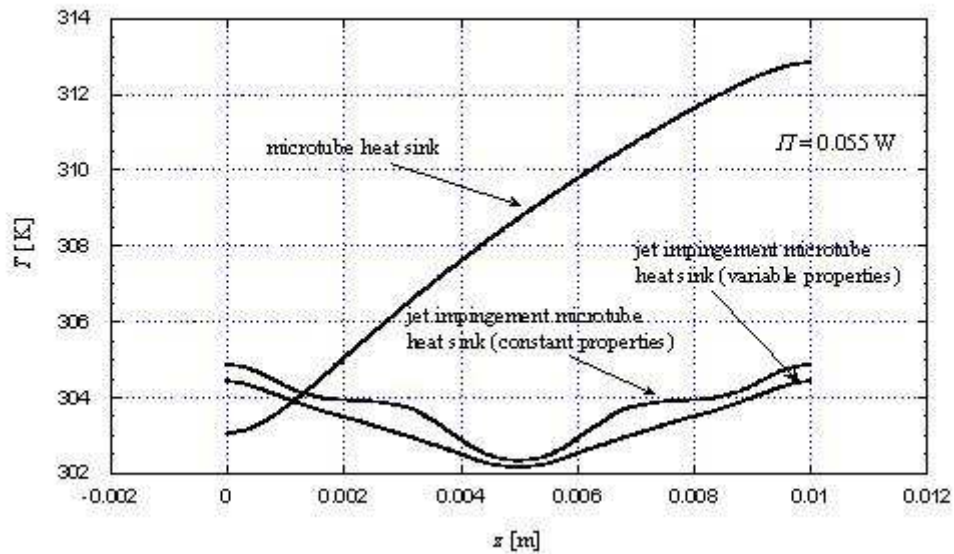


Fig. 4.1.5 The temperature distribution of a bottom heat sink surface along the fluid flow for $II=0.055$ W and two different configurations

In the Fig. 4.1.6, the thermal resistance versus pumping power is presented. Following these observations, it is obvious the thermal resistance for jet impingement microtube heat sink is lower than the thermal resistance of the classic microtube heat sink for the whole range of the pumping power.

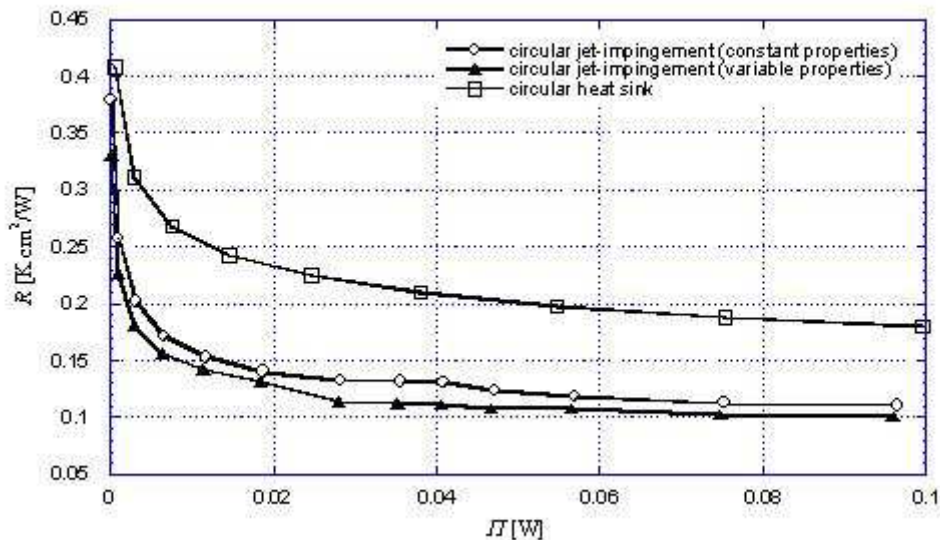


Fig. 4.1.6 Thermal resistance R versus pumping power for three different cases

The fluid viscosity distribution at the outlet cross-section for various mass flow rates is presented in the Fig. 4.1.7. For the low flow rates and higher outlet temperatures there is a large variation of viscosity along the cross-section. As it is expected the lower viscosity is observed near the tube wall. For the higher mass flow rates the swirl flow creates the higher mixing of the fluid and more uniform viscosity.

The similar conclusion might be outlined for a density distribution (Fig. 4.1.8) at the outlet cross-section. For lower mass flow rates and higher temperatures the variations in fluid density is observed from tube wall to the axis. Contrary to one that might expect, the portions of the fluid with higher density are not pushed toward the tube wall because of the lower variations in fluid density.

In Figs. 4.1.9 and 4.1.10, the fluid path lines for two different mass flow rates are presented. It is observed that for the low flow rates the swirl flow is created without mixing. The flow behavior is similar to the boundary layer one, except for the inlet portion of the tube. For the higher flow rates the swirl flow created by the tangential fluid inlet, increases the fluid mixing and heat transfer coefficient.

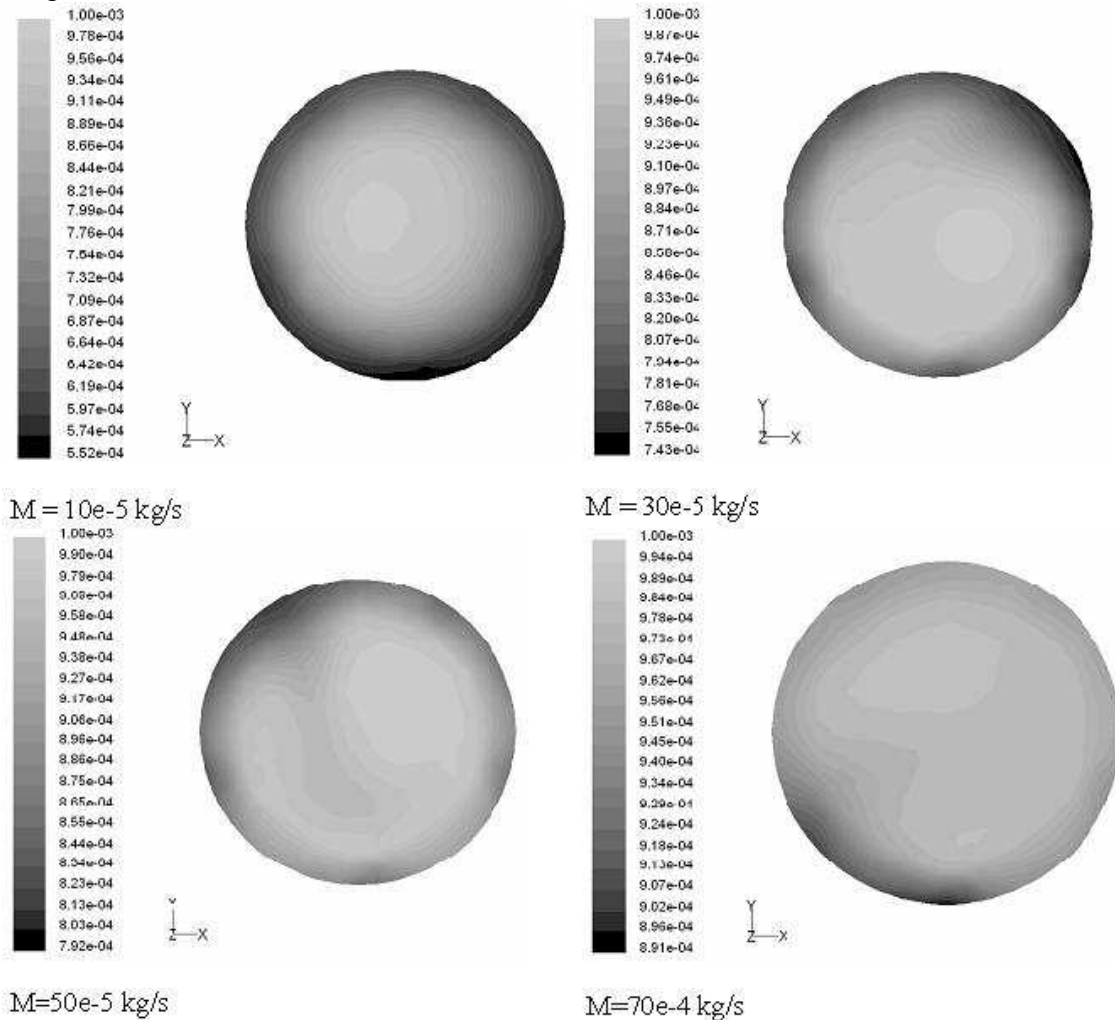


Fig. 4.1.7 The viscosity distribution at the outlet cross section of the microtube for various mass flow rates

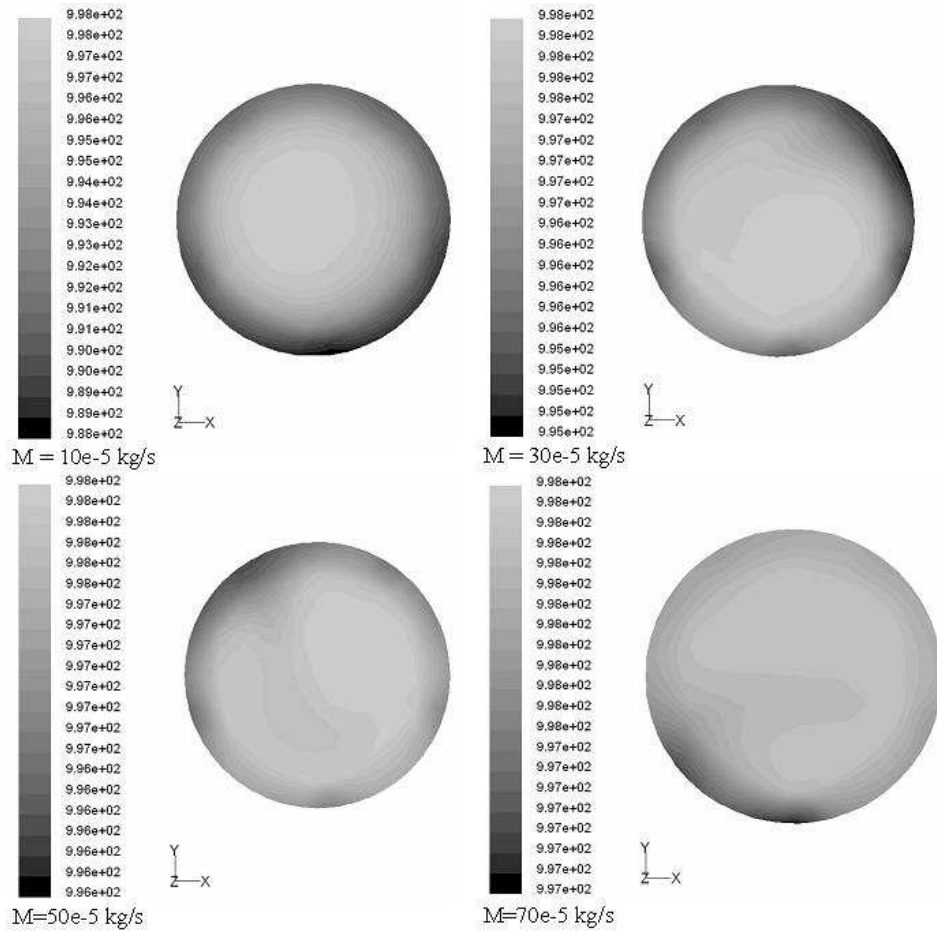


Fig. 4.1.8 The density distribution at the outlet cross section of the microtube for various mass flow rates

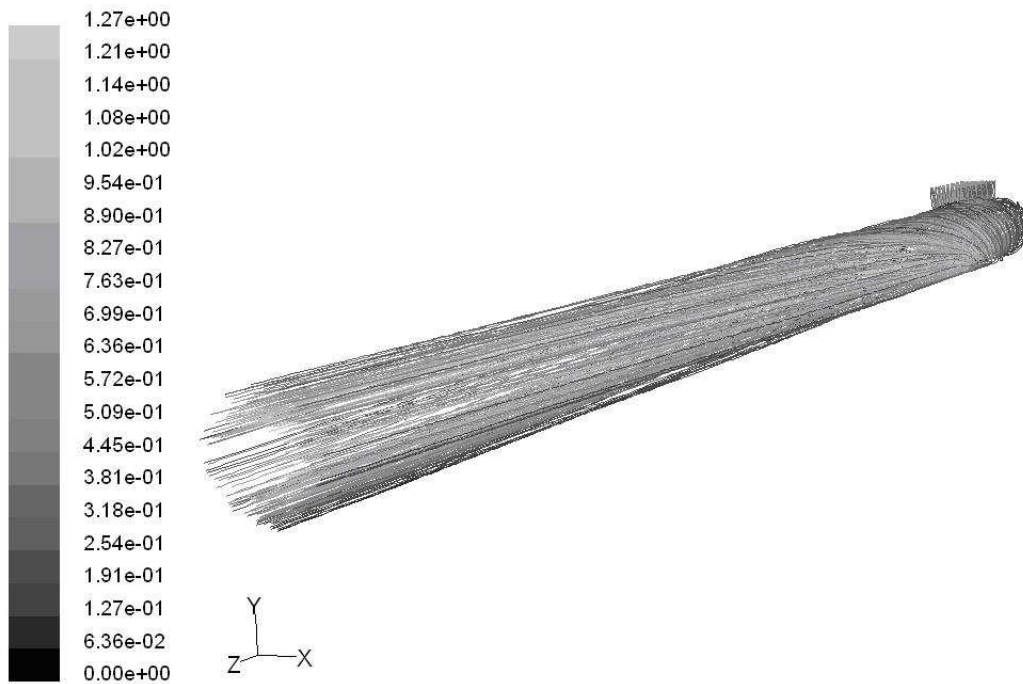


Fig. 4.1.9 The axial velocity path lines for single microtube mass flow rate $M = 10 \cdot 10^{-5} \text{ kg/s}$

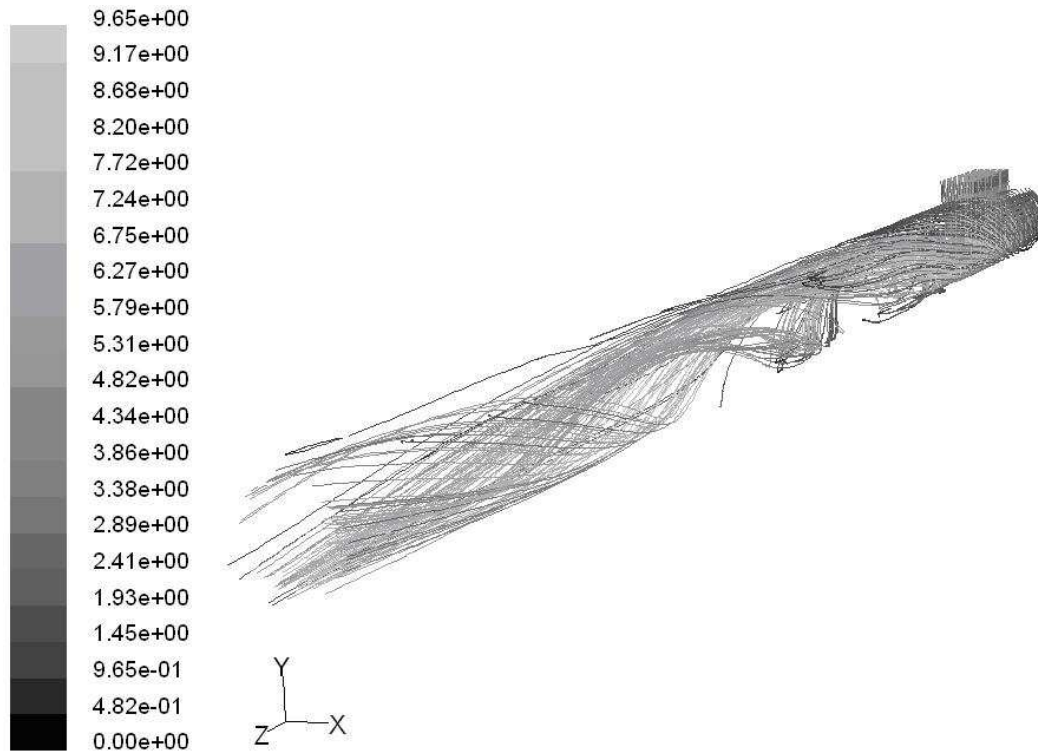


Fig. 4.1.10 The axial velocity path lines for single microtube mass flow rate $M = 80 \cdot 10^{-5} \text{ kg/s}$

4.1.3. Conclusions

The numerical modeling of the tangential jet impingement microtube heat sink is presented. The obtained results for temperature and velocity fields are used for performance evaluation against the classic microtube heat sink, in terms of thermal resistance and pumping power. It is concluded that both, lower peak temperature and lower temperature difference are associated to jet impingement heat sink. Therefore an additional effort regarding the inlet manifold is fully justified considering the thermal benefits.

On the other hand, the fluid viscosity has a great influence on a temperature and velocity field and thermal parameters of the heat sink. This observation is valid for the lower flow rates and higher temperatures. Due to the small variations in fluid density, the portions of the fluid with higher density are not pushed toward the tube wall.

4.2 Effects of inlet geometry on heat transfer and fluid flow of tangential micro-heat sink

The comfort of everyday life implies the miniaturization of devices like computers or optoelectronic installation. The high power devices used in defense electronics or alternative energy resources are also the subject of this trend. The thermal management of high heat fluxes dissipated by them became the challenging issue in the last decade and still is a high interest topic. Since the Tuckerman and Pease [26] experiment, the micro-channel heat sink became a very attractive solution for thermal management of the high heat flux devices. It combines two modes of heat transfer: increasing heat transfer coefficient by decreasing the channel diameter and heat conduction through the channel walls. Although the heat flux was high, $q = 780 \text{ W/cm}^2$, disadvantages like large temperature difference or a high pressure drops are encountered.

To optimize micro-channel heat sink performances a large number of the reports were announced, both for single layer [103-106] and double layer or stacked microchannel heat

sinks arrangements [107-108]. Xu et al [109] presented the three-dimensional numerical simulations of conjugate heat transfer in conventional and interrupted microchannel heat sinks. It was observed that the heat transfer was enhanced remarkably for the interrupted microchannel heat sink than the conventional one. Liu et al [110] presented the improved design of fractal branching channel net used for cooling of rectangular electronic chip. It is found that the best total branching levels is 7 regardless the mass, pressure drop or the pumping power. If the surface area for cooling is fixed, the optimum ratio of length to width is 1.87. Hooman [111] presented the fully developed forced convection in a rectangular microchannel filled with or without a porous medium. The micro-heat sink was investigated analytically based on the Fourier series approach. It was found that for each aspect ratio, Nu increases with Pr and this effect becomes more pronounced as Kn increases. Gurrum et al [112] reported the thermal enhancement analysis on phase change materials enclosed inside copper microchannels within semiconductor devices. Sert and Beskok [113] announced the new micro-heat spreader concept for efficient transport of large, concentrated heat loads utilized in various thermal management applications, mainly in electronic cooling. Sobhan and Garimella [29] presented the critical review on microchannel heat transfer and fluid flow.

Although most of the configurations consider the rectangular cross-section of the channels, Kroeker et al [96] presented the numerical investigation regarding the pressure drop and thermal characteristics of heat sinks with circular micro-channels. The constant property laminar heat transfer of the water through the microtubes is considered. It was found that proposed heat sink have higher thermal resistance and requires lower pumping power compared to the microchannel heat sink for the same Re and hydraulic diameter. On the other hand, based on the unit pumping power, the microtube heat sink can dissipate slightly larger heat rate than the microchannel heat sink.

As the heat transfer coefficient is lower for a boundary layer flow in microchannels, the solutions that include thermal and hydrodynamic disturbance of the fluid flow might be benefic for thermal performances of the heat sink.

Sung and Mudawar realized a series of experiments and numerical investigations on hybrid microchannel heat sink that combines the cooling improvements of micro-channel flow and jet impingement. The single [98] and multiple jet slots [43] have been investigated, as well as the single phase and two-phase heat transfer. The heat flux of $q = 1127 \text{ W/cm}^2$ has been achieved without incurring CHF.

Lelea [116] analyzed a micro-heat sink with impingement jet positioned tangentially to the tube at the middle of the microtube. The water was used as the working fluid and laminar regime ($Re < 1000$) was considered. For $q = 100 \text{ W/cm}^2$ the temperature of a sink bottom wall was almost uniform with maximum temperature of $T = 304 \text{ K}$.

It has to be noticed that heat transfer enhancement of the turbulent flow inside the tubes applying the tangentially injection of the air, was reported by Dhir and Chung [114]. In this case, six injectors are placed at the inlet of the tube. It was found an average heat transfer enhancement of 35 – 40 % on a constant pumping power basis. It was observed that a high maximum axial velocity near the wall produces higher heat flux from the wall. Moreover high turbulence level in the middle region of the tube improves mixing and, thus, the rate of heat transfer.

The heat transfer enhancement of the pipe flow with the swirl injected fluid was investigated experimentally by Gul [115]. The tube diameter and length were $D_i = 20 \text{ mm}$ and $L = 1 \text{ m}$ while the tube wall was electrically heated. It was found an increase in the Nu number by 60 % and the augmentation of heat transfer is the function of the tangential to total flow momentum ratio and Reynolds number.

The present report presents the geometric optimization of the micro-heat sink that leads to the optimal thermal performances based on a constant pumping power. The tube

diameter considered in this research was $D_i = 900 \mu\text{m}$ as well as four different inlet rectangular cross-sections were analyzed. Besides, the fundamental analysis regarding the mechanism of the heat transfer enhancement was performed, based on an axial and tangential velocity fields.

4.2.1. Problem description and numerical solution

4.2.1.1. Numerical details

The microtube heat sink assembly proposed for numerical analysis is presented in the Fig. 4.1.1. It might be observed that feeding of the microtube heat sink is realized through the gaps on the top surface of the heat sink. The cross section of the microtube with the inlet channel is presented in the Fig. 4.1.2. The geometry, flow and thermal conditions are presented in the table 1. In the table 2 the dimensions of the four inlet cross-sections are presented. It has to be stated that for the micro-heat sink with $D_i = 300 \mu\text{m}$ the inlet cross-section has the dimension of the case 3. The geometry, flow and thermal conditions for micro-heat sink with $D_i = 300 \mu\text{m}$ are presented in [18]. It can be noticed that the microtube is thermally and hydrodynamically symmetrical with respect to the boundary positioned at the half-length of the microtube. So, only the left part of the microtube is analyzed. Lelea et al [24] and Lelea [46,116] have analyzed numerically and experimentally the laminar heat transfer and fluid flow of the water through the single microtube. It was concluded that conventional theories are applicable to the microtubes with diameters down to $100 \mu\text{m}$. So the set of the Navier-Stokes equations can be used to analyze the present phenomena, as follows:

The conservation of mass

$$\frac{\partial(\rho \cdot u_i)}{\partial x_i} = 0 \quad (4.2.1)$$

The conservation of momentum

$$\frac{\partial(u_i \cdot \rho \cdot u_j)}{\partial x_i} = -\frac{\partial p}{\partial x_j} + \frac{\partial}{\partial x_i} \left(\mu \frac{\partial u_j}{\partial x_i} \right) \quad (4.2.2)$$

The conservation of energy

$$\frac{\partial(\rho \cdot c_p \cdot u_i \cdot T)}{\partial x_i} = \frac{\partial}{\partial x_i} \left(k \frac{\partial T}{\partial x_i} \right) \quad (4.2.3)$$

For the micro-tube heat sink presented in this paper, the following boundary conditions are settled:

- The fluid flow is stationary, incompressible and laminar;
- The fluid properties were considered as temperature dependent with following equations:

Dynamic viscosity:

$$\mu(t) = 2.6412018 \cdot 10^{-4} + 0.0014009 \cdot e^{-\frac{t}{31.0578605}}$$

Density:

$$\rho(t) = 1000.0 \cdot \left(1 - \frac{t + 288.9414}{508929.2 \cdot (t + 68.12963) \cdot (t - 3.9863)^2} \right)$$

Thermal conductivity:

$$k(t) = -0.58166 + 6.355 \cdot 10^{-3} \cdot T - 7.964 \cdot 10^{-6} \cdot T^2$$

Specific heat:

$$c_p(t) = 8958.9 - 40535 \cdot T + 0.11243 \cdot T^2 - 1.014 \cdot 10^{-4} \cdot T^3$$

Table 1 The geometry, thermal and flow conditions of the micro-tube heat sink with tubes $D_i = 900 \mu m$

$D_i = 900 \mu m$					
B, cm	$H, \mu m$	L, cm	$b_{ch}, \mu m$	L_{ch}, mm	$h_{ch}, \mu m$
1	1500	1	225 and 450	1 and 2	150
$w_m, \mu m$	$D_i, \mu m$	N	$M, kg/s$	Re	T_{in} K
1050	900	9	$35 \cdot 10^{-5} -$ $68 \cdot 10^{-5}$	400 - 1000	293

Table 2 Dimensions of the inlet cross – section for micro-heat sink with tubes $D_i = 900 \mu m$

$D_i = 900 \mu m$, Dimensions of the inlet cross - section

	case 1	case 2	case 3	case 4
$b_{ch}, \mu m$	225	225	450	450
L_{ch}, mm	1	2	1	2

- The viscous dissipation is neglected because of the low flow rates;
- The uniform velocity field and the constant temperature are imposed at the channel inlet, while at the outlet the partial derivatives of the velocity and temperature in the stream-wise direction are vanishing;
- The conjugate heat transfer between the solid and fluid flow is considered and the no-slip velocity conditions at the solid-fluid interface;

The conjugate heat transfer procedure, implies the continuity of the temperature and heat flux at the solid – liquid interface defined as,

$$x = R_i : T_s|_{R_+} = T_f|_{R_-}$$

$$k_s \left(\frac{\partial T_s}{\partial x} \right)_{R_+} = k_f \left(\frac{\partial T_f}{\partial x} \right)_{R_-}$$

$$y = R_i : T_s|_{R_+} = T_f|_{R_-}$$

$$k_s \left(\frac{\partial T_s}{\partial y} \right)_{R_+} = k_f \left(\frac{\partial T_f}{\partial y} \right)_{R_-}$$

Also at the inlet cross-section:

$$y = R_i + h_{ch}; R_i - w_{ch} < x < R; 0 < z < l_{ch}/2$$

$$M = M_{in} \text{ and } T = T_{in}$$

All the outer surfaces of the heat sink are insulated except the bottom one in contact with the chip:

$$y = -[H - (D_i + h_{ch}) + R_i]; -W_m < x < W_m; 0 < z < L/2$$

$$q = k_s \frac{\partial T}{\partial y}$$

At the outlet of the microtube the following boundary conditions are prescribed:

$$z = L/2$$

$$\frac{\partial v}{\partial z} = 0; \frac{\partial w}{\partial z} = 0; \frac{\partial u}{\partial z} = 0; \frac{\partial T}{\partial z} = 0$$

At the symmetry boundaries:

$$z = 0$$

$$\frac{\partial v}{\partial z} = 0; \frac{\partial w}{\partial z} = 0; \frac{\partial u}{\partial z} = 0; \frac{\partial T}{\partial z} = 0$$

$$x = \pm W_m/2$$

$$\frac{\partial v}{\partial x} = 0; \frac{\partial w}{\partial x} = 0; \frac{\partial u}{\partial x} = 0; \frac{\partial T}{\partial x} = 0$$

The set of the partial differential equations with the boundary conditions are solved using the Fluent commercial solver [102] with methods described in [18]. The Simple algorithm is used for the velocity-pressure coupling solution and second order upwind scheme for equations discretization. The under-relaxation factors are used for pressure field ($\alpha = 0.3$) and momentum conservation ($\alpha = 0.7$). The convergence criterion is defined as:

$$R^\phi = \frac{\sum_{cells,P} \left| \sum_{nb} a_{nb} \cdot \phi_{nb} + b - a_p \phi_p \right|}{\sum_{cells,P} \left| a_p \phi_p \right|} \quad (4.2.4)$$

The residuals for velocity components and continuity equation were 10^{-5} and for temperature field 10^{-8} . Two different quasi-structured grids have been used to test the grid sensitivity, Mesh 1 with total of 247842 cells and Mesh 2 with total of 583625 cells. In the Fig. 4.2.3 the temperature distribution at the centerline of the heat sink bottom surface is presented for these two grids. For a grid independence test case 3 was considered with a mass flow rate of a single micro-tube $M = 1.2 \cdot 10^{-3}$ kg/s. A difference between these two grids is lower than 1 % along the axial direction (Fig. 4.2.3), so the mesh nr. 1 is used for further calculations.

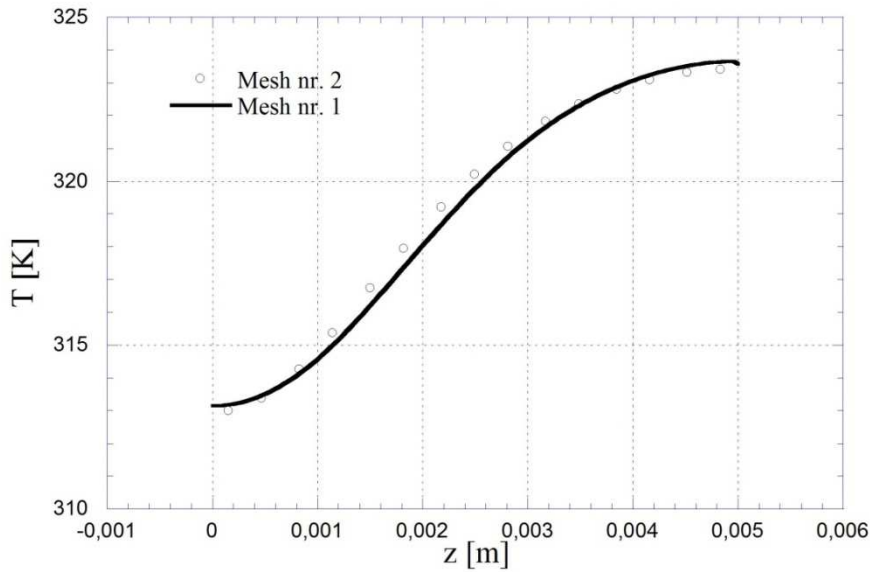


Fig. 4.2.3 The grid independence test

4.2.1.2. The experimental validation of the numerical model

In the absence of the experimental results for the novel concept of the micro-tube heat sink presented in the paper, the validation of the numerical model was made with the experimental results obtained for water flow through the tube with tangential injections of the fluid [115]. The length of the test section was $L_h = 1$ m, a tube diameter $D_i = 20$ mm with a wall thickness of 0.7 mm, the injections diameter $d_j = 4$ mm with a length of $l = 25$ mm. The turbulent fluid flow regime was imposed with $Re = 24000$. The thermocouples used for determination of the wall temperature are located at $x/L = 0.1, 0.2, 0.3, 0.4, 0.5, 0.6, 0.7, 0.8, 0.9, 1$. The schematic presentation of the test section is presented in the Fig. 4.2.4. The uniform velocity is imposed at the inlet cross-sections while at the exit the velocity gradients are vanishing in the axial direction. Also, the conjugate heat transfer problem is considered. The swirl intensity was expressed as a ratio between the momentum of the injected fluid to the momentum of the total axial flow:

$$\frac{M_t}{M_T} = \left(\frac{m_j}{m_T} \right)^2 \cdot \left(\frac{D}{d_j} \right)^2 \cdot \frac{\sin \theta}{N_j} \quad (4.2.5)$$

where the momentum of the injected fluid is expressed as:

$$M_j = \frac{m_j^2}{\pi \cdot d_j^2 \cdot \rho / 4} \quad (4.2.6)$$

and the tangential momentum of the injected fluid is defined as:

$$M_t = M_j \cdot \sin \theta \quad (4.2.7)$$

while the momentum of the total axial flow is calculated with the following equation:

$$M_T = \frac{m_T^2}{\pi \cdot D^2 \cdot \rho / 4} \quad (4.2.8)$$

The experimental results used for validation of the numerical model have considered the ratio $M_t / M_T = 11.705$. The governing equations are the Navier – Stokes partial differential equations with standard k - ε model:

Continuity equation:

$$\frac{\partial(\rho \cdot u_i)}{\partial x_i} = 0 \quad (4.2.9)$$

The conservation of momentum

$$\frac{\partial(u_i \cdot \rho \cdot u_j)}{\partial x_i} = -\frac{\partial p}{\partial x_j} + \frac{\partial}{\partial x_i} \left((\mu + \mu_t) \frac{\partial u_j}{\partial x_i} \right) \quad (4.2.10)$$

The conservation of energy

$$\frac{\partial(\rho \cdot c_p \cdot u_i \cdot T)}{\partial x_i} = \frac{\partial}{\partial x_i} \left(\left(k + \frac{c_p \cdot \mu_t}{Pr_t} \right) \frac{\partial T}{\partial x_i} \right) \quad (4.2.11)$$

where μ_t is a turbulent viscosity defined as:

$$\mu_t = \frac{C_\mu \cdot \rho \cdot k^2}{\varepsilon} \quad (4.2.12)$$

The turbulent kinetic energy equation:

$$\frac{\partial(\rho \cdot u_i \cdot k)}{\partial x_i} = \frac{\partial}{\partial x_i} \left(\left(k + \frac{\mu_t}{\sigma_k} \right) \frac{\partial k}{\partial x_i} \right) + G - \rho \cdot \varepsilon \quad (4.2.13)$$

where the production of the turbulent energy is defined as:

$$G = -\rho u_i u_j \frac{\partial u_j}{\partial u_i} \quad (4.2.14)$$

The dissipation rate of the turbulent kinetic energy:

$$\frac{\partial(\rho \cdot u_i \cdot \varepsilon)}{\partial x_i} = \frac{\partial}{\partial x_i} \left((k + \frac{\mu_t}{\sigma_\varepsilon}) \frac{\partial \varepsilon}{\partial x_i} \right) + C_1 \cdot G \cdot \frac{\varepsilon}{k} - C_2 \cdot \rho \cdot \frac{\varepsilon^2}{k} \quad (4.2.15)$$

The constants used in the above equations have the following values: $C_1 = 1.44$, $C_2 = 1.92$, $C_\mu = 0.09$, $\sigma_k = 1.0$, $\sigma_\varepsilon = 1.3$ and $Pr_t = 0.85$. The total number of 410066 nodes have been used for numerical computations (Fig. 4.2.5). Considering the uncertainty for Nu number of 7 % [115] a good agreement between the numerical and experimental results are observed in the Fig. 4.2.6.

The second validation was made with the results obtained by Bowers and Mudawar for micro-tube heat sink with lateral feeding of the micro-tubes [117]. The micro-heat sink assembly, made of nickel, has the length $L = 28.6$ mm, tube diameter $D_i = 510 \mu\text{m}$ and R-113 as the working fluid. Only the central part of the heat sink (10mm x 10 mm) was heated. The micro-heat sink is basically the same as the one presented in the Fig. 1, except the absence of the impingement inlet cross-sections. The structured numerical grid with 268320 nodes was used. Although the scope of the research was the two-phase heat transfer a few data at the beginning of the heating were in the single phase regime. Temperature difference presented in the Fig. 4.2.7, is a difference between the temperature at the top of the micro-tube (midway between the inlet and outlet cross-section) and a temperature at the inlet cross-section. The very good agreement between the experimental and numerical results is observed, considering the uncertainties of the wall heat flux (Fig. 4.2.7). As described also in Kroecker et al [96] the uncertainties are expressed through the difference between the heat flux measured electrically and a sensible heat determined by the heat balance equation.

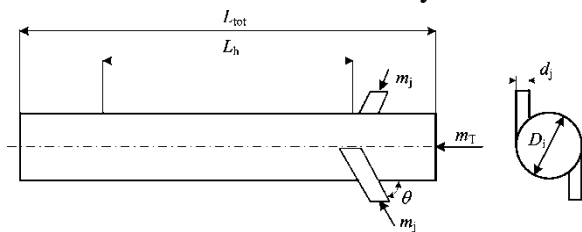


Fig. 4.2.4 The schematic presentation of the experimental installation used in [115]

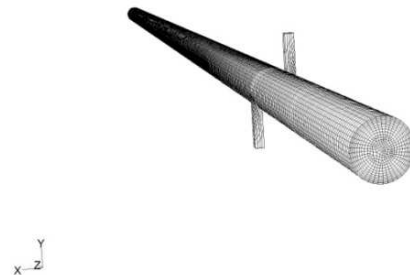


Fig. 4.2.5 The grid of the physical domain used in the experiment [115]

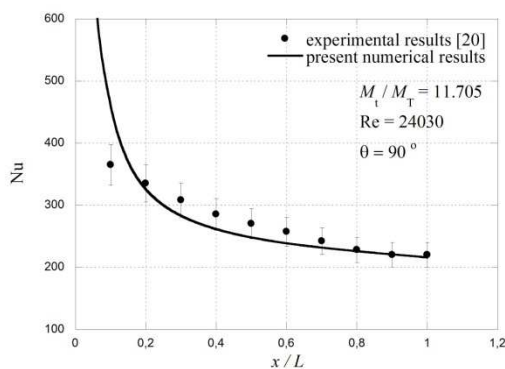


Fig. 4.2.6 The experimental validation of the numerical model with results presented by Gul [115]

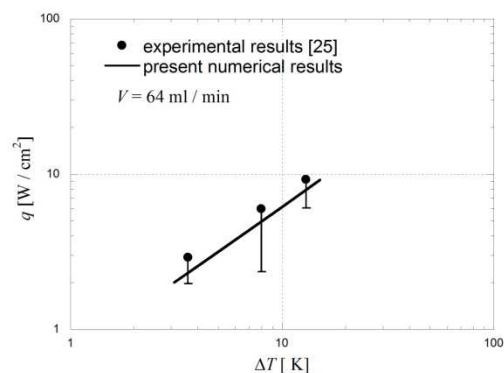


Fig. 4.2.7 The experimental validation of the numerical model with results used in Bowers and Mudawar [117]

4.2.2. Results and discussion

The performance evaluation of the micro-heat sink is presented in terms of the temperature distribution along the bottom wall based on a fixed pumping power, for various inlet cross section geometries. To make the insight in thermal results, the axial and tangential velocity distributions are presented at different axial locations. It has to be noticed that the heat flux was the same for all runs, $q = 100 \text{ W/cm}^2$ with inlet temperature $T_{\text{in}} = 293 \text{ K}$.

The pumping power is defined as:

$$\Pi = M \cdot \frac{\Delta p}{\rho} \quad (4.2.16)$$

while the local Nu number is calculated as:

$$Nu = \frac{h \cdot D_i}{k_f} \quad (4.2.17)$$

where h is the local heat transfer coefficient defined as:

$$h = \frac{q}{T_w - T_b} \quad (4.2.18)$$

Also the Re is defined with the following equation:

$$Re = \frac{4 \cdot (M / 2)}{\pi \cdot D_i \cdot \mu} \quad (4.2.19)$$

In the Fig. 4.2.8 the temperature distribution along the bottom wall of the heat sink is presented for $D_i = 900 \text{ }\mu\text{m}$ and four different inlet cross-sections based on a fixed total pumping power (for 9 micro-tubes) $\Pi = 0.02 \text{ W}$. It might be observed that the lowest temperature is obtained for case 3 (inlet channel width that covers half of the tube cross-section and shorter length $L_{\text{ch}}=1 \text{ mm}$) $T_{\text{min}} = 313.2 \text{ K}$ and $\Delta T = 10.17 \text{ K}$. The highest temperature is observed for case 2 (inlet channel width that covers the quarter of the tube and longer length $L_{\text{ch}}= 2 \text{ mm}$) $T_{\text{min}} = 315.6 \text{ K}$ and $\Delta T = 10.7 \text{ K}$. Cases 1 and 4 lies between these two cases.

The explanation for this thermal behavior of the micro-heat sink might be found from the axial and tangential velocity distribution presented in the Figs. 4.2.9 and 4.2.11. Velocity distributions are presented for the mid plane $x = 0 \text{ m}$ at various axial locations. For $\Pi = 0.02 \text{ W}$ the axial velocity distribution has the similar behavior for all cases. Contrary to the boundary layer flow, the axial velocities are higher near the tube wall and lower in the core of the fluid flow, regardless the axial location. On the other hand, the maximum axial velocities near the wall are observed near the impingement zone ($z = 0.001 \text{ m}$). After that, the axial velocity close to the wall decreases and increases in the core flow. If the magnitude of the axial velocity is analyzed, it might be noticed that the highest axial velocities are realized for case 3 ($u = 2.7 \text{ m/s}$) at $z = 0.001$ and $u = 1.7 \text{ m/s}$ at $z = 0.002 \text{ m}$. For the rest of the axial locations axial velocities are around $u = 1 \text{ m/s}$. The axial velocities for case 2, having the worst thermal performances, are around $u = 1 \text{ m/s}$, regardless the axial location.

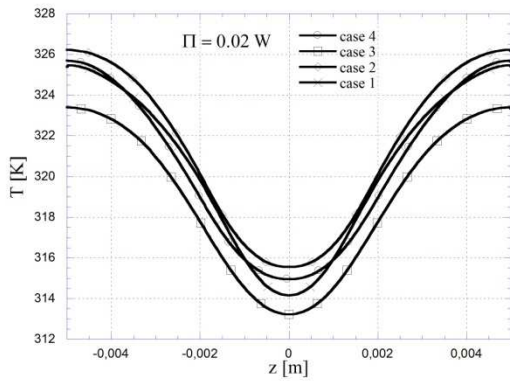


Figure 4.2.8. The temperature variation along the centerline at the bottom wall of the heat sink for $\Pi = 0.02$ W

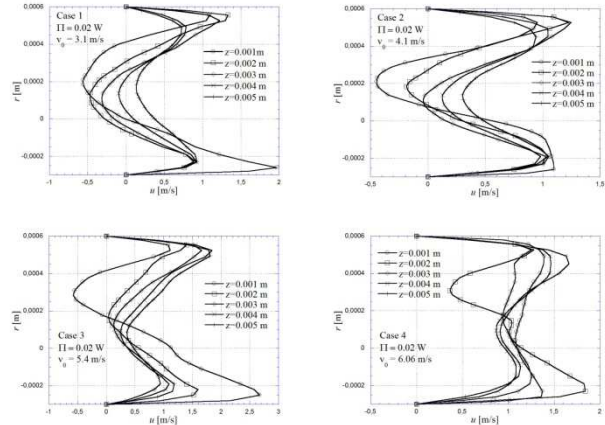


Figure 4.2.9. The axial velocity distribution along the tube radius at the midline $x = 0$ and various axial locations for $D_i = 900$ μm .

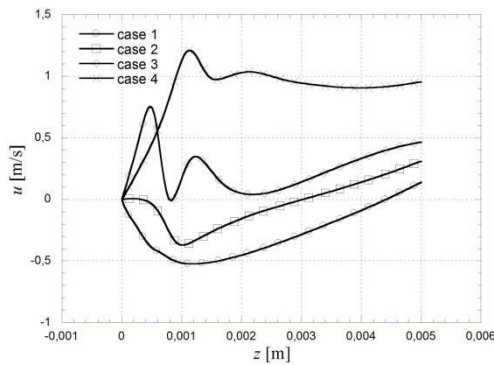


Figure 4.2.10. The axial velocity distribution along the centerline of the microtube for $D_i = 900$ μm and $\Pi = 0.02$ W.

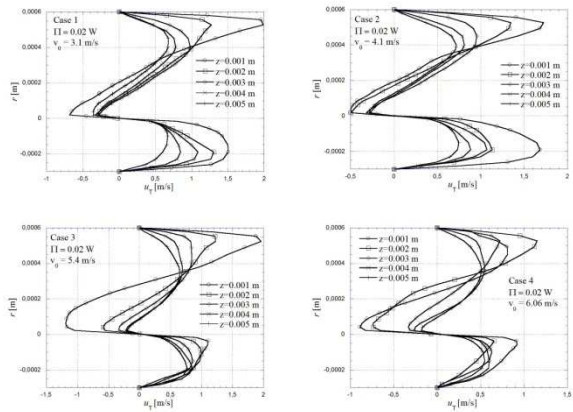


Figure 4.2.11. The tangential velocity distribution along the tube radius at the midline $x = 0$ and various axial locations for $D_i = 900$ μm .

It can be noticed that reversed flow is established in the core of the tube ($u < 0$), except for the case 4 with a wide and long cross-section. The reversing is vanishing as the flow is going downstream. Dhir and Chung [114] reported the same observation for the tangential injection of the air. The same conclusion might be outlined from Fig. 4.2.10 where the axial velocity distribution along the fluid flow is presented at the axis of the tube. It is observed that for the narrow inlet-cross-sections the negative velocities are higher. For the wide and long cross section (case 4) the reversed flow is not established.

In the case of the tangential velocities, they are decreasing downstream for all four cases (Fig. 4.2.11). Due to the swirl motion of the fluid, the higher tangential velocities are observed near the tube wall and decreases toward the tube axis. The higher tangential velocities are observed for cases 1 and 4 ($u_T = 1,5$ m/s) while for cases 3 and 4 tangential velocity is $u_T = 0,5 - 1$ m/s. Moreover for all cases, the reversed flow is observed in the core of the tube ($u_T < 0$).

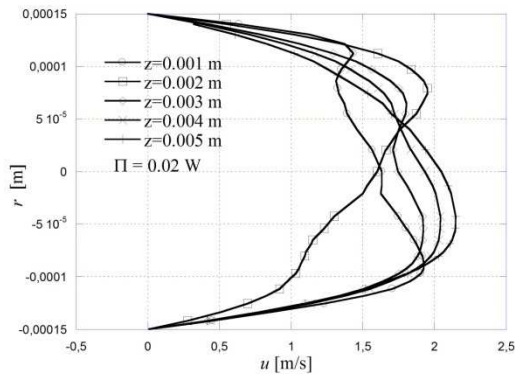


Figure 4.2.12. The axial velocity distribution along the tube radius at the midline $x = 0$ and various axial locations for $D_i = 300 \mu\text{m}$.

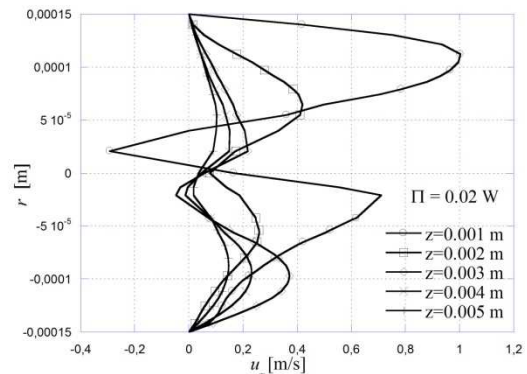


Figure 4.2.13. The tangential velocity distribution along the tube radius at the midline $x = 0$ and various axial locations for $D_i = 300 \mu\text{m}$.

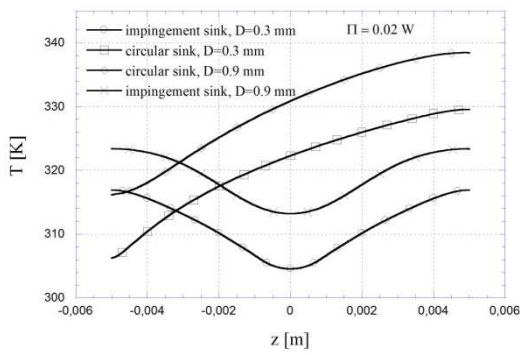


Figure 4.2.14. The temperature variation along the bottom wall of the micro-heat sink for two different micro-tube diameters and $\Pi = 0.02 \text{ W}$.

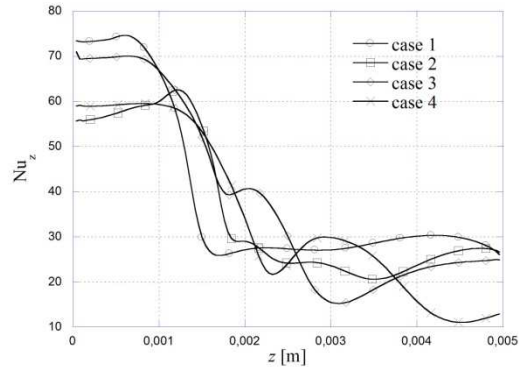


Figure 4.2.15. The local Nu distribution along the bottom line of the microtube for $D_i = 900 \mu\text{m}$ and $\Pi = 0.02 \text{ W}$.

For the case of the lower diameter micro-tubes, $D_i = 300 \mu\text{m}$, the axial velocities are representing in the Fig. 4.2.12 for total pumping power (27 micro-tubes) $\Pi = 0.02 \text{ W}$. Compared to the microtubes with $D_i = 900 \mu\text{m}$ it can be observed a different axial velocity distribution. Due to the lower cross-section there is no reverse flow in the core of the fluid flow where the highest velocities are observed. Moreover, the highest velocity gradients are observed at the bottom tube wall. For total $\Pi = 0.02 \text{ W}$ the maximum $u = 2.2 \text{ m/s}$ is obtained near the tube exit $z=0.005 \text{ m}$.

The tangential velocities, presented in the Fig. 4.2.13, exhibits the same behavior as in the case of the larger micro-tube diameter $D_i = 900 \mu\text{m}$. The tangential velocities are decreasing downstream toward the tube exit cross-section. Also these are lower near the tube axis and higher near the tube wall.

In the Fig. 4.2.14 the axial temperature distribution at the centerline of the bottom wall of the sink is presented for two diameters $D_i = 300$ and $900 \mu\text{m}$. Once again it has to be stated that comparison is made for fixed total pumping power (9 micro-tubes for $D_i = 900 \mu\text{m}$ and 27 micro-tubes for $D_i = 300 \mu\text{m}$). For both diameters the tangential micro-heat sink has better thermal performances than the conventional microheat sink with lateral inlet/outlet cross section. Moreover the impingement heat sink with $D_i = 300 \mu\text{m}$ has lower minimum temperature ($T_{\min} = 305 \text{ K}$) compared with impingement heat sink with $D_i = 900 \mu\text{m}$ ($T_{\min} = 313.2 \text{ K}$) with approximately the same temperature difference.

In the Fig. 4.2.15 the local Nu distribution along the bottom line of the microtube is presented for different inlet cross-sections and fixed pumping power $\Pi = 0.02$ W. The general outcome is that Nu has the highest values in the impingement zone and decreasing towards the outlet of the microtube. Because of the rotational motion of the fluid the Nu varies oscillatory. Moreover, the highest Nu in the impingement zone are observed for cases 3 and 1 with narrow cross-sections.

4.2.3. Conclusions

The numerical modeling of the micro-heat sink with the tangential impingement jet is realized to optimize the inlet cross-section geometry. The four different cases are considered as well as two diameters of the micro-tube. The following conclusions might be outlined:

- For the case of the higher diameter, the best results and lowest temperatures are obtained for the case 3 ($b_{ch}=225$ μm and $L_{ch}=1$ mm).
- The axial velocities are higher near the tube wall and decreases in the axis of the tube. Also the reverse flow is observed in the core of the tube.
- On the mechanism of the heat transfer, it has to be emphasized that the acceleration of the fluid flow and higher axial velocities near the tube wall are responsible for the heat transfer enhancement. For the case 3, the axial velocities are the highest with relatively lower tangential velocities. The tangential velocities are approximately at the same order of magnitude for all cases considered.
- In the case of the lower diameter of the tube the axial velocities are much higher than tangential velocities and in this case it has the prevailing influence on heat transfer augmentation. It is also interesting that, due to the lower space the axial velocities are higher in the core region. In addition, the steepest velocity gradients are observed near the bottom tube wall.

4.3. The tangential micro-heat sink with multiple fluid inlets

Following the research on tangential micro-heat sink [118,119], the analysis on number and position of the inlet jets is made in the following chapter. The results obtained for multiple inlets are compared with single inlet jet on a fixed pumping power basis.

4.3.1. Problem description and numerical solution

The microtube heat sink with multiple tangential inlets is presented in the Fig. 4.3.1. It might be observed that feeding of the microtube heat sink is realized through the multiple gaps placed on the top surface of the heat sink (Fig. 4.3.1a) while the cross section of the single microtube with the inlet channels is presented in the Fig. 4.3.1b. The geometry, flow and thermal conditions are presented in the table 1. In the same table the dimensions of the four cases with various numbers and positions of the inlet cross-sections are presented. It can be noticed that the microtube is thermally and hydrodynamically symmetrical with respect to the boundary, positioned at the half-length of the microtube. So, only the left part of the microtube is analyzed. Lelea [118,119] and Lelea et al [24] have analyzed numerically and experimentally the laminar heat transfer and fluid flow of the water through the single microtube. It was concluded that conventional theories are applicable to the microtubes with diameters down to 100 μm . So the set of the Navier-Stokes equations can be used to analyze the present phenomena, as follows:

The conservation of mass

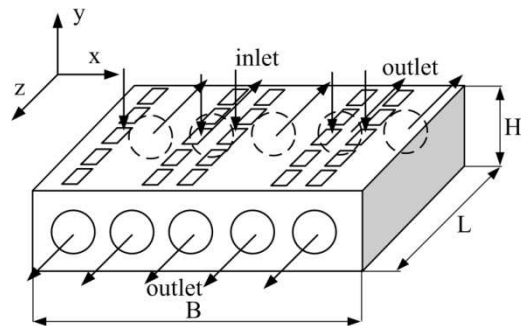
$$\frac{\partial(\rho \cdot u_i)}{\partial x_i} = 0 \quad (4.3.1)$$

The conservation of momentum

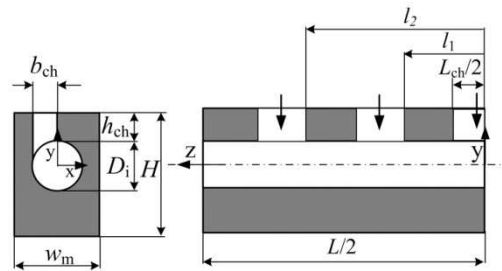
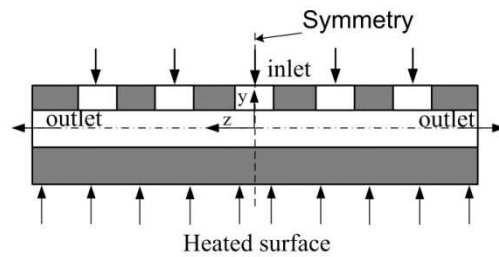
$$\frac{\partial(u_i \cdot \rho \cdot u_j)}{\partial x_i} = -\frac{\partial p}{\partial x_j} + \frac{\partial}{\partial x_i} \left(\mu \frac{\partial u_j}{\partial x_i} \right) \quad (4.3.2)$$

The conservation of energy

$$\frac{\partial(\rho \cdot c_p \cdot u_i \cdot T)}{\partial x_i} = \frac{\partial}{\partial x_i} \left(k \frac{\partial T}{\partial x_i} \right) \quad (4.3.3)$$



a) The microtube heat sink assembly



b) The single microtube geometry

Fig. 4.3.1 The microtube heat sink with multiple tangential impingement jets

Table 1 The geometry, thermal and flow conditions of the micro-tube heat sink with tubes $D_i = 900 \mu m$

$D_i = 900 \mu m$, The geometry, thermal and flow conditions					
B, cm	$H, \mu m$	L, cm	$b_{ch}, \mu m$	L_{ch}, mm	$h_{ch}, \mu m$
1	1500	1	450	1	150
$w_m, \mu m$	$D_i, \mu m$	N	$M, kg/s$	Re	T_{in}

					K
1050	900	9	12·10 ⁻⁴	821.8 – 885.2	293
<i>D_i</i> = 900 μm, Positions of the inlet cross - section					
	case 1	case 2	case 3	case 4	
<i>l</i> ₁ , mm	3.25	2.5	1.75	1.5	
<i>l</i> ₂ , mm	-	-	-	3.25	

For the micro-tube heat sink presented in this paper, the following boundary conditions are settled:

- The fluid flow is stationary, incompressible and laminar;
- The fluid properties of the water were considered as temperature dependent with following equations:

Dynamic viscosity:

$$\mu(t) = 2.6412018 \cdot 10^{-4} + 0.0014009 \cdot e^{-\frac{t}{31.0578605}}$$

Density:

$$\rho(t) = 1000.0 \cdot \left(1 - \frac{t + 288.9414}{508929.2 \cdot (t + 68.12963) \cdot (t - 3.9863)^2} \right)$$

Thermal conductivity:

$$k(t) = -0.58166 + 6.355 \cdot 10^{-3} \cdot T - 7.964 \cdot 10^{-6} \cdot T^2$$

Specific heat:

$$c_p(t) = 8958.9 - 40535 \cdot T + 0.11243 \cdot T^2 - 1.014 \cdot 10^{-4} \cdot T^3$$

- The viscous dissipation is neglected because of the low flow rates;
- The uniform velocity field and the constant temperature are imposed at the channel inlet, while at the outlet the partial derivatives of the velocity and temperature in the stream-wise direction are vanishing;
- The conjugate heat transfer between the solid and fluid flow is considered and the no-slip velocity conditions at the solid-fluid interface;

The conjugate heat transfer procedure, implies the continuity of the temperature and heat flux at the solid – liquid interface defined as,

$$x = R_i : T_s|_{R^+} = T_f|_{R^-}$$

$$k_s \left(\frac{\partial T_s}{\partial x} \right)_{R^+} = k_f \left(\frac{\partial T_f}{\partial x} \right)_{R^-}$$

$$y = R_i : T_s|_{R^+} = T_f|_{R^-}$$

$$k_s \left(\frac{\partial T_s}{\partial y} \right)_{R^+} = k_f \left(\frac{\partial T_f}{\partial y} \right)_{R^-}$$

Also at the inlet cross-section:

$$y = R_i + h_{ch} ; R_i - w_{ch} < x < R ; 0 < z < l_{ch} / 2$$

$$M = M_{in} \text{ and } T = T_{in}$$

All the outer surfaces of the heat sink are insulated except the bottom one in contact with the chip:

$$y = -[H - (D_i + h_{ch}) + R_i] ; -W_m < x < W_m ; 0 < z < L / 2$$

$$q = k_s \frac{\partial T}{\partial y}$$

At the outlet of the microtube the following boundary conditions are prescribed:

$$z = L/2$$

$$\frac{\partial v}{\partial z} = 0; \frac{\partial w}{\partial z} = 0; \frac{\partial u}{\partial z} = 0; \frac{\partial T}{\partial z} = 0$$

At the symmetry boundaries:

$$z = 0$$

$$\frac{\partial v}{\partial z} = 0; \frac{\partial w}{\partial z} = 0; \frac{\partial u}{\partial z} = 0; \frac{\partial T}{\partial z} = 0$$

$$x = \pm W_m/2$$

$$\frac{\partial v}{\partial x} = 0; \frac{\partial w}{\partial x} = 0; \frac{\partial u}{\partial x} = 0; \frac{\partial T}{\partial x} = 0$$

The set of the partial differential equations with the boundary conditions are solved using the Fluent commercial solver [102] with methods described in [18]. The Simple algorithm is used for the velocity-pressure coupling solution and second order upwind scheme for discretization. The under-relaxation factors are used for pressure field ($\alpha = 0.3$) and momentum conservation ($\alpha = 0.7$). The convergence criterion is defined as:

$$R\phi = \frac{\sum_{cells,P} \left| \sum_{nb} a_{nb} \cdot \phi_{nb} + b - a_p \phi_p \right|}{\sum_{cells,P} \left| a_p \phi_p \right|} \quad (4.3.4)$$

The residuals for velocity components and continuity equation were 10^{-5} and for temperature field 10^{-8} . Two different quasi-structured grids have been used to test the grid sensitivity, Mesh 1 with total of 235875 cells and Mesh 2 with total of 622639 cells. In the Fig. 4.3.3 the temperature distribution at the centerline of the heat sink bottom surface is presented for these two grids. For a grid independence test case 4 was considered with a mass flow rate of a single micro-tube $M = 1.2 \cdot 10^{-3}$ kg/s. A difference between these two grids is lower than 1 % for temperature distribution along the axial direction (Fig. 4.3.2), so the mesh nr. 1 is used for further calculations.

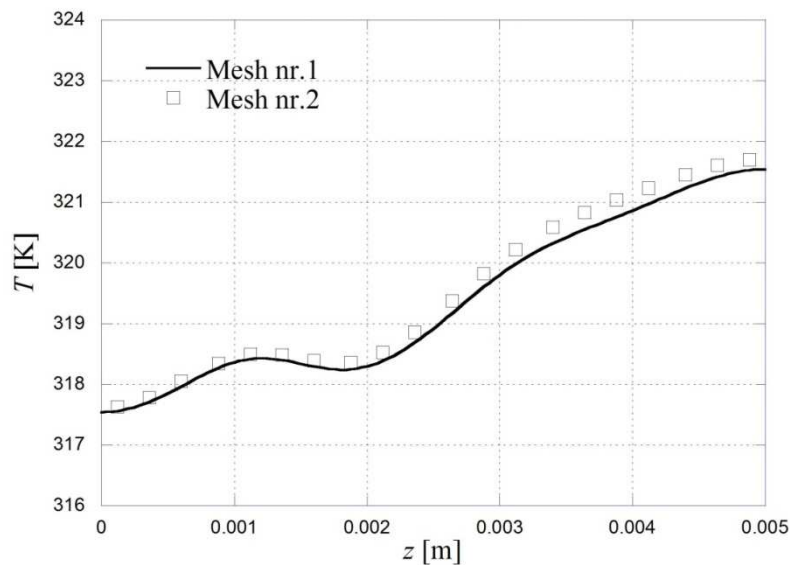


Fig. 4.3.2 Grid independence test

4.3.2. Results and discussion

The performance evaluation of the micro-heat sink is presented in terms of the temperature distribution along the bottom wall based on a fixed pumping power, for various numbers and positions of the inlet cross sections. To make the insight in thermal results, the axial velocity distributions are presented at different axial locations. It has to be noticed that the heat flux was the same for all runs, $q = 100 \text{ W/cm}^2$ with inlet temperature $T_{in} = 293 \text{ K}$. The pumping power is defined as:

$$\Pi = M \cdot \frac{\Delta p}{\rho} \quad (4.3.5)$$

while the Re is defined with the following equation:

$$\text{Re} = \frac{4 \cdot (M / 2)}{\pi \cdot D_i \cdot \mu} \quad (4.3.6)$$

In Fig. 4.3.3 the temperature distribution along the bottom line of the microchannel heat sink was presented for three inlets and compared with microchannel heat sink with single inlet for constant total pumping power $\Pi = 0.024 \text{ W}$. In the case of the microchannel heat sink with three inlets, one of them is fixed in the middle of the heat sink and the rest of the inlets are symmetrical and have three different positions. It is observed that as the second inlet is departed from the outlet cross section the minimum temperature is decreasing. Moreover the minimum temperatures are observed for case 1 ($T_{min} = 316.5 \text{ K}$), case 2 ($T_{min} = 315.5 \text{ K}$), case 3 ($T_{min} = 314.1 \text{ K}$) and $T_{min} = 312.5 \text{ K}$ for a single inlet. On the other hand the maximum temperature difference is obtained for the single inlet case ($\Delta T = 10 \text{ K}$), followed by the case 3 ($\Delta T = 7.6 \text{ K}$), case 1 ($\Delta T = 4.2 \text{ K}$) and case 2 ($\Delta T = 3.5 \text{ K}$). It has to be mentioned that for microchannel heat sink with three inlets (cases 1 – 3) the total mass flow rate for $N = 9$ microtubes is $M = 0.0108 \text{ kg/s}$ while for single inlet $M = 0.0117 \text{ kg/s}$.

In Fig. 4.3.4 the temperature distribution along the bottom line of the microchannel heat sink is presented for the case with five inlet jets (for constant pumping power, case 4(1) and constant mass flow rate case 4(2)) and compared with microtube with single inlet. For the microchannel heat sink with five inlets the temperature of the bottom surface is more uniform ($\Delta T = 4 \text{ K}$) for both cases 4(1) and 4(2). Contrary to this the minimum temperature is much higher ($T_{min} = 317.5 \text{ K}$ for case 4(1) and $T_{min} = 318.4 \text{ K}$ for case 4(2)) compared with single inlet heat sink ($T_{min} = 312.5 \text{ K}$).

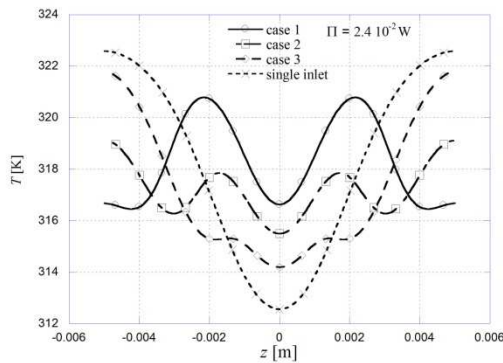


Fig. 4.3.3 The temperature variation along the centerline at the bottom wall of the heat sink for $\Pi = 0.024 \text{ W}$, cases 1 - 3 and single inlet.

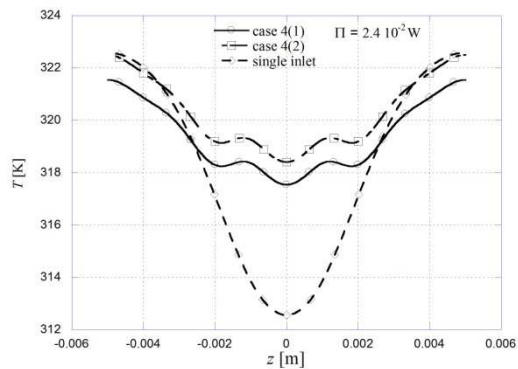


Fig. 4.3.4 The temperature variation along the centerline at the bottom wall of the heat sink for $\Pi = 0.024 \text{ W}$, case 4 and single inlet.

The axial velocity distributions along the tube radius are presented in Fig. 4.3.5, for cases 1 – 4 and fixed pumping power. It is concluded in [119] that axial velocities are responsible for heat transfer enhancement. For cases 1 and 2, where the second inlet cross-section is near the outlet of the tube and at the midway between the inlet and outlet cross-section, the axial velocity is decreasing downstream attaining the negative values near the second cross-section. At the $z = 0.004$ m the axial velocity is increasing due to the second inlet jet. For case 3 (inlet jet near the central inlet cross-section) the axial velocity is initially decreasing down to negative values (reverse flow), at $z = 0.00325$ m axial velocity is increasing up to $w = 1.5$ m/s, and decreasing to $w = 1$ m/s at $z = 0.0045$ m. In the case of 5 inlets the axial velocity is decreasing at $z = 0.0015$ m, establishing the reverse flow near the bottom wall of the microtube and increasing after that at $z = 0.00325$ and 0.004 m.

In Fig. 4.3.6 the axial velocity contours are presented for cases 1 - 4. It is observed that the maximum velocities are near the bottom wall of the microtube $w = 1.8$ m/s for case 1, $w = 1.6$ m/s for cases 2 and 3 and $w = 1.4$ m/s for case 4. Moreover there are two zones of reversed flow observed in the microtube. One is on the bottom part, near the second inlet cross-section, while another one is in the middle of the microtube between the first and second inlet jet. Besides the recirculation zone is not observed between the second and third inlet cross-section for case 4.

In Fig. 4.3.7 the separation zones delimited the reverse flow are presented. The largest one is observed in the middle of the microtube between the first and second inlet cross-section. Moreover the large separation zone is located at the beginning of the second inlet cross-section at almost the half of the microtube perimeter. There are also small separation zones at the top of the microtube after the each inlet cross-section.

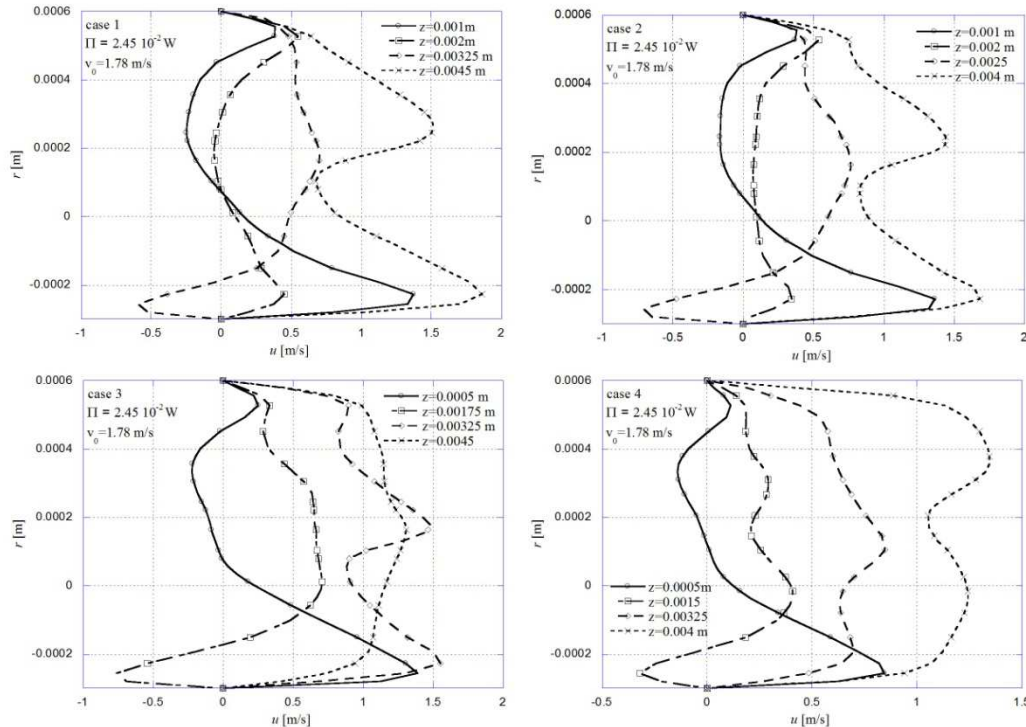


Fig. 4.3.5 The axial velocity distribution along the tube radius at the midline $x = 0$ and various axial locations

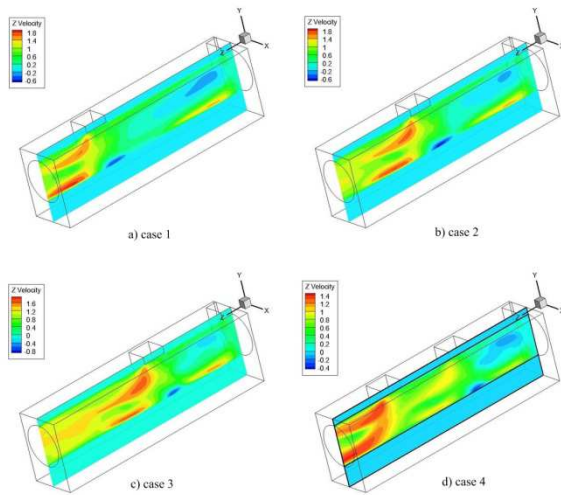


Fig. 4.3.6 The axial velocity distribution for various configurations of the inlet cross sections

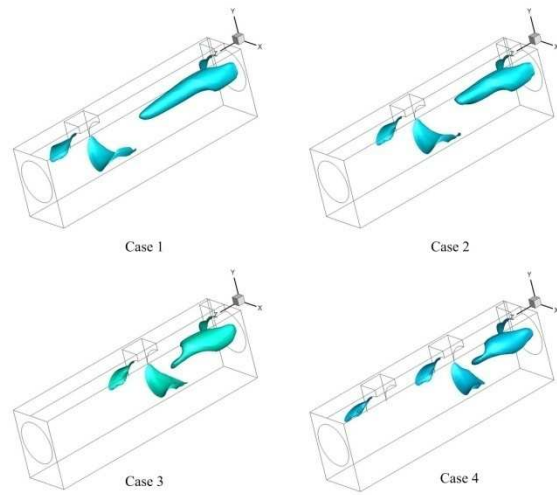


Fig. 4.3.7 The separation zones for various multiple inlets

4.3.3. Conclusions

The numerical analysis of the tangential microtube heat sink with different numbers and positions of the inlet cross-sections is presented. The following conclusions are outlined:

- In the case of tangential micro-heat sink with three inlet cross-sections the temperature distribution is dependent on the position of the second inlet jet if the first one is fixed at the center of the microtube.
- If the analysis is made on a fixed pumping power basis, the minimum temperatures are higher for multiple inlets compared with the micro-heat sink with single inlet jet. Moreover the micro-heat sink with multiple inlet jets has the lower temperature difference on a bottom surface between the inlet and outlet of the microtube.
- In the case of the microtube with multiple inlets, the recirculation zones are observed between the first and second inlet cross-section and behind the second inlet cross-section.

5. The micro-tube heat transfer and fluid flow of nanofluids

5.1. The micro-tube heat transfer and fluid flow of water based Al_2O_3 nanofluid with viscous dissipation

Today's technological developments and advances in equipments that ensure the comfort of everyday life increases the importance of microchannel heat transfer and fluid flow. The cooling of the VLSI devices, biomedical applications, micro-heat-exchangers are some of the examples where the fundamentals of the microchannel heat transfer and fluid flow are essential for a proper design of these devices. Moreover, the nanofluids that were first introduced by Choi [120], gained the interest in the recent years due to their cooling capabilities.

Yang et al [121] investigated experimentally the laminar heat transfer and fluid flow of graphite nanofluids in horizontal tubes. The experimental results show that the nanoparticles increase the heat transfer coefficient of the fluid system in laminar flow, but the increase is much less than that predicted by current correlation based on static thermal conductivity measurements.

Experimental research on developing laminar and turbulent heat transfer of water-based FMWNT nanofluid in a uniformly heated horizontal tube was made by Amrollahi et al [122]. The experimental results indicate that the convective heat transfer coefficient of these nanofluids increases by up to 33–40 % at a concentration of 0.25 wt.% compared with that of pure water both in laminar and turbulent regime.

The experimental research on heat transfer of Al_2O_3 /propanol nanofluid was made by Sommers and Yerkes [123]. The heat transfer coefficient enhancement was observed for $\text{Re}_D < 3000$ with the pressure drop increasing from 400% to 600% for the 1 wt% Al_2O_3 /propanol nanofluid.

Rea et al [124] analyzed experimentally the laminar convective heat transfer of alumina–water and zirconia–water nanofluids. The data expressed in form of dimensionless numbers (Nu and x^+), show good agreement with the predictions of the traditional models/correlations for laminar flow. This suggests that the nanofluids behave as homogeneous mixtures.

Developing heat transfer of Al_2O_3 /water nanofluids in annulus was studied numerically in Izadi et al [125] with single phase approach adopted for nanofluid modeling. It was concluded that the effect of nanoparticle concentration on the nanofluid bulk temperature is significant.

The experimental research on heat transfer of Al_2O_3 /water nanofluid in tubes was analyzed by Wen and Ding [126] and Anoop et al [127]. The results showed considerable enhancement of convective heat transfer using the nanofluids, particularly significant in the entrance region. Heris et al [128] analyzed numerically laminar-flow convective heat transfer of nanofluid in a circular tube with constant wall temperature boundary condition. The numerical results indicate that addition of nanoparticles to base liquid produces considerable enhancement of heat transfer. Also decreasing nanoparticles size at a specific concentration increases heat transfer coefficients.

The comparison of different approach for numerical modeling on heat transfer of nanofluids was presented by Lotfi et al [129] and Fard et al [130]. It was found that two-phase models are more precise than one-phase model.

The turbulent heat transfer of CuO /water nanofluids inside circular tubes was investigated experimentally by Fotukian and Esfahany [131], while natural convection of Al_2O_3 –water nanofluid was analyzed by Nada [132]. In the latter case the single-phase approach was employed with Chon et al [139] model for thermal conductivity and correlation based on Nguyen et al [141] experimental results for effective viscosity.

The liquid cooling of electronics with nanofluids was investigated by Nguyen et al [133]. It was found that for a particular particle volume concentration of 6.8%, the heat transfer coefficient increases as much as 40% compared to that of the base fluid. Koo and Kleinstreuer [134] analyzed numerically steady laminar liquid nanofluid flow in microchannels considering two types of nanofluids, CuO particles at low volume concentrations in water or ethylene glycol. It was concluded that nanoparticles of high thermal conductivity are advantageous and a channel with high aspect ratio is desirable.

Lee and Mudawar [135] analyzed experimentally the effectiveness of the nanofluids for single-phase and two-phase heat transfer in micro-channels. Higher heat transfer coefficients were achieved in the entrance region of micro-channels proving that nanoparticles have an appreciable effect on thermal boundary layer development. Ghasemi et al [136] analyzed natural convection heat transfer in an inclined enclosure filled with a CuO /water nanofluid. The results indicate that adding nanoparticles into pure water improves its heat transfer performance. Hung [137] made an analytical study on microchannel heat transfer of nanofluids including the viscous dissipation effect. It is observed that the Nusselt number is

overestimated when the viscous dissipation is neglected, and subsequently, the thermal performance of the microchannel is also overrated.

The correlations for temperature dependent effective conductivity of water based nanofluids were developed by Mintsa et al [138] and Chon et al [139]. Also a new model for assessment of the effective viscosity of water based nanofluids was developed by Masoumi et al [140]. The experimentally obtained set of data for temperature and particle size dependent effective viscosity was presented by Nguyen et al [141]. Zhoua et al [142] performed measurements of the specific heat capacity of water-based Al_2O_3 nanofluid. Finally an overview on enhancement of heat transfer using nanofluids was presented by Godson et al [143].

This chapter presents the numerical modeling of the laminar heat transfer and fluid flow of Al_2O_3 /water nanofluid in microchannels. The single phase model was used with correlations for temperature and particle size dependent effective thermal conductivity and viscosity. Moreover due to the reduce tube diameter the viscous dissipation effect was included in the analysis. The results for heat transfer coefficient were compared with the results obtained for pure water heat transfer and fluid flow.

5.1.1. Numerical details

The computational domain is presented in Fig. 2.4.1, as follows: The fluid flow domain defined at $r = 0, R_i$ and $z = 0, L$. The temperature field domain defined at $r = 0, R_o$ and $z = 0, L$. The following set of partial differential equations is used to describe the phenomena, considering the effective thermophysical properties of the fluids and viscous dissipation:

Continuity equation:

$$\frac{\partial(\rho_{eff} \cdot u)}{\partial z} + \frac{1}{r} \frac{\partial(r \cdot \rho_{eff} \cdot v)}{\partial r} = 0 \quad (5.1.1)$$

Momentum equation:

$$\frac{\partial(\rho_{eff} v u)}{\partial r} + \frac{\partial(\rho_{eff} u u)}{\partial z} = -\frac{dp}{dz} + \frac{1}{r} \frac{\partial}{\partial r} \left(\mu_{eff} r \frac{\partial u}{\partial r} \right) \quad (5.1.2)$$

Energy equation:

$$\frac{\partial(\rho_{eff} c_{p,eff} v T)}{\partial r} + \frac{\partial(\rho_{eff} \cdot c_{p,eff} u T)}{\partial z} = \left[\frac{1}{r} \frac{\partial}{\partial r} \left(k_{eff} \cdot r \frac{\partial T}{\partial r} \right) + \frac{\partial}{\partial z} \left(k_{eff} \frac{\partial T}{\partial z} \right) \right] + \mu_{eff} \cdot S_v \quad (5.1.3)$$

where the viscous dissipation term is defined as:

$$S_v = 2 \cdot \left[\left(\frac{\partial v}{\partial r} \right)^2 + \left(\frac{v}{r} \right)^2 + \left(\frac{\partial u}{\partial z} \right)^2 \right] + \left[\frac{\partial v}{\partial z} + \frac{\partial u}{\partial r} \right]^2 \quad (5.1.4)$$

At the inlet of the tube, the uniform velocity and temperature field is considered, while at the exit the temperature and velocity gradients are equal to zero.

The boundary conditions are:

$$\begin{aligned} z = 0, 0 < r < R_o: & \quad u = u_0, T = T_w = T_0 \\ 0 < z < L_{tot}: & \quad r = 0, \frac{\partial u}{\partial r} = 0, \frac{\partial T}{\partial r} = 0, v = 0 \\ & \quad r = R_i, u = v = 0 \end{aligned}$$

The Joule heating of the tube wall can be expressed either by the uniform heat generation through the tube wall or by the uniform heat flux imposed on the outer surface of the wall. For the latter case, the boundary condition is defined as,

$$r = R_o: \quad q_o = k_s \frac{\partial T}{\partial r}$$

where q_o is the heat flux based on the outer heat transfer area of the tube wall.

$$z = L_{tot}, 0 < r < R_o: \quad \frac{\partial T}{\partial z} = 0$$

The conjugate heat transfer procedure, implies the continuity of the temperature and heat flux at the solid – liquid interface defined as,

$$r = R_i : T_s |_{R_{i+}} = T_f |_{R_{i-}}$$

$$k_s \left(\frac{\partial T_s}{\partial r} \right)_{R_{i+}} = k_{eff} \left(\frac{\partial T_f}{\partial r} \right)_{R_{i-}}$$

The partial differential equations (5.1.1) – (5.1.3) together with boundary conditions are solved using the finite volume method described in [18]. First, the parabolic flow field condition is considered and the velocity field is solved. The temperature field, as a conjugate heat transfer problem, was then calculated as the elliptic problem using the obtained velocity field. The fluid flow regime is considered to be a steady-state laminar flow.

In order to test the grid sensitivity, two grids have been used. The coarser one with 250 cells in radial direction and 400 cells in axial direction and finer grid with 500 and 800 cells in z - and r - direction respectively. Differences obtained for Nu were smaller than 0.1 %, so the coarser grid has been used for further calculations. Additionally, the numerical results have been compared with experimental results obtained by Rea et al. [124] with satisfactory deviation: below 10 % for Al_2O_3 /water nanofluid and $\phi = 0.65$ %, 1.32 %, 2.76 % and below 13 % for $\phi = 6$ % (Fig. 2).

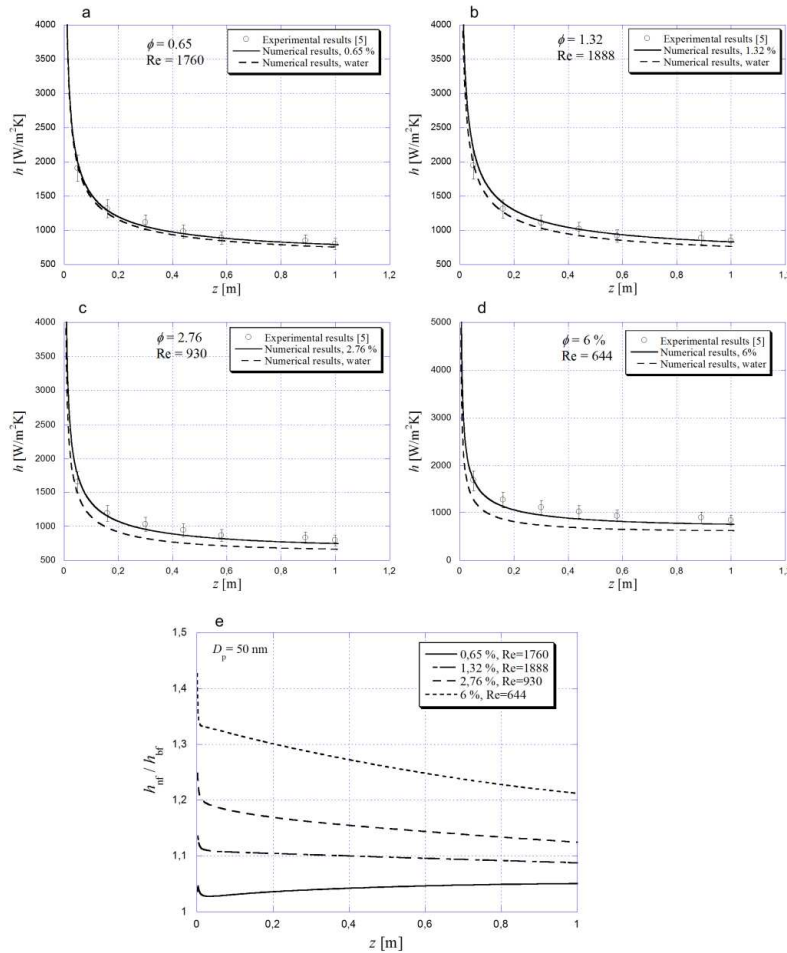


Fig. 5.1.2 The comparison of the present numerical results with experimental results [5] (a-d) and nanofluid heat transfer enhancement compared with the base fluid (e)

The nanofluid effective thermal conductivity normalized with the based fluid thermal conductivity is given as [139]:

$$\frac{k_{eff}}{k_{bf}} = 1 + 64.7 \cdot \phi^{0.7460} \left(\frac{D_{bf}}{D_p} \right)^{0.3690} \cdot \left(\frac{k_p}{k_{bf}} \right)^{0.7476} \cdot Pr^{0.9955} \cdot Re^{1.2321} \quad (5.1.5)$$

The Pr is defined as:

$$Pr = \frac{\mu}{\rho_{bf} \cdot \alpha}$$

The Re is calculated as:

$$Re = \frac{\rho_{bf} \cdot k_b \cdot T}{3 \cdot \pi \cdot \mu^2 \cdot l_{bf}}$$

where $k_b = 1.3807 \times 10^{-23}$ J/K, $l_{bf} = 0.17$ nm and $D_{bf} = 0.384$ nm.

The temperature dependent viscosity of water is defined as:

$$\mu(t) = 2.6412018 \cdot 10^{-4} + 0.0014009 \cdot e^{-\frac{t}{31.0578605}} \quad (5.1.6)$$

The effective viscosity of the water based Al_2O_3 nanofluid is calculated from the relation developed in [132] based on data presented in [141]:

$$\begin{aligned} \mu_{eff} = & -0.155 - \frac{19.582}{T} + 0.794 \cdot \phi + \frac{2094.47}{T^2} - 0.192 \cdot \phi^2 - 8.11 \cdot \frac{\phi}{T} \\ & - \frac{27463.863}{T^3} + 0.0127 \cdot \phi^3 + 1.6044 \cdot \frac{\phi^2}{T} + 2.1754 \cdot \frac{\phi}{T^2} \end{aligned} \quad (5.1.7)$$

The effective density is defined as:

$$\rho_{eff} = (1 - \phi) \cdot \rho_f + \phi \cdot \rho_p \quad (5.1.8)$$

The effective specific heat is calculated as:

$$c_{peff} = \frac{(1 - \phi) \cdot (\rho \cdot c_p)_f + \phi \cdot (\rho \cdot c_p)_p}{\rho_{eff}} \quad (5.1.9)$$

The properties of the Al_2O_3 particles are defined as [144]: $\rho_p = 3975$ kg/m³, $c_{pp} = 765$ J/kg K, $k_p = 36$ W/mK, $\alpha = 11.9 \cdot 10^{-6}$ m²/s.

Re is defined as:

$$Re = \frac{\rho_{eff} \cdot u_m \cdot D_i}{\mu_{eff}} \quad (5.1.10)$$

While the local Nu number is defined with the following equation:

$$h = \frac{q}{T_w - T_b} \quad (5.1.11)$$

The pumping power is defined as:

$$\Pi = M \cdot \frac{\Delta p}{\rho_{eff}}$$

The Brinkman number for constant wall heat flux is defined as:

$$Br = \frac{u_m^2 \cdot \mu_{eff}}{q \cdot D_i} \quad (5.1.12)$$

5.1.2. Results and discussion

The code validation with the experimental results obtained by Rea et al [124] was presented in the Fig. 5.1.2. In the same graphs the heat transfer results for water are presented for the macro-tube with diameter $D_i = 4.5$ mm and fixed Re. As it is expected for a low

particle concentration the enhancement is very low ($\sim 5\%$). As the Al_2O_3 concentration is increasing the local heat transfer enhancement is increasing. Moreover for the specific particle concentration the enhancement is higher in the entrance region and it is gradually decreasing toward the end of the tube. This observation is consistent with conclusions mentioned in [124], [126] and [135].

In the Fig. 5.1.3 the local heat transfer coefficient behavior from micro-tube is presented for various particle concentrations and $D_p = 10\text{ nm}$. The local heat transfer coefficient exhibits the boundary layer variation approaching approximately the fully developed value. As the Br is increasing the heat transfer coefficient is decreasing. This is explained by the increasing temperature difference between the wall and a fluid due to the viscous dissipation effect. As the friction between the fluid and the wall is higher consequently the wall temperature increases more rapidly than a fluid temperature so the temperature difference increases with Br. Finally the heat transfer coefficient is lower as the temperature difference is higher.

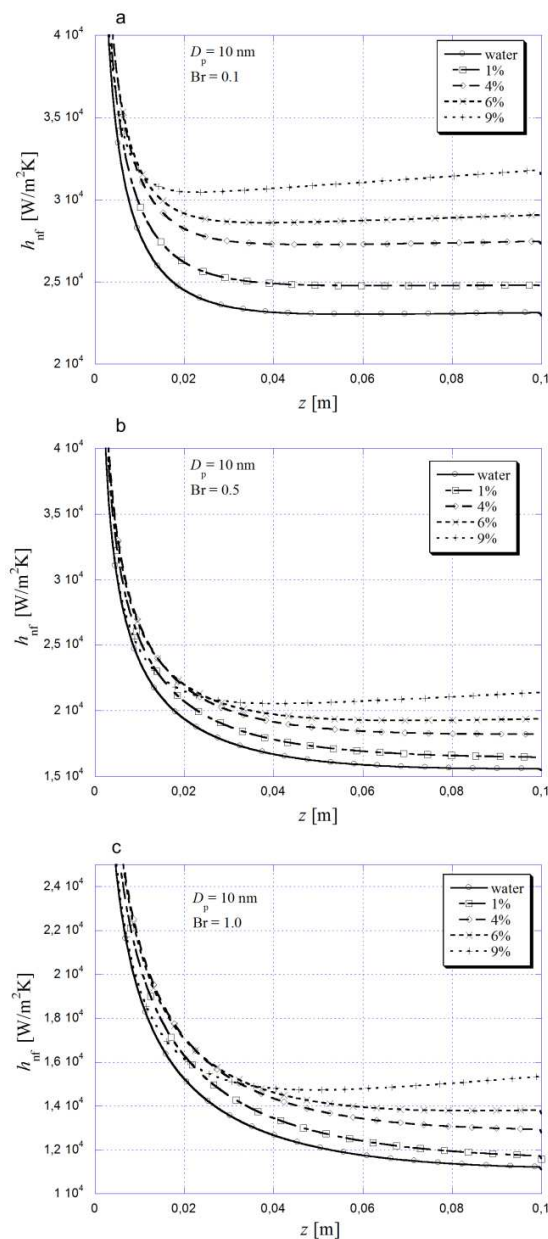


Fig. 5.1.3 The local heat transfer coefficient for $D_p = 10\text{ nm}$ and various Al_2O_3 concentrations

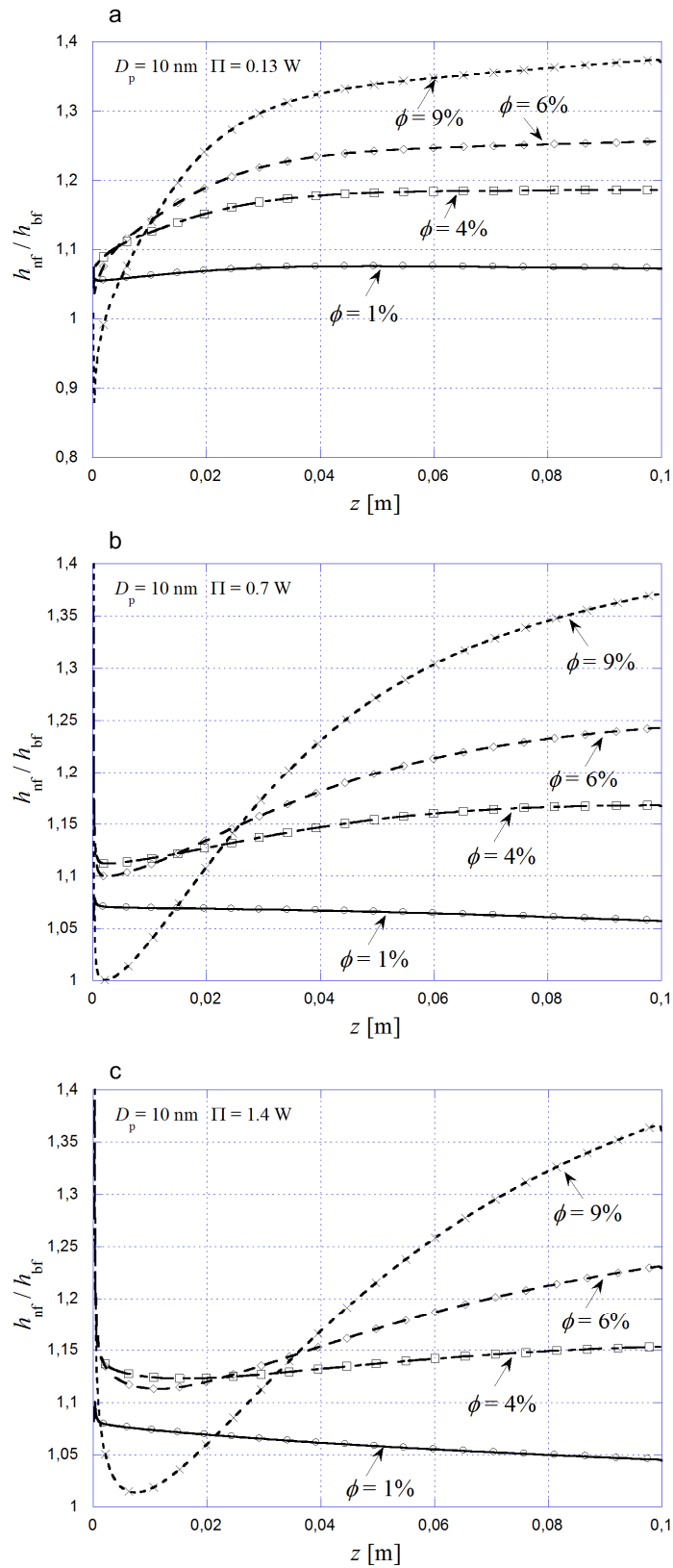


Fig. 5.1.4 The heat transfer enhancement for $D_p = 10$ nm and various Al_2O_3 concentrations

Also as the particle concentration in the nanofluid increases, the heat transfer coefficient is higher. Moreover it is observed that for higher Br, the increasing of the heat transfer coefficient with Al_2O_3 particles is lower. To analyze the local heat transfer enhancement for particular Al_2O_3 concentration and fixed pumping power, the ratio of the heat transfer coefficient for nanofluid and base fluid is presented in the Fig. 5.1.4. For $\Pi = 0.13 \text{ W}$ the local heat transfer enhancement is increasing with the axial distance and particle concentration. The maximum heat transfer enhancement is about 37 % for $\phi = 9 \%$. Similar to the macro-tubes, for low particle concentration $\phi = 1 \%$ the increasing in heat transfer coefficient is weak, about 7 %.

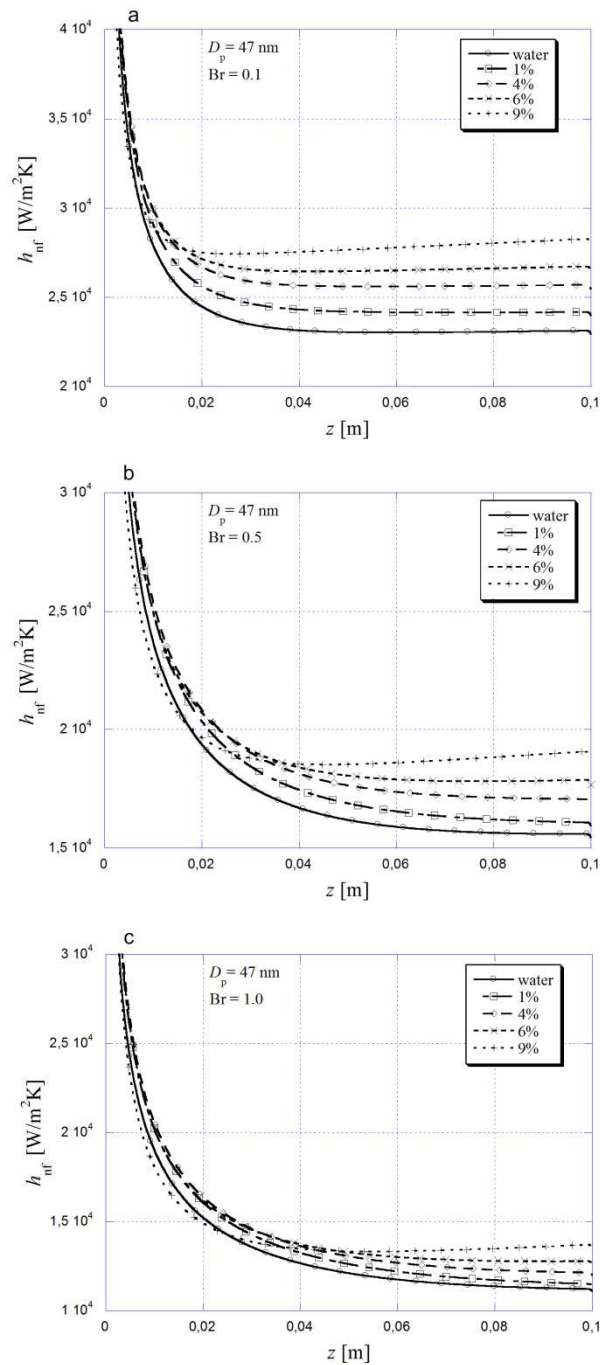


Fig. 5.1.5 The local heat transfer coefficient for $D_p = 47 \text{ nm}$ and various Al_2O_3 concentrations

For higher pumping power $\Pi = 0.7$ W and $\phi = 9\%$ the heat transfer coefficient ratio initially decreases to $h_{nf}/h_{bf} = 1$ and then increases to 1.37. The same behavior is observed for higher pumping power $\Pi = 1.4$ W. The heat transfer coefficient ratio for $\phi = 9\%$ is highest for the axial distance greater than 0.04 m. In the Fig. 5.1.5 the local heat transfer coefficient is presented for $D_p = 47$ nm and various particle concentrations. Once again the heat transfer coefficient decreases as Br increases. For $Br = 0.1$ the h_{nf} is between $2.3 \cdot 10^4$ and $2.7 \cdot 10^4$, for $Br = 0.5$, $1.5 \cdot 10^4 < h_{nf} < 1.8 \cdot 10^4$ and $Br = 1.0$, $1.2 \cdot 10^4 < h_{nf} < 1.4 \cdot 10^4$.

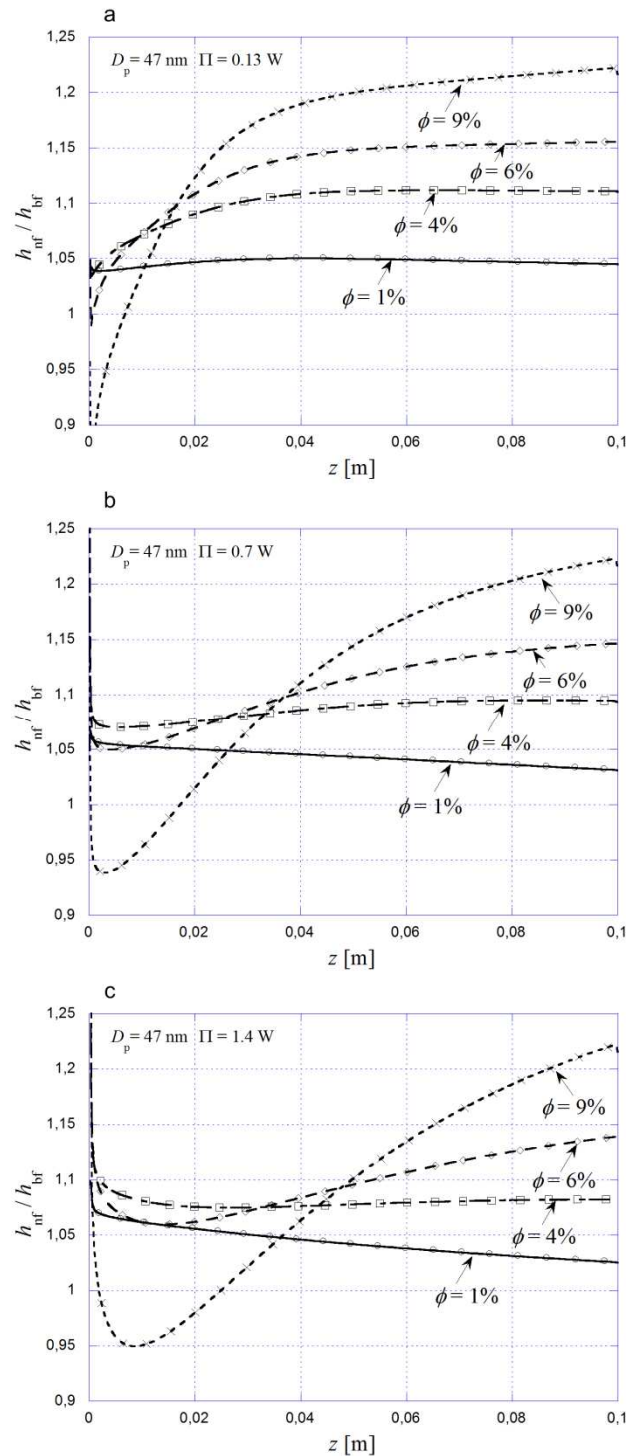


Fig. 5.1.6 The heat transfer enhancement for $D_p = 47$ nm and various Al_2O_3 concentrations

In the case of the heat transfer enhancement for nanofluid with $D_p = 47$ nm (Fig. 5.1.6), the heat transfer coefficient ratio is lower than for a nanofluid with $D_p = 10$ nm. The maximum increasing is observed for $\phi = 9$ %, about 20 %. The lowest heat transfer coefficient ratio is ~ 5 % for $\phi = 1$ % and constant regardless the axial position. Although the highest increasing in heat transfer coefficient does not depend on pumping power, for $\phi = 9$ % the heat transfer coefficient ratio varies along the axial distance. It is decreasing in the entrance region to $h_{nf} / h_{bf} = 0.95$, lower than the heat transfer coefficient for the water flow. After the half length of the tube the nanofluid with $\phi = 9$ % has the best thermal performances compared with water and other nanofluid concentrations.

The heat transfer enhancement for nanofluids with $\phi = 4$ and 6 % have almost the uniform distribution along the axial distance of the tube, $h_{nf} / h_{bf} = 1.1$ for nanofluid with $\phi = 4$ and $h_{nf} / h_{bf} = 1.2$ for nanofluid with $\phi = 6$ %.

5.1.3. Conclusions

The laminar nanofluid heat transfer in micro-tubes was numerically analyzed taking into account the viscous dissipation effect. Considering the local heat transfer coefficient distribution, the following conclusions are outlined:

- Contrary to the macro-scale heat transfer where the higher heat transfer enhancement is observed in the entrance region, in the case of the microchannel heat transfer, due to the viscous heating that is more pronounced near the tube wall, the heat transfer augmentation is constantly increasing with axial distance.
- For nanofluids with higher particle concentration $\phi = 9$ %, the large limits for heat transfer coefficient ratio along the axial distance are observed, from $h_{nf} / h_{bf} = 0.9$ (below the heat transfer coefficient of the base fluid) to $h_{nf} / h_{bf} = 1.37$.

5.2. The performance evaluation of Al_2O_3 /water nanofluid flow and heat transfer in microchannel heat sink

Most of the papers dealt with the numerical research on nanofluid flow and heat transfer, are for the macrochannels and only a few consider the microchannels. This chapter presents the numerical analysis of microchannel fluid flow and heat transfer of water based Al_2O_3 nanofluid with viscous dissipation phenomena [180]. Therefore the hydraulic diameter was set small enough ($D_h = 50$ μ m and $L_t = 4.48$ cm) in order to consider the viscous heating effect. The results emphasize the local heat transfer augmentation as the ratio between heat transfer coefficient of the nanofluid and heat transfer coefficient of the base fluid. The analysis is made on a fixed pumping power basis for various particle's diameters and particle's concentrations with two heat transfer rate directions: cooling and heating.

5.2.1. Numerical details

The one-layer microchannel heat sink is presented in the Fig. 2.3.1. Due to the symmetry plane, the half cross-section of one channel is considered in computations. The conventional set of the Navier-Stokes equations has been used for the conjugate laminar steady state heat transfer and fluid flow, as follows:

The continuity equation:

$$\frac{\partial u}{\partial x} + \frac{\partial v}{\partial y} + \frac{\partial w}{\partial z} = 0 \quad (5.2.1)$$

The momentum equation:

$$\rho_{eff} \left(u \frac{\partial u}{\partial x} + v \frac{\partial u}{\partial y} + w \frac{\partial u}{\partial z} \right) = -\frac{dp}{dz} + \left(\frac{\partial}{\partial x} \left(\mu_{eff} \frac{\partial u}{\partial x} \right) + \frac{\partial}{\partial y} \left(\mu_{eff} \frac{\partial u}{\partial y} \right) \right) \quad (5.2.2)$$

$$\rho_{eff} \left(u \frac{\partial v}{\partial x} + v \frac{\partial v}{\partial y} + w \frac{\partial v}{\partial z} \right) = -\frac{dp}{dx} + \left(\frac{\partial}{\partial x} \left(\mu_{eff} \frac{\partial v}{\partial x} \right) + \frac{\partial}{\partial y} \left(\mu_{eff} \frac{\partial v}{\partial y} \right) \right) \quad (5.2.3)$$

$$\rho_{eff} \left(u \frac{\partial w}{\partial x} + v \frac{\partial w}{\partial y} + w \frac{\partial w}{\partial z} \right) = -\frac{dp}{dy} + \left(\frac{\partial}{\partial x} \left(\mu_{eff} \frac{\partial w}{\partial x} \right) + \frac{\partial}{\partial y} \left(\mu_{eff} \frac{\partial w}{\partial y} \right) \right) \quad (5.2.4)$$

The energy equation (for both fluid and solid):

$$\rho_{eff} \cdot c_{peff} \cdot \left(u \frac{\partial t}{\partial x} + v \frac{\partial t}{\partial y} + w \frac{\partial t}{\partial z} \right) = \left(\frac{\partial}{\partial x} \left(k_{eff} \frac{\partial t}{\partial x} \right) + \frac{\partial}{\partial y} \left(k_{eff} \frac{\partial t}{\partial y} \right) + \frac{\partial}{\partial z} \left(k_{eff} \frac{\partial t}{\partial z} \right) \right) + \Phi \quad (5.2.5)$$

Where viscouse dissipation term is defined as:

$$\Phi = \mu_{eff} \cdot \left\{ 2 \cdot \left[\left(\frac{\partial u}{\partial x} \right)^2 + \left(\frac{\partial v}{\partial y} \right)^2 + \left(\frac{\partial w}{\partial z} \right)^2 \right] + \left(\frac{\partial v}{\partial x} + \frac{\partial u}{\partial y} \right)^2 + \left(\frac{\partial w}{\partial y} + \frac{\partial v}{\partial z} \right)^2 + \left(\frac{\partial u}{\partial z} + \frac{\partial w}{\partial x} \right)^2 \right\} \quad (5.2.6)$$

The thermal conductivity of the copper substrate is $k_s = 380$ W/m K. The following boundary conditions are prescribed for the system of the partial differential equations:

The conjugate heat transfer procedure, implies the continuity of the temperature and heat flux at the solid – liquid interface defined as,

$$x = W_f/2: \quad t_s|_{x+} = t_f|_{x-}$$

$$k_s \left(\frac{\partial t_s}{\partial x} \right)_{x+} = k_{eff} \left(\frac{\partial t_f}{\partial x} \right)_{x-}$$

$$y = H_t - H_c: \quad t_s|_{y+} = t_f|_{y-}$$

$$k_s \left(\frac{\partial t_s}{\partial y} \right)_{y+} = k_{eff} \left(\frac{\partial t_f}{\partial y} \right)_{y-}$$

For the heate portion of the microchannel the following boundary condition is defined:

$$y = 0:$$

$$q_o = k_s \frac{\partial t}{\partial y}$$

Also at the inlet cross-section, uniform velocity and temperature field are considered:

$$z = 0:$$

$$u = u_{in} \text{ and } t = t_{in}$$

The upper boundary is isolated defined as:

$$k_s \frac{\partial t}{\partial y} = 0$$

At the outlet of the microchannel the following boundary conditions are prescribed:

$$z = L_t$$

$$\frac{\partial T}{\partial z} = 0; \frac{\partial u}{\partial z} = 0; v = w = 0$$

At the symmetry boundary:

$$x = w_f/2 + w_c/2$$

$$v = 0; \frac{\partial w}{\partial x} = 0; \frac{\partial u}{\partial x} = 0; \frac{\partial t}{\partial x} = 0$$

$$x = 0$$

$$\frac{\partial t}{\partial z} = 0$$

The microchannel heat sink dimensions are presented in the table 1.

Table 1 The geometric data and working parameters of the microchannel heat sink

w_f	w_c	H_c	H_t	L_t	w_t	q	Re	Br
μm	μm	μm	mm	cm	cm	W/cm^2		
36	50	50	1.05	4.48	1	35	107-1760	$\pm 0.005-0.05$

The solution procedure is based on the method used in [46] for microtubes and on the Finite Volume Method described in [18]. First, the parabolic flow field condition is considered and the velocity field is solved. The temperature field, as a conjugate heat transfer problem, was then solved as the elliptic problem using the obtained velocity field. Also k acts as k_s for copper wall and k_f for the fluid. At the fluid – solid interface k is calculated as the harmonic mean value. The velocity-pressure coupling is solved using a SIMPLER method. A staggered grid is used for cross-stream velocities with power-law discretization scheme.

The convergence criterion is defined as:

$$R = \left| \sum a_{nb} \cdot \phi_{nb} + b - a_p \cdot \phi_p \right|$$

where $R < 10^{-10}$ for the velocity components and $R < 10^{-8}$ for the temperature field.

The nanofluid effective thermal conductivity normalized with the based fluid thermal conductivity is given as [139]:

$$\frac{k_{eff}}{k_{bf}} = 1 + 64.7 \cdot \phi^{0.7460} \left(\frac{D_{bf}}{D_p} \right)^{0.3690} \cdot \left(\frac{k_p}{k_{bf}} \right)^{0.7476} \cdot \text{Pr}^{0.9955} \cdot \text{Re}^{1.2321} \quad (5.2.7)$$

The Pr is defined as:

$$\text{Pr} = \frac{\mu}{\rho_{bf} \cdot \alpha} \quad (5.2.8)$$

The Re is calculated as:

$$\text{Re} = \frac{\rho_{bf} \cdot k_b \cdot T}{3 \cdot \pi \cdot \mu^2 \cdot l_{bf}} \quad (5.2.9)$$

where $k_b = 1.3807 \times 10^{-23}$ J/K, $l_{bf} = 0.17$ nm and $D_{bf} = 0.384$ nm.

The temperature dependent viscosity of water is defined as:

$$\mu(t) = 2.6412018 \cdot 10^{-4} + 0.0014009 \cdot e^{-\frac{t}{31.0578605}} \quad (5.2.10)$$

The effective viscosity of the water based Al_2O_3 nanofluid with $d_p = 47$ nm is calculated from the relation developed in [132] based on data presented in [141]:

$$\begin{aligned} \mu_{eff} = & -0.155 - \frac{19.582}{T} + 0.794 \cdot \phi + \frac{2094.47}{T^2} - 0.192 \cdot \phi^2 - 8.11 \cdot \frac{\phi}{T} \\ & - \frac{27463.863}{T^3} + 0.0127 \cdot \phi^3 + 1.6044 \cdot \frac{\phi^2}{T} + 2.1754 \cdot \frac{\phi}{T^2} \end{aligned} \quad (5.2.11)$$

The effective density is defined as:

$$\rho_{eff} = (1 - \phi) \cdot \rho_f + \phi \cdot \rho_p \quad (5.2.12)$$

The effective specific heat is calculated as:

$$c_{peff} = \frac{(1-\phi) \cdot (\rho \cdot c_p)_f + \phi \cdot (\rho \cdot c_p)_p}{\rho_{eff}} \quad (5.2.13)$$

For the Al₂O₃ nanofluid with $d_p = 13$ and 28 nm the procedure described in [140] is used. The effective viscosity is a sum of base fluid viscosity and apparent viscosity:

$$\mu_{eff} = \mu_{bf} + \mu_{app} \quad (5.2.14)$$

The base fluid viscosity (water) is calculated by the equation (5.2.10), while the apparent viscosity of the nanofluid is defined by the following relation:

$$\mu_{app} = \frac{\rho_p \cdot V_b \cdot d_p^2}{72 \cdot C \cdot \delta} \quad (5.2.15)$$

where the Brownian velocity is defined as:

$$V_b = \frac{1}{d_p} \sqrt{\frac{18 \cdot K_b \cdot T}{\pi \cdot \rho_p \cdot d_p}} \quad (5.2.16)$$

A distance between the centers of the particles is obtained from:

$$\delta = \sqrt[3]{\frac{\pi}{6 \cdot \phi}} \cdot d_p \quad (5.2.17)$$

The correction factor is defined as:

$$C = \mu_{bf}^{-1} \cdot [(c_1 \cdot d_p + c_2) \cdot \phi + (c_3 \cdot d_p + c_4)] \quad (5.2.18)$$

where: $c_1 = -1.2331 \cdot 10^3$, $c_2 = -1.5331 \cdot 10^{-6}$, $c_3 = 94.383$ and $c_4 = -4.5731 \cdot 10^{-7}$

The properties of the Al₂O₃ particles are defined as [144]: $\rho_p = 3975$ kg/m³, $c_{pp} = 765$ J/kg K, $k_p = 36$ W/mK, $\alpha = 11.9 \cdot 10^{-6}$ m²/s.

Re is defined as:

$$Re = \frac{\rho_{eff} \cdot u_m \cdot D_h}{\mu_{eff}} \quad (5.2.19)$$

The average heat transfer coefficient, based on the peripherally averaged heat flux and wall temperature, is defined as:

$$h_{ave} = \frac{q|_{\Gamma}}{t_w|_{\Gamma} - t_b} \quad (5.2.20)$$

The Brinkman number for constant wall heat flux is defined as:

$$Br = \frac{u_m^2 \cdot \mu_{eff}}{q \cdot D_h} \quad (5.2.21)$$

The effective viscosity is evaluated at the inlet temperature. The pumping power is defined as:

$$\Pi = \dot{m} \cdot \frac{\Delta p}{\rho_{eff}} \quad (5.2.22)$$

5.2.2. The code validation

The results of the grid sensitivity testing for nanofluid with $d_p = 28$ nm, $\phi = 5$ % and $\Pi = 1$ W (Re = 877) is presented in Fig. 2. Three different grids were tested (9x18x50, 15x30x100 and 25x40x180). It is observed that a difference between the second (15x30x100) and third mesh (25x40x180) is below 0.1 % for bulk temperature and less than 1 % for average wall temperature. So, the second mesh is used for further calculations.

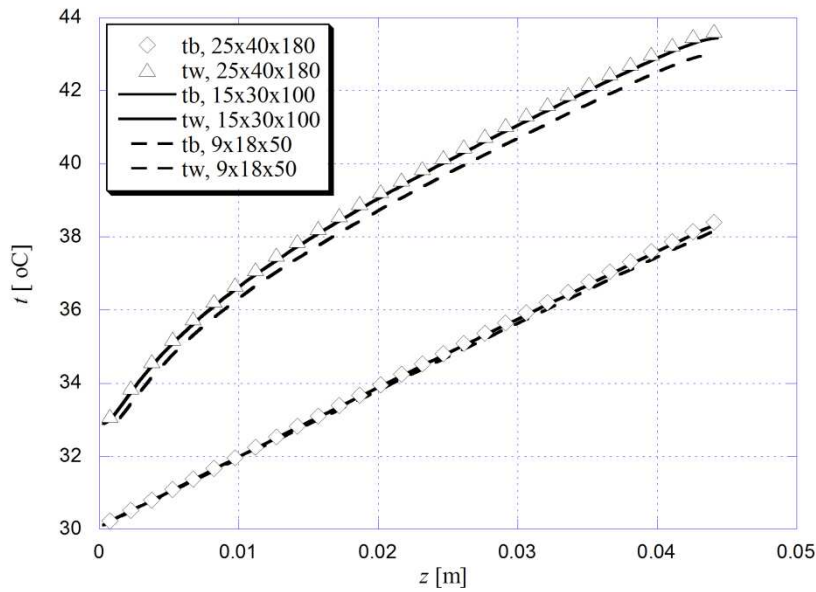


Fig. 5.2.2 The mesh sensitivity testing for nanofluid with $d_p = 28 \text{ nm}$, $\phi = 5 \%$ and $\Pi = 1 \text{ W}$ ($Re = 877$)

The numerical results were also compared with the experimental results obtained by Lee and Mudawar [135] for microchannel heat sink with 21 microchannels ($w \times H = 215 \times 821 \mu\text{m}$). The heat transfer rate was $Q = 300 \text{ W}$ with alumina - water nanofluid and $\phi = 2 \%$. In the Fig. 5.2.3 the temperature difference between the inlet and outlet cross-sections versus mass flow rate is presented. The maximum difference is 8 % for lower flow rates. In the Fig. 5.2.4 the local inner wall temperature versus axial distance is presented for the fixed mass flow rate $m = 5.49 \text{ g/s}$. The maximum deviation was observed near the exit of the microchannel heat sink, about 4 %.

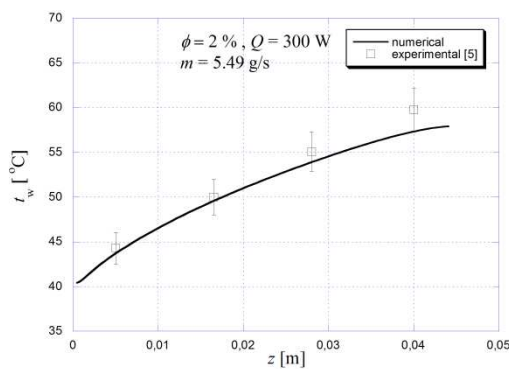


Fig. 5.2.3 The comparison between the experimental and numerical results for the local wall temperature

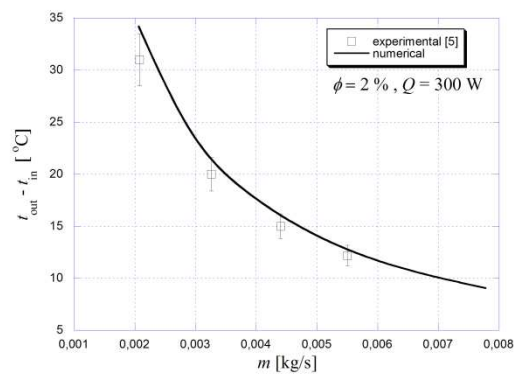


Fig. 5.2.4 The comparison between the experimental and numerical results for the temperature difference between the inlet and outlet temperature

5.2.3. Results and discussion

The analysis on the heat transfer enhancement of the nanofluids was done through the local heat transfer coefficient ratio between the nanofluid and the base fluid (Figs. 5.2.5 – 5.2.13). The Al_2O_3 nanofluids with three different diameters of the particles ($d_p = 13, 28$ and 47 nm) and various concentrations $\phi = 1 - 9$ % were used considering the limits established for the relations of the viscosity and thermal conductivity validated by the experimental results. The comparison of the heat transfer results is made on a basis of the fixed pumping power ($\Pi = 0.1$ and 1).

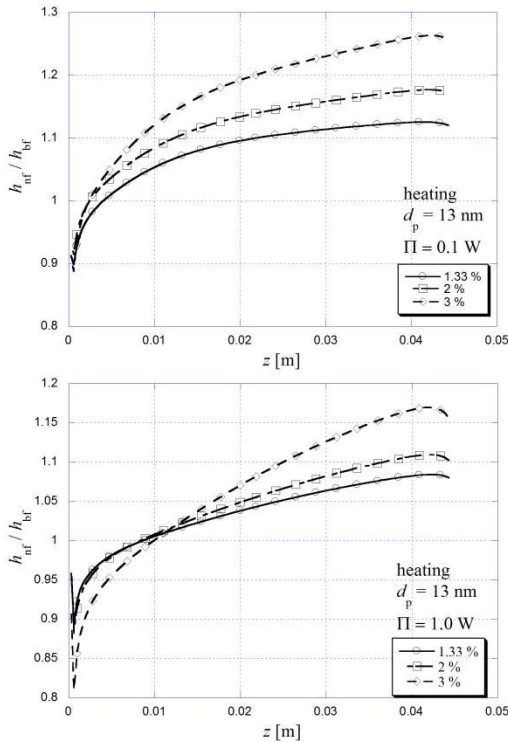


Fig. 5.2.5 The local heat transfer enhancement for the heating case and $d_p = 13$ nm

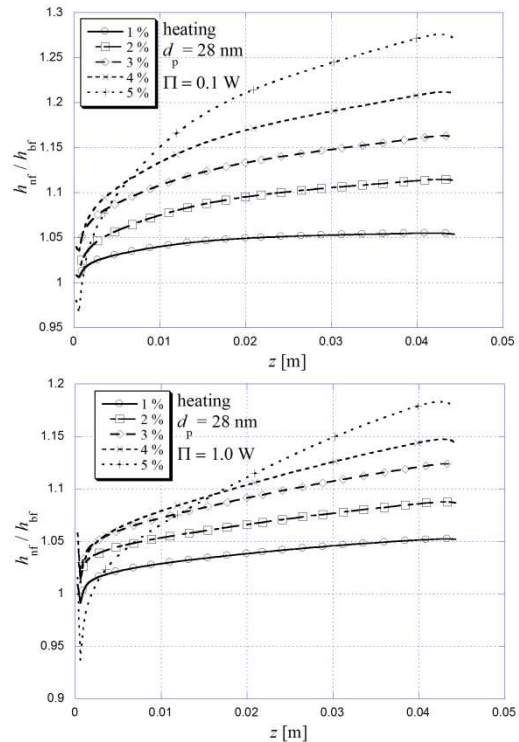


Fig. 5.2.6 The local heat transfer enhancement for the heating case and $d_p = 28$ nm

For the heating case of the nanofluids with $d_p = 13$ nm (Fig. 5.2.5) the general trend shows the increasing of the heat transfer enhancement along the microchannel. This is in the contradiction with the observations obtained for the cases where the analysis is made on a basis of constant Re [124,126]. If the results obtained for the local heat transfer coefficients are compared on a fixed Re basis, the enhancement is higher in the entrance region and decreasing toward the channel outlet.

Moreover as the pumping power is low the increasing in particles concentration results in higher heat transfer enhancement. The maximum heat transfer enhancement is near the outlet cross-section, about 27 % for $\phi = 3$ %. For nanofluids with low concentrations $\phi = 1.33$ % the heat transfer augmentation is slightly over 10 %. Also if one compares the heat transfer results for two different pumping powers it is obvious that heat transfer enhancement is higher for lower pumping powers. Moreover in the case of $\Pi = 1.0$ W the nanofluid with $\phi = 3$ % has the lower heat transfer characteristics compared with nanofluids with $\phi = 1.33$ and 2 %, as long as axial distance is lower than $z = 0.01$ m.

The similar conclusions are valid for nanofluids with $d_p = 28$ nm (Fig. 5.2.6) and five different concentrations. In this case the heat transfer enhancements are more flattened

compared with nanofluids with $d_p = 13$ nm as the concentrations are small. For example for nanofluids with $\phi = 1\%$ the heat transfer ratio is 1.05 and constant for almost entire length of the microchannels. On the other hand when the concentration of the particles is $\phi = 5\%$ the heat transfer enhancement is superior as the axial distance is over $z = 0.015$ m.

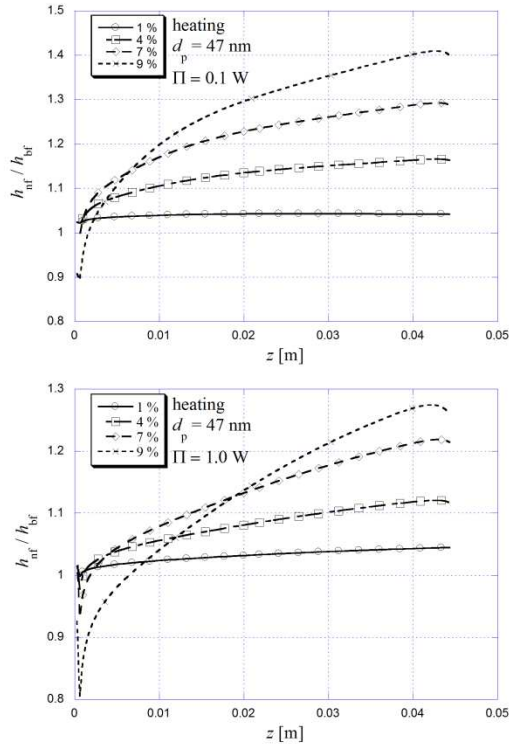


Fig. 5.2.7 The local heat transfer enhancement for the heating case and $d_p = 47$ nm

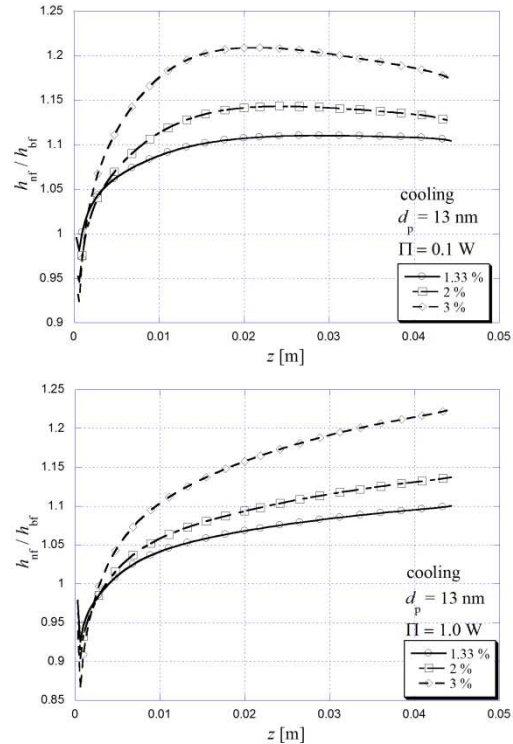


Fig. 5.2.8 The local heat transfer enhancement for the cooling case and $d_p = 13$ nm

In the Fig. 5.2.7 the local heat transfer behavior is presented for the nanofluids with $d_p = 47$ nm and four different concentrations of the nanoparticle. Once again the increasing trend of the heat transfer ratio along the microchannel is observed with limits between 5 and 40%. For higher pumping power the nanofluid with $\phi = 9\%$ has the best thermal characteristics as the axial distance is larger than $z = 0.02$ m.

Fig. 5.2.8 presents the local heat transfer results for $d_p = 13$ nm and cooling of the fluid. The similar heat transfer behavior is observed as for the heating case. The heat transfer enhancement is increasing as the concentration of the particles is increasing. For particle concentration of $\phi = 1.33\%$ the heat transfer coefficient ratio initially increases, attains maximum at 21% over the value for water and decreases after that. The reason for decreases of the heat transfer coefficient lies in a temperature dependent viscosity. In the case of Al_2O_3 nanofluid with $\phi = 3\%$ the viscosity is almost 2.6 times higher than a viscosity of the water. So as the fluid is cooled the viscosity near the wall is decreasing that results in the lower velocities and implicit in the lower heat transfer coefficients. This phenomena is considerable in the second half of the microchannel.

The heat transfer results for cooling of the nanofluid with $d_p = 28$ nm are presented in the Fig. 5.2.9. It is interesting that nanofluid with highest particle's concentration and higher pumping power, has the best characteristics only in the second half of the tube. Once again for lower pumping power and higher concentration the heat transfer ratio is decreasing after $z = 0.02$ m.

Fig. 5.2.10 presents the heat transfer results for nanofluid with $d_p = 47$ nm. For low pumping power and higher particle's concentration $\phi = 9$ % the heat transfer ratio decreases for 5 % in the second half of the tube.

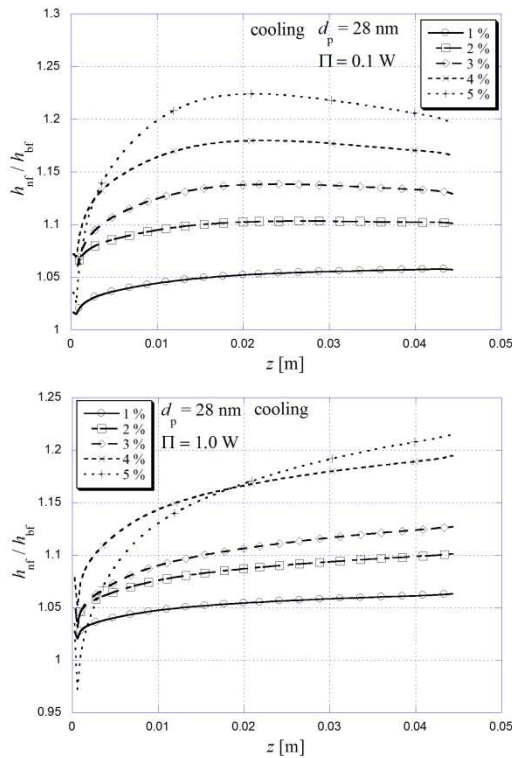


Fig. 5.2.9 The local heat transfer enhancement for the cooling case and $d_p = 28$ nm

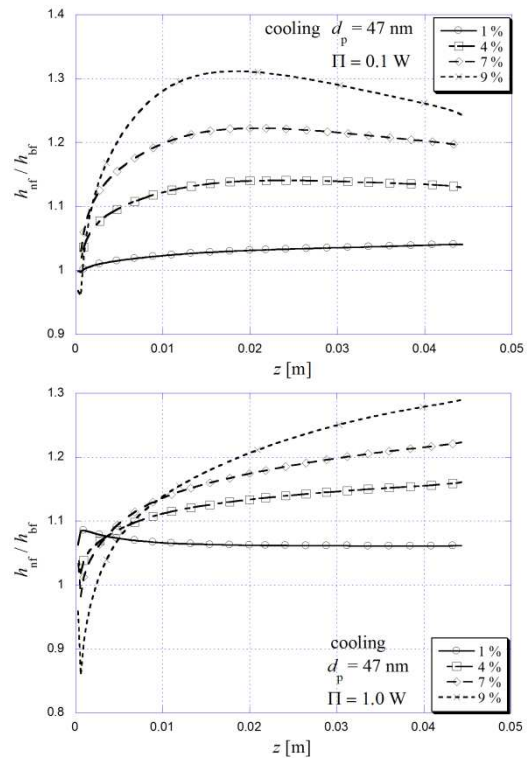


Fig. 5.2.10 The local heat transfer enhancement for the cooling case and $d_p = 47$ nm

Figs. 5.2.11 and 5.2.12 present analysis on heat transfer enhancement versus diameter of the particles for pumping powers $\Pi = 0.1$ and 1.0 W, $\phi = 1$ and 3 % and an axial position near the exit of the microchannel ($z = 0.04$ m). For the heating cases the heat transfer ratio is decreasing as the diameter of the particle increases. In the case of cooling this conclusion is still valid for lower pumping power $\Pi = 0.1$ W. If the pumping power is increasing to $\Pi = 1$ W, the heat transfer ratio remains constant for $d_p > 28$ nm. Moreover for $\Pi = 0.1$ W and $\phi = 1$ % the relations for heating and cooling case are almost overlapping so the heat transfer enhancement is not affected by the heat transfer rate direction regardless of the particle's diameter. Also for $\Pi = 1$ W and $\phi = 3$ % if the particles diameter is $d_p = 28$ nm the heat transfer ratio is the same for the heating and cooling cases.

The ratio between the local heat transfer coefficient with viscous heating effect and without this effect for $d_p = 47$ nm and $\phi = 9$ % is presented in the Fig. 5.2.13. For low pumping power $\Pi = 0.1$ W ($Re=107$, $Br=0.005$ for heating and $Re=169$, $Br=-0.005$ for cooling) the influence of the viscous heating is weak. However for a higher pumping power $\Pi = 1$ W ($Re=327$, $Br=0.05$ for heating and $Re=446$, $Br=-0.05$ for cooling) deviation is about 30 % for cooling and 20 % for heating if the viscous dissipation effect is not considered. In addition if the nanofluid is heated the heat transfer coefficient is overestimated if the viscous heating effect is not taking into account. Contrary for a cooling case it is underestimated. The explanation lies in the temperature difference between the wall and bulk temperature of the fluid due to the viscous dissipation effects.

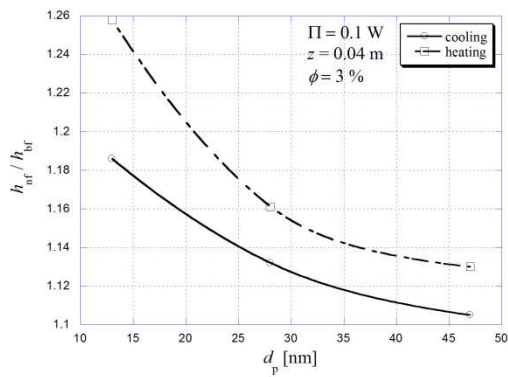
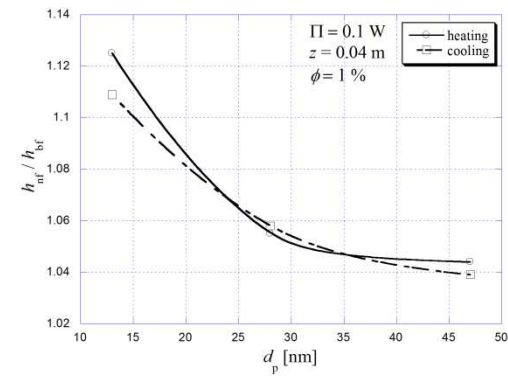


Fig. 5.2.11 The heat transfer enhancement versus particle's diameter for $\phi = 1$ and 3 %, $\Pi = 0.1$ W and $z = 0.04$ m

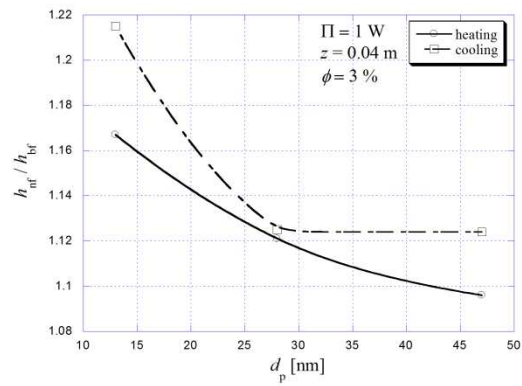
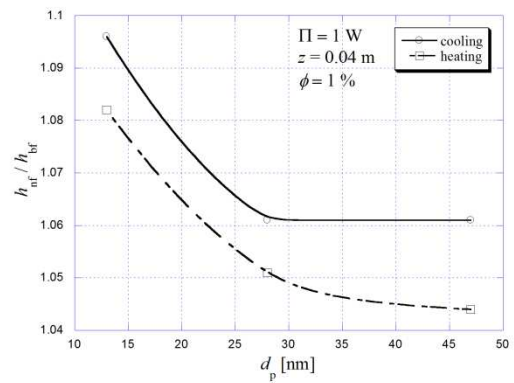


Fig. 5.2.12 The heat transfer enhancement versus particle's diameter for $\phi = 1$ and 3 %, $\Pi = 1$ W and $z = 0.04$ m

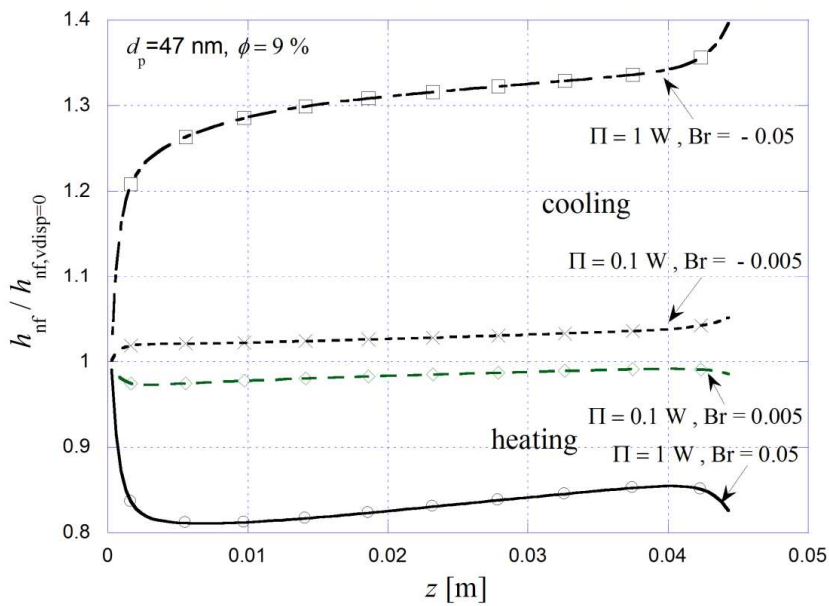


Fig. 5.2.13 The ratio between the heat transfer coefficient with and without viscous heating effect

5.2.4. Conclusions

Numerical modeling on heat transfer and fluid flow of the water based Al_2O_3 nanofluid through the microchannel heat sink is performed. The analysis is made on a basis of the constant pumping power and emphasizes the influence of the viscous heating on the heat transfer enhancement. The following conclusions are outlined:

- The homogenous model used for numerical prediction of the heat transfer and fluid flow through microchannels, along with the two relations for viscosity [132,140] and one for thermal conductivity [139], gives the acceptable deviation compared with experimental results.
- Contrary to the analysis based on a $\text{Re} = \text{const}$ basis, in this case the heat transfer enhancement rises along the microchannels. Also the heat transfer augmentation increases as the particle's concentration increases.
- Moreover heat transfer enhancement is higher for the heating case than for cooling if the pumping power is low. For the higher pumping powers the heat transfer enhancement is higher if the nanofluid is cooled. It is also observed that in some circumstances of cooling, the local heat transfer augmentation decreases along the second half of the microchannel.
- Heat transfer augmentation decreases as the particle's diameter increases. For higher pumping power and cooling case it remains constant as long as particle's diameter is $d_p > 28 \text{ nm}$.
- If the viscous heating effect is not considered the heat transfer coefficient of the nanofluid ($d_p = 47 \text{ nm}$ and $\phi = 9 \%$) is underestimated for 30 % in the case of cooling and overestimated for 20 % for the heating case.

6. The thermal and hydrodynamic analysis of the extended surfaces used for compact heat exchangers

It is known that convective heat transfer enhancement could be obtained both through additional heat transfer surface and by interrupting the heat transfer area in the streamwise direction which will cause the interruption of the heat transfer boundary layer. There is a great number of reports that analyze this topic for various types of channels and tubes. The heat transfer fluid flow is influenced by various parameters such as the number and height of the fins, fluid flow regime, and fluid type. Although most of the papers deal with fins of constant height, there are some reports that analyze the influence of interrupting heat transfer surface both on the heat transfer and fluid flow characteristics. For example, three dimensional heat transfer fluid flow through the tubes with the fins interrupted in the streamwise direction was analyzed by Kelkar and Patankar [146]. The fins with two different geometry arrangements are considered, in line and staggered together, with different length and number of fins. It is observed that the heat transfer results for the in line arrangements of the fins are similar to those of the staggered ones, but the pressure drop is lower for the in line arrangement. It is also observed that in some cases heat transfer augmentation is lower for these two kinds of arrangements compared with the continuous fins of the same height. In this paper the analysis of the laminar heat transfer fluid flow through channels with trapezoidal fins of periodically varying cross-section in the streamwise direction is presented. The fins are also inclined to the base surface. After a finite initial length, periodically fully developed behavior of the heat transfer fluid flow is obtained.

6.1 Problem Description

The airside of the compact heat exchanger is presented in Fig. 6.1. The fins are located both on the upper and lower side of the channel. They are inclined to the base surface with in line position. The number of fins is large perpendicular to the flow direction. Therefore it is sufficient to take into consideration only one line of fins presented in Fig. 6.2. Obviously, the test section has a finite number of successive fins in the flow direction. If the thickness of the fins is small, the fluid flow can be considered as parabolical in the streamwise direction. In other words, the calculations are performed downstream until the periodically fully developed conditions are attained. From Fig. 6.2 it is clear that the problem is plane-symmetrical with reference to the centerline between two rows of fins. In Fig. 6.3 one can observe that the inclined position of the fins defines a cyclic conditions on the left and right boundaries of the test section (X^- and X^+), with zero fluxes on the upper boundary (Y^+) as a result of the plane-symmetrical definition of the problem. The thermal boundary conditions on the solid surfaces of the channel walls and fins are those corresponding to the constant temperature, which means that the fins are made from a high conductivity material. The inclined fin surface is adjusted as a stepped boundary with very high values of the viscosity and material thermal conductivity.

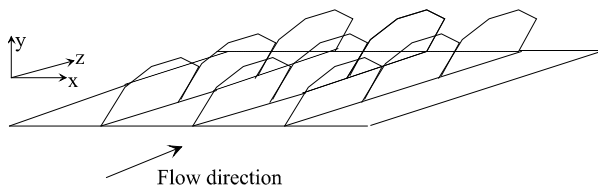


Fig. 6.1 The position of the fins on the airside of the heat exchanger

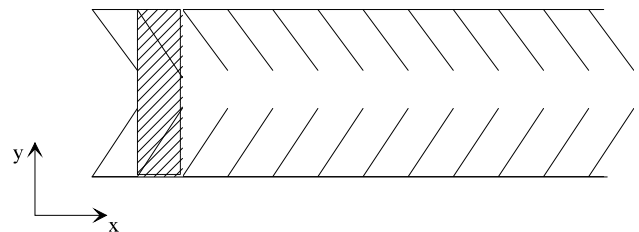


Fig. 6.2 The domain cross-section

The same model, with stepped boundary, was applied for a varying shape of the trapezoidal fin in the streamwise direction. This means that the heat fluid flow has three parts. The first part, where each successive cross-section has one more solid cell, the second part with constant height of the fin and a third part where number of solid cells is decreasing. Successive cross-sections for the first part of the fin with the simplified grid are presented in Fig. 6.4.

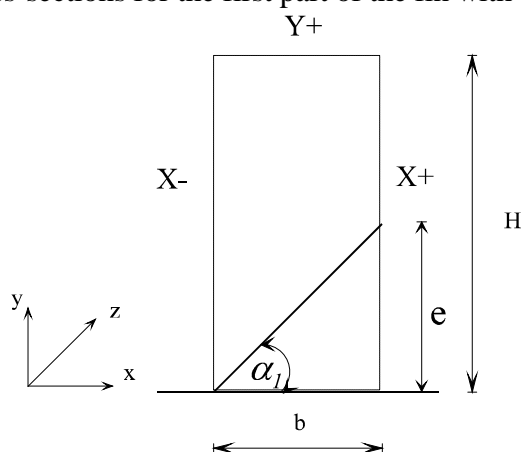


Fig. 6.3 The domain cross-section geometry

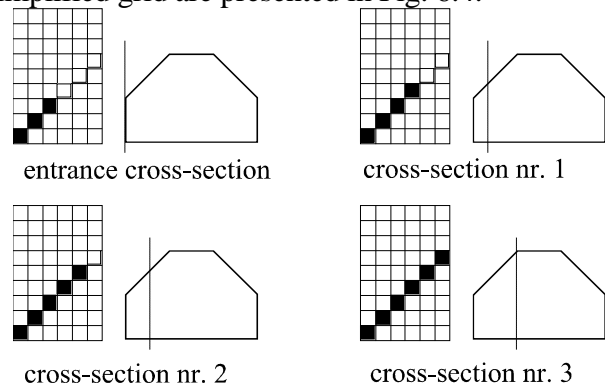


Fig. 6.4 Grid domain for successive cross-section in the flow direction

The marching technique applied to this parabolic flow employs the constant mass flow rate from the inlet of the channel and in each successive cross-section. In the case of the second part of the fin, of constant height, the same number of solid cells is considered in each cross

section and the mass rate conservation is verified. In the third part the gain of the mass flow rate obtained through the ‘loss’ of solid cells in each successive cross-section is balanced through the cross-section velocities (u and v) of the appropriate cell. The problem can appear in the first part, where a loss of the mass flow rate, caused by the new solid cell, could not be anymore recuperated by the cross-section velocities because of their zero values on the side walls of the solid cells. Therefore, only for this part of the fin, cross-section velocities of the new solid cell are left to their non-zero values, resulting from the mass conservation for the whole cross-section, with no axial flow through this new solid cell. In this way, the momentum transferred from the upstream cross-section is dispersed in the current cross-section through the cross-section velocities and the mass conservation of the cross-section is satisfied. For a stationary laminar parabolic heat transfer fluid flow with constant fluid properties, the following well-known system of partial differential equations can be applied:

- continuity equation:

$$\frac{\partial U}{\partial X} + \frac{\partial V}{\partial Y} + \frac{\partial W}{\partial Z} = 0 \quad (6.1)$$

- Navier - Stokes equations:

- x direction:

$$U \frac{\partial U}{\partial X} + V \frac{\partial U}{\partial Y} + W \frac{\partial U}{\partial Z} = -\frac{\partial P}{\partial X} + \frac{\partial^2 U}{\partial X^2} + \frac{\partial^2 U}{\partial Y^2} \quad (6.2)$$

- y direction:

$$U \frac{\partial V}{\partial X} + V \frac{\partial V}{\partial Y} + W \frac{\partial V}{\partial Z} = -\frac{\partial P}{\partial Y} + \frac{\partial^2 V}{\partial X^2} + \frac{\partial^2 V}{\partial Y^2} \quad (6.3)$$

- z direction:

$$U \frac{\partial W}{\partial X} + V \frac{\partial W}{\partial Y} + W \frac{\partial W}{\partial Z} = -\frac{d\bar{P}}{dZ} + \frac{\partial^2 W}{\partial X^2} + \frac{\partial^2 W}{\partial Y^2} \quad (6.4)$$

- energy conservation equation:

$$U \frac{\partial \theta}{\partial X} + V \frac{\partial \theta}{\partial Y} + W \frac{\partial \theta}{\partial Z} = \frac{1}{Pr} \left(\frac{\partial^2 \theta}{\partial X^2} + \frac{\partial^2 \theta}{\partial Y^2} \right) \quad (6.5)$$

- with non-dimensional variables:

$$X = \frac{x}{b}; Y = \frac{y}{b}; Z = \frac{z}{b \cdot Re}; Re = \frac{w_{in} \cdot b}{\nu}$$

$$V = \frac{v \cdot b}{\nu}; U = \frac{u \cdot b}{\nu}; W = \frac{w}{w_{in}}; \bar{P} = \frac{\bar{p}}{\rho \cdot w_{in}^2}; P = \frac{p \cdot b^2}{\rho \cdot \nu^2}; \theta = \frac{t - t_{in}}{t_w - t_{in}} \quad (6.6)$$

The boundary conditions for the system of partial differential equations are as follows: for solid surfaces:

$$U = V = W = 0 \quad (0 < Z \leq Z_{out})$$

$$\theta = 1; \quad (0 < Z \leq Z_{out})$$

at the entrance of the channel:

$$W = 1; U = V = 0 \quad (Z = 0)$$

$$\theta = 0 \quad (Z = 0).$$

6.2 Numerical Details

The system of parabolic partial differential equations is solved using the procedure explained in [18,147]. The velocity-pressure coupling is solved using a SIMPLER method. A staggered grid is used for cross-stream velocities with power-law discretization scheme. Due to

the specific geometry resulting from the inclined position of the fins, TDMA-cycle algorithm is used to solve the velocity, pressure and temperature fields. The fluid type used for calculations was air with $Pr = 0.7$. Numerical runs were performed downstream until periodically fully developed conditions are attained.

The numerical runs were performed for two values of the parameter $B = (L/b)/Re$, 10^{-1} and 10^{-2} . These two values of parameter B are chosen in order to ensure the laminar fluid flow regime. All numerical runs were made for constant channel geometry, $H/b = 1.5$; $e/b = 1$; $s_1 = s_2 = s_3$; $e_1 = e_2$ and $\alpha_1 = \alpha_2 = 45^\circ$ as presented in the Fig. 6.6. To compare these type of interrupted fins, two kinds of inclined continuous fins were considered, with height equal to the non-interrupted surface of the trapezoidal fin ($e/b = 0.5$) and equal to the full length of the trapezoidal fin ($e/b = 1$).

After the exploratory runs, a 20×30 ($X \times Y$) grid is used with 30 axial steps. The results obtained for the finer grid, of 39×26 and 39 axial steps, for the case of the trapezoidal fins with $B = 10^{-1}$, show satisfactory differences, less than 1%. The results for two different grids are presented in the table 1. For these two grids, the local variations of the fRe versus non-dimensional axial distance is presented in the Fig. 6.5. Again there is no evidence on differences between the obtained results for these two grids.

Table 1 Periodically fully developed friction factor fRe and Nu number for trapezoidal fin with the $B = 10^{-1}$ and for two different grids

Grid size	Nu - number	fRe
30x20x30	37.665	541.224
39x26x39	37.623	536.385

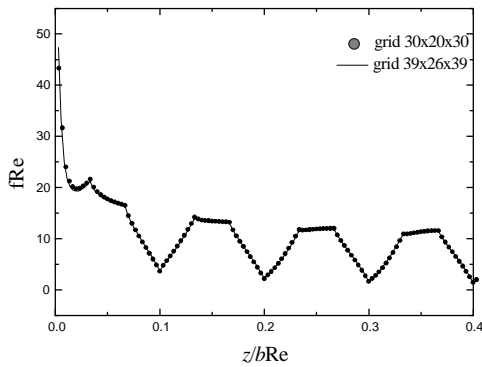


Fig. 6.5 The local values of the fRe versus non-dimensional axial distance for two different grids

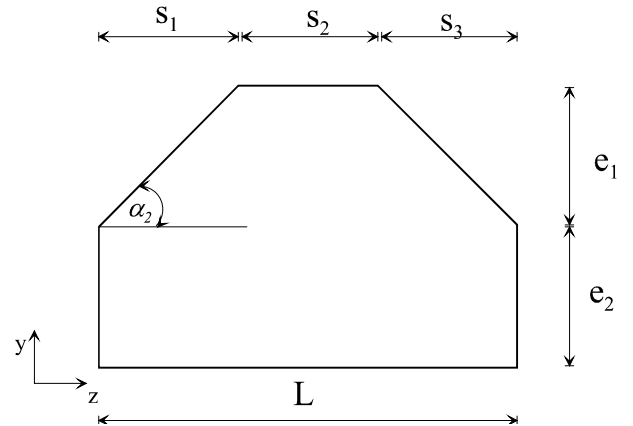


Fig. 6.6 Trapezoidal fin

6.3. Thermal and Hydrodynamic Characteristics

The thermal characteristics are expressed by the Nu - number, based on the calculated temperature field with the following formula:

$$Nu = \frac{h \cdot b}{k} \tag{6.7}$$

where h is calculated with:

$$h = \frac{Q}{A \cdot \Delta t_{log}} \tag{6.8}$$

where A is the heat transfer area based on the channel wall and Δt_{log} is the log mean temperature difference, defined as:

$$\Delta t_{log} = \frac{(t_w - t_{bin}) - (t_w - t_{bout})}{\log \frac{t_w - t_{bin}}{t_w - t_{bout}}} \quad (6.9)$$

where t_{bin} and t_{bout} are bulk temperatures at the inlet and outlet of each successive fins, the bulk temperature being defined as:

$$t_b = \frac{\int wtdA}{\int_A w dA} \quad (6.10)$$

The hydrodynamic characteristics are expressed by the fin average friction factor:

$$f = \frac{(\Delta p / L) \cdot b}{\rho \cdot w_{in}^2 / 2} \quad (6.11)$$

6.4. Hydrodynamic Results

The fin averaged values of the friction factor were compared with the values of the friction factor for a smooth channel without fins, $fRe_0 = 96$. The ratio fRe/fRe_0 versus the number of fins are presented in Fig. 7. It is observed that the highest pressure drop is obtained for a continuous fin with $e/b = 1$, followed by the trapezoidal fin with $B = 10^{-2}$, trapezoidal fin with $B = 10^{-1}$ and finally continuous fin with $e/b = 0.5$. For example, the friction factor for the channel with longer continuous fin is 8 times greater than friction factor for the bare channel, while friction factor for the shorter continuous fin is only 2 times greater than the friction factor for the bare channel. The periodically fully developed values of the friction factor for interrupted fins, as well as fully developed values of the friction factor for the continuous fins are presented in Table 2.

Table 2 Fully developed and periodically fully developed friction factor

	bare channel	trapezoidal fin with $B = 10^{-1}$	trapezoidal fin with $B = 10^{-2}$	continuous fin with $e/b = 0.5$	continuous fin with $e/b = 1.0$
fRe	96	541.224	614.88	200.376	764.64

6.5. Thermal Results

The analysis regarding the thermal characteristics is based on calculated values of Nu - number. Once again Nu-number values of the finned channels are compared to those without fins as Nu/Nu_0 ratio. Nusselt number for the bare channel is $Nu_0 = 7.54$. In Fig. 6.8 Nu/Nu_0 ratio versus number of fins is presented. It is observed that the best heat transfer performances have the channel with continuous fins with $e/b = 1$ where heat transfer augmentation is 6 times, followed by trapezoidal fins with augmentation of 5.3 for $B = 10^{-2}$ and 5 times for $B = 10^{-1}$ and finally continuous fins with $e/b = 0.5$ where Nu number is 2.7 times greater than Nu number for the bare channel. It is clear that the heat transfer area provided by longer continuous fins contribute much more to the heat transfer phenomena than interrupting the thermal boundary layer made by trapezoidal fins for parameter values B taking into account in this paper. In Table 3 the fully developed and periodically fully developed values for finned surfaces are presented.

Table 3 Fully developed and periodically fully developed Nu number

	bare channel	trapezoidal fin with $B = 10^{-1}$	trapezoidal fin with $B = 10^{-2}$	continuous fin with $e/b = 0.5$	continuous fin with $e/b = 1.0$
Nu	7.54	37.665	40.32	20.592	45.0

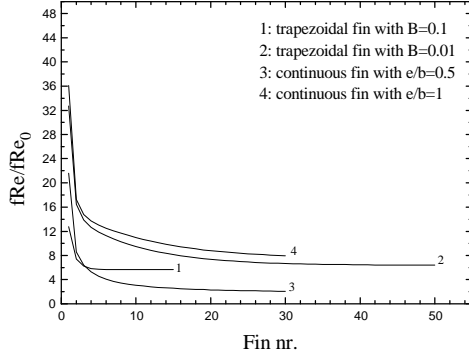


Fig. 6.7 Friction factor ratio versus fin number for four fin types

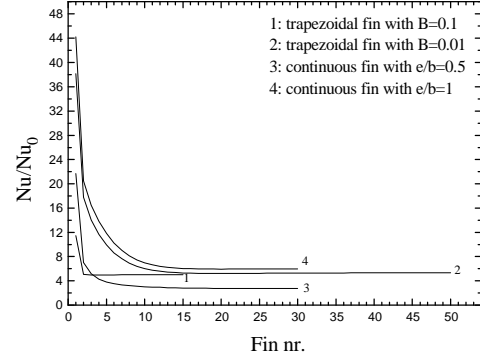


Fig. 6.8 Nu number ratio versus number fin number for four fin types

6.6. Performance Evaluation

For a better understanding of the performances of each heat transfer surface it is useful to make the evaluation analysis based on a same pumping power and heat exchanger size. In other words we are interested in the increase in heat transfer rate in comparison to the bare channel for fixed fluid pumping power and heat exchanger volume. The pumping power is calculated with the following equation:

$$\Pi = \frac{\dot{M}}{\rho} \Delta p \quad (6.12)$$

where \dot{M} is mass flow rate, fixed for each cross section and defined as:

$$\dot{M} = \rho \cdot S \cdot w_{in} \quad (6.13)$$

The heat rate is defined with a following equation:

$$Q = \dot{M} \cdot c_p \cdot (t_b - t_{in}) \quad (6.14)$$

where t_b is the cross section bulk temperature. From equations (6.12) and (6.13) and taking into account Re number the pumping power can be written as:

$$\Pi = \left(\frac{1}{2} \frac{\mu^3 H}{\rho^2 b^2} \right) \cdot \frac{\Delta p}{\rho w_{in}^2 / 2} \cdot \text{Re}^3 \quad (6.15)$$

Finally the heat rate ratio of the finned and bare channel can be written as:

$$\frac{Q}{Q_0} = \frac{(\text{Re} \cdot \theta)_{fin}}{(\text{Re} \cdot \theta)_0} \quad (6.16)$$

The procedure for obtaining the heat rate ratio defined by equation (6.16) is presented in [148]. Therefore here will be briefly described only some of the aspects. Based on the selected Re - number, the ratio $L_{ex}/b\text{Re}$ is calculated. For this value and selected parameter $B=L/b\text{Re}$ the pressure drop $\Delta p/(\rho w_{in}^2/2)$ and pumping power $\Delta p/(\rho w_{in}^2/2) \cdot \text{Re}^3$ for the finned surface are obtained. Based on this latter value the Re_0 number for the parallel plate channel is determined

for which the pumping power is the same. Finally, with this Re_0 number, the temperature difference θ is obtained. The heat rate augmentation versus Re number for two different heat exchanger lengths, $L_{ex}= 30$ and 50 , and for Re number range $100 < Re < 1000$, is presented in Figs. 6.9 and 6.10. Inspecting the graphics, several conclusions can be outlined. Again the longer continuous fins has higher heat rate ratio, about 4.5 times for shorter heat exchangers and 4 times for longer ones. At the same time trapezoidal fins have the same performances regardless the parameter B values, for both exchanger lengths, except for shorter heat exchanger when $Re > 500$. The smallest heat transfer augmentation is observed for continuous fins with $e/b = 0.5$, with 2 respectively 2.5 times augmentation. Similar trend was observed in [146] for staggered and continuous fins in the case of the $Pr=0.7$. The explanation lies in the fact that the entrance length is shorter for the low viscosity fluids and consequently interrupting the boundary layer is less beneficial for the heat transfer augmentation.

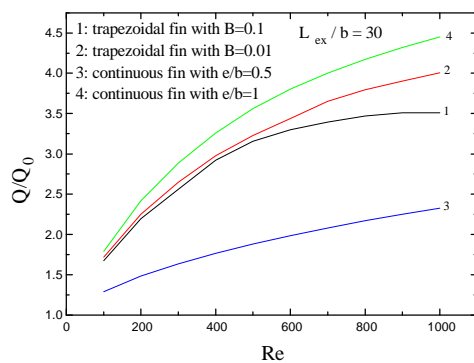


Fig. 6.9 Heat rate augmentation versus Re number for the exchanger length $L_{ex}/b = 30$

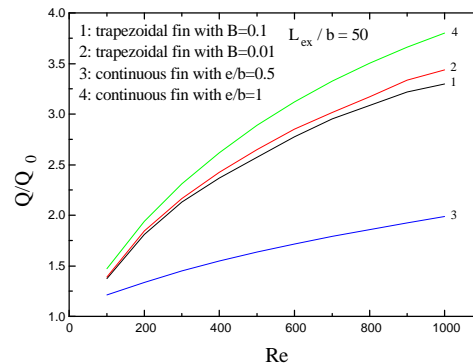


Fig. 6.10 Heat rate augmentation versus Re number for the exchanger length $L_{ex}/b = 50$

6.7. Conclusions

The heat transfer fluid flow through channels with trapezoidal and continuous fins are presented. The parabolic regime procedure is applied with slightly different approach of cross section velocity field caused by the applied stepped boundary in the streamwise direction. Several conclusions can be outlined:

- greater heat transfer area provided by continuous fins of same height as trapezoidal fins, determines better heat transfer performances rather than interrupted thermal boundary layers made by interrupted surfaces. At the same time the pressure drop is greater for continuous fins of the same height as trapezoidal fins;
- based on the evaluation analysis for fixed pumping power and same heat exchanger volume, again heat rate augmentation is greater for continuous fins with $e/b = 1$ followed by trapezoidal fins and continuous fins of $e/b = 0.5$;
- greater heat rate improvement is observed for the shorter heat exchangers.

Professional development plan

1. Research activities of the mixing phenomena in microchannels

Micromixer is the most important component in microfluidic systems. They can be classified into two main types: active and passive ones. Each type has its specific mixing concepts, capacity, mixing speed, and operating conditions. Generally, two steps occur in the mixing process in these micromixers: heterogeneous mixing created by convection, and homogeneous mixing at the molecular level caused by diffusion between adjacent domains [149].

In the process industry, the concept of micro-technology aims at miniaturization of process devices as well as integration of reaction and unit operation elements to save space and energy. The increasing demands of process industry, pharmacy, analysis and biochemistry, for novel and effective mixing technologies as well as the smooth execution of highly exothermic or explosive chemical reactions have led to the intensive development of the microfluidic systems. The small dimensions allow rapid diffusive mixing to occur in as little as 100 μs . These lamellar systems achieve surface-to-volume ratios of $30000 \text{ m}^2 \cdot \text{m}^{-3}$, compared to batch reactors with typical surface-to-volume ratios of $4 \text{ m}^2 \cdot \text{m}^{-3}$. Therefore the understanding of the flow and mixing behavior in microscale devices such as microreactors and mixers is critical to their effective design and optimization [150].

Although the processes of design and fabrication of passive systems are generally known to be simpler than those of active ones, the flow control is a critical problem in these systems [151]. Therefore, the optimum design of passive mixing systems is very important and needs a preprocessing step, such as mathematical simulation [152,153,154]. In a passive mixing, the flow stream is controlled by adjusting its dimensions, such as the height, length and width, because of the absence of any external power resource. Thus, careful consideration of the design of the micro-channels and obstructions is essential to raise the passive mixing performance. Mixing in passive mixers usually is induced by driving fluids through channels with cleaved geometries. Repeated lamination and splitting of flows in microfluidic channels were used to increase interfacial area and thus mixing quality [155,156,157,158,159,160]. An alternative way is to make use of chaos, because chaotic fluid path lines can disperse fluid species effectively, even in smooth and regular flow fields [161,162,163,164,165]. Cha et al. [166] reported a novel micromixer, named a chessboard mixer, to expand interfaces between mixing fluids. Circular micromixers are another type of multi-lamination mixers, which utilizes self-rotation of the sample fluids from multiple injection channels to produce three-dimensional vortices in the circular mixing chamber at low Re [167]. Chung et al. [168], Sundaram and Tafti [169] also proposed a passive micromixer utilizing self circulation of the fluid in the mixing chamber. Lin et al. [170] proposed a novel three-dimensional vortex micromixer which also utilizes self-rotation effects to mix fluids in a circular chamber at low Re . Swirling mixing was analyzed by Neilda et al. [171] while 3-D vortex mixing was reported by Lin et al. [172]. Systematic investigation on T- mixers has been presented by Hoffmann et al. [173]. To enhance the performance in Y-mixers, Yi and Bau [174] used a hybrid Y- mixer with a 90° bend to generate vortices at low Reynolds numbers. A Y-shaped “ μDD ” microfluidic diffusion diluter has been developed by Holden et al. [175], which creates streams with different concentrations. Broboana et al. [176] investigated the unsteady diffusion process in Y-shaped micromixer.

Moreover, the nanofluid passive mixing in microchannels has an immediate application in the area of process industry and Bio-MEMS for nanodrug delivery [177]. For example, hypodermic syringes with a hollow pointed needle have been one of the most commonly used for body fluid extraction, vaccination, and medication devices. It creates fear

of injection-related pain among patients, and there has been increasing concern regarding the transmission of bloodborne pathogens such as HIV and hepatitis.

On the other hand, human skin is composed of three layers: epidermis, dermis, and subcutaneous tissue. The outermost layer of the epidermis is stratum corneum, a layer of dead cells, which is a protective diffusion barrier layer preventing the loss of body fluids and blocking the entry of external materials into the body. Sensory fibers in the cutaneous nerves detect external stimuli such as temperature, pressure, and those causing pain, and generate signals that are relayed through a nerve pathway to the brain. The pain associated with an injection using a hypodermic syringe is because the needle is large and penetrates deep into the skin with excessive contact with these sensory fibers.

With advances in MEMS technology, it is possible to make microneedles that are long enough to penetrate the epidermis, but short enough not to penetrate deep into the dermis layer and subcutaneous tissue for minimally invasive trans-dermal drug delivery and body fluid sampling. Moreover, microneedles and microneedle arrays can be used as stand-alone devices as well as a part of more sophisticated smart biological detection and delivery systems in which microneedles are integrated with microfluidics and biosensors or microelectronics. Clinically useful drug delivery systems need to deliver a certain amount of a drug that can be therapeutically effective, and often over an extended period of time. Such requirements can be met by the micro scale drug delivery systems. Moreover, microfluidics of nanodrug delivery was analyzed by Li and Kleinstreuer [178] and Kleinstreuer et al. [179].

Considering the analysis presented in the previous chapters the following topics are proposed for analysis:

- nanofluid or nanoparticle mixing in microchannels;
- the thermal influence on mixing phenomena in microchannels;
- based on a fundamental research on the issues mentioned previously, the new concept of bio-MEMS for passive mixing will be developed based on a swirl fluid motion in the circular micromixer;

Besides, due to the numerical difficulties related to the so-called false or numerical diffusion, the special attention will be paid to minimize it by choosing the appropriate higher order numerical discretization schemes, suitable flow oriented mesh and comparing with available experimental results.

First of all the proposed research will try to fill the gaps in the microchannel fluid flow and heat transfer with aspects related to the nanofluid flow, swirling nanofluid motion and nanofluid mixing. Analyzing the existing and accessible literature one can conclude that these phenomena are barely attacked so the primarily goal will be to increase the fundamental understanding and knowledge of these processes.

2. Developing of the laboratory for experimental research on microscale devices

One of the issues that is proposed to be developed is related to development of the facility and laboratory for experimental research on heat transfer and fluid flow in microscale. The experimental setup is basically the same as that proposed in the chapter 1 (Figs. 1.1 and 1.2) and used in the research performed at the University of Tokyo Institute of Industrial Science. The followings are some of the topics that are proposed to be analyzed:

- The single-phase heat transfer and fluid flow in tangential microchannel heat sinks;
- The two-phase heat transfer and fluid flow in tangential microchannel heat sinks;
- The nanofluid flow and heat transfer in microchannel heat sinks of various flow configurations;

3. The numerical analysis of the nanofluid flow in microchannel heat sinks

In the case of the nanofluid flow in the microchannels a single-phase and two-phase approach might be applied. The single-phase (homogenous) approach assumes that fluid phase and particles are in thermal equilibrium and move with the same velocity considering the effective fluid properties. The two phase approach considers each phase separately. The first approach was applied by Lelea & Nisulescu [145] and Lelea [180] for microchannel heat transfer and fluid flow with reasonable deviation from experimental results. Despite these findings the two-phase approach will be applied and compared especially in context of swirling motion in the microchannels.

4. The further development of the laboratory for numerical analysis in thermal engineering

The most of the topics presented in the chapters 2 – 6 are made in the laboratory for numerical simulations in thermal engineering (<http://ldorin.byethost9.com/>). The research proposed in chapter 1 related to the mixing phenomena in microchannels, will be initially developed in this lab. In addition, the numerical analysis in the field of nanofluid swirling flow will be made. Moreover, the physical infrastructure will be constantly improved in order to fulfill the conditions for some complex simulations.

5. The plan for educational development

The experience gained through the research on microchannel heat transfer was partially included in the lectures at the graduate and undergraduate levels (Numerical methods in thermal engineering, Design of thermal systems). Moreover, in some of the laboratory works the numerical modeling of the thermal phenomena in microscale devices are treated. It is intended to constantly improve the lectures with the new findings in the areas described above.

Besides, if the experimental laboratory for microscale devices will be established, it will be also included in the group of practical applications. In addition, the research team will be extended with graduate students.

6. The probable tools used for professional development

The financial support for the future research topics described above is expecting from the research grants from the National Research Council. Project proposal is already submitted with the topic related to the mixing phenomena in microchannel and it is under evaluation. It has to be stated that more or less, this topic is not dependent of the financial support as the research is proposed to be done with numerical simulations. Moreover, the experimental research on microscale devices with tangential inlet jets is the topic that will be submitted to the next competition for ERC-Grants.

References

- [1] S. Nishio, Attempts to apply micro heat transfer to thermal management - invited lecture, International Conference on Heat Transfer and Transport Phenomena in Microscale, Banff, Canada, (2000), 32 - 40.
- [2] D.R. Reyes, D. Iossifidis, P.A. Auroux, A. Manz, Micro total analysis systems, introduction, theory and technology, *Analytical Chemistry* 74 (12) (2002), 2623 - 2636.
- [3] J. Lee, H. Moon, J. Fowler, C.J. Kim, T. Schoellhammer, Addressable micro liquid handling by electric control of surface tension, The 14th IEEE International Conference on Micro Electro Mechanical Systems 2001, MEMS 2001, (2001) 499 – 502.
- [4] G.P. Celata, M. Cumo, M. Guglielmi, G. Zummo, Experimental investigation of hydraulic and single phase heat transfer in 0.130 mm capillary tube, International Conference on Heat Transfer and Transport Phenomena in Microscale, Banff, Canada, (2000) 108-113.
- [5] A.F. Mills, *Heat Transfer*, Irwin Inc., (1992).
- [6] G.M. Mala, D. Li, C. Werner, H.J. Jacobasch, Y.B. Ning, Flow characteristics of water through a microchannel between two parallel plates with electrokinetic effects, *International Journal of Heat and Fluid Flow*, 18 (5) (1997) 489-496.
- [7] J. Judy, D. Maynes, W.B. Web, Liquid flow pressure drop in microtubes, International Conference on Heat Transfer and Transport Phenomena in Microscale, Banff, Canada, (2000) 149-154.
- [8] Z.X. Li, D.X. Du, Z.Y. Guo, Experimental study on flow characteristics of liquid in circular microtubes, International Conference on Heat Transfer and Transport Phenomena in Microscale, Banff, Canada, (2000) 162-167.
- [9] C.Y. Yang, H.T. Chien, S.R. Lu, R.J. Shyu, Friction characteristics of water, R-134a and air in small tubes, International Conference on Heat Transfer and Transport Phenomena in Microscale, Banff, Canada, (2000) 168-174.
- [10] X.F. Peng, G.P. Peterson, Convective heat transfer and flow friction for water flow in microchannel structures, *International Journal of Heat and Mass Transfer*, 39 (12) (1996) 2599-2608.
- [11] W. Qu, G.M. Mala, D. Li, Heat transfer for water flow in trapezoidal silicon microchannels, *International Journal of Heat and Mass Transfer*, 43 (21) (2000) 3925-3936.
- [12] X.F. Peng, G.P. Peterson, Forced convection heat transfer of single-phase binary mixtures through microchannels, *Experimental Thermal and Fluid Science*, 12 (1) (1996) 98-104.
- [13] X.F. Peng, G.P. Peterson, The effect of thermofluid and geometrical parameters on convection of liquid through conventional micro channel, *International Journal of Heat and Mass Transfer*, 38 (1) (1995) 127-137.
- [14] P. Gao, S. Person, M. Marinnet, Hydrodynamics and heat transfer in a two-dimensional microchannel, Twelfth International Heat Transfer Conference, Grenoble France, August 18-23, 2 (2002) 183-188 .
- [15] B. Agostini, B. Watel, A. Bontemps, B. Thonon, Experimental study of single-phase friction factor and heat transfer coefficient in mini-channels, International Symposium on Compact Heat Exchangers, Grenoble France, August 24, (2002) 110-115.
- [16] Moffat R.J., Using Uncertainty Analysis in the Planning of an Experiment, *Journal of Fluids Engineering*, 107 (1985) 173-179.
- [17] Moffat R.J., Contributions to the Theory of Single – Sample Uncertainty Analysis, *Journal of Fluids Engineering*, 104 (1982) 173 – 179.
- [18] S.V. Patankar, *Numerical Heat Transfer and Fluid Flow*, McGraw Hill, (1980).
- [19] R.K. Shah, A.L. London, *Laminar Flow Forced Convection in Ducts, Advances in Heat Transfer - Supplement 1*, Academic Press, New York (1978).

- [20] S. Nishio, Single-Phase Laminar Flow Heat Transfer and Two-Phase Oscillating Flow, 1st International Conference on Microchannels and Minichannels, Rochester USA (2003). (Proceedings)
- [21] W. Urbanek, J.N. Zemel, H.H. Bau, An investigation of the temperature dependence of Poiseuille numbers in microchannel flow, *J. Micromech. Microeng.* Vol. 3(4), pp.206-209 (1993).
- [22] K.C. Toh, X.Y. Chen, J.C. Chai, Numerical computation of fluid flow and heat transfer in microchannels, *International Journal of Heat and Mass Transfer* 45, pp. 5133 – 5141 (2002).
- [23] J. Judy, D. Maynes, W.B. Webb, Characterization of frictional pressure drop for liquid flows through microchannels, *International Journal of Heat and Mass Transfer* 45, pp. 3477-3489 (2002).
- [24] D. Lelea, S. Nishio, K. Takano The experimental research on microtube heat transfer and fluid flow of distilled water, *International Journal of Heat Mass Transfer* 47 (2004) 2817 - 2830.
- [25] Poiseuille, Recherches experimentales sur la mouvement des liquids dans les tubes de tres petits diametres, *Academie des Sciences, Comptes Rendus* 12, pp. 112-115 (1841). (Report)
- [26] D. B. Tuckerman and R. F. W. Pease. High-Performance Heat Sinking for VLSI, *IEEE Electron.Device Lett.*, vol. EDL-2, pp. 126–129, 1981.
- [27] P. Y. Wu and W. A. Little, Measurement of Friction Factor for the Flow of Gases in Very Fine Channels Used for Micro Miniature Joule Thompson Refrigerators, *Cryogenics* 23 (1983) 273–277.
- [28] P. Y. Wu and W. A. Little, Measurement of the Heat Transfer Characteristics of Gas Flow in Fine Channel Heat Exchangers for Micro Miniature Refrigerators, *Cryogenics* 24 (1984) 415–420.
- [29] S.V. Garimella, C.B. Sobhan, Transport in microchannels – a critical review, *Annual Review of Heat Transfer* 13, (2003) 1–50.
- [30] G. L. Morini, Single-phase convective heat transfer in microchannels: A review of experimental results, *Int. J Thermal Sciences*, 43 (2004), pp. 631—651.
- [31] I.Tiselj, G.Hetsroni, B.Mavko, A.Mosyak, E.Pogrebnyak Z.Segal, Effect of axial conduction on the heat transfer in micro-channels, *International Journal of Heat Mass Transfer* 47 (2004) 2551 - 2565.
- [32] P.S. Lee, S.V. Garimella, D. Liu, Investigation of heat transfer in rectangular microchannels, *International Journal of Heat Mass Transfer* 48 (2005) 1688 - 1704.
- [33] M. Bahrami, M. M. Yovanovich, J. R. Culham, Convective heat transfer of laminar, single-phase flow in randomly rough microtubes, 2005 ASME International Mechanical Engineering Congress Exposition, Nov. 5-11, 2005, Orlando, FL, USA, pp. 1 – 9.
- [34] D. Lelea, Some considerations on frictional losses evaluation of a water flow in microtubes, *International Communications in Heat and Mass Transfer* (2005).
- [35] J. Koo, C. Kleinstreuer, Viscous dissipation effects in microtubes and microchannels, *International Journal of Heat Mass Transfer* 47 (2004) 3159 - 3169.
- [36] G. Maranzana, I. Perry, D. Maillet, Mini- and micro-channels: influence of axial conduction in the walls, *International Journal of Heat Mass Transfer* 47 (2004) 3993 – 4004.
- [37] S. Piva, G. Pagliarini, Experimental investigation on exponential heating of a laminar flow, *Experimental Heat Transfer, Fluid Mechanics and Thermodynamics* (1993) 546 – 552.
- [38] M. Faghri, E.M. Sparrow, Simultaneous wall and fluid axial conduction in laminar pipe-flow heat transfer, *Journal of Heat Transfer* 102 (1980) 58 – 63.
- [39] M.A. Cotton, J.D. Jackson, The effect of heat conduction in a tube wall upon forced convection heat transfer in the thermal entry region, *Numerical Methods in Thermal Problems*, Pineridge Press Vol. IV (1985) 504 – 515.

- [40] J.P. Chiou, The advancement of compact heat exchanger theory considering the effects of longitudinal heat conduction and flow nonuniformity, Symposium on compact heat exchangers – history, technological advancement and mechanical design problems, Book No. G00183, HTD- Vol. 10, ASME, New York (1980).
- [41] J.Li,G.P.Peterson,P.Cheng, Three-dimensional analysis of heat transfer in a micro-heat sink with single phase flow, *International Journal of Heat and Mass Transfer* 47 (2004) 4215 – 4231.
- [42] S.S. Shevade, M.M. Rahman, Heat transfer in rectangular microchannels during volumetric heating of the substrat, *International Communications in Heat and Mass Transfer* 34 (2007) 661-672.
- [43] M.K. Sung, I. Mudawar, Single-phase hybrid micro-channel/micro-jet impingement cooling, *International Journal of Heat and Mass Transfer* 51 (2008) 4342 - 4352.
- [44] P. Naphon, O. Khonseur, Study on the convective heat transfer and pressure drop in the micro-channel heat sink, *International Communications in Heat and Mass Transfer* (2008), doi:10.1016/j.icheatmasstransfer.2008.09.001.
- [45] Y.J. Cheng, Numerical simulation of stacked microchannel heat sink with mixing-enhanced passive structure, *International Communications in Heat and Mass Transfer* 34 (2007) 295–303.
- [46] D. Lelea, The conjugate heat transfer of the partially heated microchannels, *Heat and Mass Transfer* 44 (2007) 33 – 41.
- [47] Y. Mishan, A. Mosyak, E. Pogrebnyak, G. Hetsroni, Effect of developing flow and thermal regime on momentum and heat transfer in micro-scale heat sink, *International Journal of Heat and Mass Transfer* 50 (2007) 3100–3114
- [48] P. Sharath, C. Rao, M. M. Rahman, H. M. Soliman, Numerical Simulation of Steady-State Conjugate Heat Transfer in a Circular Microtube inside a Rectangular Substrate, *Numerical Heat Transfer, Part A: Applications*, 49 (7) (2006) 635 – 654.
- [49] K. K. Ambatipudi, M. M. Rahman, Analysis of Conjugate Heat Transfer in Microchannel Heat Sinks, *Numerical Heat Transfer, Part A: Applications*, 37 (7) (2000) 711 – 731.
- [50] E. Y. K. Ng, S. T. Poh, CFD Analysis of Double-Layer Microchannel Conjugate Parallel Liquid Flows with Electric Double-Layer Effects, *Numerical Heat Transfer, Part A: Applications*, 40 (7) (2001) 735 – 749.
- [51] P.W. Hwang, C.Y. Soong, Investigation of variable-property microchannel flows with electro-thermo-hydrodynamic interactions at constant pressure gradient or constant flow rate, *International Journal of Heat and Mass Transfer* 51 (2008) 210–223.
- [52] H.S. Kou, J.J. Lee, C.W. Chen, Optimum thermal performance of microchannel heat sink by adjusting channel width and height, *International Communications in Heat and Mass Transfer* 35 (2008) 577–582.
- [53] Q.-W. Wang, C.-L. Zhao, M. Zeng, Y.-N. Wu, Numerical Investigation of Rarefied Diatomic Gas Flow and Heat Transfer in a Microchannel Using DSMC with Uniform Heat Flux Boundary Condition—Part II: Applications, *Numerical Heat Transfer, Part B: Fundamentals*, 53 (2) (2008) 174 – 187.
- [54] C. Hong, Y. Asako, Heat Transfer Characteristics of Gaseous Flows in a Microchannel and a Microtube with Constant Wall Temperature, *Numerical Heat Transfer, Part A: Applications*, 52 (3) (2007) 219 – 238.
- [55] H. P. Kavehpour, M. Faghri, Y. Asako, Effects of Compressibility and Rarefaction on Gaseous Flows in Microchannels, *Numerical Heat Transfer, Part A: Applications*, 32 (7) (1997) 677 – 696.
- [56] H. Sun, M. Faghri, Effects of Rarefaction and Compressibility of Gaseous Flow in Microchannel using DSMC, *Numerical Heat Transfer, Part A: Applications*, 38 (2) (2000) 153 – 168.

- [57] G.P. Celata, M. Cumo, V. Marconi, S.J. McPhail, G. Zummo, Microtube liquid single-phase heat transfer in laminar flow, *International Journal of Heat and Mass Transfer* 49, (2006), 3538-3546.
- [58] J.T. Liu, X.F. Peng, B.X. Wang, Variable-property effect on liquid flow and heat transfer in microchannels, *Chemical Engineering Journal* 141 (2008) 346–353.
- [59] Y. F. Yap, J. C. Chai, T. N. Wong, N. T. Nguyen, K. C. Toh, H. Y. Zhang, Particle Transport in Microchannels, *Numerical Heat Transfer, Part B: Fundamentals*, 51(2) (2007) 141 – 157.
- [60] S. L. Broderick, B. W. Webb, D. Maynes, Thermally Developing Electro-osmotic Convection in Microchannels with Finite Debye-Layer Thickness, *Numerical Heat Transfer, Part A: Applications*, 48 (10) (2005) 941 – 964.
- [61] H. Herwig, S. P. Mahulikar, Variable property effects in single-phase incompressible flows through microchannels, *International Journal of Thermal Sciences* 45 (2006) 977–981.
- [62] F. Hong, P. Cheng, Three dimensional numerical analyses and optimization of offset strip-fin microchannel heat sink, *International Communications in Heat and Mass Transfer* 36 (2009) 651–656.
- [63] ***, 3M™ Novec™ 7600 Engineered Fluid, 3M Electronics Markets Materials Division, (2008).
- [64] M.E. Arici, O. Aydin, Conjugate heat transfer in thermally developing laminar flow with viscous dissipation effects, *Heat and Mass Transfer* 45 (2009) 1199–1203.
- [65] G.P. Celata, G.L. Morini, V. Marconi, S.J. McPhail, G. Zummo, Using viscous heating to determine the friction factor in microchannels – An experimental validation, *Experimental thermal and fluid science*, 30 (2006) 725-731.
- [66] C. Rands, B.W. Webb, D. Maynes, Characterization of transition to turbulence in microchannels, *International Journal of Heat and Mass Transfer* 49 (2006) 2924–2930.
- [67] C. Nonino, S.D. Giudice, S. Savino, Temperature-Dependent Viscosity and Viscous Dissipation Effects in Simultaneously Developing Flows in Microchannels With Convective Boundary Conditions, *Journal of Heat Transfer* 129 (2007) 1187-1194.
- [68] C. Nonino, S.D. Giudice, S. Savino, Effects of viscous dissipation and temperature dependent viscosity in thermally and simultaneously developing laminar flows in microchannels, *International Journal of Heat and Fluid Flow* 28 (2007) 15-27.
- [69] Y.M. Hung, A comparative study of viscous dissipation effect on entropy generation in single-phase liquid flow in microchannels, *International Journal of Thermal Science* 48 (2009) 1026-1035.
- [70] K. Hooman, A. Ejlali, Effects of viscous heating, fluid property variation, velocity slip, and temperature jump on convection through parallel plate and circular microchannels, *International Communications in Heat and Mass Transfer* 37 (2010) 34–38.
- [71] J. van Rij, T. Ameal, T. Harman, The effect of viscous dissipation and rarefaction on rectangular microchannel convective heat transfer, *International Journal of Thermal Sciences* 48 (2009) 271–281.
- [72] K. Hooman, F. Hooman, M. Famouri, Scaling effects for flow in micro-channels: Variable property, viscous heating, velocity slip, and temperature jump, *International Communications in Heat and Mass Transfer* 36 (2009) 192–196.
- [73] G. Tunc, Y. Bayazitoglu, Heat transfer in microtubes with viscous dissipation, *International Journal of Heat and Mass Transfer* 44 (2001) 2395-2403.
- [74] M. B. Turgay, A. G. Yazicioglu, Effect of Surface Roughness in Parallel-Plate Microchannels on Heat Transfer, *Numerical Heat Transfer, Part A: Applications*, 56 (2009) 497 – 514.

- [75] H.E. Jeong, J.T. Jeong, Extended Graetz problem including streamwise conduction and viscous dissipation in microchannel, *International Journal of Heat and Mass Transfer* 49 (2006) 2151–2157.
- [76] M.S. El-Genk, I.H. Yang, Friction numbers and viscous dissipation heating for laminar flows of water in microtubes, *Journal of Heat Transfer* 130 (2008) 082405-1-13.
- [77] Y.S. Yeoun, J. Yogesh, Conjugate Heat Transfer in an Optical Fiber Coating Process, *Numerical Heat Transfer, Part A: Applications*, 51:2 (2007), 109 - 127.
- [78] D. Lelea, Effects of temperature dependent thermal conductivity on Nu number behavior in micro-tubes, *International Communications in Heat and Mass Transfer* 37 (2010) 245-249.
- [79] Chen CH (2006) Slip-flow heat transfer in a microchannel with viscous dissipation. *Heat and Mass Transfer* 42: 853-860.
- [80] Magyari E, Barletta A (2007) Analytical series solution for the fully developed forced convection duct flow with frictional heating and variable viscosity. *Heat and Mass Transfer* 45: 251 – 259.
- [81] Hung YM (2009) A comparative study of viscous dissipation effect on entropy generation in single-phase liquid flow in microchannels. *International Journal of Thermal Science* 48: 1026-1035.
- [82] Li Z, Huai X, Tao Y, Huanzhuo C (2007) Effects of thermal property variations on the liquid flow and heat transfer in microchannel heat sinks. *Applied Thermal Engineering* 27: 2803-2814.
- [83] Lee PS, Garimella SV (2006) Thermally developing flow and heat transfer in rectangular microchannels of different aspect ratios. *International Journal of Heat and Mass Transfer* 49: 3060-3067.
- [84] Qu W, Mudawar I (2002) Experimental and Numerical Study of Pressure Drop and Heat Transfer in Single-phase Micro-channel Heat Sink. *International Journal of Heat and Mass Transfer* 45: 2549 - 2565.
- [85] Fedorov A, Viskanta R (2000) Three Dimensional Conjugate Heat Transfer in the Microchannel Heat Sink for Electronic Packaging. *International Journal of Heat and Mass Transfer* 41: 399 – 415.
- [86] Rahman MM (2000) Measurements of Heat Transfer in Microchannels Heat Sinks. *International Communications in Heat and Mass Transfer* 27: 495 – 506.
- [87] Li J, Peterson GP, Cheng P (2004) Three-dimensional analysis of heat transfer in a micro-heat sink with single phase flow. *International Journal of Heat and Mass Transfer* 47: 4215 – 4231.
- [88] Wei X, Joshi YK (2004) Stacked microchannel heat sinks for liquid cooling of microelectronics component. *ASME Journal of Electronic Packaging* 126: 60–66.
- [89] Patterson MK, Wei X, Joshi Y, Prasher R (2004) Numerical study of conjugate heat transfer in stacked microchannel. *Inter Society Conference on Thermal Phenomena* 372-380.
- [90] Kim SJ, Kim D (1999) Forced Convection in Microstructures for Electronic Equipment Cooling. *Journal of Heat Transfer* 121: 639-645.
- [91] Kim SJ, Kim D, Lee DY (2000) On the local thermal equilibrium in microchannel heat sink. *International Journal of Heat and Mass Transfer* 43: 1735 - 1748.
- [92] Liu S, Zhang Y, Liu P (2007) Heat transfer and pressure drop in fractal microchannel heat sink for cooling of electronic chips. *Heat Mass Transfer* 44: 221–227.
- [93] Aynur TN, Kudussi L, Egrican N (2006) Viscous dissipation effect on heat transfer characteristics of rectangular microchannels under slip flow regime and H1 boundary conditions. *Heat Mass Transfer* 42: 1093–1101.
- [94] Chen CH (2006) Slip-flow heat transfer in a microchannel with viscous dissipation. *Heat Mass Transfer* 42: 853–860.

- [95] Hassan I (2006) Thermal-Fluid Membranes devices: A decade of progress and challenges ahead. *ASME Journal of Heat Transfer* 128: 1221-1233.
- [96] Kroeker CJ, Soliman HM, Ormiston SJ (2004) Three-dimensional thermal analysis of heat sinks with circular cooling micro-channels. *International Journal of Heat and Mass Transfer* 47: 4733 - 4744.
- [97] Ryu JH, Choi DH, Kim SJ (2003) Three-dimensional numerical optimization of a manifold microchannel heat sink. *International Journal of Heat and Mass Transfer* 46: 1553 - 1562.
- [98] Sung MK, Mudawar I (2006) Experimental and numerical investigation of single-phase heat transfer using a hybrid jet-impingement/micro-channel cooling scheme. *International Journal of Heat and Mass Transfer* 49: 682 - 694.
- [99] Genic SB, Jacimovic BM, Janjic B (2007) Experimental research of highly viscous fluid cooling in cross-flow to a tube bundle. *International Journal of Heat and Mass Transfer* 50: 1288 - 1294
- [100] Wang KC, Chiou RT (2006) Local mass/heat transfer from a wall-mounted block in rectangular channel flow. *Heat and Mass Transfer* 42: 660 - 670.
- [101] Incropera FP, DeWitt DP, Bergman TL, Lavine AS, *Fundamentals of Heat and Mass Transfer*, 6th Edition, Wiley (2006).
- [102] Ansys Fluent 14.0 documentation. Ansys 2012.
- [103] Y. Mishan, A. Mosyak, E. Pogrebnyak, G. Hetsroni, Effect of developing flow and thermal regime on momentum and heat transfer in micro-scale heat sink, *International Journal of Heat and Mass Transfer* 50 (2007) 3100-3114.
- [104] J. D. Mlcek, N.K. Anand, M. J. Rightley, Three-dimensional laminar flow and heat transfer in a parallel array of microchannels etched on a substrate, *International Journal of Heat and Mass Transfer* 51 (2008) 5182–5191.
- [105] O. Mokrani, B. Bourouga, C. Castelain, H. Peerhossaini, Fluid flow and convective heat transfer in flat microchannels *International Journal of Heat and Mass Transfer* 52 (2009) 1337-1352.
- [106] Y. Chen, C. Zhang, M. Shi, J. Wu, Three-dimensional numerical simulation of heat and fluid flow in noncircular microchannel heat sinks, *International Communications in Heat and Mass Transfer* 36 (2009) 917-920.
- [107] M. H. Saidi, R. H. Khiabani, Forced Convective Heat Transfer in Parallel Flow Multilayer Microchannels, *ASME Journal of Heat Transfer* 129 (2007) 1230-1236.
- [108] Y.J. Cheng, Numerical simulation of stacked microchannel heat sink with mixing-enhanced passive structure, *International Communications in Heat and Mass Transfer* 34 (2007) 295-303.
- [109] J. Xu, Y. Song, W. Zhang, H. Zhang, Y. Gan, Numerical simulations of interrupted and conventional microchannel heat sinks, *International Journal of Heat and Mass Transfer* 51 (2008) 5906–5917.
- [110] S. Liu, Y. Zhang, P. Liu Heat transfer and pressure drop in fractal microchannel heat sink for cooling of electronic chips, *Heat Mass Transfer* 44 (2007) 221–227.
- [111] K. Hooman, Heat and fluid flow in a rectangular microchannel filled with a porous medium, *International Journal of Heat and Mass Transfer* 51 (2008) 5804–5810.
- [112] S.P. Gurrum, Y.K. Joshi, J. Kim, Thermal Management of High Temperature Pulsed Electronics using Metallic Phase Change Materials, *Numerical Heat Transfer, Part A: Applications*, 42 (8) (2002) 777 – 790.
- [113] C. Sert, A. Beskok, Oscillatory Flow Forced Convection in Micro Heat Spreaders, *Numerical Heat Transfer, Part A: Applications*, 42 (7) (2002) 685 – 70.

- [114] F. Chang, V.K. Dhir, Mechanisms of Heat Transfer Enhancement and Slow Decay of Swirl in Tubes using Tangential Injection, *International Journal of Heat Fluid Flow* 16 (1995) 78-87.
- [115] H. Gul, Enhancement of Heat Transfer in a Circular Tube With Tangential Swirl Generators, *Experimental Heat Transfer* 19(2) (2006) 81 – 93.
- [116] D. Lelea, The microtube heat sink with tangential impingement jet and variable fluid properties, *Heat and Mass Transfer* 45(9) (2009) 1215 – 1222.
- [117] M.B. Bowers, I. Mudawar, Two-Phase Electronic Cooling Using Mini-Channel and Micro Channel Heat Sinks: Part 1 - Design Criteria and Heat Diffusion Constraints, *Journal of Electronic Packaging* 116 (1994) 290-297.
- [118] D. Lelea, The microtube heat sink with tangential impingement jet and variable fluid properties, *Heat and Mass Transfer* 45(9) (2009) 1215 – 1222.
- [119] D. Lelea, Effects of inlet geometry on heat transfer and fluid flow of tangential micro-heat sink, *International Journal of Heat and Mass Transfer* 53 (2010) 3562–3569.
- [120] Choi SUS. Enhancing thermal conductivity of fluids with nanoparticles, in *Developments and Applications of Non-Newtonian Flows*. ASME FED 231/MD 66 (1995) 99–103.
- [121] Y. Yang, Z. G. Zhang, E. A. Grulke, W. B. Anderson, G. Wu, Heat transfer properties of nanoparticle-in-fluid dispersions (nanofluids) in laminar flow, *International Journal of Heat and Mass Transfer* 48 (2005) 1107–1116.
- [122] A. Amrollahi, A.M. Rashidi, R. Lotfi, M. Emami Meibodi, K. Kashefi, Convection heat transfer of functionalized MWNT in aqueous fluids in laminar and turbulent flow at the entrance region, *International Communications in Heat and Mass Transfer* 37 (2010) 717–723.
- [123] A. D. Sommers, K. L. Yerkes, Experimental investigation into the convective heat transfer and system-level effects of Al₂O₃-propanol nanofluid, *J Nanopart Res* 12 (2010) 1003–1014.
- [124] U. Rea, T. McKrell, L. Hu, J. Buongiorno, Laminar convective heat transfer and viscous pressure loss of alumina–water and zirconia–water nanofluids, *International Journal of Heat and Mass Transfer* 52 (2009) 2042–2048.
- [125] M. Izadi, A. Behzadmehr, D. Jalali-Vahida, Numerical study of developing laminar forced convection of a nanofluid in an annulus, *International Journal of Thermal Sciences* 48 (2009) 2119–2129.
- [126] D. Wen, Y. Ding, Experimental investigation into convective heat transfer of nanofluids at the entrance region under laminar flow conditions, *International Journal of Heat and Mass Transfer* 47 (2004) 5181–5188
- [127] K.B. Anoop, T. Sundararajan, S.K. Das, Effect of particle size on the convective heat transfer in nanofluid in the developing region, *International Journal of Heat and Mass Transfer* 52 (2009) 2189–2195.
- [128] S. Zeinali Heris, S.Gh. Etemad, M. Nasr Esfahany, Numerical Investigation of Nanofluid Laminar Convective Heat Transfer through a Circular Tube, *Numerical Heat Transfer, Part A: Applications*, 52(11) (2007) 1043 – 1058.
- [129] R. Lotfi, Y. Saboohi, A.M. Rashidi, Numerical study of forced convective heat transfer of Nanofluids: Comparison of different approaches, *International Communications in Heat and Mass Transfer* 37 (2010) 74–78.
- [130] M.H. Fard, M.N. Esfahany, M.R. Talaie, Numerical study of convective heat transfer of nanofluids in a circular tube two-phase model versus single-phase model, *International Communications in Heat and Mass Transfer* 37 (2010) 91–97.

- [131] S.M. Fotukian, M. Nasr Esfahany, Experimental study of turbulent convective heat transfer and pressure drop of dilute CuO/water nanofluid inside a circular tube, *International Communications in Heat and Mass Transfer* 37 (2010) 214–219
- [132] E. Abu-Nada, Effects of variable viscosity and thermal conductivity of Al₂O₃–water nanofluid on heat transfer enhancement in natural convection, *International Journal of Heat and Fluid Flow* 30 (2009) 679–690.
- [133] C. T. Nguyen, G. Roy, C. Gauthier, N. Galanis, Heat transfer enhancement using Al₂O₃–water nanofluid for an electronic liquid cooling system, *Applied Thermal Engineering* 27 (2007) 1501–1506.
- [134] J. Koo, C. Kleinstreuer, Laminar nanofluid flow in microheat-sinks, *International Journal of Heat and Mass Transfer* 48 (2005) 2652–2661.
- [135] J. Lee, I. Mudawar, Assessment of the effectiveness of nanofluids for single-phase and two-phase heat transfer in micro-channels, *International Journal of Heat and Mass Transfer* 50 (2007) 452–463
- [136] B. Ghasemi, S.M. Aminossadati, Natural Convection Heat Transfer in an Inclined Enclosure Filled with a Water-Cuo Nanofluid, *Numerical Heat Transfer, Part A: Applications*, 55(8) (2009) 807 – 823.
- [137] Y.M. Hung, Analytical Study on Forced Convection of Nanofluids with Viscous Dissipation in Microchannels, *Heat Transfer Engineering*, 31(14) (2010) 1184 – 1192.
- [138] H. A. Mintsa, G. Roy, C. T. Nguyen, D. Doucet, New temperature dependent thermal conductivity data for water-based nanofluids, *International Journal of Thermal Sciences*, 48 (2009) 363–371.
- [139] C. H. Chon, K. D. Kihm, S. P. Lee, S.U.S. Choi, Empirical correlation finding the role of temperature and particle size for nanofluid (Al₂O₃) thermal conductivity enhancement, *Applied Physics Letters* 87 (2005) 153107-(1-3).
- [140] N. Masoumi, N. Sohrabi, A. Behzadmehr, A new model for calculating the effective viscosity of nanofluids, *J. Phys. D: Appl. Phys* 42 (2009) 055501-(1-6).
- [141] C.T. Nguyen, F. Desgranges, G. Roy, N. Galanis, T. Mare, S. Boucher, H. Angue Mintsa, Temperature and particle-size dependent viscosity data for water-based nanofluids – Hysteresis phenomenon, *International Journal of Heat and Fluid Flow* 28 (2007) 1492–1506.
- [142] S.Q. Zhoua, R. Ni, Measurement of the specific heat capacity of water-based Al₂O₃ nanofluid, *Applied Physics Letters* 92 (2008) 093123-(1-3).
- [143] L. Godson, B. Raja, D. Mohan Lal, S. Wongwises, Enhancement of heat transfer using nanofluids—An overview, *Renewable and Sustainable Energy Reviews* 14 (2010) 629–641.
- [144] R. Perry, D. Green, *Perry's Chemical Engineers' Handbook*, McGraw-Hill, New York, NY, 1999.
- [145] D. Lelea, C. Nisulescu, The micro-tube heat flow of water based Al₂O₃ nanofluid with viscous dissipation, *International Communications in Heat and Mass Transfer* Volume 38, Issue 6, July 2011, Pages 704-710.
- [146] Kelkar, K. M., Patankar, S.V., Numerical Prediction of Fluid Flow and Heat Transfer in a Circular Tube with Longitudinal Fins Interrupted in Stream Wise Direction, *Journal of heat transfer*, Vol. 112, p. 342 - 348, 1990.
- [147] Patankar, S.V., Spalding, D.B., A calculation procedure for heat, mass and momentum transfer in three-dimensional parabolic flows, *International journal of heat mass transfer*, Vol 15, p. 1787 - 1806, 1972.
- [148] Sparow E.M., Liu, C.H., Heat Transfer, Pressure Drop and Performance Relationships for In-Line, Staggered, and Continuous Plate Heat Exchangers, *International journal of heat mass transfer*, Vol. 22, p. 1613-1625, 1979.

- [149] V. Kumar, M. Paraschivoiu, K.D.P. Nigam, Single-phase fluid flow and mixing in microchannels, *Chemical Engineering Science* 66 (2011) 1329–1373
- [150] Elmabruk A. Mansur, YE Mingxing, WANG Yundong, DAI Youyuan, A State-of-the-Art Review of Mixing in Microfluidic Mixers, *Chinese Journal of Chemical Engineering*, 16(4) 503-516 (2008).
- [151] Jeffrey T. Coleman, David Sinton, A sequential injection microfluidic mixing strategy, *Microfluid Nanofluid* (2005) 1: 319–327.
- [152] M. A. Ansari, Kwang-Yong Kim, Sun Min Kim, Numerical study of the effect on mixing of the position of fluid stream interfaces in a rectangular microchannel, *Microsyst Technol* (2010) 16:1757–1763.
- [153] Minghou Liu, Chen Xie, Xiangfeng Zhang, Yiliang Chen, Numerical simulation on micromixer based on synthetic jet, *Acta Mech Sin* (2008) 24:629–636.
- [154] Wonjin Jeon, Chee Burm Shin, Design and simulation of passive mixing in microfluidic systems with geometric variations, *Chemical Engineering Journal* 152 (2009) 575–582.
- [155] Lilin Wang, Jing-Tang Yanga, Ping-Chiang Lyuc, An overlapping crisscross micromixer, *Chemical Engineering Science* 62 (2007) 711 – 720.
- [156] S. Hardt, H. Pennemann, F. Schonfeld, Theoretical and experimental characterization of a low-Reynolds number split-and-recombine mixer, *Microfluid Nanofluid* (2006) 2: 237–248.
- [157] Wei-Feng Fanga, Jing-Tang Yang, A novel microreactor with 3D rotating flow to boost fluid reaction and mixing of viscous fluids, *Sensors and Actuators B* 140 (2009) 629–642.
- [158] Jang Min Park, Dong Sung Kim, Tae Gon Kang, Tai Hun Kwon, Improved serpentine laminating micromixer with enhanced local advection, *Microfluid Nanofluid* (2008) 4:513–523.
- [159] Kevin L. McIlhany, Stephen Wiggins, Optimizing mixing in channel flows: kinematic aspects associated with secondary flows in the cross-section, *Microfluid Nanofluid* (2011) 10:249–262.
- [160] Beom Seok Kim, Bong Seop Kwak, Sangwoo Shin, Sanghoon Lee, Kyung Min Kim, Hyo-Il Jung, Hyung Hee Cho, Optimization of microscale vortex generators in a microchannel using advanced response surface method, *International Journal of Heat and Mass Transfer* 54 (2011) 118–125.
- [161] Kuo-Wei Lin, Jing-Tang Yang, Chaotic mixing of fluids in a planar serpentine channel, *International Journal of Heat and Mass Transfer* 50 (2007) 1269–1277.
- [162] Jayaprakash Sivasamy, ZhizhaoChe, TeckNengWonga, Nam-Trung Nguyen, LeventYoba, A simple method for evaluating and predicting chaotic advection in microfluidic slugs, *Chemical Engineering Science* 65 (2010) 5382–5391.
- [163] E. Gouillart, O. Dauchot, J.-L. Thiffeault, Measures of mixing quality in open flows with chaotic advection, *Physics of Fluids* 23, 013604 _2011
- [164] T.N.T. Nguyena, Min-Chan Kimb, Joon-Shik Park, N.-E. Lee, An effective passive microfluidic mixer utilizing chaotic advection, *Sensors and Actuators B* 132 (2008) 172–181.
- [165] Kuo-Wei Lin, Jing-Tang Yang, Chaotic mixing of fluids in a planar serpentine channel, *International Journal of Heat and Mass Transfer* 50 (2007) 1269–1277.
- [166] Cha, J., Kim, J., Ryu, S.K., Park, J., “A highly efficient 3D micromixer using soft PDMS bonding”, *J. Micromech. Microeng.*, 16, 1778-1782 (2006).
- [167] Zhao, B., Moore, J.S., Beebe, D.J., “Principles of surface-directed liquid flow in microfluidic channels”, *Anal. Chem.*, 74, 4259-4268 (2002).
- [168] Chung, Y.C., Hsu, Y.L., Jen, C.P., Lu, M.C., Lin, Y.C., “Design of passive mixers utilizing microfluidic self-circulation in the mixing chamber”, *Lab Chip*, 4, 70-79 (2004).
- [169] Sundaram, N., Tafti, D.K., “Evaluation of microchamber geometries and surface conditions for electrokinetic driven mixing”, *Anal. Chem.*, 76, 3785-3793 (2004).

- [170] Lin Jin Ming, Huang Li Zhang, Chen Guo Nan, A three-dimensional vortex microsystem designed and fabricated for controllable mixing, *Sci China Ser B-Chem Aug.* 2009, vol. 52 no. 8 1080-1084.
- [171] Adrian Neilda, Tuck Wah Nga, Gregory J. Sheardb, Matthew Powersa, Stefano Oberti, Swirl mixing at microfluidic junctions due to low frequency side channel fluidic perturbations, *Sensors and Actuators B* 150 (2010) 811–818.
- [172] Che-Hsin Lin, Chien-Hsiung Tsai, Chih-Wen Pan, Lung-Ming Fu, Rapid circular microfluidic mixer utilizing unbalanced driving Force, *Biomed Microdevices* (2007) 9:43–50.
- [173] Hoffmann, M., Raebiger, N., Schlueter, M., Blazy, S., Bothe, D., Stemich, C., Warnecke, A., 2003. Experimental and numerical investigations of T-shaped micromixers. In: *Proceedings of the 11th European Conference on Mixing, Bamberg, Germany*, pp. 269–276
- [174] Yi, M., Bau, H.H., 2003. The kinematics of bend-induced mixing in micro-conduits. *International Journal of Heat and Fluid Flow* 24, 645–656.
- [175] Holden, M., Kumar, S., Beskok, A., Cremer, P., 2003. Microfluidic diffusion diluter: bulging of PDMS microchannels under pressure-driven flow. *Journal of Micromechanics and Microengineering* 13, 412–418.
- [176] Diana Broboana, Catalin Mihai Balan, Thorsten Wohland, Corneliu Balan, Investigations of the unsteady diffusion process in microchannels, *Chemical Engineering Science* 66 (2011) 1962–1972.
- [177] Wanjun Wang, Steven A. Soper, *Bio-MEMS Technologies and Applications*, CRC press Taylor & Francis Group 2007.
- [178] J. Li, C. Kleinstreuer, Microfluidics analysis of nanoparticle mixing in a microchannel system, *Microfluid Nanofluid* (2009) 6:661–668.
- [179] C. Kleinstreuer, J. Li, J. Koo, Microfluidics of nano-drug delivery, *International Journal of Heat and Mass Transfer* 51 (2008) 5590–5597.
- [180] D. Lelea, The performance evaluation of Al₂O₃/water nanofluid flow and heat transfer in microchannel heat sink, *International Journal of Heat and Mass Transfer* 54 (2011) 3891–3899